Plasma Physics Reports, Vol. 30, No. 9, 2004, pp. 717–729. Translated from Fizika Plazmy, Vol. 30, No. 9, 2004, pp. 771–783.

TOKAMAKS

Stiffness and Rigidity of the Temperature Profile in a Tokamak

Yu. N. Dnestrovskij, A. Yu. Dnestrovskij, and S. E. Lysenko

Nuclear Fusion Institute, Russian Research Centre Kurchatov Institute, Moscow, 123182 Russia

Received October 30, 2003; in final form, January 8, 2004

Abstract—The notions of "stiffness" and "rigidity" of the temperature profile in a tokamak are introduced and formalized. By stiffness is meant the consistency of the profile when the plasma density, boundary temperature, and heating power change. By rigidity is meant the strong dependence of the central temperature on the boundary temperature. Analytical and numerical estimates carried out in a transport model with critical temperature gradients show that, at a low boundary temperature (the L-mode), the profiles are, as a rule, stiff but are not rigid. For a sufficiently high temperature pedestal in the H-mode, there exists a parameter range in which the profiles are stiff and at the same time rigid. However, when the pedestal temperature is too high and the deposited power profile is flat, the temperature profile may be neither stiff nor rigid. This behavior of the electron temperature profile was observed in a number of H-mode discharges with high plasma densities in the DIII-D and JET tokamaks. An analysis is also made of the stiffness and rigidity of the temperature profiles in the MAST and T-10 tokamaks. © *2004 MAIK "Nauka/Interperiodica".*

1. INTRODUCTION

Beginning with the familiar paper by B. Coppi [1], the consistency (preservation) of the temperature profiles in a tokamak has been pointed out in many studies. For a number of reasons, only the electron temperature profile has been discussed so far. However, in recent experiments on the ASDEX Upgrade tokamak, the evolution of both the electron and ion temperature profiles was traced in several regimes [2]. Those experiments have provided additional evidence for the conservation of the shape of the relative temperature profiles when the plasma parameters change considerably. To the best of our knowledge, this is the first evidence that the ion temperature profiles maintain their shape even better than do the electron temperature profiles.

Along with the notion of profile consistency, the notion of profile stiffness is often used in the literature. Unfortunately, the latter is somewhat ambiguous. Stiffness is most frequently understood as the consistency of the relative profile shape when the discharge conditions change. Sometimes, however, the profile is regarded as being stiff if the magnitudes of the temperature inside the plasma column are proportional to the boundary temperature. This second definition of stiffness is not actually equivalent to the first one. It is only when the relative temperature profile maintains its shape over the entire plasma column (up to the plasma boundary) that the definitions are equivalent. However, in experiments, the profile consistency is usually observed only in the so-called gradient zone $0.4a < r < 0.8a$, where a is the minor plasma radius. In the edge plasma region $r > 0.8a$, there can be a transition layer [3] in which the strong relationship between the temperature profile within the plasma and the boundary conditions is violated. In the present paper, for brevity, the property of the plasma to conserve the temperature profile will be called the profile stiffness (or simply stiffness), while the strong relationship between the magnitudes of the central temperature and the boundary temperatures will be called the profile rigidity (or simply rigidity). More precise definitions will be given below.

In transport models, the consistency of the temperature profile shape is described using the notion of the critical temperature gradient. When the temperature gradient becomes greater than its critical value, the heat flux increases sharply, so that the temperature profile changes only slightly. The critical temperature gradient can be defined in different ways. Ryter *et al.* [4] related the critical gradient to the stability boundary of drift oscillations such as the ion temperature gradient (ITG) mode, the electron temperature gradient (ETG) mode, and the trapped electron mode (TEM). In our earlier papers [5, 6], the critical gradient was treated as being connected with the canonical profiles of the temperature and current, which were defined in terms of the minimum of the free plasma energy functional.

Our purpose in the present paper is to find out the conditions under which the electron and ion temperature profiles acquire the property of being stiff and rigid. In Section 2, more rigorous definitions are given of the notions of stiffness and rigidity. In Section 3, examples of discharges with different deposited power profiles are considered in terms of the transport model with a critical gradient [6] and the conditions under which the temperature profile is stiff and rigid are determined. In Section 4, results are presented from numerical simulations of the effects related to the profile stiffness and rigidity in the T-10 and MAST tokamaks. In the last part of this section, results are reported of computer simulations of a number of high-density H-mode

1063-780X/04/3009-0717$26.00 © 2004 MAIK "Nauka/Interperiodica"

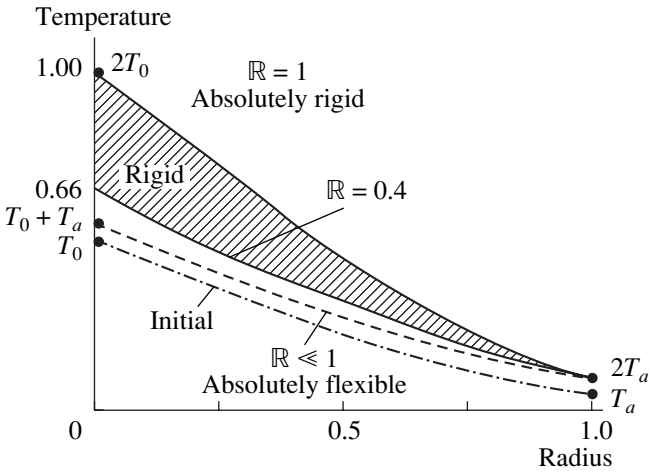

Fig. 1. What happens to the profile when the boundary temperature T_a is increased by a factor of two? If the profile is absolutely flexible, then the central temperature increases by an amount equal to T_a. If the profile is absolutely rigid, then the central temperature doubles. The region of rigid profiles is hatched.

discharges in the DIII-D and JET tokamaks. It is shown that, in these discharges, the electron temperature profiles do not possess the property of being stiff and rigid. In the Conclusion, the limiting values of the plasma parameters at which the temperature profiles may or may not be stiff and rigid are discussed.

2. DEFINITION OF THE STIFFNESS AND RIGIDITY OF THE TEMPERATURE PROFILE

In order to define the profile stiffness, we introduce the *stiffness coefficient*

$$\mathbb{S} = (T(r = 0.4a) - T_a)/(T(r = 0.8a) - T_a). \quad (1)$$

Here, T is the electron (or ion) temperature and $T_a = T(r = a)$ is the temperature of the particles of a given species at the plasma boundary. In what follows, all definitions and formulas will refer to the electrons, as well as to the ions.

The temperature profile is called stiff if ratio (1) depends weakly on the plasma density n, deposited power P_{tot}, and boundary temperature T_a.

The choice of the surface $r = 0.4a$ in stiffness coefficient (1) is dictated by the fact that, in the region $r < 0.4a$, the temperature profile is often perturbed by sawtooth oscillations. The choice of the surface $r = 0.8a$ is governed by the existence of a transitional ("soft") layer in the edge plasma (see the Introduction). The inner region $0.4a < r < 0.8a$ is often referred to as a gradient zone. Ratio (1) contains the temperatures at the boundary surfaces of this zone. The magnitude of the ratio can depend on the plasma current, plasma geometry, and deposited power profile [7]. As the deposited power profile changes from peaked to flat, the stiffness coefficient $\mathbb{S}$ decreases. In particular, for H-mode discharges in ASDEX-U, we have $\mathbb{S}_i \approx 2.3$ and $\mathbb{S}_e \approx 5$ [2]. The reasons for choosing ratio (1) as a basis for the definition of stiffness will be discussed in Section 3.1.3.

The notion of the profile rigidity is associated with the dependence of the central temperature $T_0 = T(r = 0)$ on the boundary temperature $T_a = T(r = a)$. In order to define this notion, it is convenient to introduce the *rigidity coefficient*

$$\mathbb{R} = (T_a/T_0)dT_0/dT_a. \quad (2)$$

The stiff temperature profile is called rigid if the coefficient $\mathbb{R}$ satisfies the condition

$$\mathbb{R} > \mathbb{R}_0 = 0.4. \quad (3)$$

Integrating coefficient (2) over T_0 gives

$$T_0 = CT_a^{\mathbb{R}}. \quad (4)$$

The profile is rigid if the exponent in this relationship satisfies condition (3). The magnitude of $\mathbb{R}$ depends on many factors, such as the boundary temperature, the magnitude and profile of the deposited power, and the plasma geometry. From the examples given below, it will be clear that, for a low boundary temperature, condition (3) fails to hold and the temperature profile is not rigid.

The notion of the profile rigidity is illustrated in Fig. 1, which shows how the temperature profiles characterized by different values of the rigidity coefficient $\mathbb{R}$ can change as the boundary temperature T_a increases by a factor of two. If the profile is not rigid (or, in other words, is "flexible"), $\mathbb{R} \ll 1$, then the central temperature can be expected to increase by the same amount as the boundary temperature, $\delta T_0 = \delta T_a$ (see the "absolutely flexible" profile in Fig. 1). If the profile is "absolutely rigid" ($\mathbb{R} = 1$), then, by virtue of relationship (4), the central temperature depends linearly on the boundary temperature. In Fig. 1, the region of rigid profiles, satisfying inequality (3), is hatched.

3. ANALYTIC ESTIMATES OF THE REGION OF STIFF AND RIGID PROFILES

3.1. Linearized Temperature Equation with a Critical Gradient

As an example, we consider the temperature equation for a circular-cross-section plasma column with the minor radius a and the major radius R. By the temperature T here we mean the electron temperature, but the analysis below also refers to the ion temperature. The heat flux Γ is described by the following expression with the critical gradient [6]:

$$-\Gamma = \kappa[dT/dr - (dT_c/dr)T/T_c] + \kappa_0 dT/dr. \quad (5)$$

Here, κ and κ_0 are the main and background thermal conductivities ($\kappa \gg \kappa_0$), T_c is the canonical temperature

profile, and r is the radial coordinate. The background thermal conductivity κ_0 includes the neoclassical thermal conductivity and the anomalous thermal conductivity, which is not associated with the critical gradients. Note that expression (5) for the heat flux admits a heat pinch. If the gradient dT/dr becomes smaller than the critical gradient $(dT_c/dr)\ T/T_c$, heat flux (5) can change its sign. This problem will be discussed in more detail below in Section 3.2. We introduce the dimensionless critical gradient $\Omega_c = R/L_{Tc} = -R/T_c dT_c/dr$ and dimensionless coordinate $\rho = r/a$, in terms of which expression (5) for the heat flux takes the form

$$-\Gamma = ((\kappa + \kappa_0)/a)[dT/d\rho + \lambda T], \tag{6}$$

where

$$\lambda = (\kappa/(\kappa + \kappa_0))\lambda_0, \quad \lambda_0 = \Omega_c/A \quad (\lambda < \lambda_0), \tag{7}$$

and $A = R/a$ is the aspect ratio. The parameter λ describes the rate at which the solution increases exponentially from the boundary of the plasma toward its center. In this section, we are assuming that the quantities κ, κ_0, and λ are constant over the plasma radius and are independent of T. Having made these assumptions, we also ignore both the toroidicity-induced corrections in the expression for the divergence and the ion–electron energy exchange term to write the time-independent temperature equation in the form

$$-(1/\rho)d/d\rho\{\rho(\kappa + \kappa_0)/a^2[dT/d\rho + \lambda T]\} = P. \tag{8}$$

Here,

$$P = P(\rho) = P_0 f(\rho) \tag{9}$$

is the deposited power profile, $f(\rho)$ is a dimensionless function,

$$P_0 = P_{\text{tot}}/(2VF(1)), \tag{10}$$

$$F(\rho) = \int_0^\rho f(\rho')\rho' d\rho', \tag{11}$$

P_{tot} is the total deposited power, and V is the plasma volume. Under the above assumptions, Eq. (8) is linear. Integrating this equation once, we obtain

$$dT/d\rho + \lambda T = -T^*. \tag{12}$$

Here,

$$T^* = T_a^* g(\rho) \tag{13}$$

is the characteristic temperature that depends on the magnitude and profile of the deposited power and on the thermal conductivity,

$$T_a^* = P_{\text{tot}}/(R(\kappa + \kappa_0)(2\pi)^2), \tag{14}$$

$$g(\rho) = P_{\text{tot}}(\rho)/(\rho P_{\text{tot}}), \quad (g(0) = 0, g(1) = 1), \tag{15}$$

and

$$P_{\text{tot}}(\rho) = \int_{V_\rho} P dV = P_{\text{tot}} F(\rho)/F(1)$$

is the power deposited within a surface of radius ρ. By virtue of expression (6) and Eq. (12), we have $\Gamma = (\kappa + \kappa_0)T^*/a$.

We consider the boundary-value problem for Eq. (12) with the boundary condition

$$T(\rho = 1) = T_a. \tag{16}$$

Since Eq. (12) is linear, the solution to this problem can be represented as the sum

$$T = T_1 + T_2, \tag{17}$$

where

$$T_1 = T_a \exp(\lambda(1 - \rho)) \tag{18}$$

is the solution to Eq. (12) with zero on the right-hand side that satisfies boundary condition (16) and

$$T_2 = T_a^* G(\rho),$$
$$G(\rho) = \int_\rho^1 \exp(\lambda(\rho' - \rho)) g(\rho') d\rho' \geq 0 \tag{19}$$

is a particular solution to inhomogeneous equation (12) that satisfies the zero boundary condition $T_2(\rho = 1) = 0$. The solution T_1 depends linearly on the boundary condition and its profile coincides (to within the replacement of $\kappa + \kappa_0$ by κ) with the canonical temperature profile $T_c = \exp(\lambda_0(1 - \rho))$. The profile of the solution is peaked centrally because of the presence of the heat pinch. The solution T_2 depends on the magnitude and profile of the deposited power and is independent of the boundary condition.

Substituting relationships (17)–(19) into formula (1) yields the following expression for the stiffness parameter:

$$\mathbb{S} = \exp(0.4\lambda)\mathbb{S}_0, \tag{20}$$

where

$$\mathbb{S}_0 = \{1 - \exp(-0.6\lambda) + \gamma G(0.4)\exp(-0.6\lambda)\}/\{1 - \exp(-0.2\lambda) + \gamma G(0.8)\exp(-0.2\lambda)\}, \tag{21}$$

$$\gamma = T_a^*/T_a. \tag{22}$$

Using formula (2) and relationships (17)–(19), we obtain the rigidity criterion

$$\mathbb{R} = 1/\{1 + \gamma\exp(-\lambda)G(0)\} > \mathbb{R}_0. \tag{23}$$

Expressions (20) and (21) for $\mathbb{S}$ and expression (23) for $\mathbb{R}$ contain two dimensionless physical parameters: λ, given by formula (7), and γ, given by formula (22). The first parameter, λ, depends on the plasma geometry and

on the parameter q. The second parameter, γ, depends on the total deposited power and the boundary temperature, as well as on the plasma density (through the thermal conductivity). By the definition of stiffness, the temperature profile is stiff if the parameter $\mathbb{S}$ is independent of γ. Since the numerator and denominator in expression (21) are both linear in γ, the parameter $\mathbb{S}$ is generally a weak function of γ. In the limits of infinitely large ($\gg 1$) and infinitely small ($\ll 1$) values of the parameter γ, it drops out of the expression for $\mathbb{S}$, so that the temperature profile is stiff. The intermediate case $\gamma \sim 1$ will be considered below in the discussion of particular examples.

The rigidity criterion can be rewritten as the following condition for the parameter γ:

$$\gamma < \gamma^{\max}, \tag{24}$$

where

$$\gamma^{\max} = (1/R_0 - 1)/(\exp(-\lambda)G(0)) = 1.5\exp(\lambda)/G(0). \tag{25}$$

3.2. Nonlinear Temperature Equation without a Heat Pinch

When the gradient dT/dr is sufficiently small, the heat flux Γ given by expression (5) changes its sign. A reversal of the direction of the heat flux at a constant sign of the temperature gradient is usually called the heat pinch effect. Since the question of whether this effect does indeed occur in experiments remains open, it is expedient to consider, along with expression (5), the following expression for the heat flux, which does not allow a heat pinch:

$$\begin{aligned} -\Gamma &= \kappa[dT/dr - (dT_c/dr)T/T_c] \\ &\times H(-[(dT/dr)/T - (dT_c/dr)/T_c]) + \kappa_0 dT/dr, \end{aligned} \tag{26}$$

where $H = H(x)$ is the Heaviside step function defined as $H(x) = 1$ for $x \geq 0$ and $H(x) = 0$ for $x < 0$. Note that expression (26) for the heat flux is strongly nonlinear. Below, we will use the following notation for the dimensionless argument of the Heaviside function:

$$\Delta = [\Omega_T - \Omega_c], \tag{27}$$

where

$$\begin{aligned} \Omega_T &= -(R/a)(dT/d\rho)/T > 0, \\ \Omega_c &= -(R/a)(dT_c/d\rho)/T_c > 0 \end{aligned} \tag{28}$$

is the critical gradient and T_c is the canonical temperature profile. If

$$\Delta > 0, \tag{29}$$

then the Heaviside function H in expression (26) is equal to unity and fluxes (5) and (26) coincide. If inequality (29) fails to hold in the gradient zone, then the profile ceases to be stiff, in which case the temperature profile within the gradient zone becomes flatter than the canonical profile. Using Eq. (12), we can reduce inequality (29) to

$$T^*(\rho)/T(\rho) > \lambda/\beta, \tag{30}$$

where

$$\beta = \kappa/\kappa_0 \gg 1. \tag{31}$$

Inserting expressions (13) and (17)–(19) for T^* and T into inequality (30) and resolving the resulting inequality with respect to the parameter γ, we arrive at the following new condition, which is equivalent to those above:

$$\gamma > \gamma^{\min}(\rho), \tag{32}$$

where

$$\gamma^{\min}(\rho) = \lambda\exp(\lambda(1-\rho))/[g(\rho)\beta - \lambda G(\rho)]. \tag{33}$$

We emphasize that this condition, which determines the boundary of the region of stiff and rigid temperature profiles, stems from the assumption that there is no heat pinch and from the fact that expression (26) for the heat flux contains the Heaviside function. By virtue of inequality (31), the denominator in expression (33) is positive almost everywhere, i.e., everywhere except possibly for a small neighborhood of the plasma axis $\rho = 0$ where the function $g(\rho)$ is small.

At the boundary of the plasma column ($\rho = 1$), we have $g = 1$, $G = 0$, and $\gamma^{\min}(1) = \lambda/\beta$, so that inequality (32) takes the form

$$\gamma > \lambda/\beta. \tag{34}$$

Inequality (30) is usually satisfied even for H-mode discharges. This indicates that, at the plasma edge, the temperature gradient exceeds the critical gradient and the Heaviside function in expression (26) is equal to unity for this region.

For sufficiently large (>1) values of the parameter λ, the quantity $\gamma^{\min}(\rho)$ increases exponentially toward the plasma axis, so that, within a certain surface of radius $\rho = \rho_0$, inequality (32) may fail to hold. In the region $\rho < \rho_0$, the Heaviside function is equal to zero, $H = 0$, and the temperature profile becomes flatter. It is clear that, for this effect to be pronounced, the surface of radius ρ_0 should occur inside the gradient zone. Since, in this case, the characteristic surface is the one having the radius $\rho = 0.5$, we consider the quantity $\gamma^{\min}(\rho)$ precisely at this radius:

$$\begin{aligned} \gamma^{\min} &\equiv \gamma^{\min}(\rho = 0.5) \\ &= \lambda\exp(\lambda/2)/[g(0.5)\beta - \lambda G(0.5)]. \end{aligned} \tag{35}$$

If $\gamma < \gamma^{\min}$, then the temperature profile ceases to be stiff and loses its possible rigidity. Hence, the temperature profile is stiff under the condition

$$\gamma > \gamma^{\min} \text{ (stiffness condition)}, \tag{36}$$

and is rigid under the condition

$$\gamma^{\min} < \gamma < \gamma^{\max} \text{ (rigidity condition)}, \tag{37}$$

where γ^{max} is defined by expression (25).

The above considerations, as well as formula (35), are valid for $\lambda > 1$. For small-aspect-ratio tokamaks, we have $\lambda < 1$ (the canonical profiles are flatter [6]) and the exponential factor in expression (33) changes only slightly over the cross section of the plasma column. As a result, as the parameter γ decreases, inequality (32) may begin to be violated at the plasma edge rather than in the plasma core. Numerical simulations for the MAST tokamak that will be described in Section 4 confirm that this can be the case.

3.3. Examples

3.3.1. Deposited power profiles. The value of the parameter $\mathbb{S}$, defined by expression (20), and rigidity criterion (37) depend on the deposited power profile through the function $G(\rho)$. Here, we consider four characteristic profiles, namely, the localized profile

$$f = f_l = 1 \ \ (\rho < \rho_0), \quad f_l = 0 \ \ (\rho > \rho_0) \ \ \rho_0 \sim 0.1 \ll 1 \quad (38l)$$

and three profiles in the form of power-low functions

$$f = f_j = \rho^{j-2} \ \ (0 < \rho < 1, j = 1, 2, 3). \quad (38j)$$

The corresponding functions $g(\rho)$ are given by the relationships

$$g_l(\rho) = \rho/\rho_0^2 \ \ (\rho < \rho_0), \quad g_l(\rho) = 1/\rho \ \ (\rho > \rho_0) \quad (39l)$$

$$g_j = \rho^{j-1} \ \ (0 < \rho < 1, j = 1, 2, 3). \quad (39j)$$

The plots of functions (38) are shown in Fig. 2. Note that the dimensionless parameter

$$\xi = 2P(1)V/P_{tot} \quad (40)$$

characterizes the deposited power profile and is equal to zero for a localized profile and to j for profiles in the form of power-low functions.

3.3.2. Localized input power profile f_l. We consider a localized deposited power profile separately because, in this case, the function $G(\rho)$ cannot be expressed in terms of elementary functions. In the region $\rho > \rho_0$, the function $G(\rho)$ has the form

$$G_l(\rho) = \exp(-\lambda\rho)(\mathrm{Ei}(\lambda) - \mathrm{Ei}(\lambda\rho)), \quad (41)$$

where

$$\mathrm{Ei}(x) = \mathrm{pv}\int_{-\infty}^{x} \exp(z)/z\,dz \quad (42)$$

is the integral exponent (the symbol "pv" denotes the principal value of the integral). In the region $0.2 < x < 2.5$, the integral exponent $\mathrm{Ei}(x)$ is well approximated by a linear function:

$$\mathrm{Ei}(x) \approx 3.12(x - 0.4).$$

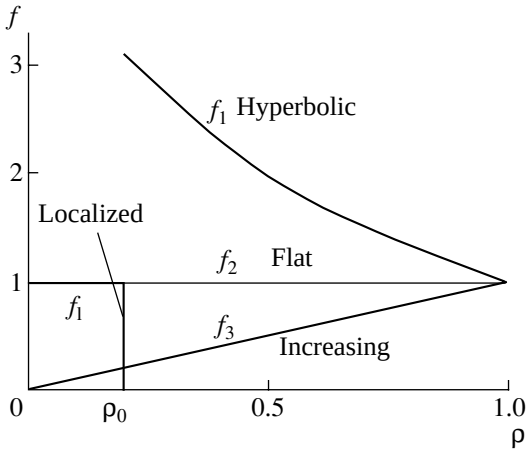

Fig. 2. Plots of the function f for four profiles of the deposited power.

As a result, we can write the following approximate expression for the function $G(\rho)$:

$$G_l(\rho) \approx 3.12\lambda(1-\rho)\exp(-\lambda\rho) \quad (\rho_0 < \rho < 1, 0.2 < \lambda\rho < 2.5, 0.2 < \lambda < 2.5). \quad (43)$$

Substituting expression (43) into expression (21) yields

$$\mathbb{S}_{01} = [1 - \exp(-0.6\lambda) + 1.87\gamma\lambda\exp(-\lambda)]/[1 - \exp(-0.2\lambda) + 0.62\gamma\lambda\exp(-\lambda)]. \quad (44)$$

To find γ^{max}, we need to determine the value $G(0)$,

$$G_l(0) = G_l(\rho_0) + \Delta G, \quad (45)$$

$$\Delta G = \int_0^{\rho_0} g(\rho')\exp(\lambda(\rho' - \rho))d\rho' \approx 1/2 \quad (\text{for} \quad \rho_0 \sim 0.1 \ll 1). \quad (46)$$

Using expressions (25) and (43)–(46), we obtain

$$G_l(0) = 3.12\lambda + 1/2, \quad \gamma_l^{max} = 1.5\exp(\lambda)/(3.12\lambda + 1/2). \quad (47)$$

3.3.3. Deposited power profiles f_j in the form of power-low functions. In this case, the functions $G_j(\rho)$ are expressed in terms of elementary functions. Thus, we have

$$(j = 1) \quad G_1(\rho) = [\exp(\lambda(1-\rho) - 1]/\lambda. \quad (48)$$

$$\mathbb{S}_{01} = [1 - \exp(-0.6\lambda)]/[1 - \exp(-0.2\lambda)]. \quad (49)$$

For $j = 1$ (which corresponds to a hyperbolic deposited power profile), the function $\mathbb{S}_0$ is independent of γ, so that the temperature profile is stiff for all γ values. We also have

$$(j = 2) \quad G_2(\rho) = (1/\lambda^2)[(\lambda - 1)\exp(\lambda(1-\rho)) + 1 - \lambda\rho], \quad (50)$$

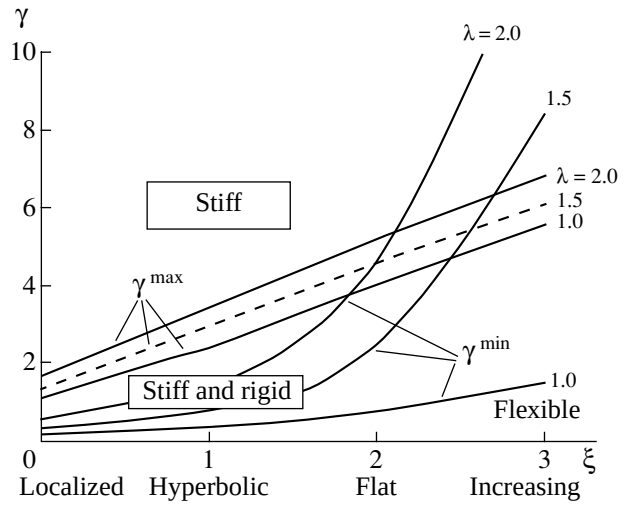

Fig. 3. Regions of stiff, rigid, and flexible temperature profiles in a parameter plane.

$$(j = 3)$$

$$G_3(\rho) = (1/\lambda^3) \times [(\lambda^2 - 2\lambda + 2)\exp(\lambda(1-\rho)) - (\lambda^2\rho^2 - 2\lambda\rho + 2)]. \quad (51)$$

The parameter $G(0)$ characterizes the peakedness of the temperature profile. Knowing $G(0)$ and using expression (25), we can calculate γ^{max}. The dependence of γ^{max} on ξ for different values of λ is shown in Fig. 3. It can be seen that γ^{max} increases almost linearly with ξ. The dependence of γ^{min} on ξ will be considered later.

3.3.4. Estimates of the dimensionless parameters for T-10, JET, and MAST. In addition to λ and γ, formula (35) for γ^{min} also contains the dimensionless parameter $\beta = \kappa/\kappa_0$. Let us examine the possible values of this parameter in more detail. We describe the coefficient κ by the same expression as that adopted in [6]:

$$\kappa = \alpha/M(1/A)^{3/4}q(\rho = 1/2)q_{cyl}(\rho = 1) \times T^{1/2}(\rho = 1/4)n/B(3/R)^{1/4}. \quad (52)$$

Here, the coefficient κ is expressed in 10^{19} m^{-1} s^{-1}, α is equal to 3.5 for electrons and to 5 for ions, M is the relative mass of an ion, the temperature T is in keV, the plasma density n is in 10^{19} m^{-3}, the magnetic field B is in T, and the major plasma radius R is in m. In these units, we have

$$\gamma = T_a^*/T_a = 15.6P_{tot}/(R(\kappa + \kappa_0))/T_a, \quad (53)$$

where the total deposited power P_{tot} is given in MW.

As for the coefficient κ_0, the experimental data on its value and its variation over the cross section of the plasma column, as well as on its dependence on the plasma parameters, are very unreliable. The most straightforward way of determining the coefficient κ_0 and the ratio κ/κ_0 is to carry out experiments with strongly localized off-axis heating, e.g., with off-axis electron cyclotron resonance heating (ECRH). In the T-10 experiments [8], an ECRH power of about 0.5 MW was deposited in the vicinity of the surface $\rho_{EC} = 0.4$. In this case, the thermal diffusivity $\chi = \kappa_0/n$ in the region $\rho \sim 0.3 < \rho_{EC}$ was equal to $\chi \approx 0.25$ m^2/s and, in the region $\rho \sim 0.45 > \rho_{EC}$, it was equal to $\chi = (\kappa + \kappa_0)/n \approx 1.8$ m^2/s. This indicates that, in the latter discharge region, the ratio in question is approximately equal to $\kappa/\kappa_0 \approx 6$. The ratio κ/κ_0 can also be determined from the ratio of the temperature gradients inside and outside the transport barrier. The ratio so determined usually lies between 5 and 10.

In this section, we assume that the coefficient β is constant over the entire cross section of the plasma column, is the same for all the shots under discussion, and is equal to $\beta = \kappa/\kappa_0 = 6$. Note that this assumption does not contradict the above experimental data. The dependence of γ^{min} on the parameter ξ for the chosen value of β and for different values of the parameter λ is also presented in Fig. 3. In this figure, the region $\gamma > \gamma^{max}$ corresponds to stiff temperature profiles, which is usually the case in L-mode discharges. In the region between the curves γ^{max} and γ^{min}, the temperature profiles are stiff and rigid simultaneously. Finally, in the region $\gamma < \gamma^{min}$, the temperature profiles are flexible, i.e., they are neither stiff and nor rigid. In this case, the Heaviside function drives the term with the critical gradient to zero, so that the temperature profiles are flat. By virtue of formula (35), the quantity γ^{min} is almost inversely proportional to the parameter $\beta = \kappa/\kappa_0$. Consequently, the relative errors in determining β and γ^{min} are essentially the same.

In order to determine the parameter λ, which is defined by formula (7), we turn to the results of [5, 6]. In those papers, an algorithm for calculating the critical gradient Ω_c was developed and the critical gradients were determined numerically for a large number of shots on seven different tokamaks. It is convenient to represent the calculated results in terms of their dependence on the self-similarity parameter $Aq/(k(q + 4))$. In order to diminish the spread in the calculated points, we normalize the critical gradient to the dimensionless ratio $Aq/(q + 4)$. The results of calculating the normalized critical gradient $\Omega_c(q + 4)/Aq$ are displayed in Fig. 4. Knowing the discharge parameters A, q, and k and using Fig. 4, we can find Ω_c. Then, using formula (7), we can determine the sought-for value of λ. In what follows, the estimates will be made in terms of the physical units utilized in formulas (52) and (53).

(i) Estimates for T-10.

We consider a representative T-10 discharge, namely, shot no. 32 913, with localized off-axis ECRH and with the parameters

$$M = 2, \quad A = 5, \quad q(1) = 4, \quad q(1/2) = 1.5,$$
$$n = 1.86 \times 10^{19}\ \mathrm{m}^{-3}, \quad B = 2.5\ \mathrm{T}, \quad R = 1.5\ \mathrm{m}, \quad (54)$$
$$T_e(1/4) = 2\ \mathrm{keV}, \quad T_e(1) = 0.04\ \mathrm{keV}, \quad P_{\mathrm{tot}} = 0.5\ \mathrm{MW}.$$

Using expression (53) and parameter values (54), we find $\kappa = 3.2$, $\kappa_0 = 0.53$, and $\gamma(\text{T-10}) = 1.27 \times P_{\mathrm{tot}}[\mathrm{MW}]/T_a[\mathrm{keV}] = 35$.

From Fig. 4 we then obtain $\lambda = 1.85$. These parameters, as well as the quantities $\gamma^{\max}$, $\gamma^{\min}$, and $\mathbb{S}$, calculated from formulas (20), (25), (35), and (44), are included in the table. We can see that $\gamma \gg \gamma^{\max}$; consequently, in the ECRH regime in T-10, the temperature profile is stiff but is not rigid.

(ii) Estimates for JET.

Here, we consider representative L- and H-mode discharges with the parameters [11]

$$M = 2,\ A = 3,\ q(1) = 4,\ q(1/2) = 1.5,\ n = 4 \times 10^{19}\ \mathrm{m}^{-3},$$
$$B = 3\ \mathrm{T},\ R = 3\ \mathrm{m},\ T_e(1/4) = 9\ \mathrm{keV}, \quad (55)$$
$$T_{eL}(1) = 0.25\ \mathrm{keV},\ T_{eH}(1) = 2\ \mathrm{keV},\ P_{\mathrm{tot}} = 16\ \mathrm{MW}.$$

Using expression (52) and parameter values (55), we find $\kappa = 18$, $\kappa_0 = 3$, $\gamma_{\mathrm{L}}(\mathrm{JET}) = 0.25P_{\mathrm{tot},\,e}[\mathrm{MW}]/T_a[\mathrm{keV}] = 8$, and $\gamma_{\mathrm{H}} = 1$.

For the plasma density value indicated above, the deposited power profile can be approximated by a hyperbolic function with $j = 1$. The parameter values calculated with this approximation are also given in the table. It is easy to see that, in the L-mode, the temperature profile is stiff but is not rigid, while, in the H-mode, the profile is both stiff and rigid.

We now consider the electron plasma component in a high-density H-mode discharge in JET, namely, in shot no. 52022 [11]. In this case, the profile of the power deposited in plasma electrons is markedly peaked at the plasma boundary, so that the quantity $\gamma^{\min}$ can be estimated from the half-sum $\gamma^{\min} \approx [\gamma^{\min}(j = 2) + \gamma^{\min}(j = 3)]/2$. The parameters of the shot at hand are as follows:

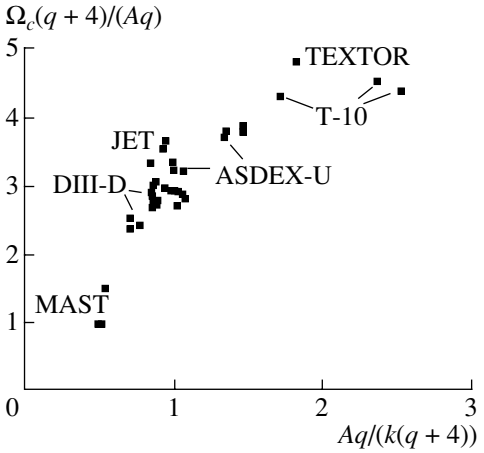

Fig. 4. Dependence of the normalized critical gradient on the parameter $Aq/(k(q + 4))$ for six different tokamaks.

$$M = 2,\ A = 3,\ q(1) = 4,\ q(1/2) = 1.5,\ n = 8 \times 10^{19}\ \mathrm{m}^{-3},$$
$$B = 3\ \mathrm{T}, \quad R = 3\ \mathrm{m}, \quad T_e(1/4) = 3\ \mathrm{keV}, \quad (56)$$
$$T_e(1) = T_{e,\,\mathrm{ped}} = 0.8\ \mathrm{keV}, \quad P_{\mathrm{tot}} = 10\ \mathrm{MW}.$$

The parameter values calculated for this shot are also presented in the table. We can see that $\gamma < \gamma^{\min}$, so that the temperature profile is flexible.

(iii) Estimates for MAST.

We consider MAST shot no. 6326 with the parameters

$$M = 2, \quad A = 1.55, \quad q(1) = 6.6, \quad q(1/2) = 1.5,$$
$$n = 4.2 \times 10^{19}\ \mathrm{m}^{-3}, \quad B = 0.5\ \mathrm{T}, \quad R = 0.8\ \mathrm{m}, \quad (57)$$
$$T_e(1/4) = 1.2\ \mathrm{keV},\ T_e(1) = 0.04\ \mathrm{keV},\ P_{\mathrm{tot},\,e} = 1.9\ \mathrm{MW}.$$

In this case, the deposited power profile is nearly flat and can be approximated by a power-low function with $j = 2$. The corresponding calculated parameter values are also shown in the table. Note that, for the small-aspect-ratio MAST tokamak with a weak magnetic

Table

Tokamak and operating mode	κ	κ/κ_0	λ	γ	$\gamma^{\max}$	$\gamma^{\min}$	$\mathbb{S}$	Profile
T-10 shot no. 32913	3.2	6	1.85	35	1.5	0.47	6.3	Stiff with large $\mathbb{S}$
JET, L-mode, $j = 1$	18	6	1.5	8	2.9	0.65	4.2	Stiff
JET, H-mode, $j = 1$	18	6	1.5	1	2.9	0.65	4.2	Stiff and rigid
JET shot no. 52022, $j = 2$ and 3	20	6	1.3	1.38	4.45	3.4	–	Flexible, $\gamma < \gamma^{\min}$
MAST shot no. 6326, $j = 2$	63	6	0.53	12	3.2	0.25	2.3	Stiff with small $\mathbb{S}$

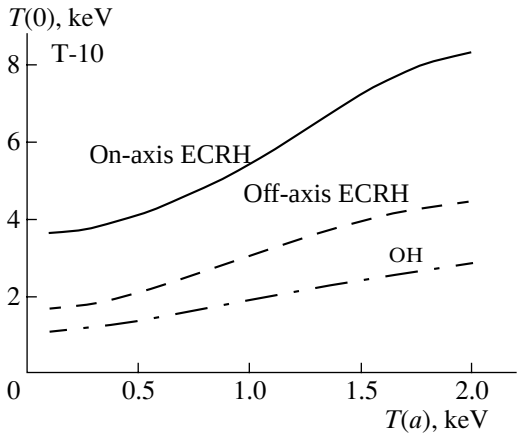

Fig. 5. Dependence of the central electron temperature on the boundary temperature T_a at the end of the Ohmic heating stage (dashed-and-dotted curve), at the end of the off-axis ECRH stage (dashed curve), and at the end of the on-axis ECRH stage (solid curve) for the parameters of T-10 shot no. 32913.

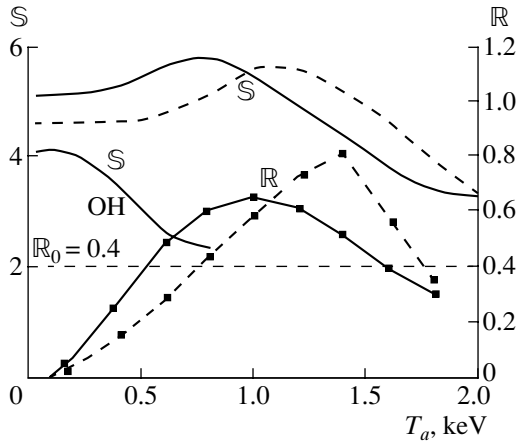

Fig. 6. Dependence of the stiffness and rigidity parameters on the boundary temperature in the stages of on-axis ECRH (dashed curve), off-axis ECRH (solid curves), and Ohmic heating (OH). The remaining parameters correspond to T-10 shot no. 32913.

field, the coefficient κ is very large and the parameter λ is, on the contrary, small in comparison to those in moderate-aspect-ratio tokamaks. That is why, even for L-mode discharges in MAST, the parameter γ, though it is six times smaller than that for T-10, is nevertheless not small enough for the temperature profile to be rigid.

4. NUMERICAL SIMULATIONS

4.1. Increase in the Boundary Temperature in T-10

Since expression (26) for the heat flux is strongly nonlinear, the general transport problem can be solved only numerically. To do this, we invoke the previously developed canonical profile transport model (CPTM), which is briefly described in [6] (where one can find references to earlier works on the subject). In the CPTM, the behavior of the electron and ion temperatures is described by heat fluxes of the form of (26), which account for radiation and contain the ion–electron energy exchange term. The model also includes the diffusion equation for the poloidal magnetic flux. The values of the plasma density and its radial profile are assumed to be known from experiment.

The dependence of the central electron temperature $T_e(0) = T_{e0}$ on the boundary temperature $T_e(a) = T_a$ was simulated using T-10 shot no. 32913 with parameters (55) as an example. The initial stage of the discharge ($t < 0.55$ ms) consists of Ohmic plasma heating. Then, during the time interval $0.55 < t < 0.62$ s, the plasma was heated by two 140-GHz gyrotrons with a total power of 0.4 MW, which provided off-axis power deposition (in the vicinity of a surface of radius r_{EC} = 12 cm). Finally, during the time interval $0.8 < t < 0.86$ s, the plasma was heated by one 130-GHz 0.53-MW gyrotron providing on-axis power deposition (in the plasma core region of radius r_{EC} = 1–1.5 cm). Under the T-10 conditions, and for a localized deposited power profile $P(\rho)$, the region of rigid temperature profiles is determined by inequality (37), with $\gamma^{\min} = 0.47$ and $\gamma^{\max} = 1.5$ (see table).

We begin the analysis by noting that our simulations of the T-10 discharge in question are simply conjectural because the boundary temperatures assumed here are inaccessible in experiments. Since T-10 is equipped with a solid limiter, the actual temperature at the plasma boundary does not exceed 50–100 eV in all operating regimes. Simulations for boundary temperatures of up to about 2 keV are of interest from the standpoint of comparing the calculated results with experimental data from tokamaks in which such boundary temperatures are actually achievable.

The simulation results are illustrated in Fig. 5, which shows how the central electron temperature T_{e0} depends on the boundary temperature T_a in different discharge stages. In this figure, the dashed-and-dotted curve (OH) refers to the end of the Ohmic heating stage (t = 0.5 s), the dashed curve (off-axis ECRH) refers to the time at which two gyrotrons that provide off-axis plasma heating are switched off (t = 0.6 s), and the solid curve (on-axis ECRH) refers to the time at which the gyrotron that heats the plasma core is switched off (t = 0.86 s). The three curves are seen to exhibit similar behavior. As long as the boundary temperature T_a is low, there will be a transition layer in the plasma edge that weakens the coupling between T_{e0} and T_a. It can be seen that, for $T_a < 0.2$ keV, the temperature T_{e0} is essentially independent of T_a. For $T_a > 0.3$ keV, the coupling between T_{e0} and T_a becomes pronounced and the electron temperature profile becomes more rigid.

Figure 6 demonstrates the dependence of the stiffness parameter $\mathbb{S}$, defined by formula (1), on the boundary temperature in three different heating stages. When $T_a < 0.2$ keV, the parameter $\mathbb{S}$ remains nearly constant throughout each of the discharge stages and lies within the range $4 < \mathbb{S} < 5.1$. For higher boundary temperatures T_a, the behavior of $\mathbb{S}$ is different in different stages. In the Ohmic heating stage (OH), the current profile flattens and the voltage decreases. As a result, the total deposited power decreases and its profile flattens. Accordingly, the quantity $\gamma^{\min}$ approaches $\gamma^{\max}$, the region of a rigid temperature profile does not originate, the parameter $\mathbb{S}$ rapidly decreases, and the temperature profile becomes flat and loses its stiffness. In the ECRH stage, the parameter $\mathbb{S}$ begins to decrease at $T_a \sim 1$ keV. Accordingly, for a localized ECRH power profile, formula (35) gives $\gamma^{\min} = \gamma = 1.27P_{\text{tot}}[\text{MW}]/T_a^{\max}[\text{keV}] \approx 0.6$; this value is close to the estimate presented in the table ($\gamma^{\min} = 0.47$).

Figure 6 also illustrates the behavior of the rigidity parameter $\mathbb{R} = (T_a/T_0)dT_0/dT_a$ in both of the ECRH stages. We can see that the dependence $\mathbb{R}(T_a)$ is nonmonotonic. At low boundary temperatures T_a, there is a transition layer in the edge plasma, $\mathbb{R} < \mathbb{R}_0$, and the temperature profiles are not rigid. As T_a increases, the parameter $\mathbb{R}$ also increases and the rigidity condition $\mathbb{R} > \mathbb{R}_0$ ($\gamma < \gamma^{\max}$) begins to be satisfied. This is seen to take place at $T_a \sim 0.5$ keV. For this boundary temperature, we have $\gamma = 1.27P_{\text{tot}}/0.5 = 1.3 \approx \gamma^{\max}$; this value is again close to the estimate presented in the table ($\gamma^{\max} = 1.5$). The rigidity $\mathbb{R}$ reaches its maximum values, $\mathbb{R} \sim 0.65$–0.8, at $T_a \sim 1$–1.2 keV. As the temperature T_a increases further, the left-hand inequality in conditions (37) begins to be violated and the temperature profile becomes less rigid.

Figure 7 depicts the radial profiles of the relative electron temperature gradient $\Omega_T = -R(dT/dr)/T$ and of the critical gradient $\Omega_c = -R(dT_c/dr)/T_c$ at $T_a = 1.8$ keV for the on-axis heating stage. It can be seen that, in the region $8 < r < 21$ cm, the relative temperature gradient is lower than the critical gradient. This is the reason why the rigidity parameter $\mathbb{R}$ decreases at high boundary temperatures. As a result, the temperature profile becomes flat and loses its stiffness and rigidity.

4.2. Increase in the Boundary Temperature in MAST

Because of the small aspect ratio of MAST and because of its weak operating magnetic field, the behavior of the temperature profiles in this device differs radically from that in moderate-aspect-ratio tokamaks. The main differences are as follows:

(i) The value of the critical gradient Ω_c is small (see Fig. 4), with the result that the temperature profiles are flatter than those in moderate-aspect-ratio tokamaks.

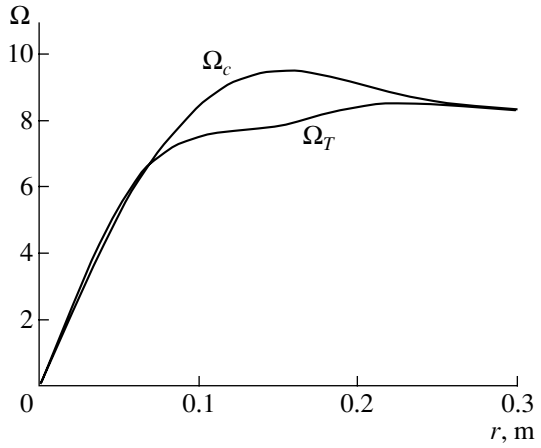

Fig. 7. Critical and relative electron temperature gradients calculated for a boundary temperature of 1.8 keV and for the parameters corresponding to T-10 shot no. 32913.

(ii) The value of the thermal conductivity κ (see table) is high, which is a consequence of the following semi-empirical dependence of the coefficient κ in expression (53) on the aspect ratio, major plasma radius, and magnetic field: $\kappa \sim A^{-3/4}B^{-1}R^{-1/4}$. Estimates from formula (53) show that the thermal conductivity κ for MAST is about three times higher than that for JET. Formula (53) was derived by comparing the experimental and numerical results for DIII-D and JET, which have an aspect ratio of $A \sim 3$, with those for T-10 and TEXTOR, which have an aspect ratio of $A \sim 5$. In all these devices, the magnetic field is nearly the same, $B \sim 2.5$–3 T. That formula (53) applies to START and MAST, which have low aspect ratios A and operate with weak magnetic fields B, was confirmed in our earlier studies [5, 6, 9], so that we can safely use it here for calculations.

The tendency of κ to decrease as B and R increase was pointed out in several other papers, among which was a paper by Rebut *et al.* [10], who assumed the dependence $\kappa \sim B^{-1}$, and a paper by Garbet [3], who considered the dependence $\kappa \sim B^{-2}R^{-1}$. Note that expression (26) for the heat flux contains the product $\kappa(\Omega_{Te} - \Omega_c)$. This indicates that, if κ is high, then the difference $\Omega_{Te} - \Omega_c$ is small, the heat flux being the same. As a result, the temperature profile in MAST is far closer to the canonical profile than those in the other tokamaks under discussion.

(iii) Under the MAST conditions, the coefficient κ_0 is determined very unreliably. As was mentioned above, the most straightforward way of determining the background thermal conductivity is to measure it in experiments with strongly localized off-axis plasma heating. However, such experiments are impossible to carry out in MAST. That is why the calculations

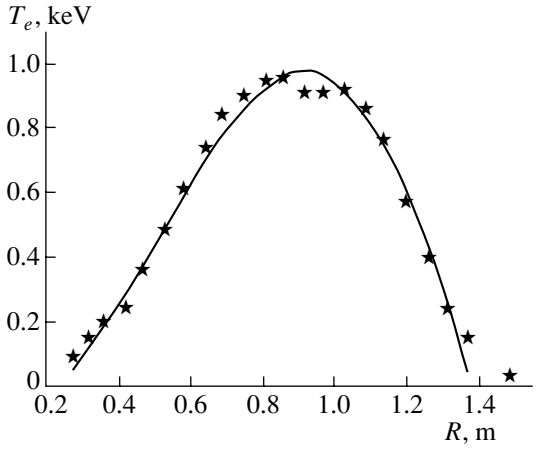

Fig. 8. Calculated (solid curve) and measured (asterisks) temperature profiles for MAST shot no. 6252.

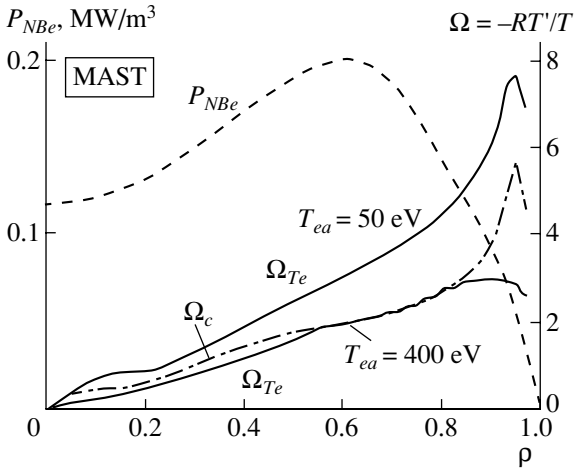

Fig. 9. Radial profiles of the critical gradient and the calculated electron temperature gradient for the same MAST shot. At the boundary electron temperature T_{ea} = 50 eV, the profile of the relative electron temperature gradient lies above the profile of the critical gradient. At T_{ea} = 400 eV, the profiles coincide over a large portion of the cross section of the plasma column. The radial profile of the power P_{NBe} deposited in plasma electrons is also shown by the dashed line.

described in this section were performed with the formula [6]

$$\kappa_0 = C_0 T^{1/2}(\rho = 1/2)/R, \qquad (58)$$

where C_0 = 1–2. For C_0 = 1, we have $\kappa/\kappa_0 \sim 10$–12.

(iv) The energy of hot neutrals ($E_0 < 50$ keV) used for auxiliary neutral beam injection (NBI) heating is low. For such energies, the total cross sections for charge exchange and ionization are still high and, at densities of $n > 4 \times 10^{19}$ m^{-3}, an appreciable fraction of the neutral beam power is absorbed by the edge plasma (especially in the H-mode). As a result, the profile of the power deposited in plasma electrons turns out to be radially increasing.

The dependence of the central electron temperature $T_e(0) = T_{e0}$ on the boundary temperature T_a was simulated using as an example MAST shot no. 6252 with the parameters

$$\begin{gathered} M = 2, \quad A = 1.45, \quad q(1) = 8.6, \quad q(1/2) = 1.5, \\ n = 4.1 \times 10^{19}\ \text{m}^{-3}, \quad I = 0.73\ \text{MA}, \quad B = 0.46\ \text{T}, \\ R = 0.8\ \text{m}, \quad a = 0.55, \quad T_e(1) = 0.05\ \text{keV}, \\ P_{NBe} = 1.85\ \text{MW}, \quad P_{NBi} = 0.45\ \text{MW}. \end{gathered} \qquad (59)$$

Figure 8 shows the calculated (heavy curve) and measured (asterisks) electron temperature profiles. From this figure, it is clear that the model adopted here reliably describes the experiment. Figure 9 shows the radial profiles of the critical gradient Ω_c and of the electron temperature gradient Ω_{Te}. We can see that, over the entire cross section of the plasma column, the temperature gradient exceeds the critical gradient ($\Omega_{Te} > \Omega_c$), condition (29) is satisfied, and the Heaviside function is equal to unity. The dashed curve in Fig. 9 shows the calculated radial profile of the power deposited in plasma electrons. This profile is seen to be nonmonotonic: it is peaked in the vicinity radius $\rho = 0.65$.

Now, we proceed to a description of the results from simulations of an increase in the boundary temperature. In Fig. 9, we also plot the radial profile of the relative temperature gradient calculated for T_a = 0.4 keV. In the region $0.5 < \rho < 0.8$, the T_e profile is seen to be very close to the canonical profile. However, in the regions $0 < \rho < 0.5$ and $\rho > 0.8$, the temperature profile is flatter than the canonical profile and the Heaviside function is equal to zero. Figure 10 shows the radial profiles of the effective thermal diffusivity χ_e^{eff} calculated for two different values of the boundary temperature, T_a = 0.05 and 0.4 keV. We can see that, although the plasma temperature increases with T_a (and, accordingly, the thermal conductivity κ increases), the effective thermal diffusivity over the entire plasma column decreases by a factor of 2 to 3 as the electron temperature profile approaches the canonical profile.

Figure 11 illustrates the dependence of the central temperature $T_e(0)$, the stiffness coefficient $\mathbb{S}$, and the rigidity coefficient $\mathbb{R}$ on the boundary temperature T_a. It can be seen that the electron temperature profile is rigid in the range $0.12 < T_a < 0.27$ keV. For boundary temperatures above 0.27 keV, the profile ceases to be stiff and rigid. The loss of stiffness and rigidity at such a low boundary temperature (in comparison with that in T-10) is attributed to the fact that the aspect ratio is small and the deposited power profile is peaked at the plasma edge.

It is important to point out the following feature of MAST discharges: during the transition to the H-mode,

the pedestal temperature is very low, $T_{\text{ped}} < 0.15$ keV. Presumably, this is explained by the fact that a pronounced temperature pedestal can form only when the temperature profile is stiff. It is only in this case that the transport barrier with steep temperature gradients can build up. Our analysis shows that, as the pedestal temperature increases, the temperature profile becomes less stiff and can even lose its stiffness. This indicates that, throughout the H-mode stage, the pedestal temperature should remain lower than a certain maximum temperature $T_{a,\max}$. Our simulations have allowed us to estimate this maximum temperature by $T_{a,\max} < 0.2$ keV (in Fig. 11, the rigidity coefficient $\mathbb{R}$ at this temperature reaches its maximum value). This estimate is in reasonable agreement with the maximum pedestal temperature in the MAST shot in question.

4.3. Simulations of High-Density H-Mode Discharges in DIII-D and JET

In our earlier paper [6], we investigated scaling for the relative gradient of the measured electron temperature, $\Omega_{Te}^{\exp} = -(R/T_e^{\exp})dT_e^{\exp}/dr$, by comparing the data from the ITER database [11] for discharges in eight different tokamaks. For most of these discharges, the relative temperature gradient was found to be reasonably well described in terms of only one parameter, namely, the self-similarity parameter $A^2q/k(q+4)$ or $Aq/k(q+4)$. Such a scaling was possible because of the stiffness of the electron temperature profiles in these discharges. However, for some discharges considered in that paper—two high-density H-mode discharges in DIII-D (shot nos. 77557, 77559) and in JET (shot nos. 52015, 52022)—the scaling yielded more peaked electron temperature profiles than the measured ones. Now, we are going to show that this discrepancy, the causes of which were not clarified in [6], is explained by the violation of the left-hand inequality in conditions (37), i.e., by the loss of stiffness and rigidity in these four discharges.

There are two main factors that cause the electron temperature profile to become flatter. One other reason for the flattening of the profiles is a "competition" between the values of the discharge parameters. Thus, the features of the above two DIII-D discharges are as follows:

(i) There is a high pedestal in the plasma density, $n \sim (4\text{–}5) \times 10^{19}$ m^{-3}. For a plasma heated by a neutral beam with an energy of $E_0 \sim 75$ keV, such a high density pedestal leads to a relatively flat profile of the absorbed NBI power.

(ii) For a pedestal temperature of $T_{e,\text{ped}} \sim 0.6$–$0.8$ keV and for a neutral beam particle energy of $E_0 \sim 75$ keV, up to about 70% of the power absorbed by the edge plasma goes into heating the electrons. As a result, the profile of the power deposited in the electrons is far flatter than that of the power deposited in the ions. In some cases, the former is peaked at the plasma edge.

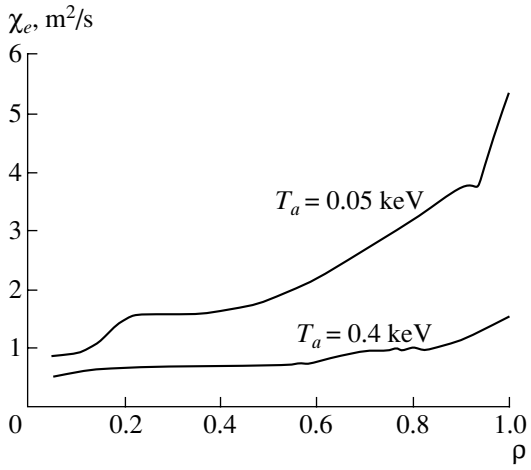

Fig. 10. Radial profiles of the electron thermal diffusivity for different boundary temperatures in MAST shot no. 6252.

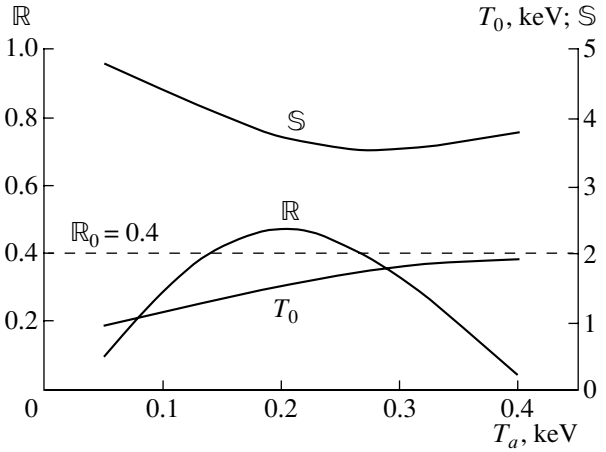

Fig. 11. Rigidity $\mathbb{R}$, stiffness $\mathbb{S}$, and central electron temperature calculated as functions of the boundary temperature for the parameters of MAST shot no. 6252.

The flat profile of the power going into heating the electrons and sufficiently high pedestal temperature cause the electron temperature gradient to decrease, with the result that, over an appreciable portion of the cross section of the plasma column, the gradient of T_e turns out to be lower than the critical gradient.

The experimental data and numerical results are compared in Figs. 12–15. Figure 12 shows the measured and calculated electron temperature profiles for DIII-D shot no. 77 559 with the parameters $I = 1$ MA, $n = 4.8 \times 10^{19}$ m^{-3}, and $P_{NBI} = 10.2$ MW. The figure also shows the profile of the power deposited in the electrons. Radial profiles of the dimensionless gradients $\Omega_{Te}^{\exp} = -(R/T_e^{\exp})dT_e^{\exp}/dr$, $\Omega_{Te} = -(R/T_e)dT_e/dr$, and

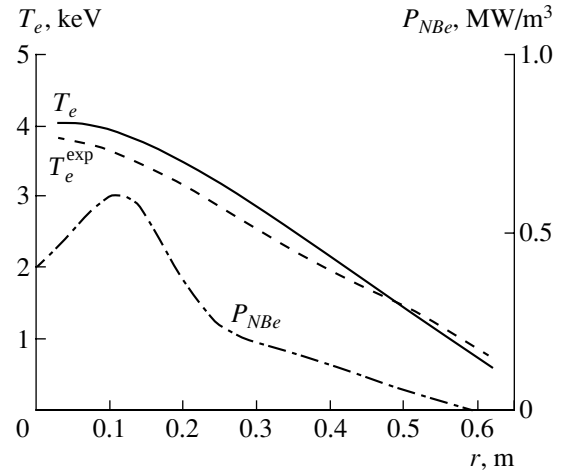

Fig. 12. Calculated (solid curve) and measured (dashed curve) electron temperature profiles for DIII-D shot no. 77559. The radial profile of the power deposited in plasma electrons is also shown by the dashed-and-dotted curve.

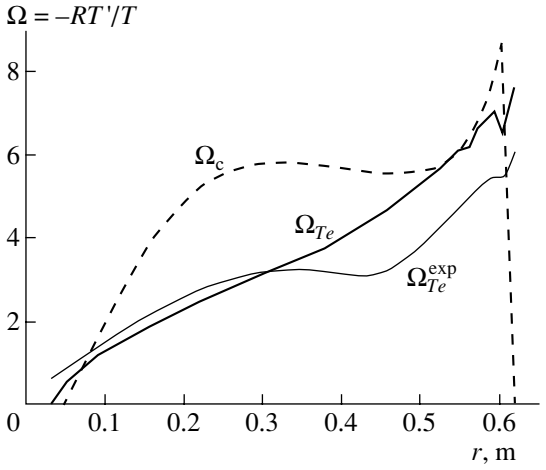

Fig. 13. Radial profiles of the measured and calculated temperature gradients and of the relative critical gradient for DIII-D shot no. 77559.

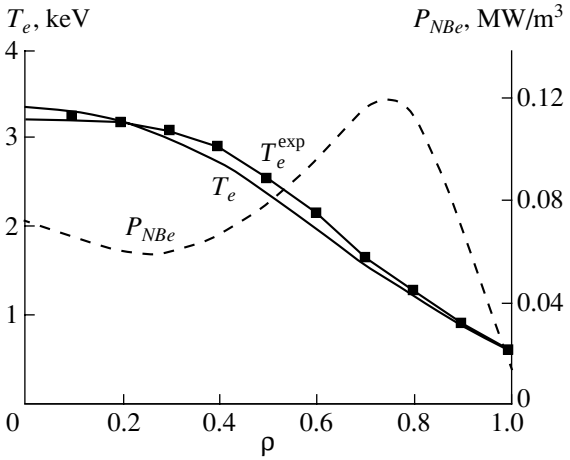

Fig. 14. Calculated (solid curve) and measured (squares) electron temperature profiles for JET shot no. 52022. The radial profile of the power deposited in plasma electrons is also shown by the dashed curve.

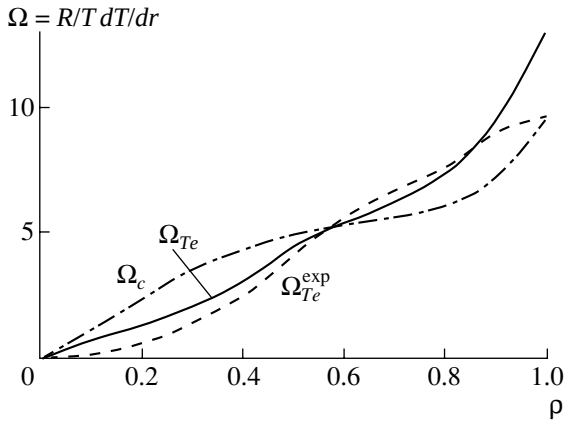

Fig. 15. Radial profiles of the measured and calculated temperature gradients and of the relative critical gradient for JET shot no. 52022.

$\Omega_c = -(R/T_c)dT_c/dr$ are shown in Fig. 13. It can be seen that, in the region $r < 0.5$ m, the gradients Ω_{Te}^{exp} and Ω_{Te} are markedly lower than the critical gradient Ω_c. In this region, the Heaviside function is equal to zero, $H = 0$. As a result, the electron temperature profile $T_e(\rho)$ is flexible, i.e., it is neither stiff nor rigid.

These properties of the two DIII-D discharges are also possessed by the two JET discharges mentioned above. The results of simulating JET shot no. 52022 with the parameters $I = 2.48$ MA, $n = 8.93 \times 10^{19}$ m^{-3}, and $P_{NBI} = 14.2$ MW are illustrated in Figs. 14 and 15, which refer to the time $t = 60.44$ s. Figure 14 displays the calculated and measured radial profiles of the electron temperature, as well as the profile of the power P_{NBe} deposited in the electrons. The profile of P_{NBe} is seen to be peaked at the plasma edge. This is because the high pedestal in the plasma density, $n_{ped} \sim 5.5 \times 10^{19}$ m^{-3}, prevents the neutral beam from penetrating into the plasma core. Radial profiles of the relative gradients Ω_{Te}, Ω_{Te}^{exp}, and Ω_c for JET are depicted in Fig. 15, which thus corresponds to Fig. 13 for DIII-D. One can see that, in the region $\rho < 0.6$ in JET, the profiles of the gradients Ω_{Te} and Ω_{Te}^{exp} lie below the profile of the critical gradient Ω_c. For JET shot no. 52015 with a higher plasma density, $n = 9.6 \times 10^{19}$ m^{-3}, and with the NBI power $P_{NBI} = 11.8$ MW, the relative gradients behave in a similar manner.

Hence, experiments confirm that the temperature profiles can become flexible when the pedestal temperature is sufficiently high and the profiles of the power deposited in the plasma are either flat or peaked at the plasma edge. Because the temperature profiles are neither stiff nor rigid, the temperature gradients in the corresponding discharges do not conform to the scaling based on experimental data from discharges with stiff profiles [6, 9].

5. CONCLUSIONS

In the present paper, we have introduced and formalized the notions of stiffness and rigidity of the temperature profile in a tokamak. Analytical estimates and numerical simulations carried out in terms of a model with critical gradients show that, at a low boundary temperature (in the L-mode), the profiles are, as a rule, stiff but are not rigid. In the H-mode, there exists a parameter range in which the profiles can become rigid. However, when the pedestal temperature is sufficiently high and the deposited power profile is flat, the temperature profile can lose its stiffness and rigidity. Such behavior of the electron temperature profile was observed in a number of H-mode discharges in DIII-D and JET. In the small-aspect-ratio MAST tokamak, the temperature profiles are flatter than those in moderate-aspect-ratio tokamaks. As a result, the maximum pedestal temperature in the H-mode in MAST turns out to be markedly lower than that in other tokamaks. In the case of injection of low-energy neutrals, the deposited power profile is flat, which also prevents an increase in the pedestal temperature in MAST. The existence of the region of flexible temperature profiles is confirmed by the absence of a heat pinch.

ACKNOWLEDGMENTS

We are grateful to Xavier Garbet for providing us with a copy of his paper [3] prior to its publication. This work was supported in part by the Russian Federal Program for State Support of Leading Scientific Schools (project no. NSh-1608.2003.2), the RF Ministry of Atomic Energy (contract no. 856), and the Consulting Agreement no. QS06588 with UKAEA (United Kingdom).

REFERENCES

1. B. Coppi, Comments Plasma Phys. Control. Fusion **5**, 261 (1980).
2. G. Tardini, A. G. Peeters, G. V. Pereverzev, *et al.*, Nucl. Fusion **42**, 258 (2002).
3. X. Garbet, P. Mantica, F. Ryter, *et al.*, Plasma Phys. Controlled Fusion **46**, 1351 (2004).
4. F. Ryter, C. Angioni, M. Beurskens, *et al.*, Plasma Phys. Controlled Fusion **43**, A323 (2001).
5. Yu. N. Dnestrovskij, A. Yu. Dnestrovskij, S. E. Lysenko, and S. V. Cherkasov, Fiz. Plazmy **28**, 963 (2002) [Plasma Phys. Rep. **28**, 887 (2002)].
6. Yu. N. Dnestrovskij, A. Yu. Dnestrovskij, S. E. Lysenko, and S. V. Cherkasov, in *Proceedings of the 19th IAEA Conference on Fusion Energy, Lyon, 2002*, Rep. TH/P1-04.
7. E. Minardi and H. Weisen, Nucl. Fusion **41**, 113 (2001).
8. K. A. Razumova, V. F. Andreev, A. A. Borshchegovskij, *et al.*, Plasma Phys. Controlled Fusion **45**, 1247 (2003).
9. Yu. N. Dnestrovskij, A. Yu. Dnestrovskij, S. E. Lysenko, *et al.*, Fiz. Plazmy **30**, 3 (2004) [Plasma Phys. Rep. **30**, 1 (2004)].
10. P. H. Rebut, P. P. Lallia, and M. L. Watkins, in *Proceedings of the 12th IAEA Conference on Fusion Energy, Nice, 1988* (IAEA, Vienna, 1989), Vol. 2, p. 1047.
11. D. Boucher, J. W. Connor, W. A. Houlberg, *et al.* (The ITER 1D Modelling Working Group), Nucl. Fusion **40**, 1955 (2000); http://tokamak-profiledb.ukaea.org.uk/.

Translated by I.A. Kalabalyk

Plasma Physics Reports, Vol. 30, No. 9, 2004, pp. 730–739. Translated from Fizika Plazmy, Vol. 30, No. 9, 2004, pp. 784–794.

BEAMS IN PLASMA

Unsteady Beam–Plasma Discharge: II. Nonlinear Theory

Yu. P. Bliokh*, M. G. Lyubarsky, V. O. Podobinsky***, and Ya. B. Fainberg*****

**Technion, Haifa, Israel*

***Kharkov National University, pl. Svobody 4, Kharkov, 61077 Ukraine*

****Institute of Plasma Electronics and New Acceleration Methods, National Science Center Kharkov Institute of Physics and Technology, ul. Akademicheskaya 1, Kharkov, 61108 Ukraine*

Received October 15, 2003; in final form, November 12, 2003

Abstract—The mathematical model constructed in the first part of our paper is used to numerically investigate the development of the beam–plasma instability in a traveling-wave tube amplifier in the presence of a residual neutral gas. It is shown that the self-generation of ion acoustic waves in a plasma-filled amplifier can give rise to a modulation regime with a rigid excitation threshold. The dependence of the threshold for the self-modulation instability on the amplifier parameters is determined. The effect of self-modulation on the spectral and energy characteristics of the amplifier is analyzed. © *2004 MAIK "Nauka/Interperiodica"*.

1. INTRODUCTION

In recent years, high-power microwave devices operating in a continuous-wave mode have been created on the basis of plasma-filled waveguide structures (PWSs) [1, 2]. In order to adequately describe the excitation of a PWS by an electron beam, a self-consistent theory of the beam–plasma instability (BPI) has been elaborated that takes into account both variations in the medium (plasma) parameters under the action of high-power microwave radiation and the effect of these variations on the excitation and propagation of radiation. Note that plasma nonlinearity influences primarily the excitation of a synchronous wave by a beam rather than its propagation.

Plasma nonlinearity can be caused by several effects. One of them is related to the action of the ponderomotive force on a plasma [3]. The development of a theory allowing for this action in a quasistatic approximation was started in [4, 5]. A theory that takes into consideration the action of an unsteady ponderomotive force on the generation and amplification of microwave oscillations in a long-pulse plasma-filled traveling-wave tube (TWT) was elaborated in [6–10]. In those papers, it was shown that the displacement of the plasma out from the region where the amplitude of the microwave oscillations is maximum results in two new effects: the onset of low-frequency modulation of a microwave signal a PWS by an electron beam were confirmed experimentally by the examples of hybrid structures [11] and a magnetized plasma waveguide [10].

The second cause of plasma nonlinearity is the onset of a beam–plasma discharge (BPD) in a PWS [12]. The point is that, in many microwave devices, plasma is produced by collisional ionization of a neutral gas by the beam electrons. In [6–10], it was assumed that the excitation of a high-power microwave field results only in the spatial redistribution of the plasma density and does not influence the plasma source itself. This is true, however, either for a fully ionized plasma or for relatively small amplitudes of microwave oscillations, when the oscillatory energy of the plasma electrons is insufficient to ionize the neutral component of the plasma. Otherwise, a BPD develops in the system. The BPD is an additional plasma source whose power and spatial distribution depend on the parameters of the excited wave. In the first part of our paper [13], we developed an analytic theory that took into account the effect of a BPD on the wave amplification in a linear magnetized plasma-filled TWT amplifier. Here, by linear amplifier we mean an amplifier with a small amplitude of the output signal such that the nonlinearity of the beam particle motion in the field of the excited wave can be ignored; however, the entire beam–wave–plasma system is considered to be nonlinear. As was shown in [13], the plasma propagating from the source region toward the beam causes effects similar to those occurring under the action of the ponderomotive force (e.g., the loss of stability of a steady-state amplification regime and a transition to the self-modulation mode) and some new effects. The latter are related to the threshold character of the BPD and manifest themselves, in particular, in the rigid character of the excitation of low-frequency instability.

In the present paper, we use the mathematical model developed in [13] to numerically investigate the effect of a BPD on BPI in a nonlinear plasma-filled TWT amplifier. The paper is organized as follows. Section 2 describes the mathematical model and the main theoretical results concerning the stability of the steady-state operating regimes of a linear TWT amplifier. In Section 3, the stability of the steady-state operating regimes of a nonlinear amplifier is studied numerically and the results obtained are compared to the analytic predictions. In Section 4, the effect of low-frequency

1063-780X/04/3009-0730$26.00 © 2004 MAIK "Nauka/Interperiodica"

instability on the power and spectral characteristics of the amplifier is analyzed. In the Conclusion, we formulate the main results that follow from the theory proposed.

2. MATHEMATICAL MODEL

Let us consider the TWT amplifier that is a slow-wave structure partially filled with a magnetized plasma in which a nonrelativistic electron beam propagates. We will assume that a residual neutral gas is present in this structure. If the amplitude $E_0(z, t)$ of the microwave field in a certain region exceeds the threshold value $E_{cr} = \omega\sqrt{2mW_i}/e$ (where ω is the wave frequency and W_i is the ionization energy of the gas), then a BPD develops there. A mathematical model of such a TWT amplifier was developed in [13]. The model includes

(i) time-independent BPI equations describing the amplification of a microwave in a nonuniform unsteady plasma,

$$\frac{\partial\varepsilon}{\partial\zeta} + i\mathcal{N}(\zeta, \tau)\varepsilon = -\frac{1}{2\pi}\int_0^{2\pi} e^{-i\varphi(\varphi_0, \zeta)}d\varphi_0,$$
$$\frac{\partial^2\varphi}{\partial\zeta^2} = \mathrm{Re}(\varepsilon e^{i\varphi}) \quad (1)$$

with initial conditions

$$\varepsilon(0, \tau) = |\varepsilon|_0, \quad \varphi(0, \tau) = \varphi_0,$$
$$\frac{\partial\varphi}{\partial\zeta}(0, \tau) = 0, \quad 0 \le \varphi_0 \le 2\pi; \quad (2)$$

(ii) and linear equations describing the plasma dynamics in the presence of a plasma source S (in our case, a BPD),

$$\frac{\partial\eta}{\partial\tau} + \frac{\partial u}{\partial\zeta} = S(\zeta, \tau), \quad \frac{\partial u}{\partial\tau} + \frac{\partial\eta}{\partial\zeta} = 0 \quad (3)$$

with boundary conditions on the left ($\zeta = 0$) and right ($\zeta = l$) boundaries of the structure,

$$(1 + \gamma)\eta(0, \tau) + (1 - \gamma)u(0, \tau) = 0,$$
$$(1 + \gamma)\eta(l, \tau) - (1 - \gamma)u(l, \tau) = 0. \quad (4)$$

In Eqs. (1)–(4), the following dimensionless variables are introduced: ζ is the longitudinal coordinate; τ is time; ε is the amplitude of the amplified wave; φ is the phase of a beam particle in the wave; φ_0 is the initial value of the phase in the beam injection plane $\zeta = 0$; $\mathcal{N}(\zeta, \tau) = \eta(\zeta, \tau) - \frac{1}{\zeta_0}\int_0^{\zeta_0}\eta(\zeta, \tau)d\zeta$ is the detuning of the wave phase velocity; ζ_0 is the length of the region where the wave amplification is linear; η and u are the averaged (over the beam cross section) perturbations of the plasma density and plasma velocity, respectively; $S = S_0(\theta_1(\zeta, \tau) - \theta_2(\zeta, \tau))(|\varepsilon|^2(\zeta, \tau) - \varepsilon_i^2)$, S_0 is the neutral gas pressure; ε_i is the normalized threshold value of the wave amplitude E_{cr} introduced above; $\theta_{1,2} = \theta(\zeta - \zeta_{1,2})$, $\theta(\zeta)$ is the Heaviside function; $\zeta_{1,2}(\tau)$ are the coordinates of the left and right boundaries of the BPD region, respectively (these coordinates are the solutions to the equation $|\varepsilon|(\zeta, \tau) = \varepsilon_i$; at $|\varepsilon|(l) > \varepsilon_i$, the right boundary corresponds to the output of the amplifier, $\zeta_2 \equiv l$); and γ is the coefficient of reflection of an ion-acoustic wave from the system boundaries (the inequalities $-1 < \gamma < 1$ and $\gamma < 0$ correspond to the conservation of the phase of a low-frequency wave when it is reflected from the boundary, while $\gamma > 0$ corresponds to the case where the phase of the reflected wave changes by π).

The procedure of deriving Eqs. (1) and (3) and the relationships between the dimensionless and dimensional variables are described in detail in [10, 13]. Here, we only mention the main conditions under which the above equations are valid:

(i) The spatial growth rate of BPI must be small compared to the wavenumber of a microwave and the plasma density perturbations caused by the BPD must small compared to the initial density.

(ii) The ion-acoustic velocity must be low compared to the group velocity of the microwave wave, $v_g \gg c_s$. This condition, which is usually satisfied by a large margin in the cases that are of practical interest, allows one to use time-independent equations for BPI and to describe the time evolution of the plasma parameters by the time dependence of the wave phase velocity.

(iii) the maximum amplitude of the microwave field in the amplifier must be close to the threshold value E_{cr}. This condition allows one to use a linear approximation for the dependence of the ionization cross section $\sigma \sim (W - W_i)$ of the neutral gas molecules by the plasma electrons on their average oscillator energy $W = e^2|E|^2/2m\omega^2$ (note that this condition is satisfied in a rather wide energy range, $W_i \le W \le 1.5W_i$).[1]

The set of Eqs. (1)–(4) represent a closed mathematical model of a BPD in a magnetized plasma-filled TWT amplifier. It can easily be seen that, under given boundary and initial conditions (the parameters l, $|\varepsilon|_0$, and γ), this model contains two intrinsic parameters: S_0 and ε_i.

[1] We assume that the amplifier is filled with a low-pressure, weakly ionized gas, so that the condition that the plasma is weakly collisional, $l_{e,n} > L$, is satisfied (here, $l_{e,n}$ is the mean free path of electrons in elastic collisions with neutrals and L is the amplifier length). In this case, the total energy of electrons is mainly determined by their oscillatory energy. Estimates of the electron mean free path under typical experimental conditions [10, 11] show that $l_{e,n} > 10^2$ cm $> L$ by the instant of the BPD onset.

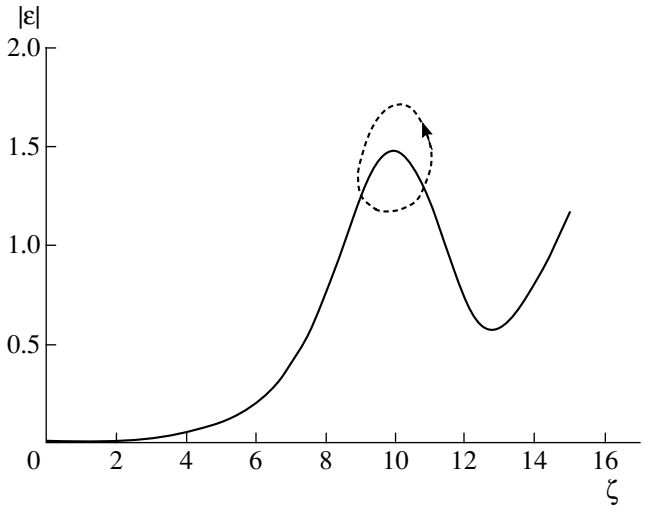

Fig. 1. Spatial profile of the stationary amplitude of the microwave field in the case of a uniform plasma for $|\varepsilon|_0 = 0.01$.

Let us find stationary solutions to the set of Eqs. (1) and (3) with conditions (2) and (4). Assuming that $\partial/\partial\tau \equiv 0$, from Eqs. (3) and (4) we obtain

$$\eta_{st} = \frac{1}{2}\frac{1-\gamma}{1+\gamma}S_0\int_{\zeta_1}^{\zeta_2}(|\varepsilon|_{st}^2(\zeta) - \varepsilon_i^2)d\zeta = \text{const}. \quad (5)$$

Let us now turn to Eq. (1). It can be seen from Eq. (5) that, in a steady-state regime, the plasma is uniform. It then follows from the definition of the phase-velocity detuning $\mathcal{N}$ that $\mathcal{N}_{st} \equiv 0$. This means that, in a steady-state regime, Eqs. (1) and (3) are unrelated, and the effect of the BPD reduces merely to a uniform increase in the density. In the general case (even for a uniform plasma), the spatial profile of the wave amplitude can be found from Eq. (1) only numerically. For a uniform plasma, this profile is well known and has the shape shown in Fig. 1.

In the case of linear amplification ($|\varepsilon(\zeta)| \ll 1$), steady-state solutions to Eq. (1) can be found by analytically. The steady-state solution satisfying conditions (2) has the form

$$\varepsilon_{st}(\zeta) = \frac{|\varepsilon|_0}{3}\sum_{i=1}^{3}\exp(\lambda_i\zeta), \quad (6)$$

where λ_i are the roots of the equation $\lambda^3 = i/2$.

Taking into account that the function $|\varepsilon|_{st}(\zeta) = \varepsilon_i$ is monotonic and assuming that the amplifier length is sufficiently large ($l \gg 1$) and the BPD region is short ($\zeta_2 - \zeta_1 \ll l$), from the equality $|\varepsilon|_{st}(\zeta) = \varepsilon_i$ we obtain

$$\zeta_1 = \frac{1}{\beta}\ln\frac{3\varepsilon_i}{|\varepsilon|_0}, \quad \zeta_2 = l, \quad (7)$$

where $\beta = 2^{-4/3}\sqrt{3}$. Analogously, from Eqs. (5), (6) and (7) it follows that

$$\eta_{st} = \frac{\beta}{2}\frac{1-\gamma}{1+\gamma}S_0\varepsilon_i^2(l-\zeta_1)^2. \quad (8)$$

The stability of steady-state solutions (6) and (8) was examined analytically in [13]. It was shown that, if the amplifier parameters satisfy the relationship

$$P = P_c \equiv \frac{3}{2^{1/3}}\frac{1+\gamma}{1-\gamma}\left(\frac{\mu_n^4}{\mu_n^2-1}-1\right), \quad (9)$$

then the steady-state regime becomes unstable and changes to a self-modulation regime as either the beam current or the gas pressure increases. This effect is attributable to the excitation of ion-acoustic waves by a localized plasma source (the BPD). The dispersion relation for these waves has the form

$$\Omega_n l = 2\pi n, \quad n = 1, 2, \ldots . \quad (10)$$

In relationship (9), we introduced the quantity $P \equiv S_0\int_{\zeta_1}^{l}|\varepsilon|_{st}^2(\zeta)d\zeta$ and the parameter $\mu_n \equiv \Omega_n/2\beta$, characterizing the ratio between the spatial scales of the ion-acoustic wave and the microwave field (it follows from Eq. (3) that, in dimensionless variables, $K \equiv \Omega$, where Ω and K are the frequency and wavenumber of a low-frequency wave, respectively).

The function $P_c(\mu)$ has a minimum at $\mu = \bar{\mu} = \sqrt{2}$; hence, the ion-acoustic wave with the frequency $\Omega_k = 2\pi k/l$ (where k is an integer), which is the closest to $\bar{\Omega} = 2\sqrt{2}\beta$, will be excited first.

3. STABILITY OF STEADY STATES OF A NONLINEAR AMPLIFIER

The problem of the stability of the steady states of a nonlinear amplifier can be solved only numerically. The results of such a study are presented below.

In solving the set of Eqs. (1) with initial conditions (2), the electron beam dynamics was simulated by the macroparticle method and Eqs. (3) with boundary conditions (4) were solved by the method of characteristics.

3.1. Stability of Steady-State Solutions in the Absence of Reflection from the Boundaries ($\gamma = 0$)

Let us examine how the stability of the steady-state amplification regime depends on the sort of the working gas (which is characterized by the parameter ε_i), its pressure (the parameter S_0), and the initial amplitude of the microwave field $|\varepsilon|_0$.

Let us fix the initial amplitude: $|\varepsilon|_0 = 0.01$. Assuming that the amplifier length is $l = 9.5$, we obtain that the field intensity in the amplifier is lower than the maximum field value $|\varepsilon|_{tr} \approx 1.47$, determined by the trapping

of the beam electrons by the field of the amplified wave (it can seen from Fig. 1 that the maximum field at the amplifier output is reached at the length $l = l_{tr} = 10.0$). Numerical calculations show that, at a given value of the parameter ε_i, there is the threshold value of the pressure $S_0 = (S_0)_c$ (and, accordingly, the threshold value of the parameter $P = P_c$) at which the steady-state regime becomes unstable. Figure 2 shows the dependence of $(S_0)_c$ and P_c on the parameter ε_i. The right vertical line corresponds the value $\varepsilon_{i,\max} = 1.41$, above which a BPD is absent. The left vertical line indicates the value $\varepsilon_{i,\min} = 1.15$, which is the applicability limit for the linear approximation of the dependence of the ionization cross section on the plasma electron energy. It follows from the results of numerical calculations presented in Fig. 2 that, as in case of a linear TWT amplifier (see formula (9)), the threshold value of the parameter P does not depend on the sort of gas, $P_c \approx 6.5$. The period of the ion-acoustic wave excited in the course of instability is $T \equiv 2\pi/\Omega = 2.8$. Note that expressions (9) and (10) yield the following values of these parameters: $P_c \approx 7.1$ and $T = 3.1$.

Similar calculations were performed for different values of the parameters $|\varepsilon|_0$ and l. The results obtained allow us to conclude that, first, the threshold value of the parameter P does not depend on the sort of gas at $l \le l_{tr}$ ($P_c \approx 6.5$) and, second, expressions (9) and (10) can be used as estimates even in the case of a nonlinear amplifier; in this case, the error does not exceed 10%.

Below, we will examine how the parameter P_c depends on the other parameters. The corresponding dependences $(S_0)_c$ will not be analyzed, because they can easily be found from definition of the parameter P.

Let us choose the amplifier length such that the condition $l > l_{tr}$ is satisfied. Figure 3 shows the results of numerical calculations. The limiting values marked in the figure are $\varepsilon_{i,\max} = 1.475$ and $\varepsilon_{i,\min} = 1.2$. It follows from this figure that, in most of the range of ε_i, the value of P_c remains constant ($P_c \approx 4.3$); however, this value is approximately 1.5 times smaller than in the case of $l \le l_{tr}$ (see Fig. 2). Only at the very small length of the region occupied by the BPD ($\varepsilon_i \approx \varepsilon_{i,\max}$), the value of P_c increases with increasing ε_i and tends to $P_c \approx 6.5$ at $l < l_{tr}$.

To understand the reason for this behavior of the parameter P_c, we calculated the dependence of this parameter on the initial field amplitude $|\varepsilon|_0$ in an amplifier with $l = 10.0$ and $\varepsilon_i = 1.2$. The calculated dependence is shown in Fig. 4. The vertical dotted line sows the value $|\varepsilon|_{0,\min} = 0.00475$, below which a BPD is not excited at the given value of ε_i. It follows from this figure that P_c remains constant ($P_c \approx 6.5$) up to $|\varepsilon|_0 = 0.01$. At this value of the initial amplitude, the field at the amplifier output reaches its maximum possible value, $|\varepsilon|_{tr} \approx 1.47$. At higher values of $|\varepsilon|_0$, P_c rapidly decreases to $P_c \approx 4.3$. It should be noted that, at the given ampli-

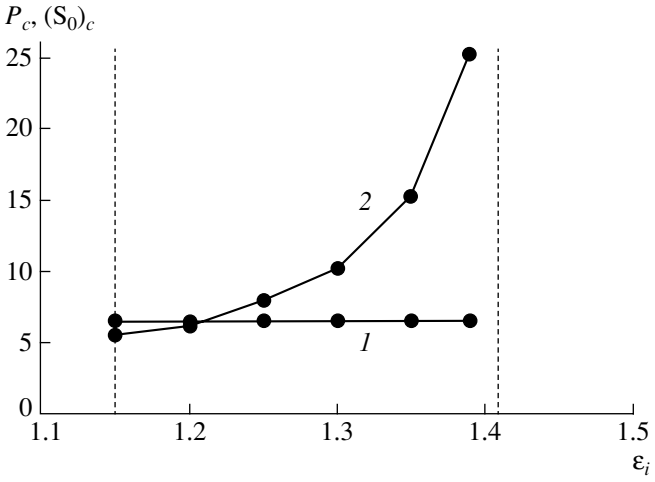

Fig. 2. Parameters (*1*) P_c and (*2*) $(S_0)_c$ vs. parameter ε_i for $l < l_{tr}$, $|\varepsilon|_0 = 0.01$, and $l = 9.5$.

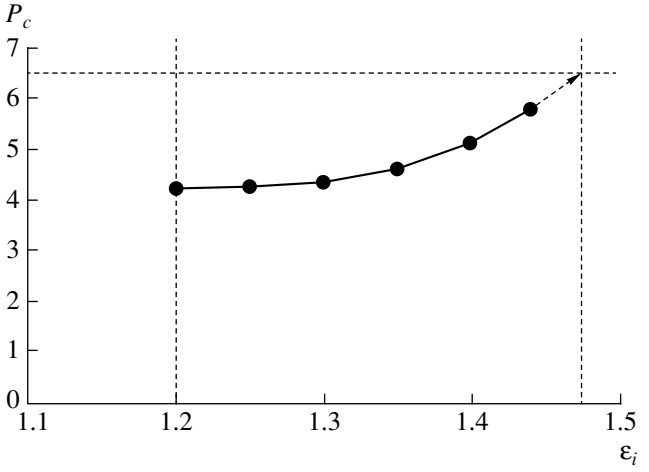

Fig. 3. Parameter P_c vs. ε_i for $l > l_{tr}$, $|\varepsilon|_0 = 0.01$, and $l = 11.0$.

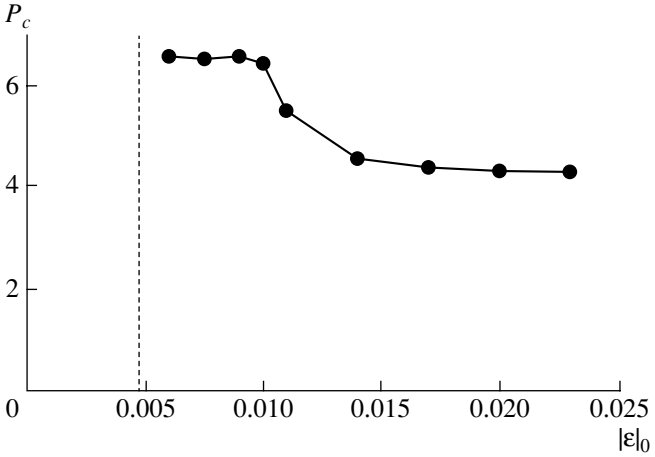

Fig. 4. Parameter P_c vs. initial field amplitude $|\varepsilon|_0$ for $\varepsilon_i = 1.2$ and $l = 10.0$.

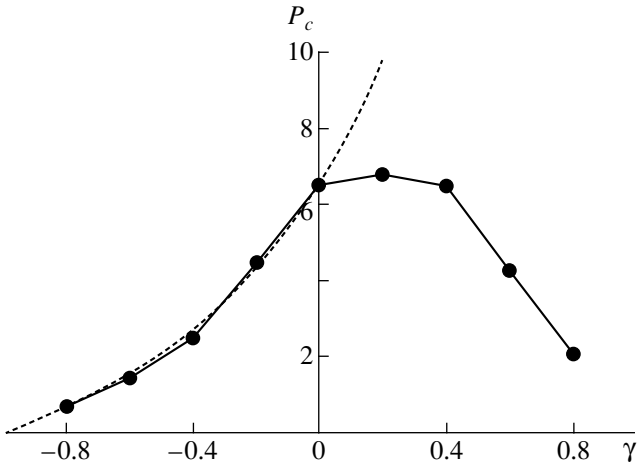

Fig. 5. Parameter P_c vs. reflection coefficient γ for $l < l_{tr}$, $|\varepsilon|_0 = 0.01$, $l = 9.5$, and $\varepsilon_i = 1.2$.

fier length, the value of the initial amplitude $|\varepsilon|_0 = (|\varepsilon|_0)_{tr} = 0.01$ separate two characteristic regions. At $|\varepsilon|_0 < (|\varepsilon|_0)_{tr}$, the electron bunch formed in the course of BPI is in the decelerating phase of the wave throughout the entire BPD region. At $|\varepsilon|_0 > (|\varepsilon|_0)_{tr}$, there is an interval within the BPD region where the bunch is in the accelerating phase. As the difference $|\varepsilon|_0 - (|\varepsilon|_0)_{tr}$ increases, the length of this interval increases and, at $|\varepsilon|_0 \approx 0.014$, becomes comparable to the length of the interval within which the bunch is in the decelerating phase. Therefore, we may suppose that, in the accelerating phase of the wave, the beam is less stable against the plasma density perturbations as compared to the decelerating phase.

Taking into consideration the aforesaid, the analysis of the data presented in Figs. 2–4 allows us to draw the following conclusion. At $\gamma = 0$, the entire four-dimensional (S_0, $|\varepsilon|_0$, l, ε_i) region of the amplifier parameters can be conventionally divided into three domains:

(i) In the first domain, the beam is in the decelerating phase of the wave throughout the entire BPD region. The threshold value of the parameter P in this domain is nearly constant and equal to $P_c \approx 6.5$.

(ii) In the second domain, the length of the BPD region is on the order of unity and is nearly evenly shared between the intervals within which the beam is in the decelerating and accelerating phases. In this domain, the threshold value of the parameter P is also nearly constant and equal to $P_c \approx 4.3$.

(iii) In the third domain, the interval in the BPD region where the beam is in the accelerating phase is very short. In this domain, the value of P_c varies within the limits determined by its values in the above two domains.

3.2. Influence of Reflections on the Stability of Steady-State Solutions $\gamma \neq 0$

Let us consider how reflections of ion-acoustic waves from the amplifier boundaries influence the threshold for the onset of instability of a steady-state regime. Let us choose the amplifier parameters $|\varepsilon|_0 = 0.01$ and $l = 9.5$, such that the condition $l < l_{tr}$ is satisfied. Let us fix the parameter ε_i ($\varepsilon_i = 1.2$). Figure 5 shows the results of numerical calculations of the dependence of the threshold value of the parameter P on the reflection coefficient γ. The dotted line shows the dependence

$$P_c = 6.5\frac{1+\gamma}{1-\gamma}, \qquad (11)$$

which follows from the linear theory. It can be seen that, at $\gamma \leq 0$ (the phase of the reflected ion-acoustic wave does not change), the behavior of the function $P_c(\gamma)$ for a nonlinear amplifier is satisfactorily described by expression (9), derived for the case of a linear amplifier. At $\gamma > 0$ (the phase of the reflected wave changes by π), P_c does not increase with increasing γ, as is predicted by formula (9), but, first (within the interval $0 < \gamma < 0.5$), remains almost constant and, at $\gamma > 0.5$, rapidly decreases. In our opinion, such behavior of $P_c(\gamma)$ can be explained as follows:

At $l < l_{tr}$, the source of plasma density perturbations (the BPD) is located near the right boundary of the interaction region, where, at $\gamma = -1$, there is an antinode or, at $\gamma = 1$, a node of low-frequency oscillations of the plasma-filled cavity (at another values of $|\gamma|$, there are a maximum or minimum, respectively, of the amplitude of the density oscillations). The excitation of oscillations by an external force is most efficient when the force is applied to the antinode region of the eigenmodes of a bounded system (or to the region where their amplitude is maximum). Hence, at $l < l_{tr}$, density oscillations are excited more efficiently at $\gamma \leq 0$ than at $\gamma > 0$; accordingly, the threshold values of $P_c(\gamma)$ are lower at $\gamma \leq 0$ than at $\gamma > 0$. At $|\gamma| \longrightarrow 1$, the Q factor of the cavity increases; hence, we have $P_c(\gamma) \longrightarrow 0$, regardless of the sign of γ.

If the length l is so large ($l > l_{tr}$) that the maximum of the filed of the amplified wave is reached far from the right boundary, the excitation efficiency of low-frequency eigenmodes at $\gamma > 0$ is approximately the same as at $\gamma < 0$, because the perturbation source (the BPD) is located neither in the antinode nor in the node of oscillations. Figure 6 shows a typical dependence $P_c(\gamma)$ at $l > l_{tr}$. A decrease in the total level of $P_c(\gamma)$ in comparison to the case $l < l_{tr}$ is attributed to a change in the phase of an electron bunch in the amplified wave in the BPD region, as was described in the previous section. A fair agreement between the calculated curve and analytic dependence (11) (in which γ is replaced with $-\gamma$; see the dotted line in Fig. 6) in the ($P_c < 4$, $\gamma > 0$) domain is probably due to the same effect.

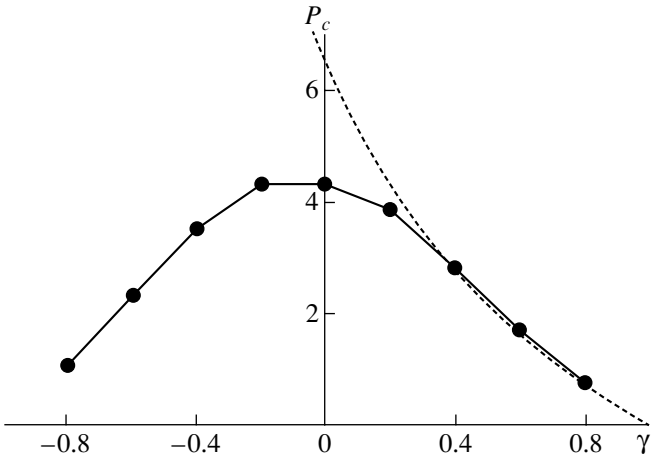

Fig. 6. Parameter P_c vs. reflection coefficient γ for $l > l_{tr}$, $|\varepsilon|_0 = 0.01$, $l = 11.0$, and $\varepsilon_i = 1.3$.

4. INFLUENCE OF LOW-FREQUENCY MODULATION OF A MICROWAVE FIELD ON THE SPECTRAL AND POWER CHARACTERISTICS OF A TWT AMPLIFIER IN THE BPD REGIME

Let us consider the dynamics of the processes in an amplifier after the onset of low-frequency instability ($P \geq P_c$). We will vary the value of the parameter S_0 and fix the remaining parameters. Let us choose the initial microwave field amplitude ($|\varepsilon|_0 = 0.01$) and the amplifier length ($l = 10.0$) such that the output amplitude in the steady-state regime is maximum ($|\varepsilon(l)| \approx 1.47$); i.e., the TWT amplifier operates in the optimum regime (see Fig. 1). The other parameters are $\gamma = 0$ and $\varepsilon_i = 1.2$.

Figure 7a shows the time evolution of the microwave field amplitude $|\varepsilon|(l, \tau)$ and the plasma density $\eta(l, \tau)$ at the amplifier output after the onset of instability. The dotted line shows the value of the microwave field amplitude $|\varepsilon| = \varepsilon_i$, starting from which a BPD is excited. Figure 7b shows the time dependence of the plasma density at the amplifier input, $\eta(0, \tau)$. We draw the reader's attention to two important circumstances.

First, the amplitude of the ion-acoustic wave propagating toward the beam (the amplitude of plasma density oscillations at the input of the TWT amplifier, Fig. 7b) is several times larger than the amplitude of the copropagating wave (Fig. 7a, curve *2*). It is the counterpropagating wave that produces the distributed feedback in the system, so that the microwave amplifier transforms into a generator of low-frequency oscillations. Large-amplitude oscillations of the plasma density in the counterpropagating wave cause large-amplitude oscillations of the microwave field (Fig. 7a, curve *1*). That the amplitudes of the counter- and copropagating waves do not coincide is explained by the fact that, in the self-modulation regime, the maximum of the microwave field in the (ε, ζ) plane describes an ellipsoid around its steady-state value in

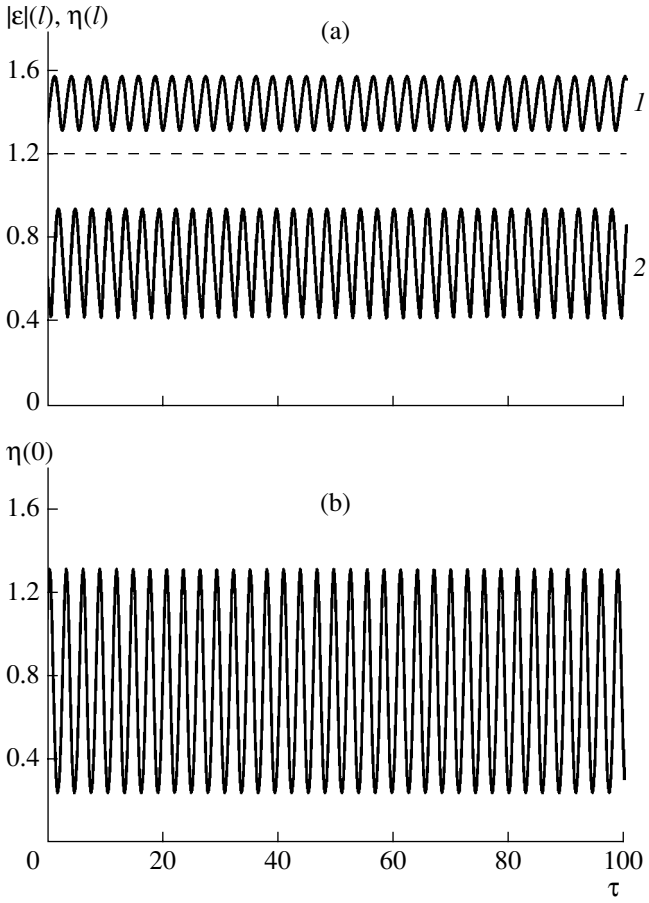

Fig. 7. Time dependences of (a) the microwave field amplitude (curve *1*) and the plasma density at the amplifier output (curve *2*) and (b) plasma density at the amplifier input at the threshold of instability for $|\varepsilon|_0 = 0.01$, $l = 10.0$, $\varepsilon_i = 1.2$, $S_0 = 3.25$, and $\gamma = 0$.

the anticlockwise direction. In Fig. 1, this curve is shown by the dotted line and the direction of motion is indicated by the arrow. Due to such motion of the field maximum, the power of the source moving toward the beam exceeds that of the source moving in the same direction as the beam. The higher power source more efficiently pumps the low-frequency wave propagating in the same direction with it (toward the beam), because the interaction with this wave is more prolonged in comparison to the wave propagating toward the source (in the beam propagation direction).

Second, it follows from numerical calculations that the microwave amplitude and the amplitude of steady-state plasma density oscillations in Fig. 7 do not depend on the small excess over the instability threshold. Only the time during which the self-modulation regime is established depends on this value. Thus, in the BPD regime, a plasma-filled TWT amplifier has a "rigid" threshold for the excitation of oscillations. A characteristic feature of this process is that the amplitude of oscillations of the output power becomes large just after

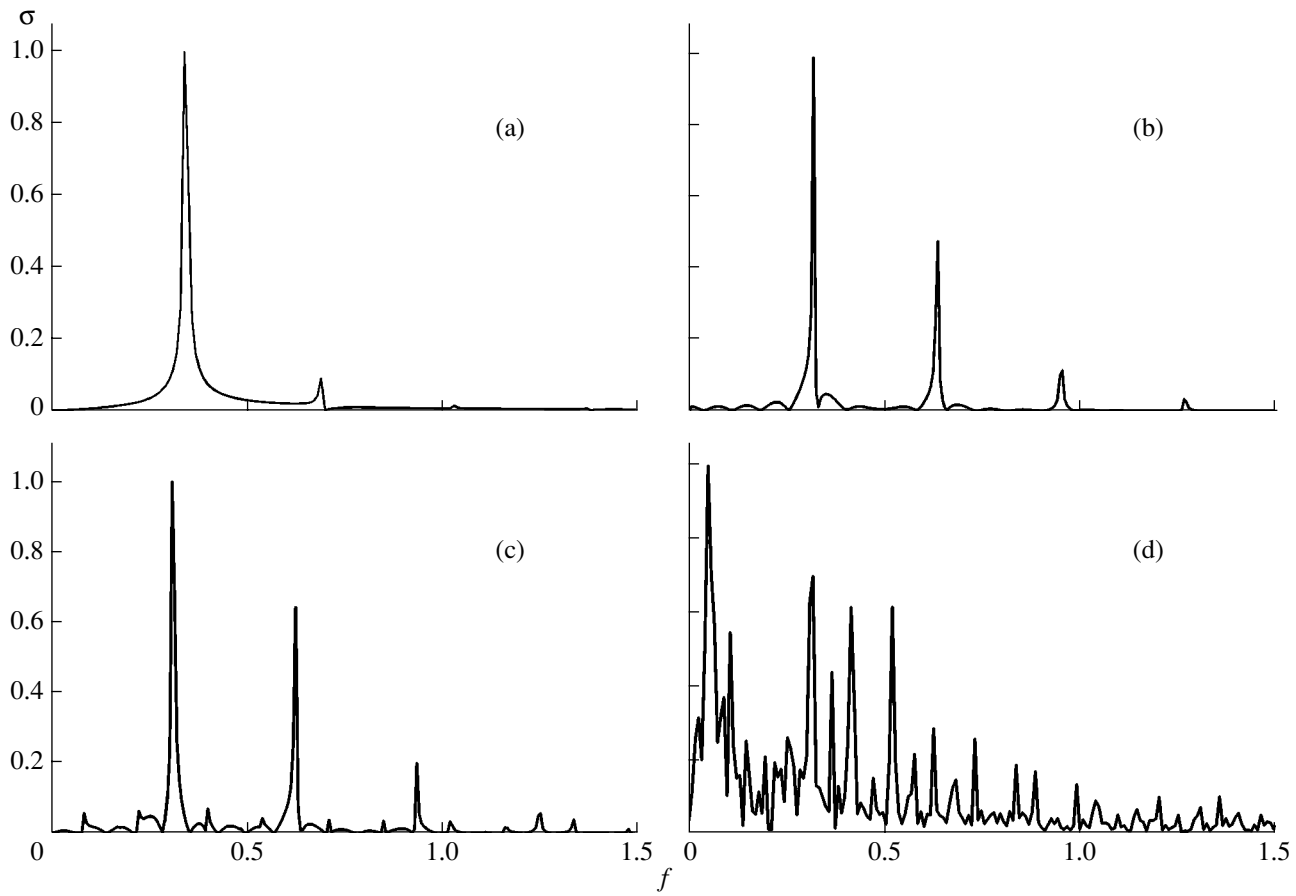

Fig. 8. Dynamics of the spectrum of the output signal of the amplifier in the BPD regime for $|\varepsilon|_0 = 0.01$, $l = 10.0$, $\varepsilon_i = 1.2$, and $\gamma = 0$ for S_0 = (a) 3.25, (b) 15.0, (c) 20.0, and (d) 40.0.

the onset of instability (see Fig. 7a).[2] In our opinion, the "rigid" character of excitation is caused by the oscillations of the boundaries of the BPD region.

Let us now consider how the modulation of the microwave field amplitude influences the spectral characteristics of the amplifier. Figure 8 shows how the spectrum of the output signal from the TWT amplifier changes with increasing parameter S_0. The values of the remaining parameters are the same as in Fig. 7. In Fig. 8, the spectral density normalized to its maximum value σ is plotted on the ordinate, while the dimensionless frequency f is plotted on the abscissa. It follows from Fig. 8a that, after the steady-state amplification regime becomes unstable, an almost single-mode regime of oscillations of the microwave amplitude is established (S_0 = 3.25). Figure 8b illustrates a multimode regime of the low-frequency self-modulation at a sufficiently large value of the parameter S_0 = 15.0. It is clearly seen from Fig. 8c that the value S_0 = 20.0 is the threshold for the stochastization of the plasma-filled TWT amplifier. The amplifier now demonstrates all the characteristic features of a generator (there are parameter regions in which regular and stochastic self-modulation occur), specifically, the generator of low-frequency oscillations. It should be noted that the parameter S_0 at the threshold for stochastization is six times larger than its value at the instability threshold, $(S_0)_c$ = 3.25. Thus, the low-frequency generator has a rather wide band of regular self-modulation. It follows from Fig. 8d (S_0 = 40.0) that, when the parameter S_0 is two times larger than the threshold value for stochastization, the spectrum has a strong stochastic component.

After the steady-state amplification regime becomes unstable, ion-acoustic waves propagating in the TWT amplifier result in low-frequency oscillations of the output microwave power. From the standpoint of the choice of the optimum operating regime, an important characteristic of the structure is the dependence of the average power on the neutral gas pressure (parameter S_0). It is well known that the efficiency of a TWT amplifier (the ratio of the output wave power to the beam power $P_b = \frac{1}{2} n_b S_b m v_b^3$, where S_b is the area of the beam cross section) is proportional to the dimensionless wave

[2] As was shown in [10], a similar amplifier in which plasma nonlinearity is caused by the ponderomotive force has a "soft" excitation threshold: the oscillation amplitude of the output power is proportional to the excess over the threshold.

amplitude squared, $|\varepsilon|^2$. The proportionality factor is determined by the parameters of the slow-wave structure and beam. Summing the results of numerical calculations of the time evolution of the output microwave power for different values of the parameter S_0, we obtain the dependence $\overline{|\varepsilon|^2}(S_0)$, which is shown in Fig. 9.

It follows from Fig. 9 that, starting from $S_0 = (S_0)_c = 3.25$ (the modulation threshold), plasma nonlinearity caused by the action of a nonsteady source (the BPD) leads to a rather fast decrease in the mean square value of the field amplitude with increasing S_0. We note that a similar decrease in $\overline{|\varepsilon|^2}(l)$ with increasing the beam current or the plasma density also takes place when an unsteady regime arises due to plasma nonlinearity caused the action of the ponderomotive force [10]. Let us consider this problem in more detail.

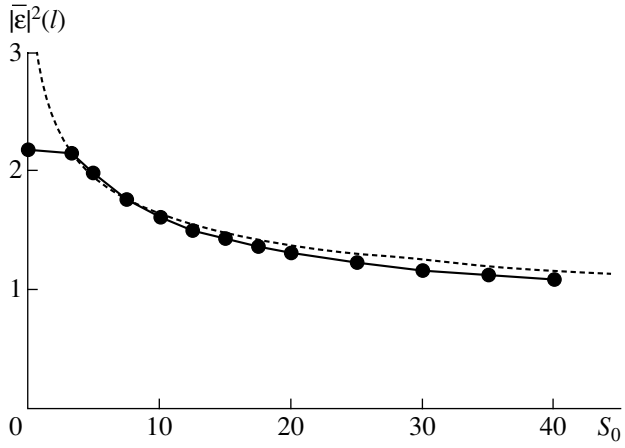

Fig. 9. Mean square value of the microwave field amplitude vs. parameter S_0 for $|\varepsilon|_0 = 0.01$, $l = 10.0$, $\varepsilon_i = 1.2$, and $\gamma = 0$.

Under the action of the ponderomotive force, a region with a reduced plasma density appears in the vicinity of the maximum of the microwave field in a steady-state operating regime of the TWT amplifier. The phase velocity of the amplified microwave propagating through the region with a reduced density decreases. This leads to an increase in the time during which the wave is in resonance with the decelerating beam. As a result, the field amplitude decreases substantially (by a factor of 1.5) as compared to the case of a uniform plasma. When the steady-state regime becomes unstable, the region with a reduced plasma density begins to move toward the beam (i.e., toward the amplifier input). Its role now becomes adverse because the wave phase velocity begins to deviate from the beam velocity already in the stage of the bunch formation. This causes strong (up to 100%) oscillations of the microwave field amplitude over one ion-acoustic wave period. Thus, the average field amplitude decreases in comparison to the steady-state amplitude. At even larger ponderomotive force, the fragmentation of time scales begins to manifest itself (the time dependence of the plasma density over one period of the low-frequency wave has the shape of narrow depressions, whereas the time dependence of the field amplitude has the shape of narrow peaks), which leads to a further decrease in the average amplitude of the amplified wave.

If plasma nonlinearity is caused by the presence of an unsteady source (the BPD), then rather strong oscillations of the plasma density and field amplitude arise just after the steady-state regime becomes unstable (Fig. 7). Since the density oscillations are symmetric about their mean value (which determines the frequency of the most amplified microwave) at the instant at which the steady-state regime becomes unstable ($S_0 = (S_0)_c = 3.25$), (see Fig. 9), the mean square value of the field amplitude is equal to its steady-state value. As the parameter S_0 increases, the symmetry of plasma density oscillations breaks. The adverse effect of the enhanced (in comparison to its mean value) plasma density on the behavior of the microwave field amplitude increases, thus decreasing its average value. At large values of the parameter S_0, the time dependence of the plasma density over one period of the low-frequency wave has the shape of a single narrow peak (Fig. 10b). It follows from Fig. 10a that the time dependence of the output amplitude of the microwave wave has the shape of small peaks and much larger dips relative to the threshold level for the excitation of a BPD (Fig. 10a, dotted line). For this reason, the increase in the excess parameter $S_0/(S_0)_c$ is accompanied by a smoother decrease in the mean square value of the filed amplitude in comparison to the case with the ponderomotive force.

It follows from Fig. 9 that a transition to the regime of stochastic self-modulation of the amplifier signal ($S_0 > 20.0$) only slightly influences the character of the dependence $\overline{|\varepsilon|^2}(S_0)$.

The dependence $\overline{|\varepsilon|^2}(S_0)$ cannot be obtained from model (1)–(4) analytically throughout the entire range of S_0 variations. Nevertheless, it follows from Fig. 9 that this dependence in the self-modulation regime is rather simple. We will try to construct this dependence from the following considerations. First, the mean square value of the microwave field amplitude at the amplifier output should be proportional to the amplitude squared in the steady-state regime; i.e., $\overline{|\varepsilon|^2}(l) \sim |\varepsilon|^2_{\text{st}}(l)$. Second, this value decreases with increasing ratio $S_0/(S_0)_c$. Numerical calculations show that the dependence

$$\overline{|\varepsilon|^2}(l) = |\varepsilon|^2_{\text{st}}(l)\left(\frac{S_0}{(S_0)_c}\right)^{-\frac{1}{4}} \qquad (12)$$

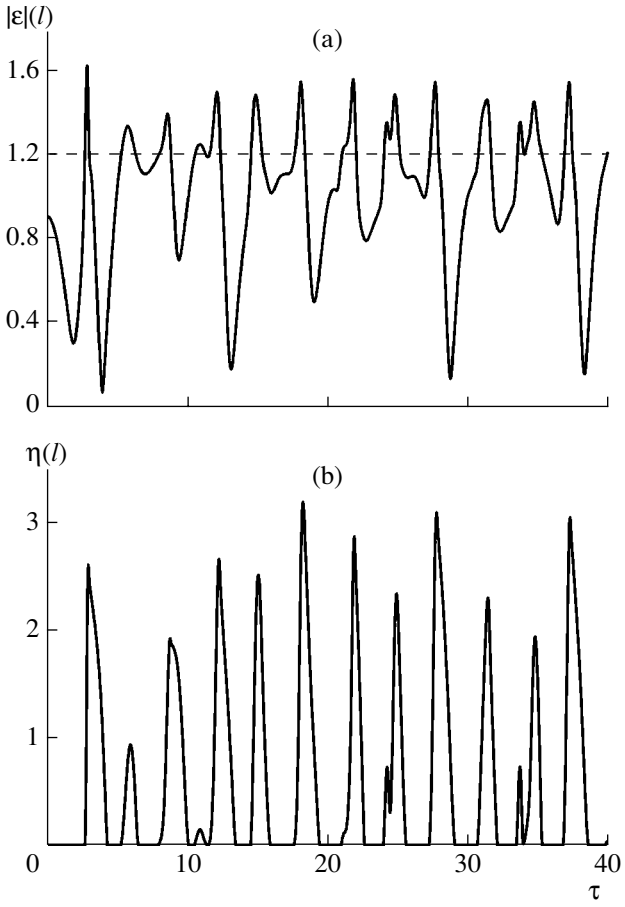

Fig. 10. Time dependences of (a) the microwave field amplitude and (b) plasma density at the amplifier output in the regime of developed low-frequency modulation for $|\varepsilon|_0 = 0.01$, $l = 10.0$, $\varepsilon_i = 1.2$, $S_0 = 30.0$, and $\gamma = 0$.

adequately describes the behavior of the mean square value of the microwave field amplitude over a wide range of the amplifier lengths and the reflection coefficients of ion-acoustic waves. Dependence (12) is shown in Fig. 9 by the dotted line.

Numerical calculations show that the average power of the microwave field at the amplifier output depends strongly on the coefficient of reflection of ion acoustic waves from the amplifier boundaries. The average power decreases significantly for large reflection coefficients ($|\gamma| \approx 1$). This also follows from expression (12), because $(S_0)_c$ decreases with increasing $|\gamma|$, as was shown in the previous section.

In conclusion, we note that a comparison of the theory of an unsteady BPD developed in this paper with the experimental data from [10] is a rather laborious problem, one which is beyond the scope of this paper. Here, we only give estimates of the parameters S_0 and $(S_0)_c$ under experimental conditions: the working gas is argon, $W_i = 16$ eV, and the pressure in the middle of the pressure range corresponding to the existence of a BPD is 10^{-5} torr. To estimate S_0, we use an expression from [13] and the calculated dependences of the other parameters from [10]. As a result, we arrive at the estimate $S_0 \approx 2.5$. As was shown in [10], a waveguide filled with a plasma has the very high coefficient of the reflection of ion-acoustic waves from its boundaries, $|\gamma| > 0.6$. Numerical calculations carried out at these values of the reflection coefficient show that, under experimental conditions, this parameter is $(S_0)_c < 1$. It follows from the comparison of this value with the above estimate of S_0 that, even with the use of such a low-power beam (in the experiments described in [10], a beam with a power of $P_b = 50$ W was used), it is necessary to take into consideration the possibility of the existence of a regime with an unsteady BPD.

5. CONCLUSIONS

It follows from the nonlinear BPI theory elaborated in this paper that, as the neutral gas pressure or the beam current increases, the steady-state operating regime of a plasma-filled TWT amplifier becomes unstable. The onset of instability is caused by the plasma density perturbations arising in the BPD region. Propagating toward the beam, these perturbations affect the conditions of microwave amplification and change the field distribution in the amplifier, thereby causing a distributed delayed feedback. This means that the microwave amplifier also operates as a source of low-frequency oscillations of the wave amplitude, thus demonstrating the features peculiar to the latter, in particular, a transition to the regular and stochastic self-modulation modes.

The average microwave power at the output of the TWT amplifier in the modulation regime decreases as the neutral gas pressure or the beam current increases. The boundary conditions at the ends of a plasma-filled structure have a substantial effect on both the parameter values corresponding to the change of the amplification regimes and the average output power.

Note that the theory of an unsteady BPD developed in this paper must be adapted to a particular TWT amplifier. The reason is that the plasma density in a real experimental setup changes as the neutral gas pressure or the beam current varies; this, in turn, causes variations in both the frequency of a microwave that is in resonance with the beam and the growth rate of BPI. As a result, the remaining dimensionless parameters also vary. The character of these variations depends on the design of a particular slow-wave structure. In this paper, we have studied the characteristics of this regime that are related to the physical processes occurring in any plasma-filled TWT amplifier in the presence of a residual neutral gas, regardless of the design features of the slow-wave structure.

ACKNOWLEDGMENTS

We are grateful to the anonymous referee for his valuable remarks about the role of elastic collisions in the process of ionization of the residual gas. One of the authors (Yu.P. Bliokh) also acknowledges his financial support from the Center for Absorption in Science, the Ministry of Immigrant Absorption, State of Israel.

REFERENCES

1. Yu. P. Bliokh, E. A. Kornilov, L. A. Mitin, and Ya. B. Fainberg, Fiz. Plazmy **20**, 767 (1994) [Plasma Phys. Rep. **20**, 690 (1994)].
2. L. A. Mitin, V. I. Perevodchikov, M. A. Zav'yalov, *et al.*, Fiz. Plazmy **20**, 733 (1994) [Plasma Phys. Rep. **20**, 662 (1994)].
3. M. A. Miller, Izv. Vyssh. Uchebn. Zaved. Radiofiz. **1**, 110 (1958).
4. N. I. Aĭzatskiĭ, Izv. Vyssh. Uchebn. Zaved. Radiofiz. **20**, 857 (1977).
5. V. B. Krasovitskiĭ and V. I. Kurilko, Zh. Éksp. Teor. Fiz. **51**, 445 (1966) [Sov. Phys. JETP **24**, 300 (1966)].
6. Yu. P. Bliokh, Ya. B. Fainberg, M. G. Lyubarskii, and V. O. Podobinskii, Proc. SPIE **3158**, 182 (1997).
7. Yu. P. Bliokh, Ya. B. Fainberg, M. G. Lyubarsky, *et al.*, Phys. Plasmas **5**, 4061 (1998).
8. K. Yu. Bliokh, Yu. P. Bliokh, M. G. Lyubarsky, and V. O. Podobinsky, Izv. Vyssh. Uchebn. Zaved. Prikl. Nelineinaya Din. **7**, 29 (1999).
9. Yu. P. Bliokh, M. G. Lyubarsky, G. S. Nusinovich, and V. O. Podobinsky, Izv. Vyssh. Uchebn. Zaved. Prikl. Nelineinaya Din. **7**, 56 (1999).
10. Yu. P. Bliokh, M. G. Lyubarsky, N. M. Zemlyansky, *et al.*, Fiz. Plazmy **29**, 336 (2003) [Plasma Phys. Rep. **29**, 307 (2003)].
11. A. N. Antonov, Yu. P. Bliokh, E. A. Kornilov, *et al.*, Fiz. Plazmy **26**, 1097 (2000) [Plasma Phys. Rep. **26**, 1027 (2000)].
12. E. A. Kornilov, E. A. Lutsenko, R. M. Nikolaev, *et al.*, Zh. Éksp. Teor. Fiz. **38**, 685 (1960) [Sov. Phys. JETP **11**, 493 (1960)].
13. Yu. P. Bliokh, M. G. Lyubarsky, V. O. Podobinsky, and Ya. B. Fainberg, Fiz. Plazmy **29**, 801 (2003) [Plasma Phys. Rep. **29**, 740 (2003)].

Translated by E.L. Satunina

Plasma Physics Reports, Vol. 30, No. 9, 2004, pp. 740–755. Translated from Fizika Plazmy, Vol. 30, No. 9, 2004, pp. 795–810.

PLASMA OSCILLATIONS AND WAVES

Theory of the ICR Heating of a Plasma Column: Methodological Note

A. V. Timofeev

Russian Research Centre Kurchatov Institute, pl. Kurchatova 1, Moscow, 123182 Russia

Received November 11, 2003

Abstract—A set of wave equations is derived that describes electromagnetic waves at frequencies on the order of the ion gyrofrequency in a plasma column with an arbitrary electron temperature. This set takes into account, in particular, the resonant interaction of electrons with waves in the transit-time magnetic pumping regime. The effect of the amplification of the electromagnetic fields of current-carrying antennas by the plasma is analyzed. The evolution of the fields with an increase of plasma density from a zero value (vacuum) is considered. The main parameters are determined for minority ion cyclotron resonance heating in the planned EPSILON system.

1. INTRODUCTION

The characteristic wavelength of the electromagnetic waves used for ion cyclotron resonance (ICR) plasma heating is usually comparable to or exceeds the plasma dimensions. Such waves are excited by an antenna, so that the structure of their electromagnetic fields is largely governed by the antenna shape. Current-carrying antennas in which the electric current has both longitudinal and transverse (azimuthal) components have proved to be the most successful for ICR heating of the plasma column. Among these are helical antennas and Nagoya type III antennas. In a helical antenna, the current-carrying conductor has the form of a helix wound around the plasma column. In a Nagoya type III antenna, the current-carrying conductor consists of purely longitudinal and purely azimuthal portions. ICR plasma heating is provided by the transverse (left-polarized) component of the RF electric field. Such antennas are advantageous in that the transverse electric field generated by them can be amplified (rather than weakened) by the presence of plasma. The reason for this is that the antennas in question excite two different electromagnetic modes whose transverse electric fields are in antiphase. The plasma responds differently to these modes, which can lead to the amplification of the total transverse electric field (see, e.g., [1, 2]). The objective of the present paper is to analyze the physical nature of the electromagnetic fields generated by a current-carrying antenna in vacuum and to consider how the fields evolve with an increase of plasma density. Another objective is to discuss the influence of Alfvén and plasma resonances.

During ICR heating, the RF power is usually deposited in the so-called resonant minority ions ($\omega = \omega_i'$, where ω is the RF field frequency and ω_i' is the gyrofrequency of the minority ions). The structure of the electromagnetic fields is especially sensitive to the ratio between the field frequency and the gyrofrequency of the main plasma ions, $-\omega_i$. In what follows, a study will be made of the cases of light ($\omega > \omega_i$) and heavy ($\omega < \omega_i$) impurities.

The plasma response to electromagnetic fields depends on the electron temperature, in particular, on the temperature-dependent ratio between the wave phase velocity along the magnetic field and the electron thermal velocity. In order for the analysis to be applicable to an arbitrary value of this ratio, it is necessary to take into account the effects of the finite electron Larmor radius. Associated with these effects is, in particular, the so-called transit-time magnetic pumping (TTMP) effect—the Cherenkov resonance interaction of charged particles with the transverse (with respect to the main magnetic field) electric field of the electromagnetic waves. Along with the finite-Larmor-radius effects, the TTMP effect can become important at high plasma densities, in which case the zero-Larmor-radius approximation, used in [1–4], becomes inadequate.

Numerical methods developed in the present study were used to estimate the prospects for ICR heating in the planned EPSILON system [5]. An analysis shows that, among the various possible plasma heating methods, an optimum one seems to be the heating of a plasma with a small addition of heavy resonant ions, e.g., a hydrogen plasma with a deuterium minority at a sufficiently high electron temperature (>1 keV).

2. ELECTRIC CURRENT EXCITED BY RF OSCILLATIONS IN PLASMA

Let us formulate the approximations with which to analyze the minority ICR plasma heating. Under cyclotron resonance conditions, the ions interact most efficiently with the left-polarized component of the trans-

1063-780X/04/3009-0740$26.00 © 2004 MAIK "Nauka/Interperiodica"

verse electric field of the waves used to heat plasma. If the time dependence of the RF field is represented in the form $e^{-i\omega t}$, then this component is described by the expression $E_+ = \frac{1}{\sqrt{2}}(E_r + iE_\theta)$, written in a cylindrical coordinate system with the z axis directed along the main magnetic field. The terms "transverse" and "longitudinal" are here used to signify the direction with respect to this field. The resonant interaction of the ions with the right-polarized and longitudinal components of the electric field is governed by finite-Larmor-radius effects and, for $k\rho_i \ll 1$, is weaker than the interaction with the left-polarized component (here, k is the wavenumber and ρ_i is the mean ion gyroradius). Of course, the above assertions are valid if the plasma does not weaken the left-polarized electric field component. This turns out not to be the case for minority ICR heating.

The intensities of the interaction of the main (nonresonant) plasma ions with each of the electric field components are of the same order, so that, in describing nonresonant interaction, the effects of ion thermal motion can be ignored.

In the above approximations, the ion current is given by the expression

$$\mathbf{j}^{(i)} = -\frac{i\omega}{4\pi}((\varepsilon_\perp^{(i)} - 1)\mathbf{E}_\perp + ig^{(i)}\mathbf{E}\times\mathbf{b}). \qquad (1)$$

Here, $\varepsilon_\perp^{(i)} = \frac{1}{2}(\varepsilon_+^{(i)} + \varepsilon_-^{(i)})$, $g^{(i)} = \frac{1}{2}(\varepsilon_+^{(i)} - \varepsilon_-^{(i)})$, $\varepsilon_+^{(i)} = 1 - \frac{\omega_{pi}^2}{\omega(\omega-\omega_i)} + \frac{\omega_{pi}'^2}{\omega k_\parallel v_{Ti}'} i\sqrt{\pi} W(\zeta_i')$, $\varepsilon_-^{(i)} = 1 - \frac{\omega_{pi}^2}{\omega(\omega+\omega_i)} - \frac{\omega_{pi}'^2}{\omega(\omega+\omega_i')}$, ω_{pi} is the Langmuir frequency of the main plasma ions, ω_i is their gyrofrequency, the prime indicates the quantities characterizing the minority ions, $\zeta_i' = \frac{\omega-\omega_i'}{k_\parallel v_{Ti}'}$, $v_{Ti}' = \sqrt{\frac{2T_i'}{m_i'}}$, W is the probability integral of complex argument, and $\mathbf{b} = \mathbf{B}_0/B_0$. In expression (1), the longitudinal ion current is ignored because it is low in comparison to the longitudinal electron current.

The longitudinal electron current should be determined with allowance for both longitudinal and transverse electric fields (see, e.g., [6]). The corresponding off-diagonal elements of the dielectric tensor contain the large parameter $\left(\frac{\omega_{pe}}{\omega}\right)^2$ and also the small parameter $(k_\perp\rho_e)\chi_e$, where $\chi_e = \frac{\omega}{k_\parallel v_{Te}}$ for $\omega \ll k_\parallel v_{Te}$ and $\chi_e = \frac{k_\parallel v_{Te}}{\omega}$ for $\omega \gg k_\parallel v_{Te}$. For a plasma with hot electrons ($\omega \ll k_\parallel v_{Te}$), these tensor elements are of the same order of magnitude as the tensor elements for the ions that were used in deriving expression (1). This is why the approach employed in [1–4], in which the off-diagonal elements of the dielectric tensor were ignored because of the smallness of the electron gyroradius, requires refinements. Further analysis shows that these elements are important at fairly high plasma densities. Note that, when the temperatures of the main plasma ions and minority ions are comparable, the contribution of the former to the off-diagonal elements is small because of the factor $\chi_i = \frac{k_\parallel v_{Ti}}{\omega}$ and the contribution of the latter is also small because they are present in small quantities.

In order for the analysis to be consistent, it is also necessary to take into account the transverse electron current component driven by the longitudinal electric field. Other important components of the transverse electron current are associated with the drift of electrons in the crossed wave electric and main magnetic fields and with the TTMP effect. The additive contributions of the TTMP effect to the dielectric tensor elements are on the order of $\left(\frac{\omega_{pe}}{\omega}\right)^2 (k_\perp\rho_e)^2\delta_e$, where $\delta_e = \exp\left(-\left(\frac{\omega}{k_\parallel v_{Te}}\right)^2\right)$ is the amount of resonant electrons. As for the ions, the TTMP effect is unimportant for them because there is only a small number of resonant minority ions.

The electron current is determined in terms of the perturbation of the electron distribution function f by an RF field. The perturbed distribution function is described by the kinetic equation linearized in small perturbations:

$$\frac{df}{dt} = -\frac{e}{T_e}\mathbf{v}\cdot\mathbf{E}\, f_0,$$

where the unperturbed electron distribution function $f_0(\varepsilon, \eta)$ depends on the integrals of motion, namely, the energy $\varepsilon = mv^2/2$ and the θ component of the generalized momentum, $\eta = \frac{r^2}{2} + \frac{rv_\theta}{\omega_e}$. We consider a plasma cylinder in which the density varies in the radial direction and assume that the uniform magnetic field is directed along the z axis. In this case, it is convenient to expand the perturbed quantities in Fourier integrals, e.g., $\mathbf{E}(\mathbf{r}, t) = \int dk_r \mathbf{E}_{k_r} \exp(i(-\omega t + k_r r + m\theta + k_\parallel z))$.

The standard method of integration along the trajectories yields the expression

$$f_{k_r} = \frac{e}{T_e}\left(\frac{1}{\omega_e}\mathbf{b}\cdot(\mathbf{v}\times\mathbf{E}_{k_r})f_0 - \frac{i}{\omega - k_\parallel v_\parallel}\left(v_\parallel E_{\parallel,k_r} + i\frac{v_\perp \rho_e}{2}\frac{\omega}{c}B_{\parallel,k_r}\right)\times\left(f_0 + \frac{v_\theta}{\omega_e}\frac{\partial f_0}{\partial r}\right)\right)(1 - i\xi_e\sin(\alpha_0 - \psi)). \quad (2)$$

where $\psi = \arctan(m/rk_r)$, $\xi_e = k_\perp v_\perp/\omega_e$, and $\mathbf{b} = \mathbf{B}_0/B_0$. The electron trajectories were described by the equations $\mathbf{v}(t) = (v_\perp\cos(\alpha_0 + \omega_e t),\ v_\perp\sin(\alpha_0 + \omega_e t),\ v_\parallel)$ and $\mathbf{r}(t) = \mathbf{r}(0) + \int_0^t dt\mathbf{v}(t)$, where α_0 is the initial phase of electron gyration. In expression (2), the electron gyroradius is assumed to be small in comparison to the wavelength and the wave frequency is assumed to be much lower than the electron gyrofrequency ω_e.

Using expression (2) gives the following expressions for the density of the electron current driven by an RF electric field:

$$\left.\begin{aligned}\mathbf{j}_\perp^{(e)} &= \frac{\omega_{pe}^2}{4\pi\omega_e}\mathbf{b}\times\mathbf{E} + \frac{c}{4\pi}\nabla\times(\mathbf{b}(Q_1 B_\parallel - iN_\parallel Q_2 E_\parallel))\\ j_\parallel^{(e)} &= \frac{\omega}{4\pi}N_\parallel Q_2\left(-B_\parallel + 2i\frac{\omega_e}{\omega}N_\parallel\zeta_e^2 E_\parallel\right)\end{aligned}\right\}, \quad (3)$$

where $Q_1 = -2\left(\frac{\omega_{pe}}{\omega_e}\right)^2\frac{T_e}{m_e c^2}i\sqrt{\pi}\zeta_e W(\zeta_e)$, $Q_2 = -\frac{\omega_{pe}^2}{\omega\omega_e N_\parallel^2}(1 + i\sqrt{\pi}\zeta_e W(\zeta_e))$, $\zeta_e = \frac{\omega}{k_\parallel v_{Te}}$, and $v_{Te} = \left(\frac{2T_e}{m_e}\right)^{1/2}$. In expressions (2) and (3), the transverse electric field of the waves is expressed through the longitudinal magnetic field by means of Maxwell's equations.

3. TTMP EFFECT

Using expressions (3), we can determine the energy absorbed by the electrons. Taking the volume integral of the quantity $\mathbf{j}\cdot\mathbf{E}^*$ by parts, we arrive at the following expression for this quantity:

$$\mathrm{Re}\,\mathbf{j}\cdot\mathbf{E}^* = \frac{\omega}{4\sqrt{\pi}}\frac{m_e\omega_{pe}^2}{T_e k_\parallel^2}\zeta_e e^{-\zeta_e^2}\times\left(|E_\parallel^2| + 2\frac{k_\parallel T_e}{cm_e\omega_e}\mathrm{Im}(E_\parallel B_\parallel^*) + 2\left(\frac{k_\parallel T_e}{cm_e\omega_e}\right)^2|B_\parallel|^2\right). \quad (4)$$

The last term in parentheses on the right-hand side of expression (4) arises from the TTMP effect and the second term accounts for the interference between the Cherenkov resonance interaction and the TTMP.

Expression (4) can also be derived from the expression

$$\mathrm{Re}\,\mathbf{j}\cdot\mathbf{E}^* = \frac{n_0}{T_e}\left(\frac{\omega}{k_\parallel}\right)^2\int d\mathbf{v}\pi\delta(\omega - k_\parallel v_\parallel)|eE_\parallel + \mu_e\nabla_\parallel B_\parallel|^2 f_0, \quad (5)$$

where $\mu_e = \frac{m_e v_\perp^2}{2B}$ is the magnetic moment of an electron.

Expression (5) shows that an electron is subject not only to the force of the electric field but also to the diamagnetic force in the direction of the main magnetic field, $F_\parallel = -\mu_e\nabla_\parallel B_\parallel$. This result is quite natural because, in the case of long-wavelength low-frequency waves, an electron moving along a Larmor orbit can be regarded as a point charged particle with a nonzero magnetic moment.

Of course, an electron exchanges energy with the RF electric field rather than with the magnetic field. The rate of change of the electron energy, averaged over the cyclotron period, is described by the equation

$$\dot{w} = -e\frac{\omega_e}{2\pi}\oint d\mathbf{s}\cdot\mathbf{E}, \quad (6)$$

where the integration is carried out along a Larmor circle. Using the induction equation and the Cherenkov resonance condition $\omega = k_\parallel v_\parallel$, we can rewrite Eq. (6) as

$$\dot{w} = -\frac{e}{2c}\omega_e\rho_e^2\frac{\partial B_\parallel}{\partial t} = -v_\parallel\mu_e\frac{\partial B_\parallel}{\partial z}.$$

This equation shows that, although the electric field of the waves performs work on the transverse degree of freedom of an electron (rotation along a Larmor circle), the longitudinal energy of an electron also changes. The energy transfer from the transverse degree of freedom to the longitudinal one is governed by the action of the magnetic field of waves, which turns the electron velocity vector. This result confirms the well-known fact (see, e.g., [7]) that, whatever the polarization of waves, the energy transferred to or from a charged particle (in the case at hand, an electron) in resonant interaction in a magnetic field is distributed over the degrees of freedom in accordance with the relationship

$$\frac{\dot{w}_\parallel}{\dot{w}_\perp} = \frac{k_\parallel v_\parallel}{n\omega_e}. \quad (7)$$

Relationship (7) implies that, under the Cherenkov resonance conditions ($\omega = n\omega_e + k_\parallel v_\parallel$, $n = 0$), only the longitudinal energy of the particle changes.

To conclude this section, note that the TTMP effect can take place in the interaction of electrons with mag-

netosonic and Alfvén hydrodynamic waves, in which the longitudinal electric field is suppressed because of the high electron mobility.

4. WAVE EQUATIONS AND EXPRESSIONS FOR THE WAVE ELECTRIC FIELD

Using Maxwell's equations and expression (3) for the perturbed current density, we arrive at the following set of equations describing waves in a longitudinally homogeneous axisymmetric plasma column:

$$\left.\begin{aligned}\nabla\cdot\mathbf{E}_\perp + \frac{1}{N_\parallel^2}(\Delta_\perp + \varepsilon_\parallel)C_\parallel + Q_2 B_\parallel &= \frac{4\pi}{\omega N_\parallel} j_{\parallel,\,\mathrm{ext}}\\ (\nabla\times\mathbf{E}_\perp)_\parallel - iB_\parallel &= 0\end{aligned}\right\}. \quad (8)$$

Here,

$$\left.\begin{aligned}E_r &= l_1 C_\parallel - l_2((1+Q_1)B_\parallel - Q_2 C_\parallel)\\ &\quad -\frac{4\pi}{\omega}(iFj_{r,\,\mathrm{ext}} + Gj_{\theta,\,\mathrm{ext}})\\ iE_\theta &= -l_2 C_\parallel + l_1((1+Q_1)B_\parallel - Q_2 C_\parallel)\\ &\quad +\frac{4\pi}{\omega}(iGj_{r,\,\mathrm{ext}} + Fj_{\theta,\,\mathrm{ext}})\end{aligned}\right\}, \quad (9)$$

$C_\parallel = iN_\parallel E_\parallel$, $l_1 = F\frac{d}{dr} + G\frac{m}{r}$, $l_2 = G\frac{d}{dr} + F\frac{m}{r}$, $F = (\varepsilon_\perp - N_\parallel^2)/D$, $G = g/D$, $D = (\varepsilon_\perp - N_\parallel^2)^2 - g^2 = (\varepsilon_+ - N_\parallel^2)(\varepsilon_- - N_\parallel^2)$, $g = g^{(i)} - \frac{\omega_{pe}^2}{\omega\omega_e}$, $\varepsilon_\parallel = 1 + 2\left(\frac{\omega_{pe}}{k_\parallel v_{Te}}\right)^2(1 + i\sqrt{\pi}\,\zeta_e W(\zeta_e))$, all of the quantities having the dimension of length are normalized to c/ω, and the prime denotes the derivative with respect to the radius.

Using expressions (9), we reduce wave equations (8) to

$$\begin{aligned}&L_1 B_\parallel - L_2 C_\parallel + L_1(Q_1 B_\parallel - Q_2 C_\parallel) + B_\parallel\\ &\quad = -\frac{4\pi}{\omega}((\nabla\times F\mathbf{j}_{\mathrm{ext}\parallel}) + i\nabla_\perp\cdot(G\mathbf{j}_{\mathrm{ext}}))\\ &-L_2 B_\parallel + L_1 C_\parallel - L_2(Q_1 B_\parallel - Q_2 C_\parallel) + \frac{1}{N_\parallel^2}(\Delta_\perp + \varepsilon_\parallel)C_\parallel\\ &\quad = \frac{4\pi}{\omega}\left((\nabla\times G\mathbf{j}_{\mathrm{ext}})_\parallel + i\nabla_\perp\cdot(F\mathbf{j}_{\mathrm{ext}}) + \frac{1}{N_\parallel}j_{\parallel,\,\mathrm{ext}}\right),\end{aligned} \quad (10)$$

where $L_1 = \frac{1}{r}\frac{d}{dr}rF\frac{d}{dr} - \left(\frac{m}{r}\right)^2 F + \frac{m}{r}G_r'$ and $L_2 = \frac{1}{r}\frac{d}{dr}rG\frac{d}{dr} - \left(\frac{m}{r}\right)^2 G + \frac{m}{r}F_r'$.

Set of wave equations (10) is a generalization of the set of equations obtained in [8] for the case of cold electrons.

The circularly polarized components of the electric field are represented in terms of the solutions to Eqs. (10) by the following comparatively simple expressions:

$$\begin{aligned}E_\pm &= \frac{1}{\varepsilon_\pm - N_\parallel^2}\left(\frac{1}{\sqrt{2}}\left(\pm\frac{d}{dr} - \frac{m}{r}\right)\right.\\ &\left.\times((1+Q_1)B_\parallel + (1-Q_2)C_\parallel) - \frac{4\pi i}{\omega}j_{\pm,\,\mathrm{ext}}\right).\end{aligned} \quad (11)$$

A particularly important role in ICR plasma heating is played by the left-polarized electric field component E_+. In the vicinity of the plasma axis ($r = 0$), the radial dependence of $B_\parallel$ and $E_\parallel$ is represented in a universal form: $B_\parallel, E_\parallel \propto r^{|m|}f(r^2)$. For this region, we also have $n_0' \propto r$. Taking into account these relationships, from expressions (9) we see that, in the axial region, the waves running in the same direction as the ions move ($m < 0$) have the largest amplitude $|E_+|$; moreover, we have $E_+(0) \neq 0$ only for $m = -1$.

In the case of a high plasma density, it is more convenient to use another expression for $E_\pm$:

$$\begin{aligned}&\frac{1}{r^{1\pm m}}\frac{d}{dr}r^{1\pm m}E_\pm\\ &= -\frac{1}{\sqrt{2}}\left((\pm 1 + Q_2)B_\parallel + \frac{1}{N_\parallel^2}\left((\Delta_\perp + \varepsilon_\parallel)C_\parallel - \frac{4\pi}{\omega N_\parallel}j_{\parallel,\,\mathrm{ext}}\right)\right).\end{aligned} \quad (12)$$

Expression (12) has no fictitious singular points (see [9]) corresponding to the zeros of the denominator in expression (11) (see below).

5. FORMULATION OF THE PROBLEM FOR NUMERICAL ANALYSIS

In what follows, results will be presented from a numerical integration of wave equations (10) over the interval $(0, r_B)$ (where r_B is the radius of a perfectly conducting wall) and from a direct numerical integration of Maxwell's equations over the same interval. The current density that enters Maxwell's equations was described by the expressions derived in Section 2. The agreement between the results obtained by these two different methods guarantees the correctness of calculations; on the other hand, a comparison between the results makes it possible to determine the limits of applicability of each of the methods.

In wave equations (10), the quantities F and G become infinite at the points at which the condition $\varepsilon_-(r) = N_\parallel^2$ (where $\varepsilon_- = 1 + \frac{\omega_{pi}^2}{\omega_i(\omega_i + \omega)} + \frac{\omega_{pi}'^2}{\omega_i'(\omega_i' + \omega)}$) is satisfied. In [9], it was shown that, in this case, the solution remains regular. However, because of the presence of such fictitious singular points, the sweep method used to solve Eqs. (10) numerically can gener-

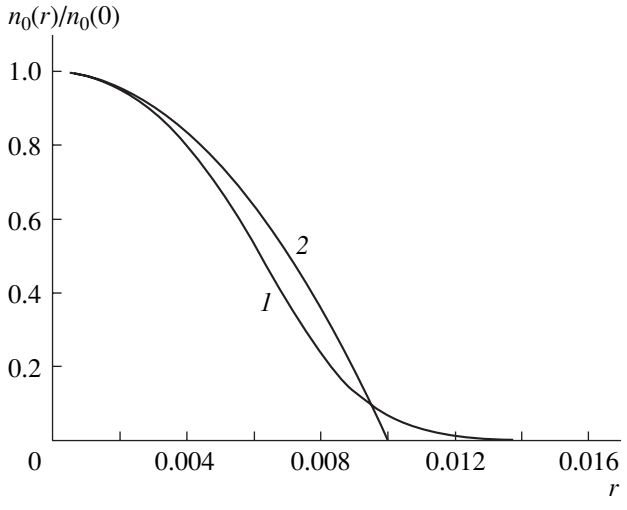

Fig. 1. Radial plasma density profiles given by (*1*) formula (13) and (*2*) formula (14).

ally fail. It is presumably for this reason that the solution to the wave equations begins to deviate from the solution to Maxwell's equations. For the waves under consideration, namely, those with a frequency on the order of the ion gyrofrequency, the fictitious singularity arises under the condition $\omega_{pi} \geq k_\| c$. The longitudinal size of a typical antenna used for ICR plasma heating is about 1 m; in this case, the density of a hydrogen plasma should be higher in order of magnitude than 10^{12} cm^{-3}. For heavier ions, the "critical" plasma density is proportional to their mass number. It should be noted that, for a plasma with hot electrons, the fictitious singularity begins to influence the solutions when the plasma density is at least one order of magnitude higher than the critical density. Note also that the singular point at which the condition $\varepsilon_+ = N_\|^2$ holds is displaced from the real axis in the complex plane because of the contribution of resonant minority ions. When the density of minority ions is not too low, solving Eqs. (10) presents no problem.

In integrating Maxwell's equations, the boundary-value problem was solved by a shooting method. In order to satisfy the boundary conditions (which imply that the solution is finite at the axis of the plasma cylinder and that the tangential components of the electric field vanish at a perfectly conducting wall), Newton's method was used. The iterative procedure begins to diverge if the solution is subject to sufficiently sharp variations over the interval of integration. In the problem under analysis, the longitudinal electric field can depend strongly (exponentially) on the radius. For a low-density plasma ($\omega_{pi} \leq k_\| c$), this exponential dependence is governed by the strong damping of Trivelpiece–Gould (TG) modes excited by the antenna (see below). For a high plasma density ($\omega_{pi} \geq k_\| c$), the exponential dependence is due to the appearance of an Alfvén resonance surface, the region inside which is opaque to lower hybrid waves (in this region, their amplitude decreases exponentially toward the plasma axis).

If the plasma density is not too high ($\omega_{pi} \leq k_\| c$), Newton's method can be made convergent by slightly reducing the integration interval, i.e., by excluding from consideration a small subinterval corresponding to the immediate vicinity of the plasma axis. This is correct because, close to the axis, the longitudinal electric field of waves is negligibly low and the longitudinal magnetic field has a simple (power-law) dependence on the radius, $\propto r^{|m|}$. The result of integrating Maxwell's equations over the remaining part of the integration interval coincides with the solution to wave equations (10). This procedure made it possible to perform calculations for low electron temperatures.

The calculations were carried out for two radial profiles of the plasma density (see Fig. 1). The first profile is given by an analytic expression implying that the plasma occupies all the integration region up to the system boundary ($r = r_B$):

$$n_0(r) = n_0(0)\left(1 - \tanh\left(\frac{r^2 - r_0^2}{2\Delta_0 r_0}\right)\right)\left(1 + \tanh\left(\frac{r_0}{2\Delta_0}\right)\right)^{-1}. \quad (13)$$

Changing the parameters r_0 and Δ_0 in expression (13) provides the possibility of modeling smooth (Gaussian) density profiles ($\Delta_0 \geq r_0$) and also steplike profiles ($\Delta_0 \ll r_0$).

The second, parabolic, profile assumes that the plasma terminates radially without contact with the wall ($r = r_p < r_B$), i.e., that there is a vacuum gap between the plasma and the wall:

$$n_0(r) = n_0(0)\begin{cases}\left(1 - \left(\frac{r}{r_P}\right)^2\right) & (r \leq r_P)\\ 0 & (r > r_P)\end{cases}. \quad (14)$$

An antenna generating electromagnetic fields was modeled by the following radial profiles of the electric current density:

$$\mathbf{j}_{\text{ext}}(\mathbf{r}) = \left(0, 1, -\frac{m}{rN_\|}\right)\frac{1}{\sqrt{\pi}\Delta_A} \times \exp\left(-\left(\frac{r - r_A}{\Delta_A}\right)^2\right) I_\theta \exp(im\theta + iN_\| z), \quad (15)$$

where $\Delta_A \ll r_A$, and

$$\mathbf{j}_{\text{ext}}(\mathbf{r}) = \left(0, 1, -\frac{m}{rN_\|}\right)\delta(r - r_A) I_\theta \exp(im\theta + iN_\| z). \quad (16)$$

In expressions (15) and (16), the electric current is normalized to the total current and the current continuity condition is taken into account.

The parameters of the smooth plasma density profile given by expression (13) were chosen so that the plasma density near the antenna was about two orders of magnitude lower than the maximum (central) density. This choice correspond to typical experimental conditions, under which the plasma density decreases from the axis to the boundary by one to two orders of magnitude.

For the second density profile, namely, that given by expression (14), the antenna was assumed to be positioned in vacuum and the antenna current density was described by expression (16). For the vacuum region ($r_P < r < r_B$), analytic solutions to Eqs. (10) were considered. In this region, the equations have the form

$$\left.\begin{aligned} \frac{1}{r}\frac{d}{dr}r\frac{dB_\parallel}{dr} + \left(1 - N_\parallel^2 - \frac{m^2}{r^2}\right)B_\parallel &= -\frac{4\pi}{\omega}\frac{1}{r}\frac{d}{dr}r j_{\theta,\,\mathrm{ext}} \\ \frac{1}{r}\frac{d}{dr}r\frac{dE_\parallel}{dr} + \left(1 - N_\parallel^2 - \frac{m^2}{r^2}\right)E_\parallel &= -\frac{4\pi i}{\omega}(j_{\parallel,\,\mathrm{ext}} - cN_\parallel\rho_{\mathrm{ext}}) \end{aligned}\right\}, \quad (17)$$

where $\rho_{\mathrm{ext}} = \frac{1}{c}\left(\frac{m}{r_A}j_{\theta,\,\mathrm{ext}} + N_\parallel j_{\parallel,\,\mathrm{ext}}\right)$ in accordance with the charge conservation condition. For current-carrying antennas, we have $\rho_{\mathrm{ext}} = 0$.

The second of Eqs. (17) implies that, for $N \gg 1$, the electric current having a nonzero divergence generates electric fields far more efficiently than does the divergence-free current (the potential electric field of the former is N^2 times stronger than the vortex field; see also below).

The matching conditions at the antenna ($r = r_A$) have the form

$$\left.\begin{aligned} B_\parallel\Big|_{r_{A-}}^{r_{A+}} &= -\frac{4\pi}{c}I_\theta \\ \frac{dB_\parallel}{dr}\Big|_{r_{A-}}^{r_{A+}} &= 0 \end{aligned}\right\}, \quad (18)$$

$$\left.\begin{aligned} E_\parallel\Big|_{r_{A-}}^{r_{A+}} &= 0 \\ \frac{dE_\parallel}{dr}\Big|_{r_{A-}}^{r_{A+}} &= -\frac{4\pi i}{c}I_\parallel \end{aligned}\right\}. \quad (19)$$

These conditions were derived by taking into account the fact that, in Eqs. (17), the radius is normalized to c/ω.

The solutions to Eqs. (17) on the interval $r_P < r < r_B$ are expressed in terms of the modified Bessel functions of the first (I_m) and second (K_m) kinds. This makes it possible to switch from the boundary conditions

$$\frac{dB_\parallel}{dr} = E_\parallel = 0 \quad (20)$$

at the wall surface ($r = r_B$) to the boundary conditions at the plasma surface ($r = r_P$),

$$B_\parallel(\rho_P)\Phi''_{\rho_P,\,\rho_B}(\rho_P, \rho_B) - B'_{\parallel,\,\rho_P}(\rho_P)\Phi'_{\rho_B}(\rho_P, \rho_B) = \frac{\rho_A}{\rho_P}\Phi''_{\rho_A,\,\rho_B}(\rho_A, \rho_B)\frac{4\pi}{c}I_\theta, \quad (21)$$

$$E_\parallel(\rho_P)\Phi'_{\rho_P}(\rho_P, \rho_B) - E'_{\parallel,\,\rho_P}(\rho_P)\Phi(\rho_P, \rho_B) = -\frac{\rho_A}{\rho_P}\Phi(\rho_A, \rho_B)\frac{4\pi i}{c\sqrt{N_\parallel^2 - 1}}I_\parallel, \quad (22)$$

where $\Phi(\rho_1, \rho_2) = I_m(\rho_1)K_m(\rho_2) - K_m(\rho_1)I_m(\rho_2)$ and $\rho_{1,2} = (N_\parallel^2 - 1)^{1/2}r_{1,2}$.

It is also necessary to account for a jump in the radial derivative of the longitudinal magnetic field $B_\parallel$ at the plasma surface ($r = r_P$):

$$\frac{dB_\parallel}{dr}\Big|_{r_P-\delta}^{r_P+\delta} = \frac{dQ_1}{dr}\Big|_{r_P-\delta}B_\parallel(r_P) - \frac{dQ_2}{dr}\Big|_{r_P-\delta}C_\parallel(r_P),$$

where $\delta \longrightarrow 0$. Boundary condition (21) contains the derivative of this component in the vacuum region at $r = r_P + \delta$.

The goal of numerical calculations was twofold: to demonstrate the main regular features of the excitation of electromagnetic fields in the plasma column and to qualitatively estimate the prospects for using minority ICR heating in the EPSILON system [5], whose parameters served as the basis for calculations (the magnetic field was ≈3 kG, the maximum plasma density was $\leq 10^{12}$ cm^{-3}, the electron temperature was ≤10 keV, the ion temperature was ≈100 eV, the system diameter was ≈30 cm, and the length of the heated region was ≈1 m).

The electromagnetic fields generated by the antenna are highly sensitive to the ratio between their phase velocity and the electron thermal velocity. In order to reveal the features in question, calculations were carried out for two limiting cases: that of hot electrons (T_e = 10 keV) and that of cold electrons (T_e = 10 eV). The general properties of the ICR plasma heating were analyzed under the assumption that the plasma temperature is constant along the radius. Note that the uniform temperature distribution is characteristic of open systems in which the plasma is heated while flowing through them. In Section 8, the closed EPSILON system is considered under the assumption that the temperature profile is parabolic.

The structure of electromagnetic fields in the plasma depends significantly on the ratio between the RF field frequency (which was chosen to be equal to the gyrof-

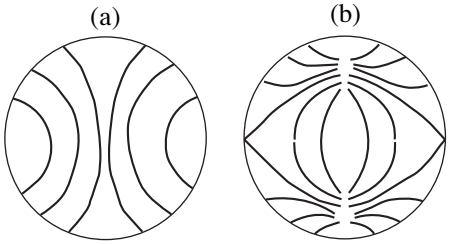

Fig. 2. Contour plots of the electric field of the lowest radial eigenmodes with the azimuthal number $m = 1$ in a plasma waveguide: (a) TE_{11} mode and (b) TM_{11} mode.

requency of the minority ions) and the gyrofrequency of the main plasma ions. The calculations were carried out for a deuterium plasma with a hydrogen minority and for a hydrogen plasma with a deuterium minority. The parameter values corresponding to the first case are as follows: $N_\parallel = 30$, $r_B = 3 \times 10^{-2}$, $r_0 = \Delta_0 = r_P/2 = 0.834 \times 10^{-2}$, $r_A = 2.5 \times 10^{-2}$, $\Delta_A = 0.5 \times 10^{-3}$. In the second case, the gyrofrequency of the main plasma ions is two times lower than that in the first case, so that the parameter values were recalculated in accordance with the relationships $N_\parallel \propto \omega^{-1}$ and $r_B, r_0, \Delta_0, r_P \propto \omega$. The plasma density was varied from zero (vacuum) to $n_0(0) = 2 \times 10^{12}$ cm^{-3}.

In Section 6, the relative density of the minority ions, $\alpha = n_i'/n_i$, is taken to be 0.3%. With this value of α, it is convenient to demonstrate the general features of the excitation of RF fields in a plasma containing several ion species. In particular, in such a plasma, the characteristic properties exhibited by the plasma waves due to the presence of plasma and/or Alfvén resonances are very pronounced. Note that an analysis of the heating efficiency as a function of α shows that the optimum α value can be close in order of magnitude to the value chosen above.

The current distribution in the azimuthal direction was assumed to correspond to the first mode ($m = -1$), which runs in the same direction as the ions (this assumption was justified in the previous section). If we consider a plane cutting the antenna at a right angle to the plasma axis, then we can see that, in the case of the first mode, the currents flowing at any given time in the opposite semicircles produced by the intersection of the antenna and the plane are oppositely directed. In calculations, each of these currents was set equal to 1 A. In all figures that show radial profiles of the electromagnetic fields, the electric and magnetic fields are expressed in V/cm and in G, respectively.

6. ELECTROMAGNETIC FIELDS IN A VACUUM WAVEGUIDE

In order to gain insight into the processes occurring when the current flows in the antenna, we first consider the excitation of electromagnetic waves in a cylindrical vacuum waveguide.

In analyzing electromagnetic waves, it is expedient to introduce the notion of the wave mode—a superposition of electric and magnetic fields that are described by an independent solution to Maxwell's equations. Two types of modes can propagate in a cylindrical waveguide: TE and TM modes. The electric field of the TE mode is perpendicular to the waveguide axis (and, accordingly, has no longitudinal component). The magnetic field of the TM mode is oriented in the same manner. This, the TE modes can be conveniently characterized by the longitudinal magnetic-field component $B_\parallel(\mathbf{r}, t)$, and the TM modes, by the longitudinal electric-field component $E_\parallel(\mathbf{r}, t)$.

In the case of a vacuum waveguide ($\varepsilon_\pm = 1$, $Q_{1,2} = 0$), it is possible to obtain the following expression for the transverse component of the electric field:

$$\mathbf{E}_\perp = \frac{i}{1 - N_\parallel^2}\left(\nabla \times (\mathbf{b} B_\parallel) + N_\parallel \nabla_\perp E_\parallel - \frac{4\pi}{\omega}\mathbf{j}_{\perp,\,\mathrm{ext}}\right). \quad (23)$$

The eigenmodes that can propagate along the waveguide are described by the solutions to Eqs. (17) with zero on the right-hand sides:

$$B_\parallel, E_\parallel \propto J_m(\kappa r),$$

where the quantity $\kappa = \sqrt{1 - N_\parallel^2}$ is determined with the help of boundary conditions (20).

Approximate contour plots of the transverse electric fields of the largest scale eigenmodes are shown in Fig. 2. These fields are seen to have a large potential component, which is generated by the charges induced at the perfectly conducting wall of the waveguide. That the charges are indeed present is indicated by the fact that the electric field component of each of the two modes that is normal to the wall surface is nonzero everywhere except for certain values of the azimuthal angle.

For low-frequency electromagnetic fields with $N_\parallel \gg 1$, which are usually used for ICR plasma heating, the waveguide in question is overcritical. Such fields can only be sustained by antennas.

In the region $r < r_A$, the solutions to Eqs. (17) that satisfy matching conditions (18) and (19) and boundary conditions (20) are given by the expressions

$$\left.\begin{aligned} B_\parallel(r) &= -\frac{\rho_A}{I_m'(\rho_B)}\Phi''_{\rho_A,\rho_B}(\rho_A, \rho_B) I_m(\rho)\frac{4\pi}{c} I_\theta \\ E_\parallel(r) &= \frac{i r_A}{I_m(\rho_B)}\Phi(\rho_A, \rho_B) I_m(\rho)\frac{4\pi}{c} I_\parallel \end{aligned}\right\}, \quad (24)$$

where $\rho = (N_\parallel^2 - 1)^{1/2} r$ (as in the previous section).

Let us consider the transverse electric field, assuming that the longitudinal size of the antenna is much larger than its transverse size, $rN_\parallel \ll 1$. To zero order in this parameter, we obtain

$$\left.\begin{aligned} B_\parallel(r) &\approx \frac{|m|}{2}\left(\frac{r}{r_A}\right)^{|m|}\left(\left(\frac{r_A}{r_B}\right)^{2|m|}-1\right)\frac{4\pi}{c}I_\theta \\ E_\parallel(r) &\approx \frac{ir_A}{2}\left(\frac{r}{r_A}\right)^{|m|}\left(\left(\frac{r_A}{r_B}\right)^{2|m|}-1\right)\frac{4\pi}{c}I_\parallel \end{aligned}\right\}. \qquad (25)$$

Using expressions (23) and (25) and taking into account the current continuity condition, we find that the resulting transverse electric field excited by the antenna vanishes. The transverse electric field is nonzero only in the next-order approximation, i.e., to within terms on the order of $(rN_\parallel)^2$, in which case it is equal in order of magnitude to $E_\perp \approx \frac{r_A}{c}I_\theta$. Recall that all of the quantities having the dimension of length are normalized to c/ω ($r_A \longrightarrow r_A\omega/c$).

The result just obtained is quite natural because the electric fields excited by current-carrying antennas are of an inductive nature and are completely governed by the time-delay effect.

As was mentioned above, the transverse electric field of the TE mode, as well as of the TM mode, also has the potential component. Let us consider the origin of this potential component in an overcritical waveguide. To do this, we first assume that the only mode that is excited in such a waveguide is the TE mode, whose longitudinal electric field is zero, $E_\parallel = 0$. In order to drive the right-hand sides of Eqs. (17) to zero, it is necessary that the antenna current have not only the θ component but also the z component. This condition, together with the charge conservation condition, gives $j'_{\parallel,\,\mathrm{ext}} = \frac{N_\parallel N_\theta}{1-N_\parallel^2}j_{\theta,\,\mathrm{ext}}$. In this case, the density of the space charges within the antenna is nonzero, $\rho'_{\mathrm{ext}} = \frac{1}{c}\frac{N_\theta}{1-N_\parallel^2}j_\theta$, and the electric field excited by them is potential.

Under the same assumptions as those made in deriving expressions (25), Poisson's equation has the approximate solution

$$\varphi \approx -\frac{r_A}{2|m|}\left(\frac{r}{r_A}\right)^{|m|}\left(\left(\frac{r_A}{r_B}\right)^{2|m|}-1\right)\frac{N_\theta}{1-N_\parallel^2}\frac{4\pi}{c}I_\theta.$$

This solution and expressions (23) and (25) imply that, under the conditions $N_\theta \gg N_\parallel \gg 1$, the potential electric field is equal in order of magnitude to $E_{\perp,\,\mathrm{pot}} \approx \frac{L_\parallel^2}{r_A c}I_\theta$;

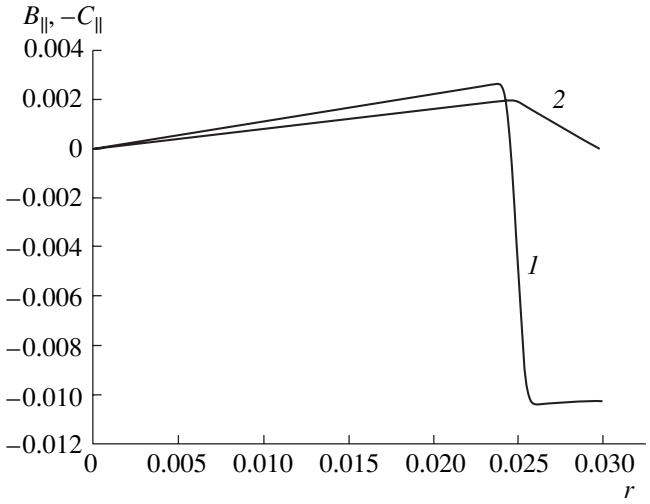

Fig. 3. Radial profiles of the electromagnetic fields (*1*) $B_\parallel$ and (*2*) $-C_\parallel$ of a helical current in an overcritical vacuum waveguide.

i.e., it is stronger than the vortex electric field by a factor of $\left(\frac{L_\parallel}{r_A}\right)^2$ (where $L_\parallel$ is the characteristic longitudinal size of the antenna). Expression (23) with $E_\parallel = 0$ produces precisely the same result.

To generate the TM mode, whose longitudinal magnetic field is zero, $B_\parallel = 0$, it is sufficient to use an antenna carrying only a longitudinal current with the density $j''_{\parallel,\,\mathrm{ext}}$. The total charge density in the antenna, $\rho'_{\mathrm{ext}} + \rho''_{\mathrm{ext}}$, is equal to zero when $j''_{\parallel,\,\mathrm{ext}} = -\frac{N_\theta}{1-N_\parallel^2}j_{\theta,\,\mathrm{ext}}$. The electric field excited by this charge is equal in order of magnitude to $E_{\perp,\,\mathrm{pot}} \approx \frac{L_\parallel}{c}I_\parallel$; for $B_\parallel = 0$, this result agrees with expression (23) at $I_\theta = 0$.

Hence, the above analysis shows that the helical current excites TE and TM modes simultaneously. The transverse potential electric fields of the modes are comparatively strong. However, they cancel one another out, so that there remains only a substantially weaker vortex field.

The potential electric fields that are generated by charges can be determined from Poisson's equation, which, at first glance, is independent of Eqs. (17). However, for the periodic processes under consideration here, Poisson's equation can be obtained from Maxwell's equations, which were used to derive Eqs. (17). Consequently, information on the potential electric fields should be contained in Eqs. (17).

The above considerations are illustrated by Fig. 3, which shows numerical results on the longitudinal electromagnetic field components contained in expression (11) for the transverse electric field, namely, on the

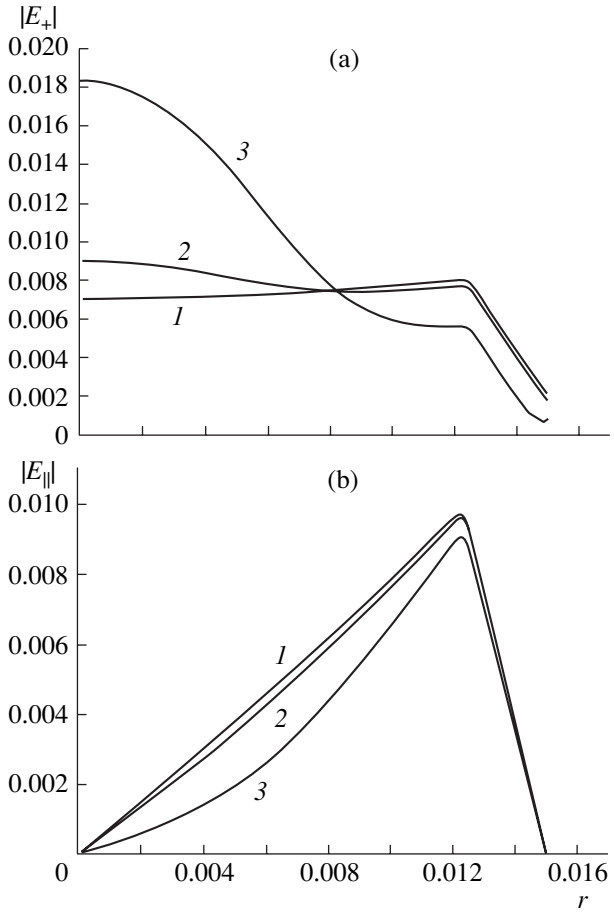

Fig. 4. Radial profiles of the electromagnetic fields of a helical current in low-density hydrogen plasmas with a 3% deuterium minority, with hot electrons (T_e = 10 keV), and with different central densities: n_0 = (*1*) 0, (*2*) 2×10^6, and (*3*) 2×10^7 cm^{-3}.

quantities $B_\parallel$ and $-C_\parallel = -iN_\parallel E_\parallel$. The sum $B_\parallel + C_\parallel$ is the magnitude of $\mathbf{E}_\perp$ in vacuum. Figure 3 implies that, inside the antenna, this sum is much smaller than either of the two quantities, $B_\parallel$ and $-C_\parallel$, which is in accord with expressions (25). Note that, at the current-carrying conductors of the antenna, the quantities $B_\parallel$ and $\frac{dC_\parallel}{dr}$ change sharply. In the limit $\Delta_A \longrightarrow 0$, these quantities undergo jumps (see matching conditions (18) and (19)).

7. ELECTROMAGNETIC FIELDS IN A PLASMA WAVEGUIDE

7.1. Amplification of the Transverse Electric Field in a Low-Density Plasma

The plasma responds differently to TE and TM modes. The TM mode has a substantial longitudinal electric field. Since the electrons actively respond to this field, the plasma exerts an important effect on the TM mode even when its density is comparatively low, $\omega_{pe} \geq \max(\omega, k_\parallel v_{Te})$. In vacuum, the TE mode has no longitudinal electric field. In the plasma, the longitudinal electric field of the TM mode is weak. The response of the plasma to the transverse electric field is far weaker. According to Eqs. (10), the plasma has a significant effect on the TE mode only under the conditions $\varepsilon_\perp, g \geq N_\parallel^2$. In the opposite case, the spatial distribution of the longitudinal magnetic field can be determined from the first of Eqs. (17), which refer to the vacuum region.

As for the TM mode, it becomes electrostatic (i.e., converts into the so-called TG mode) under the condition $N_\perp r_A \gg 1$, where $N_\perp$ is the characteristic radial refractive index. In this case, the terms with the longitudinal magnetic field in the second of Eqs. (17) can be omitted, so that the equation becomes

$$\frac{1}{r}\frac{d}{dr} r\varepsilon_\perp \frac{dE_\parallel}{dr} - \left(N_\parallel^2 \varepsilon_\parallel + \frac{m^2}{r^2}\varepsilon_\perp\right) E_\parallel = 0. \qquad (26)$$

Here, it is also assumed that $Q_{1,2} \ll 1$.

In the quasiclassical approximation, the dispersion relation for the TG modes has the form

$$\varepsilon_\perp N_\perp^2 + \varepsilon_\parallel N_\parallel^2 = 0.$$

This dispersion relation yields $N_\perp \approx \left|\frac{\varepsilon_\parallel}{\varepsilon_\perp}\right|^{1/2} N_\parallel$. For the parameter values adopted in calculations, the above condition $N_\perp r_A \gg 1$ is satisfied when the electron temperature and the density of minority ions are not too high. Otherwise, the longitudinal magnetic field $B_\parallel$ may have an appreciable effect on the distribution of $E_\parallel$.

For a vacuum waveguide such that $rN_\parallel \leq 1$, the radial dependence of the longitudinal electric field in the interval $(0, r_A)$ can be approximated by $E_\parallel \propto r^{|m|}$ (see above). If the electrons are hot ($\omega \ll k_\parallel v_{Te}$), then, by virtue of the relationship $\mathrm{Re}\,\varepsilon_\parallel \approx 1 + \left(\frac{\omega_{pe}}{k_\parallel v_{Te}}\right)^2 > 1$ and because of the absorption of RF energy by the resonant electrons and minority ions, the longitudinal electric field $E_\parallel$ decreases from the antenna toward the plasma axis somewhat more abruptly (see Fig. 4b). Since, in the TM mode, the longitudinal and transverse electric fields are mutually coupled to one another, the latter decreases accordingly. The transverse electric fields of the TM and TE modes excited by a helical current are opposite in direction (see the previous section); consequently, the screening of the TM mode leads to an increase in the total transverse electric field.

In the case of cold electrons, the presence of plasma reduces the longitudinal dielectric response, $\left(\varepsilon_\parallel = 1 - \left(\frac{\omega_{pe}}{\omega}\right)^2\right)$; therefore, an increase in the plasma density leads to an increase in the longitudinal electric

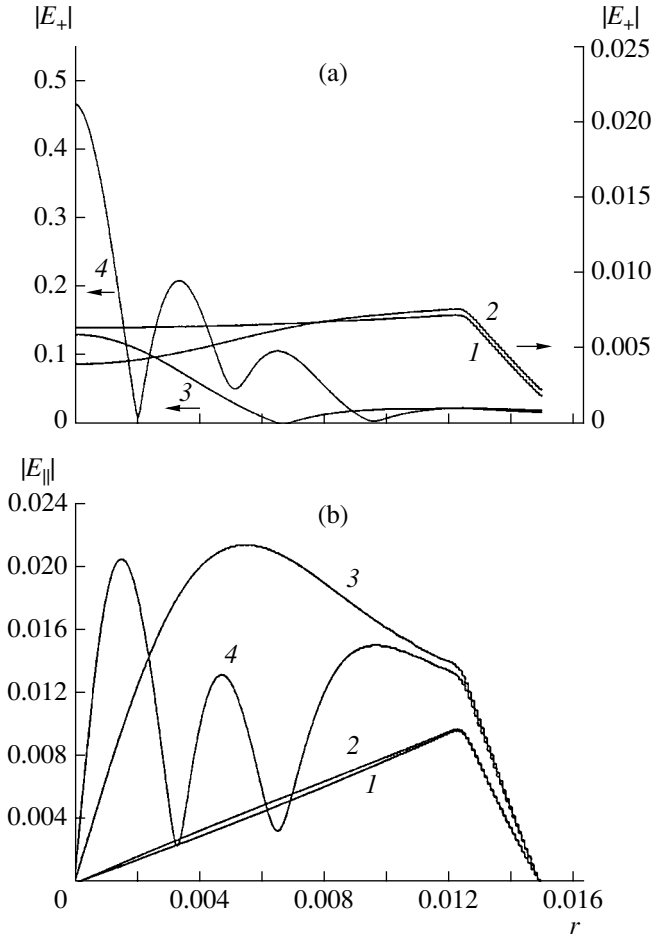

Fig. 5. Radial profiles of the electromagnetic fields of a helical current in plasmas with cold electrons (T_e = 10 eV) and with different central densities: n_0 = (*1*) 0, (*2*) 2×10^5, (*3*) 2×10^6, and (*4*) 2×10^7 cm^{-3}.

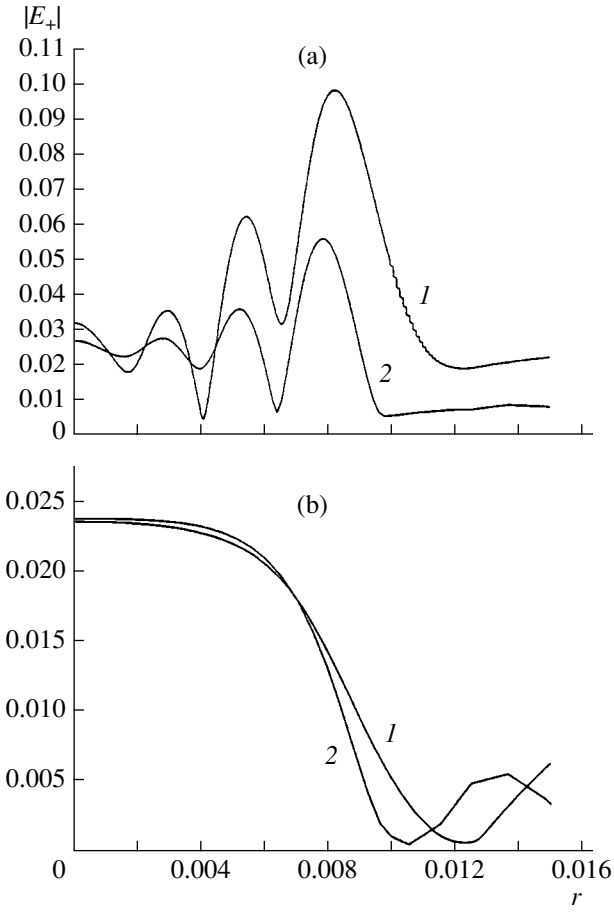

Fig. 6. Radial profiles of the electromagnetic fields of a helical current in hydrogen plasmas with a 3% deuterium minority, with (a) cold (T_e = 10 eV) and (b) hot (T_e = 10 keV) electrons, and with different density profiles given by (*1*) formula (13) and (*2*) formula (14) with the same central density $n_0 = 2 \times 10^8$ cm^{-3}.

field of the TM modes. As a result, unlike in the case of hot electrons, the transverse electric field decreases (Fig. 5a, curve *2*) as long as the condition $B_\parallel + C_\parallel > 0$ is satisfied in the axial plasma region. As the plasma density increases, the quantity $B_\parallel + C_\parallel$ changes sign; in this case, the transverse electric field begins to increase. When the longitudinal dielectric response $\varepsilon_\parallel$ becomes negative, the plasma waveguide ceases to be overcritical for TM modes and they convert into TG modes. If the parameters of the antenna current are close to those of the TG eigenmodes, then the transverse electric field of the TM mode is much stronger than that of the TE mode and, accordingly, it makes the dominant contribution to the total field.

The parameters of the TG eigenmodes are rather sensitive to the details of the radial profile of the plasma density. That is why, at a low electron temperature, even a slight difference in the profiles can produce profound differences in the amplitude and profile of the electric field of the helical current. On the other hand, in a plasma with hot electrons, TG modes do not exist, so the electric fields differ only slightly (see Fig. 6).

7.2. Moderate-Density Plasma: Plasma Resonance

As long as the ion contribution to the transverse dielectric function is small ($\varepsilon_\perp \approx 1$), the waves under consideration are purely electron waves. The higher the plasma density, the more important the role played by the ions and the greater the difference between the cases of light and heavy minority ions. In the first case (e.g., a deuterium plasma with a hydrogen minority), if the plasma density at the axis of the column is sufficiently high, then the transverse dielectric function calculated for the main plasma ions, $\varepsilon_\perp = 1 + \dfrac{\omega_{pi}^2}{\omega_i^2 - \omega^2}$, can change sign at a certain surface of radius $r = r_{pl}$. (Recall that, in the case of minority ICR plasma heating, the RF field frequency is chosen to satisfy the condition for the

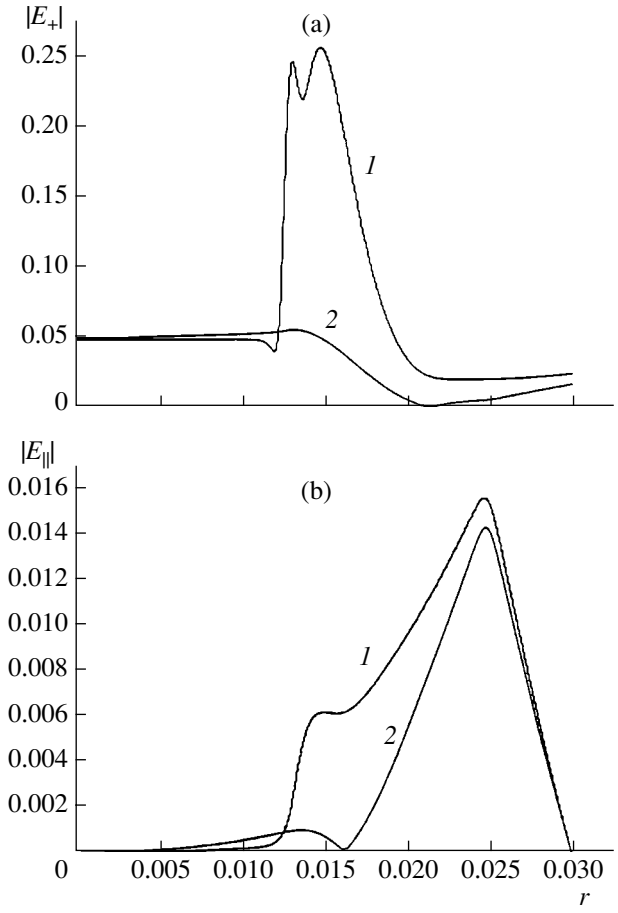

Fig. 7. Radial profiles of the electromagnetic fields of a helical current in moderate-density deuterium plasmas with a 0.3% hydrogen minority, with the same central density $n_0 = 2 \times 10^9$ cm^{-3}, and with (*1*) cold (T_e = 10 eV) and (*2*) hot (T_e = 10 keV) electrons.

field to be in cyclotron resonance with minority ions.) For the TG modes, this is a singular surface (plasma resonance surface) [see Eq. (26)]. In its vicinity, the transverse wavenumber of the TG modes and, accordingly, their transverse electric field increase abruptly. At the same time, since the plasma density is radially decreasing, the surface $r = r_{pl}$ is the boundary between the regions transparent to the TG modes ($r > r_{pl}$) and opaque to them ($r < r_{pl}$). From Fig. 7b we can see that, in the opaque region, the longitudinal electric field is essentially absent: TG modes do not penetrate into this region. The TM mode also does not penetrate deep into a plasma with hot electrons because it is damped by them. As a result, regardless of the electron temperature, the total transverse electric field in the axial region of the plasma column coincides with the vacuum field of the TE mode. In turn, the plasma begins to affect the TE mode when its density is high enough to satisfy the condition $\varepsilon_\perp \geq N_\parallel^2$ (see the next section).

The higher the plasma density, the larger the radius of the plasma resonance surface. For a sufficiently high plasma density described by a smooth radial profile of form (13), the radius of the plasma resonance surface becomes equal to the wall radius. In this case, the entire plasma column is opaque to the TG modes.

In a low-density plasma, the ion plasma component has only a slight effect on the distribution of the electromagnetic fields (see the previous section). Of course, in this case, the relative percentage of the ion species present in the plasma is unimportant. As the plasma density increases, the damping of electromagnetic waves by the ions becomes one of the main factors governing the structure of the electromagnetic fields. In order to reveal the characteristic features of the waves generated under the plasma and Alfvén resonance conditions, in numerical calculations described in this section and the next, the density of minority ions was chosen to be low, 0.3%.

In a plasma in which minority ions are heavier than the main ions, the plasma resonance surface is absent. In this case, for plasma densities satisfying the condition $\omega_{pi} \approx \omega$, the spatial structure of the electromagnetic fields does not possess any irregular properties (see Fig. 7).

7.3. High-Density Plasma: Alfvén Resonance

At sufficiently high plasma densities satisfying the conditions $\varepsilon_\perp, g \geq N_\parallel^2$, the TE mode converts into magnetosonic modes or into Alfvén modes. The approximate dispersion relation for magnetosonic and Alfvén modes has the form

$$N_\perp^2 = \frac{(\varepsilon_+ - N_\parallel^2)(\varepsilon_- - N_\parallel^2)}{(\varepsilon_\perp - N_\parallel^2)}. \qquad (27)$$

The plasma is transparent to magnetosonic modes when $\varepsilon_- > N_\parallel^2$. Alfvén modes can only propagate in a plasma whose density lies within the range determined by the conditions $\varepsilon_+ > N_\parallel^2 > \varepsilon_\perp$. These conditions imply that the frequency of Alfvén modes is lower than the ion gyrofrequency. Here, the quantities $\varepsilon_\pm = \varepsilon_\pm^{(i)} + \varepsilon_\pm^{(e)} = 1 \pm \frac{\omega_{pi}^2}{\omega_i(\omega_i \pm \omega)}$, as well as $\varepsilon_\perp$, are calculated for the main plasma ions.

Alfvén and magnetosonic modes are nonpotential—their electric and magnetic fields both oscillate. The only modes that can be excited in a dense deuterium plasma with a hydrogen minority ($\omega > \omega_i$) are magnetosonic modes. Presumably, it is this excitation process that is responsible for the amplification of the longitudinal component of the RF magnetic field in a high-density plasma (see Fig. 8). The radial profiles shown in Fig. 8 remain essentially the same regardless of the

electron temperature. This result is quite natural because the electrons have an insignificant impact on the magnetosonic mode—they merely make the longitudinal electric field vanish. The profiles are slightly different only in the boundary region, where the plasma density is low. If the plasma resonance surface occurs near the plasma boundary, then the transverse electric field in the boundary region is seen to increase abruptly (see the previous section).

In a high-density plasma, the TG modes, too, change their nature: they become nonpotential and convert into the so-called lower hybrid modes, in which, in contrast to the TG modes, the longitudinal electric and magnetic fields, $E_\parallel$ and $B_\parallel$, both alternate. Lower hybrid modes obey the following dispersion relation, which is a generalization of the dispersion relation for the TG modes:

$$N_\perp^2 = \varepsilon_\parallel \frac{\varepsilon_\perp - N_\parallel^2}{\varepsilon_\perp}. \quad (28)$$

A comparison between dispersion relations (27) and (28) shows that the characteristic spatial scale of the lower hybrid modes is small in comparison with those of Alfvén and magnetosonic modes. In the case of a plasma with light minority ions, lower hybrid modes are confined to the antenna and do not penetrate deep into the plasma. On the other hand, in a plasma with heavy minority ions ($\omega < \omega_i$), lower hybrid modes can have a considerable effect on the electromagnetic fields in the central regions of the plasma column because of the presence of Alfvén resonance. The Alfvén resonance surface is determined by the condition $\varepsilon_\perp = N_\parallel^2$. From Eqs. (26) and (27), it follows that, at this surface, the characteristic spatial scale of the long-wavelength Alfvén modes becomes equal to zero and that of the short-wavelength lower hybrid modes becomes infinite. Of course, for such values of $N_\perp$, the applicability conditions of the quasiclassical approximation, which was used to derive dispersion relations (27) and (28), fail to hold. In fact, in the vicinity of the Alfvén resonance surface, the modes occurring on different spatial scales are converted into one another.

The Alfvén resonance surface is the boundary between the regions of transparency and opaqueness for Alfvén and lower hybrid modes. For the parameter values under consideration, the characteristic wavelength of Alfvén modes is comparable to the plasma radius; as a result, the vicinity of the Alfvén resonance surface does not show up in the profiles of the Alfvén modes. At the same time, the Alfvén resonance surface can be readily seen in the spatial profiles of the lower hybrid modes. Short-wavelength lower hybrid modes differ from long-wavelength Alfvén and magnetosonic modes in that their electric field has a substantial longitudinal component. In a plasma with cold electrons ($\omega \gg k_\parallel v_{Te}$), the transparency region for lower hybrid modes is that in which the plasma density is below its resonant value ($\varepsilon_\perp < N_\parallel^2$). In a plasma with hot electrons ($\omega \ll k_\parallel v_{Te}$), the transparency region is that in which the plasma density exceeds its resonant value ($\varepsilon_\perp > N_\parallel^2$). In the first of these regions, lower hybrid

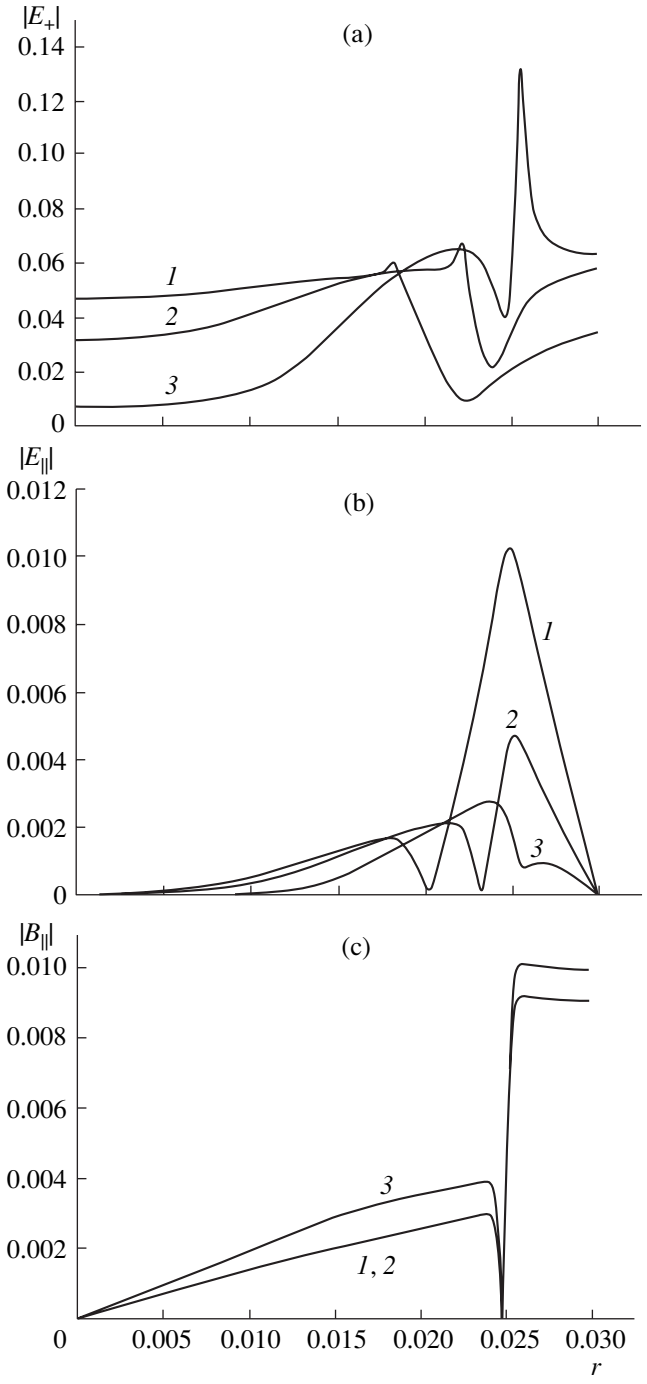

Fig. 8. Radial profiles of the electromagnetic fields of a helical current in high-density deuterium plasmas with a 0.3% hydrogen minority, with hot electrons (T_e = 10 keV), and with different central densities: n_0 = (*1*) 2×10^{10}, (*2*) 2×10^{11}, and (*3*) 2×10^{12} cm^{-3}.

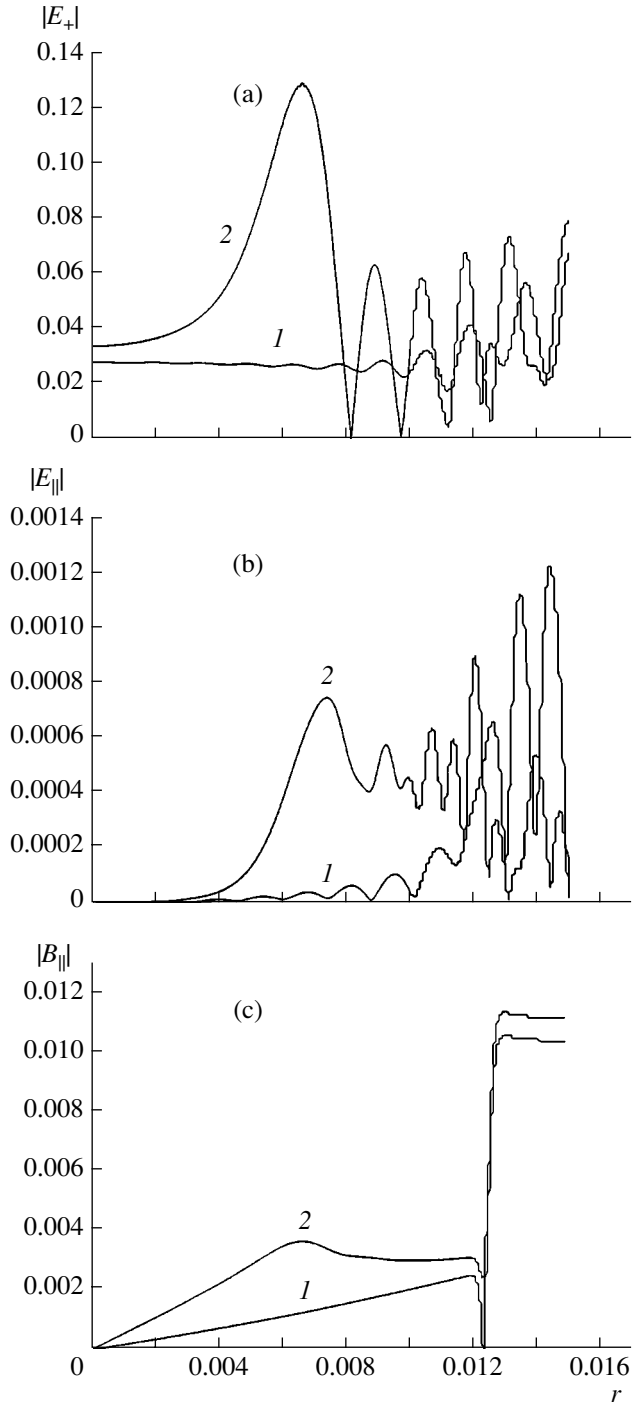

Fig. 9. Radial profiles of the electromagnetic fields of a helical current in hydrogen plasmas with a 0.3% deuterium minority, with cold electrons (T_e = 10 eV), and with different central densities: n_0 = (*1*) 2×10^{11} and (*2*) 2×10^{12} cm^{-3}.

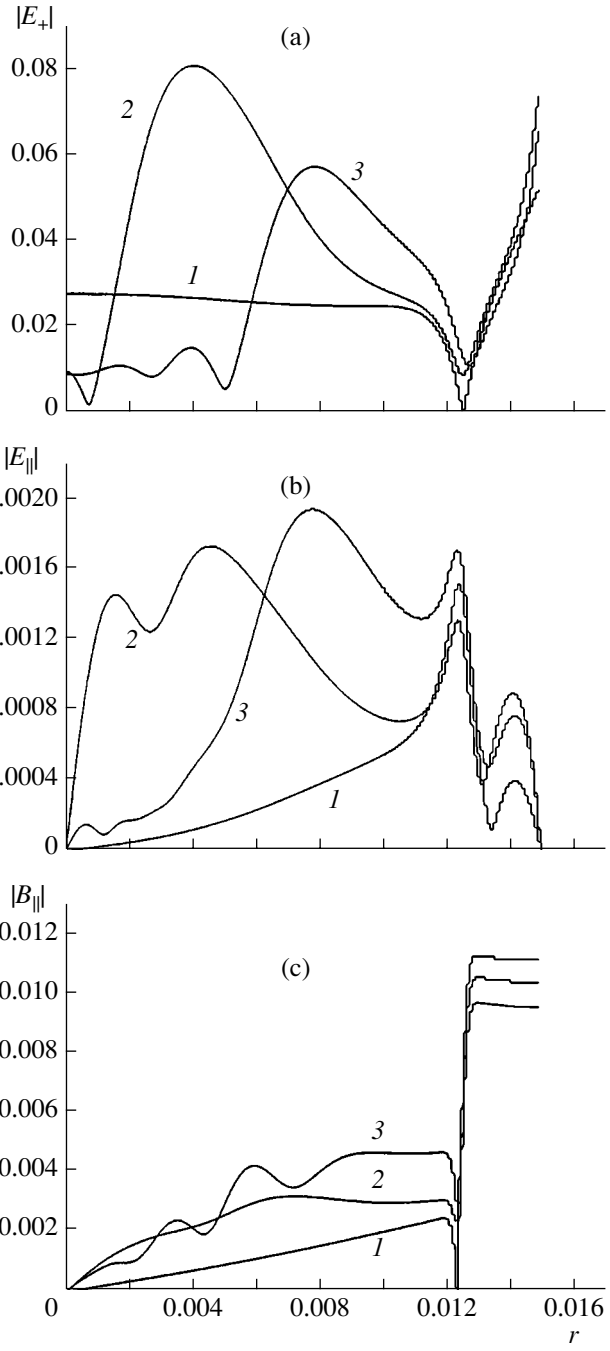

Fig. 10. Radial profiles of the electromagnetic fields of a helical current in hydrogen plasmas with a 0.3% deuterium minority, with hot electrons (T_e = 10 keV), and with different central densities: n_0 = (*1*) 2×10^{11}, (*2*) 2×10^{12}, and (*3*) 6×10^{12} cm^{-3}.

modes are potential (they do not perturb the magnetic field). In the second region, they are nonpotential (see above). These conclusions are illustrated by Figs. 9 and 10, which, in particular, show radial profiles of the longitudinal electric field.

Note that approximate dispersion relations (27) and (28) do not contain the quantities $Q_{1,2}$, in terms of which the effects of the finite Larmor radius of the ions are taken into account in general wave equations (10). Since dispersion relation (27) derives from the first of

Eqs. (10) in the approximation $E_\parallel = 0$, it should contain only the quantity Q_1. However, for the parameter values adopted here, this quantity is small and so is omitted in dispersion relation (27). Dispersion relation (28) derives from both of Eqs. (10). It is easy to see that, in the quasiclassical approximation, the quantities Q_1 and Q_2 drop out of complete dispersion relation (28).

The computational difficulties mentioned in Section 5 hindered numerical analysis of the problem of ICR heating of a high-density plasma such that $\omega_{pi} \gg k_\parallel c$. For $\omega_{pi} \leq k_\parallel c$, the properties of waves in the plasma column differ radically between the cases $\omega > \omega_i$ and $\omega < \omega_i$. In the first case, only magnetosonic modes can propagate in the plasma. In the second case, both magnetosonic and Alfvén modes are possible; moreover, from the side of higher plasma density, the transparency region for Alfvén modes is bounded by the Alfvén resonance surface. As the plasma density increases, the boundary surface of the transparency region for Alfvén modes is displaced toward the plasma periphery. In this case, whatever the ratio between ω and ω_i, the major part of the plasma column becomes transparent to magnetosonic modes (see dispersion relation (27)). The absence of Alfvén resonance in the case $\omega > \omega_i$ s favorable for ICR plasma heating because, in this case, the RF energy is not absorbed in the peripheral plasma.

The longitudinal component of the electric field of the magnetosonic modes is negligibly small. The transverse electric-field components of these modes are described by the following expression in the quasiclassical approximation (see [7]):

$$E_\pm = \text{const}\frac{N_\pm}{\varepsilon_\pm - N^2},$$

where $N_\pm = (N_r \pm iN_\theta)/\sqrt{2}$.

Taking into account Eq. (27) for $N_\perp^2$, we find

$$\frac{E_+}{E_-} = -\frac{N_+}{N_-}\frac{\varepsilon_- - N_\parallel^2}{\varepsilon_+ - N_\parallel^2}. \quad (29)$$

This relationship can also be obtained from expressions (11).

For the quantities $\varepsilon_\pm$ in relationship (29), we can use the order-of-magnitude estimates $\varepsilon_+ \approx \left(\frac{\omega_{pi}}{\omega_i}\right)^2 \max\left(1; \frac{\alpha}{k_\parallel \rho_i}\right)$ and $\varepsilon_- \approx \left(\frac{\omega_{pi}}{\omega_i}\right)^2$. Relationship (29) implies that, for $\alpha \geq k_\parallel \rho_i$, the energy input into the ions decreases as the density of minority ions increases, $W_i \propto \alpha|E_+|^2 \propto \alpha^{-1}$. This circumstance can reduce the efficiency of the heating of a dense plasma.

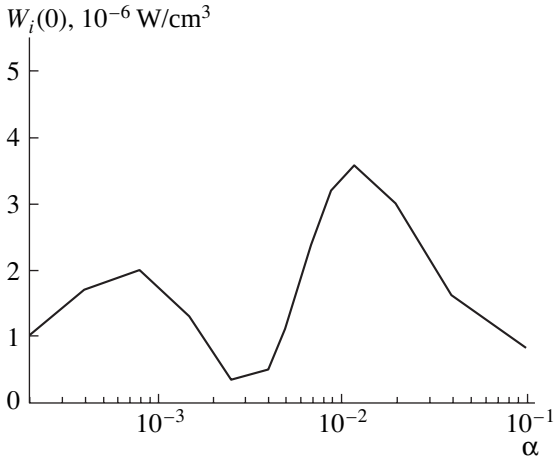

Fig. 11. Energy density deposited in the ion component at the axis of a deuterium-containing hydrogen plasma column vs. density of deuterium minority ions.

8. ION CYCLOTRON RESONANCE HEATING IN THE EPSILON DEVICE

Knowledge of the RF electromagnetic fields generated by the antenna makes it possible determine the RF power deposited in the plasma and also the antenna impedance. The corresponding calculations were carried out for different versions of the heating of a hydrogen plasma with a deuterium minority and of a deuterium plasma with a hydrogen minority under the operating conditions of the EPSILON device. The radial profile of the plasma density was given by expression (13) with $n_0(0) = 2 \times 10^{12}$ cm^{-3}. The radial electron temperature profile was assumed to be parabolic,

$$T_j(r) = T_j(0)\left(1 + \Delta - \left(\frac{r}{r_B}\right)^2\right),$$

with $\Delta = 0.01$. A study was made of the cases of hot electrons, $T_e(0) = 10$ keV ($\omega < k_\parallel v_{Te}$), and cold electrons, $T_e(0) = 100$ eV ($\omega > k_\parallel v_{Te}$).

ICR plasma heating was analyzed under the usual assumption that the energy absorbed by minority ions is redistributed over all the plasma ions by ion–ion collisions. Calculations show that, in all the plasma-heating versions in question, the efficiency with which the RF energy is transferred to the ions is of the same order of magnitude. However, the optimum version seems to be the heating of a hydrogen plasma with a deuterium minority and with hot electrons. In this version, by virtue of the condition $\omega = \omega_i' < \omega_i$, the Alfvén resonance surface occurs within the plasma column for the plasma densities under consideration. The region inside the Alfvén resonance surface, including the plasma axis, is transparent to lower hybrid modes. Hence, in the central plasma region, there can exist both large-scale magnetosonic modes and small-scale lower hybrid modes. It is presumably the interference between these modes

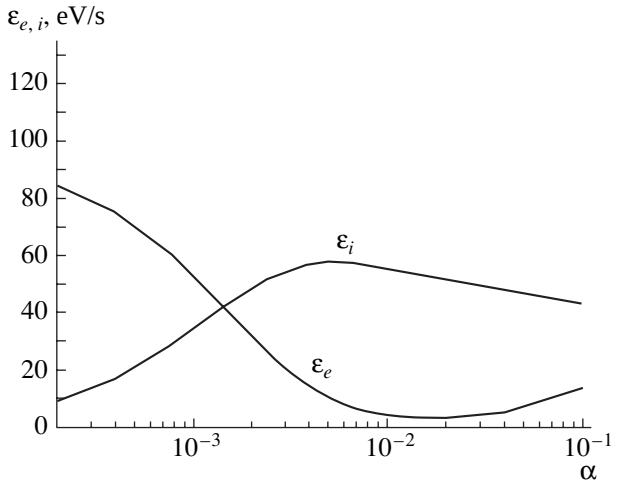

Fig. 12. Radius-averaged heating rates of the ions and electrons vs. density of deuterium minority ions in a deuterium-containing hydrogen plasma.

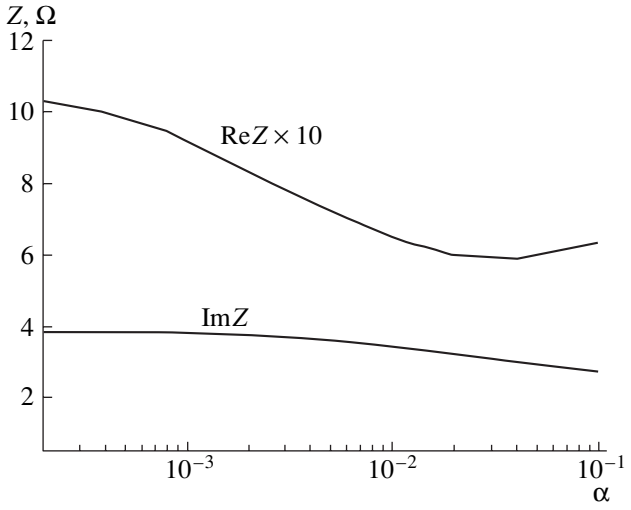

Fig. 13. Antenna impedance vs. density of deuterium minority ions in a deuterium-containing hydrogen plasma.

that is responsible for a dip in the dependence of $W_i(0)$ on the relative density $\alpha = n_i'/n_i$ of the minority ions (see Fig. 11). (Recall that, in calculations, the total antenna current was taken to be 1 A.) It should be noted that the dependence of the efficiency of minority ICR heating on the density of the impurities is characteristically nonmonotonic. It is clear that, as the density of the "absorbing agents" decreases to zero, the heating efficiency does so too. That the heating efficiency decreases as α increases is explained as being due to the following two effects: depolarization of the modes (i.e., reduction in the left-polarized component of the RF field in the central region of the plasma column) and enhancement of the absorption at the plasma periphery. This second effect ensures that, in spite of a decrease in the absorption intensity in the central plasma region, the radius-averaged ion heating rate depends weakly on α in the range $\alpha \geq 0.01$ (Fig. 12). Consequently, the antenna impedance is also a weak function of α (see Fig. 13). The radial profile $W_i(r)$ calculated for the relative minority density $\alpha = 0.012$, at which the on-axis energy input $W_i(0)$ is maximum, is shown in Fig. 14. We can see that RF power is deposited in the ion plasma component predominantly in the region around the Alfvén resonance surface. The energy absorbed by the electrons is lower than that absorbed by the ions.

In a plasma with cold electrons, the region transparent to lower hybrid modes is one outside the Alfvén resonance surface. Consequently, the maximum in the radial profile $W_i(r)$ is displaced somewhat outward in comparison with that in the case of a plasma with hot electrons (see Fig. 15). From Fig. 15 we see that, in the central plasma region, which is opaque to lower hybrid modes and in which the longitudinal RF field is negligibly weak, the electrons do not draw energy from the modes. At the same time, the electrons in the lower-density plasma region are heated even more intensely than the ions.

During ICR heating of a deuterium plasma with a hydrogen minority, the RF field frequency should be higher than the gyrofrequency of the main plasma ions. In this case, the region transparent to long-wavelength magnetosonic modes is smaller than that in the case considered above, in which both Alfvén and magnetosonic modes can propagate in the plasma. Also, for $\omega = \omega_i' > \omega_i$, Alfvén resonance is impossible, so that short-wavelength lower hybrid modes are confined to the plasma boundary. It is presumably for these reasons that the maximum density of the energy deposited in the ion plasma component at the axis of the plasma column is about five times lower than that in the case of

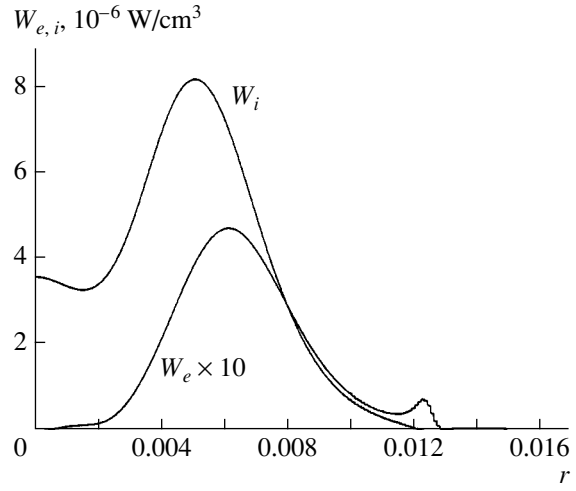

Fig. 14. Radial profiles of the energy density deposited in the ion and electron components in a deuterium-containing hydrogen plasma with hot electrons.

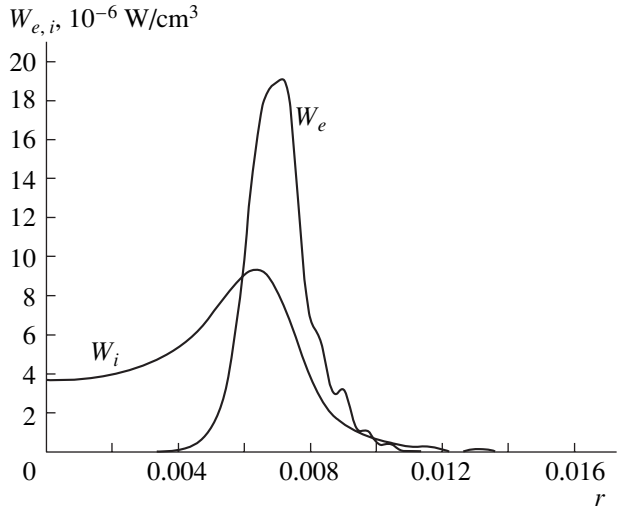

Fig. 15. Radial profiles of the energy density deposited in the ion and electron components in a deuterium-containing hydrogen plasma with cold electrons.

heating of a hydrogen plasma with a deuterium minority. On the other hand, because of the intense absorption of RF energy at the periphery of the column, the radius-averaged ion heating rate and the antenna impedance turn out to be approximately the same as those in the previous case.

9. CONCLUSIONS

In the present paper, a model description has been developed of electromagnetic waves excited in a plasma column by an external antenna at frequencies of about the ion gyrofrequency. The model takes into account the effects of the finite Larmor radius of the electrons, which, in particular, give rise to the TTMP effect. The mechanism for the amplification of the electric fields of a helical current in the plasma has been analyzed. The evolutionary pattern of changes in the wave properties of the plasma column with an increase of plasma density from a zero value (vacuum) has been obtained. The prospects for using minority ICR heating in the planned EPSILON system have been discussed.

ACKNOWLEDGMENTS

This work was supported in part by the Russian Federal Program for State Support of Leading Scientific Schools (project no. NSh-2024.2003.2).

REFERENCES

1. A. Compant La Fontaine and V. G. Pashkovsky, Phys. Plasmas **2**, 4641 (1995).
2. A. V. Timofeev, Fiz. Plazmy **25**, 232 (1999) [Plasma Phys. Rep. **25**, 207 (1999)].
3. M. L. Sawley and P. J. Paris, J. Phys. D **24**, 2135 (1991).
4. A. Compant La Fontaine, P. Louvet, P. Le Gourrierec, and A. Pailloux, Plasma Sources Sci. Technol. **8**, 125 (1999).
5. V. V. Arsenin, E. D. Dlougach, V. M. Kulygin, *et al.*, Nucl. Fusion **41**, 945 (2001).
6. *Plasma Electrodynamics*, Ed. by A. I. Akhiezer (Nauka, Moscow, 1974; Pergamon, Oxford, 1975).
7. A. V. Timofeev, *Resonance Phenomena in Plasma Oscillations* (Fizmatlit, Moscow, 2000).
8. A. V. Zvonkov and A. V. Timofeev, Fiz. Plazmy **13**, 282 (1987) [Sov. J. Plasma Phys. **13**, 158 (1987)].
9. A. V. Timofeev and K. Yu. Kharitonov, Fiz. Plazmy **15**, 674 (1989) [Sov. J. Plasma Phys. **15**, 389 (1989)].

Translated by O.E. Khadin

Plasma Physics Reports, Vol. 30, No. 9, 2004, pp. 756–760. Translated from Fizika Plazmy, Vol. 30, No. 9, 2004, pp. 811–815.

PLASMA TURBULENCE

Spectra of Langmuir Waves in a Magnetized Plasma with Low-Frequency Turbulence

T. M. Burinskaya*, J. L. Rauch, and M. M. Mogilevskiĭ***

**Institute for Space Research, Russian Academy of Sciences, Profsoyuznaya ul. 84/32, Moscow, 117810 Russia*

***Laboratory of Physics and Chemistry of the Environment, National Center of Scientific Research, France*

Received December 10, 2003

Abstract—A study is made of the formation of the spectra of Langmuir waves excited as a result of the development of beam–plasma instability in a collisionless magnetized plasma with low-frequency turbulence. Equations are derived that describe the dynamics of the formation of spectra in the quasilinear statistical approximation. The equations obtained account for small- and large-angle scattering of the electron-beam-excited waves by given background plasma density fluctuations. The scattering of Langmuir waves leads to the redistribution of their energy in phase space and, under appropriate conditions, to the appearance of a characteristic dent in the wave spectra in the frequency range where the spectral intensity is maximum. Numerical simulations carried out for plasma parameters typical of the polar cap of the Earth's magnetosphere help to explain the shape of the spectra of Langmuir waves that were recorded by the *Interball-2* satellite when it was flying through this magnetospheric region. © *2004 MAIK "Nauka/Interperiodica".*

1. INTRODUCTION

An analysis of the results of wave measurements carried out by the *Interball-2* satellite in the polar cap at altitudes of two to three Earth radii revealed small-scale bursts of Langmuir waves [1]. Modulated packets of Langmuir waves were often recorded earlier in space plasmas, e.g., the solar wind plasma [2, 3] and the plasmas in the upper part of the auroral ionosphere and in the auroral zones of the Earth's magnetosphere [4–6]. A comparison of the data from observations of the activity of Langmuir waves in different regions near the Earth shows that Langmuir waves share some common features, such as irregular structure, amplitude variation, and low-frequency modulation. Observations in the solar wind plasma and in the auroral zones revealed a correlation between the generation of Langmuir waves in a certain region and the passage of electron beams through this region. In the polar cap, small-scale bursts of Langmuir waves were also observed to be generated in the regions where electron beams with energies of 300–400 eV were propagating. The low-frequency spectra always show the presence of electrostatic waves with frequencies close to the ion Langmuir frequency. Hence, in order to interpret the experimental data, it is necessary to consider how Langmuir waves are excited by an electron beam in a plasma with low-frequency turbulence.

In this paper, we present the results from analyzing the wave measurements carried out by the *Interball-2* satellite in the polar cap and propose a theoretical model for interpreting the experimental data in the quasilinear statistical approximation.

2. EXPERIMENTAL RESULTS

Here, we use the data obtained from the *Interball-2* satellite, which was launched into Earth orbit as part of the *Interball* space project for detailed measurements at altitudes of two to three Earth radii in the inner regions of the Earth's magnetosphere. The scientific equipment on board the satellite included a very low frequency (VLF) receiver for detecting the electric and magnetic components of radiation in the frequency band from 8 Hz to 20 kHz [7] and also an ION device [8] for measuring electron and ion fluxes in the energy range from 5 eV to 20 keV. An analysis of the signals in a frequency band of up to 20 kHz revealed local small-scale bursts of Langmuir waves in the polar cap. As a rule, the signals under investigation consist of several bursts whose intensity changes in an irregular manner. The total duration of a packet of bursts is about 0.05–10 s, and the duration of an individual burst varies from 0.02 to 2–3 s. The characteristic dimensions of the spatial regions where the bursts were recorded range from a few hundred meters to 2–3 km. The signals have the form of chains of Langmuir waves modulated at low frequencies and having amplitudes of 1–40 mV/m. Figure 1 shows a representative signal waveform recorded on December 3, 1996, between 20:53:47.7 UT and 20:53:47.75 UT. For higher time resolution, Fig. 1b displays a fragment of the waveform (with a duration of 6 μs) shown in Fig. 1a. The carrier frequency of the waves corresponds to the local electron Langmuir frequency. The possible role of three-wave interactions in the formation of the low-frequency envelope of a waveform was examined by a bispectral analysis of the wave measurements [9]. For each individual event of the Langmuir wave activity, the waveform was divided into

1063-780X/04/3009-0756$26.00 © 2004 MAIK "Nauka/Interperiodica"

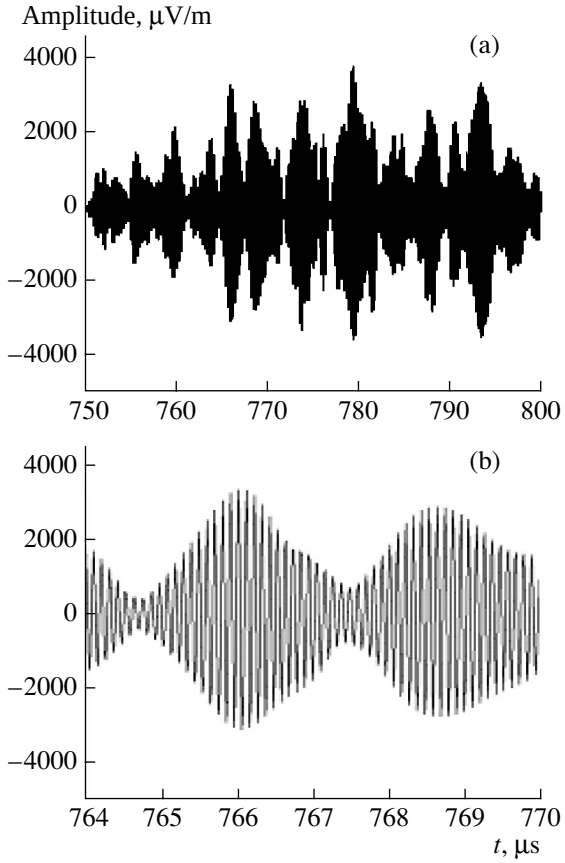

Fig. 1. (a) Waveform of Langmuir oscillations recorded on December 3, 1996, between 20:53:47.7 UT and 20:53:47.75 UT by a satellite flying through the polar cap and (b) a higher-resolution fragment of the waveform shown in Fig. 1a.

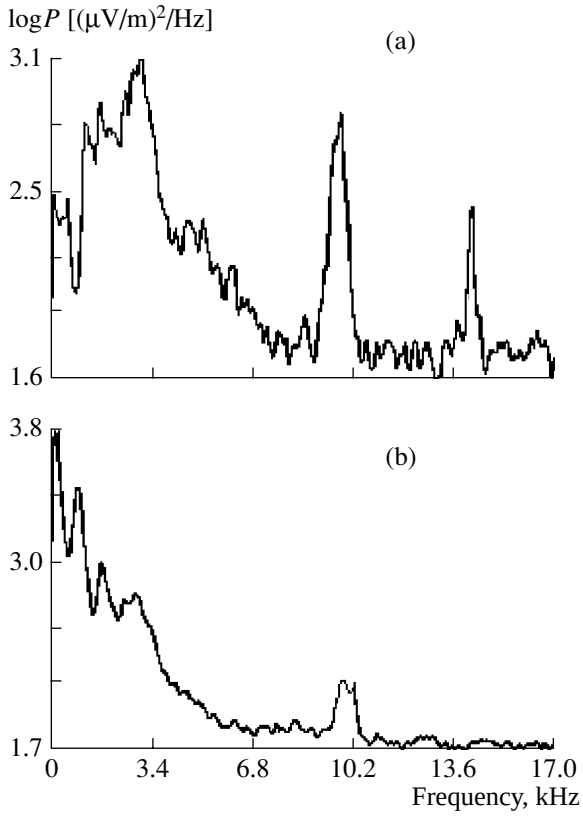

Fig. 2. Energy spectra of electric waves measured experimentally in the polar cap region on December 3, 1996.

M parts (usually, $M = 50$) and the Fourier spectrum of the electric field in the ith time interval was calculated. Then, the square of the absolute value of the normalized three-wave correlation function, $b^2(k, l)$, was determined from the formula

$$b^2(k, l) = \frac{|B(k, l)|^2}{D},$$

where

$$B(k, l) = \frac{1}{M}\sum_{i=1}^{M} E_i(\omega_k)E_i(\omega_l)E_i^*(\omega_k + \omega_l),$$

the normalization being analogous to that in [10],

$$D = \left\{\frac{1}{M}\sum_{i=1}^{M} |E_i(\omega_k)E_i(\omega_l)E_i^*(\omega_k + \omega_l)|\right\}^2.$$

The results obtained showed that the quantity $b^2(k, l)$ is, as a rule, very small; it is only in rare cases that it is as large as 0.3–0.35.

The width of the Langmuir wave spectra recorded in the region of the polar cap is about 10% of the local Langmuir frequency. Such a large spectral width cannot be attributed to the dispersion of Langmuir waves. There is also a characteristic dent in the spectra in the frequency range where they are peaked. Figure 2 shows typical spectra of the electric oscillations in the polar cap region that were recorded by the satellite on December 3, 1996. The spectrum measured between 20:53:47.7 UT and 20:53:48.5 UT is shown in Fig. 2a. The local peak at a frequency of 13.6 kHz is of artificial origin. Langmuir waves give rise to a peak at a frequency of about 10 kHz. The fragment of the waveform that corresponds to these waves is given in Fig. 1. In Fig. 2b, the spectrum measured between 20:11:17.07 UT and 20:11:18.7 UT is shown. The spectral peak at a frequency of 10 kHz is produced by the Langmuir waves. Both of the spectra in Fig. 2 show the presence of low-frequency oscillations at frequencies close to the ion Langmuir frequency. The intensity of these waves in the bottom spectrum is higher than that in the upper spectrum, while the intensity of the Langmuir waves in the right spectrum is lower than that in the upper spectrum.

3. THEORETICAL RESULTS

Experiments show that Langmuir waves were always observed against the background of low-frequency oscillations; moreover, the sizes of the regions of low-frequency turbulence were several orders of magnitude greater than those of the regions in which the Langmuir wave were recorded. The effect of the low-frequency oscillations in the plasma under investigation is that the electron-beam-excited Langmuir waves can be scattered by plasma density fluctuations and thereby can depart from resonance with the beam electrons. Because of this scattering, the energy of Langmuir waves can be transferred into the phase space regions in which the linear growth rate of the beam–plasma instability is low and can even be negative. In order to investigate the effect of scattering on the formation of the spectra of Langmuir waves, we consider the linear stage of the beam–plasma instability in a plasma with low-frequency turbulence. We will be interested in a low-density plasma in a magnetic field in which the electron gyrofrequency is much higher than the electron Langmuir frequency. Such relationships between the plasma parameters are characteristic of the polar cap region, in which the Langmuir waves in question were observed.

The basic equation for the processes under analysis is the well-known Zakharov equation for the envelope of the high-frequency potential Φ in a magnetized plasma [11]. In this equation, we treat the plasma density fluctuations $\delta n(t, r)$ as prescribed random functions such that $\langle \delta n \rangle = 0$:

$$\Delta\left[\frac{2i}{\omega_p}\left(\frac{\partial}{\partial t} + \hat{\gamma}\right) + 3\lambda_D^2\Delta_\parallel\right]\Phi - \frac{\omega_c^2}{\omega_c^2 - \omega_p^2}\Delta_\perp\Phi = \nabla\left(\frac{\delta n}{n_0}\nabla\Phi\right). \quad (1)$$

Here, n_0 is the background plasma density, ω_p and ω_c are the electron Langmuir frequency and electron gyrofrequency (it is assumed that $\omega_c > \omega_p$), and λ_D is the Debye radius. The operator $\hat{\gamma}$ describes the growth or damping of Langmuir waves, the Fourier representation of the quantity $\hat{\gamma}\Phi$ in wavenumber space being $\gamma_k\Phi(k)$, where the Fourier coefficients γ_k are assumed to be independent of the plasma density fluctuations (i.e., the inverse effect of the waves on the distribution function of the beam electrons is ignored). Equation (1) was derived under the assumptions $k_\parallel \gg k_\perp$ and $k^2\lambda_D^2 \ll 1$ and also under the inequality $k_\parallel^2 > \omega_p^3/\omega_c c^2$ (where c is the speed of light). The last assumption is made because, for $\omega_c > \omega_p$, Langmuir waves are described by the short-wavelength portion of the dispersion curve, while the long-wavelength portion at $k_\parallel^2 < \omega_p^3/\omega_c c^2$ corresponds to the whistler mode.

Switching to the Fourier representation and assuming that the given ensemble of plasma density fluctuations δn is statistically uniform in coordinate space, we can obtain the general dynamic equation for the spectral density of Langmuir waves by closing the corresponding set of equations for the Fourier coefficients in a quasilinear manner (see [12]):

$$\left(\frac{\partial}{\partial t} + 2\gamma_{\mathbf{k}}\right)W(\mathbf{k}, t) = -2\gamma_{\mathbf{k}}^{\text{ef}}(\mathbf{k}, t) + S_{\mathbf{k}}^{\text{ef}}(t) + S^{\text{sp}}. \quad (2)$$

Here and below, we use the following dimensionless variables:

$$t \equiv \omega_p t, \quad r \equiv \sqrt{2}r/\sqrt{3}\lambda_D, \quad W(k, t) \equiv W(k, t)/T_e, \quad (3)$$

where T_e is the electron temperature of the background plasma. The wave vector $\mathbf{k}$ refers to Langmuir waves and the wave vector $\mathbf{q}$ refers to low-frequency oscillations. The quantity $\gamma_{\mathbf{k}}$ is the sum of the rate of Landau damping by the background plasma and the Landau growth or damping rate due to the presence of an electron beam. The frequencies and wave vectors are nondimensionalized by dividing by ω_p and $\sqrt{2/3}\lambda_D$, respectively. The operators $\gamma_{\mathbf{k}}^{\text{ef}}$ and $S_{\mathbf{k}}^{\text{ef}}$ describe the scattering of waves by the plasma density fluctuations and the operator S^{sp} accounts for the spontaneous emission:

$$\gamma_{\mathbf{k}}^{\text{ef}} = \frac{\pi}{2}\int_{-\infty}^{\infty}\frac{d^3\mathbf{q}}{(2\pi)^3}C_{\mathbf{q}}\mu[\delta(R_+) + \delta(R_-)], \quad \mu = \frac{k_\parallel^2(k_\parallel - q_\parallel)^2}{k^2(\mathbf{k} - \mathbf{q})^2}, \quad (4)$$

$$S_k^{\text{ef}} = \pi\int_{-\infty}^{\infty}\frac{d^3\mathbf{q}}{(2\pi)^3}C_{\mathbf{q}}\mu[\delta(R_+) + \delta(R_-)]W(\mathbf{k} - \mathbf{q}, t), \quad (5)$$

$$R_\pm = (k_\parallel - q_\parallel)^2 - k_\parallel^2 - \frac{b(k_\perp - q_\perp)^2}{2(\mathbf{k} - \mathbf{q})^2} + \frac{bk_\perp^2}{2k^2} \pm \omega_q, \quad b = \frac{\omega_c^2}{\omega_c^2 - \omega_p^2}, \quad (6)$$

where ω_q is the frequency of the low-frequency oscillations. The quantity $R_\pm$ is the deviation of the sum of the wave frequencies involved from the exact resonance. Since we are interested in the resonant case $R_\pm = 0$, we use the delta function $\delta(R)$ in Eqs. (4) and (5).

The spectral correlation function of the plasma density fluctuations, $C_{\mathbf{q}}$, is given by the expression

$$\int_{-\infty}^{\infty}\frac{d^3\mathbf{q}}{(2\pi)^3}C_{\mathbf{q}} = \left\langle\left(\frac{\delta n}{n}\right)^2\right\rangle. \quad (7)$$

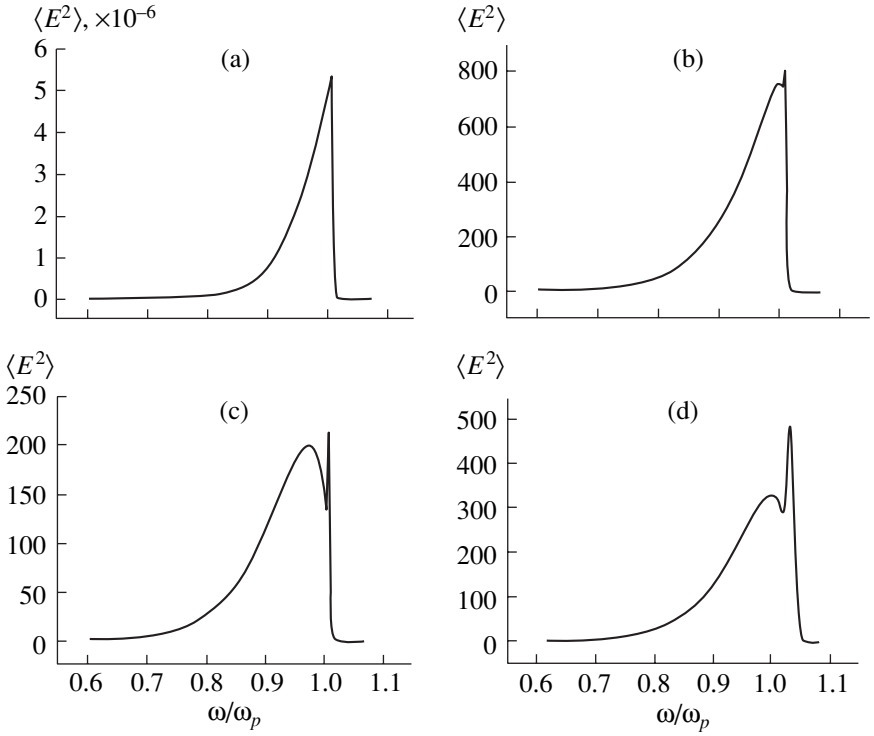

Fig. 3. Energy spectra of Langmuir waves calculated numerically for different values of $\delta n/n$ (see the text).

Equations (2)–(7) describe the diffusion of Langmuir waves in the limit in which the characteristic spatial scale q^{-1} of the plasma density fluctuations is much longer than the characteristic spatial scale k^{-1} of the Langmuir waves. In the opposite limit, these equations describe large-angle scattering of the waves. Hence, Eqs. (2)–(7) account for the processes of wave scattering through arbitrary angles.

The results of numerically solving Eqs. (2)–(7) that are presented in this paper were obtained under the assumption that the plasma density fluctuations are steady-state, $\omega_q = 0$. This assumption was made because data from measurements taken on board the *Viking* satellite showed that, during periods of magnetospheric disturbances in the polar cap region at altitudes of up to 13500 km, there were a vast variety of small-scale (<1 km) plasma density fluctuations that drifted with velocities far lower than the ion thermal speed [13]. In numerical simulations, the spectral function of the fluctuations of the background plasma density was calculated by the formula

$$C_{\mathbf{q}} = Aq_{\perp}^2 \exp\left(-\frac{q_{\parallel}^2}{2q_{\parallel 0}^2} - \frac{q_{\perp}^2}{q_{\perp 0}^2}\right), \qquad (8)$$

where $q_{\parallel 0}$ and $q_{\perp 0}$ are the characteristic wavenumbers of the density fluctuations in the directions parallel and perpendicular to the magnetic field and, by virtue of Eq. (7), the normalizing factor A has the form $A = \frac{2(2\pi)^{3/2}}{q_{\parallel 0} q_{\perp 0}^4}\left\langle\left(\frac{\delta n}{n}\right)^2\right\rangle$.

Equations (2)–(8) were solved assuming the axial symmetry with respect to the magnetic field. The numerically calculated spectra of Langmuir waves are shown in Fig. 3, in which the ordinate is $\langle E\rangle^2 = \int W(\mathbf{k}, t)\frac{d^3\mathbf{k}}{(2\pi)^3}$. The computations were carried out for parameter values typical of the polar cap plasma. The ratio of the electron gyrofrequency to the electron Langmuir frequency was taken to be $\omega_c/\omega_p = 2$, the ratio of the plasma thermal velocity to the electron beam velocity was set to be 0.06, and the ratio of the electron thermal velocity to the directed velocity of the beam was chosen to be 0.65, the ratio of the beam electron density to the background plasma density being 0.01. The characteristic dimensionless wavenumbers of the plasma density fluctuations were equal to $q_{\parallel 0} = 0.002$ and $q_{\perp 0} = 0.01$. The total time during which the processes in question were followed numerically was $3000\omega_p^{-1}$. The spectrum shown in Fig. 3a was calculated for $\delta N \equiv \langle(\delta n/n)^2\rangle^{\frac{1}{2}} = 0$, and the spectra shown in Figs. 3b and 3c were computed for $\delta N = 1$ and 4%, respectively. The spectrum shown in Fig. 3d was obtained for the same parameter values as the spectrum

in Fig. 3c, the only difference being that the ratio of the plasma thermal velocity to the electron beam velocity was taken to be 0.12. A comparison between the spectra presented in Fig. 3 shows that, as was expected, the larger the quantity δN, the lower the intensity of the Langmuir waves. The shape of the spectrum changes radically when the process of wave scattering by density fluctuations is taken into account: the spectrum becomes wider because of the redistribution of the energy of Langmuir waves in phase space and a characteristic dent (analogous to that observed in the measured spectra) appears in the calculated spectrum. The reconstruction of the waveforms from the numerically obtained results under the assumption that the scattered waves have random phases shows that the waveforms consist of modulated chains of wave packets that are similar to the experimentally observed signals. Hence, the modulation of the envelope of the packets of Langmuir waves results from the interference between waves with close frequencies that are excited by an electron beam and arise as a result of wave scattering by the background plasma density fluctuations.

4. CONCLUSIONS

The results of our investigation demonstrate that the processes of wave scattering by background plasma density fluctuations can play a governing role in the formation of the spectra of Langmuir waves excited as a result of the development of beam–plasma instability in a plasma with low-frequency turbulence. The equations describing the dynamics of the formation of the spectra of Langmuir waves in a collisionless magnetized plasma with low-frequency turbulence have been derived using the quasilinear statistical approximation. Numerical results show that the scattering of Langmuir waves leads to the redistribution of their energy in phase space and to the formation of wave spectra analogous to those observed experimentally. The calculations carried out for plasma parameters typical of the polar cap of the Earth's magnetosphere have made it possible to explain the formation of the spectra of Langmuir waves that were recorded by the *Interball-2* satellite when it was passing through this magnetospheric region.

ACKNOWLEDGMENTS

This work was supported in part by the RF Ministry of Science under the Program for State Support of Leading Scientific Schools, project no. NSh-1739.2003.2.

REFERENCES

1. T. M. Burinskaya, A. A. Rusanov, and M. M. Mogilevskiĭ, Kosm. Issled. **38**, 507 (2000).
2. R. P. Lin, W. K. Levedahl, W. Lotko, *et al.*, Astrophys. J. **308**, 954 (1986).
3. D. A. Gurnett, G. B. Hospodarsky, W. S. Kurth, *et al.*, J. Geophys. Res. **98**, 5631 (1993).
4. J. P. McFadden, C. W. Carlson, and M. H. Boehm, J. Geophys. Res. **91**, 12079 (1986).
5. K. Stasievicz, B. Holback, V. Krasnoselskikh, *et al.*, J. Geophys. Res. **101**, 21515 (1996).
6. J. Bonnel, P. Kintner, J.-E. Wahlund, *et al.*, J. Geophys. Res. **102**, 17233 (1997).
7. M. M. Mogilevskiĭ, A. M. Golyavin, T. V. Aleksandrova, *et al.*, Kosm. Issled. **36**, 630 (1998).
8. Zh. A. Sovo, A. Bart, K. Auste, *et al.*, Kosm. Issled. **36**, 53 (1998).
9. J. S. Bendat, *Nonlinear System Analysis and Identification from Random Data* (Wiley, New York, 1990).
10. V. Kravtchenko-Berejnoi, V. Krasnoselskikh, D. Mourenas, and F. Lefeuvre, in *Proceedings of the Cluster Workshop on Data Analysis Tools, Braunschweig, 1994*, p. SP-371.
11. V. V. Krasnosel'skikh and V. I. Sotnikov, Fiz. Plazmy **3**, 872 (1977) [Sov. J. Plasma Phys. **3**, 491 (1977)].
12. M. V. Goldman and D. F. DuBois, Phys. Fluids **25**, 1062 (1982).
13. G. Holmgren and P. M. Kintner, J. Geophys. Res. **95**, 6015 (1990).

Translated by O.E. Khadin

Plasma Physics Reports, Vol. 30, No. 9, 2004, pp. 761–765. Translated from Fizika Plazmy, Vol. 30, No. 9, 2004, pp. 816–820.

PLASMA DIAGNOSTICS

Plasma Diagnostics from the Dynamic Current–Voltage Characteristic of an Electric Probe

V. I. Sysun, O. V. Oleshchuk, and P. S. Gura

Petrozavodsk State University, pr. Lenina 33, Petrozavodsk, 185640 Russia

Received June 4, 2003; in final form, December 10, 2003

Abstract—A method for measuring the plasma electron density from the dynamic current–voltage probe characteristic is considered. For this purpose, an additional rectangular negative voltage pulse or a high-frequency sinusoidal voltage is applied to a negatively biased probe. Analytic expressions are derived for two cases: when the space charge sheath obeys the 3/2 law and when the voltage varies over a time shorter than the ion transit time through the sheath so that the sheath does not obey the 3/2 law. Dynamic and statistic probe methods for determining the electron density are compared experimentally. *© 2004 MAIK "Nauka/Interperiodica".*

1. INTRODUCTION

The interpretation of the current–voltage (*I–V*) probe characteristics usually assumes that the probe potential varies at a sufficiently slow rate such that the plasma region perturbed by the probe has time to rearrange in accordance to the potential variations (the quasi-steady regime).

However, the opposite case of fast variations in the probe potential (when the plasma parameters in the quasineutral region have no time to follow the potential variations and are determined by the average probe potential, whereas the electron component in the electrode sheath follows the instantaneous probe potential in accordance to Poisson's equation) is also of interest. In this case, the amplitude of the probe current variations depends only on the electron density near the sheath boundary and does not depend on the state of the probe surface (probe contamination, secondary emission, surface dielectric layers, etc.). The amplitude of the probe current variations can exceed the average (static) probe current; as a result, the sensitivity of probe measurements increases.

Let the probe be at a negative (relative to the plasma) potential U_0 corresponding to the ion saturation current. In this case, the ion sheath with the current density

$$j_0 = eNv_0 \tag{1}$$

forms near the probe. Here, N is the ion density at the sheath boundary, $v_0 = \sqrt{\frac{kT}{M}}$ is the ion-acoustic velocity, and e is the electron charge. A criterion for the existence of a collision-free sheath (the Bohm criterion) is the equality of the ion drift velocity at the sheath boundary to v_0 [1, 2]. In [3], it was shown that the velocity with which the ions enter the sheath is equal to v_0 and does not depend on the collision frequency in the quasineutral region, provided that the ion–neutral collision frequency is sufficiently low for the drift velocity of the ions within the sheath to be higher than v_0. A transition from the plasma density N at the sheath boundary to the unperturbed plasma density at various pressures was investigated in [4].

2. APPLICATION OF A STEP VOLTAGE TO THE PROBE ($U_m \gg U_0$)

Let us consider reverse currents to the anode (see [5]). The presence of an external probe inductance L inhibits instantaneous variations in the probe voltage. The parasitic external capacitance produces an additional current in the measurement circuit; this current can be compensated in the absence of a plasma. The probe voltage is determined by the equation

$$U_m = U + L\frac{di}{dt} = U + LS\frac{dj}{dt}. \tag{2}$$

When the current reaches its maximum, we have $\frac{dj}{dt} = 0$ and $U = U_m$. The current density at the probe is equal to

$$j = eNv_0 + eN\frac{d\delta}{dt}, \tag{3}$$

where δ is the length of the space charge sheath.

The first term on the right-hand side of Eq. (3) corresponds to the static ion current to the probe, and the second term describes the escape of electrons from the boundary region to the opposite electrode as the sheath length increases. Expression (3), which is valid for any probe configuration, was used in [5, 6] to calculate reverse currents to the anode.

1063-780X/04/3009-0761$26.00 © 2004 MAIK "Nauka/Interperiodica"

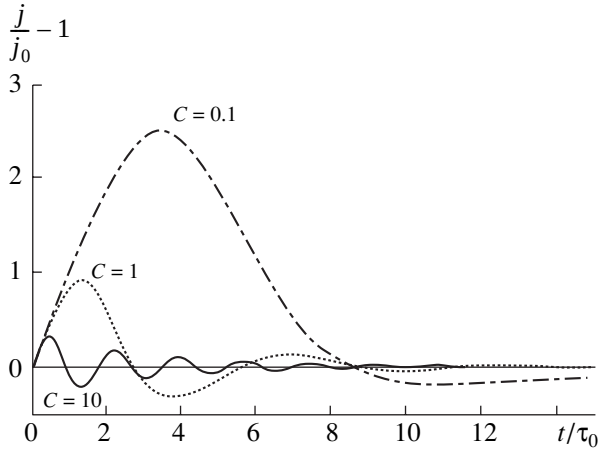

Fig. 1. Solutions to Eq. (6) at different values of the parameter *C*.

2.1. Slow Increase in the Probe Voltage

When the sheath length δ is smaller than the ion mean free path, the 3/2 law for the sheath has the form

$$\delta = \frac{AU^{3/4}}{j^{1/2}}, \tag{4}$$

where $A = \frac{2}{3}\left(\frac{2\varepsilon_0^2 e}{M}\right)^{1/4}$. Moreover, we have $\frac{d\delta}{dt} \ll \frac{\delta}{\Delta t}$, where $\Delta t = 3\delta\sqrt{\frac{M}{2eU}}$ is the ion transit time through the sheath. After simple manipulations, we obtain

$$j_\mathrm{m} - j_0 \ll \frac{eN}{3}\sqrt{\frac{2eU_\mathrm{m}}{M}} = \frac{1}{3}j_0\sqrt{\frac{2eU_\mathrm{m}}{kT}}. \tag{5}$$

Expression (5) determines the applicability of the 3/2 law.

Integrating expression (3) over time from zero to the instant at which the current reaches its maximum, we obtain

$$\int_0^{t_\mathrm{m}}(j - j_0)dt = eN(\delta - \delta_0) \approx eN\delta$$
$$= \frac{eNAU_\mathrm{m}^{3/4}}{j_\mathrm{m}^{1/2}} = \frac{eN}{j_\mathrm{m}^{1/2}}\frac{2}{3}\left(\frac{\varepsilon_0^2 2e}{M}\right)^{1/4}U_\mathrm{m}^{3/4}.$$

To derive the time dependence of the current density, it is necessary to simultaneously solve Eqs. (2), (3), and (4). Substituting Eq. (3) into Eq. (2) yields

$$U_\mathrm{m} = SLeN\frac{d^2\delta}{dt^2} + \frac{\delta^{4/3}}{A^{4/3}}\left(j_0 + eN\frac{d\delta}{dt}\right)^{\frac{2}{3}}. \tag{6}$$

This equation can be reduced to the dimensionless form

$$\frac{dy}{dt'} = 1 - C^{4/3}(1+y)^{2/3}\left[\int_0^{t'} y dt'\right]^{4/3},$$

where $y = \frac{j}{j_0} - 1$, $t' = \frac{t}{\tau_0}$, $\tau_0 = \frac{Lj_0 S}{U_\mathrm{m}}$, $C = \frac{\tau_0 v_0}{\delta_\infty}$, and $\delta_\infty = \frac{AU_\mathrm{m}^{3/4}}{j_0^{1/2}}$.

Figure 1 shows the solutions to Eq. (6) for different values of the parameter *C*. One can see that the current increases to its maximum value according to the sinusoidal law. Thus, we can assume that

$$\int_0^{t_\mathrm{m}}(j - j_0)dt \approx (j_\mathrm{m} - j_0)\frac{2}{\pi}t_\mathrm{m}.$$

As a result, we obtain the following expression for the density:

$$N = \frac{j_\mathrm{m}^{1/2}\int_0^{t_\mathrm{m}}(j - j_0)dt}{\frac{2}{3}e\left(\frac{\varepsilon_0^2 2e}{M}\right)^{1/4}U_\mathrm{m}^{3/4}} \approx \frac{3j_\mathrm{m}^{1/2}(j_\mathrm{m} - j_0)t_\mathrm{m}}{\pi e\left(\frac{2\varepsilon_0^2 e}{M}\right)^{1/4}U_\mathrm{m}^{3/4}}. \tag{7}$$

2.2. Application of a Step Voltage with a Rise Time Shorter than the Ion Transit Time through the Sheath

In this case, the ion density in the sheath can be assumed to be time-independent. Assuming that the sheath length is small in comparison to the probe size, we find from Poisson's equation that

$$\frac{d^2U}{dx^2} = -\frac{eN}{\varepsilon_0};\quad E = \frac{eN}{\varepsilon_0}x;\quad U = \frac{eN}{\varepsilon_0}\frac{x^2}{2};\quad \delta = \sqrt{\frac{2\varepsilon_0 U}{eN}}; \tag{8}$$
$$j - j_0 = eN\frac{d\delta}{dt} = (2eN\varepsilon_0)^{1/2}\frac{dU^{1/2}}{dt};$$

$$\int_0^t (j - j_0)dt = (2eN\varepsilon_0)^{1/2}U^{1/2}; \tag{9}$$

$$N = \frac{\left(\int_0^{t_\mathrm{m}}(j - j_0)dt\right)^2}{2e\varepsilon_0 U_\mathrm{m}} \approx \frac{2}{\pi^2}\frac{(j_\mathrm{m} - j_0)^2 t_\mathrm{m}^2}{e\varepsilon_0 U_\mathrm{m}}. \tag{10}$$

The applicability of the approach used is determined by the inequality inverse to inequality (5). Combining

formulas (7) and (10), for an arbitrarily increasing probe voltage we obtain

$$N = \frac{3t_m j_m^{1/2}(j_m - j_0)M^{1/4}}{\pi e(2e\varepsilon_0^2)^{1/4}U_m^{3/4}\left(1 + \frac{27 j_m^{3/2}M^{3/4}}{(2e)^{9/4}U_m^{3/4}N^{3/2}}\right)^{1/3}}. \quad (11)$$

The inductance does not enter into the expression for the density because an increase in the time t_m is balanced by a decrease in j_m. The density N is found from formula (11) by the iteration method.

3. SINUSOIDAL PROBE VOLTAGE

The use of a sinusoidal voltage in the probe diagnostics has obvious advantages: (i) such a voltage is easy to generate and (ii) it can easily be separated from noise. The probe voltage in this case has the form

$$U = U_0 + U_m \sin\omega t. \quad (12)$$

When the sheath obeys the 3/2 law, we can write

$$j - j_0 = eN\frac{d\delta}{dt} = eN\left(\frac{3A}{4U^{1/4}j^{1/2}}\frac{dU}{dt} - \frac{AU^{3/4}}{2j^{3/2}}\frac{dj}{dt}\right), \quad (13)$$

$$\frac{dj}{dt} = \frac{3U_m\omega\cos\omega t}{2(U_0 + U_m\sin\omega t)}j - \frac{(j - j_0)2j^{3/2}}{eNA(U_0 + U_m\sin\omega t)^{3/4}}. \quad (14)$$

Let us introduce the dimensionless variables

$$t' = \omega t, \quad j' = \frac{j}{j_0}, \quad C = \frac{2j_0^{3/2}}{\omega eNAU_0^{3/4}} = \frac{2v_0}{\omega\delta_0}. \quad (15)$$

Equation (14) then takes the form

$$\frac{dj'}{dt'} = \frac{3j'\cos t'\frac{U_m}{U_0}}{2\left(1 + \frac{U_m}{U_0}\sin t'\right)} - \frac{j'^{3/2}(j' - 1)C}{\left(1 + \frac{U_m}{U_0}\sin t'\right)^{3/4}}. \quad (16)$$

The applicability of the 3/2 law can be determined in a different way. At a negative variable probe potential, the reverse motion of the sheath is limited by the velocity v_0 with which the plasma ions enter the sheath,

$$\frac{d\delta}{dt} \ll v_0, \quad j - j_0 \ll j_0. \quad (17)$$

The parameter C is then limited by the inequality

$$C \gg 2\left[\left(1 + \frac{U_m}{U_0}\right)^{\frac{3}{4}} - 1\right]. \quad (18)$$

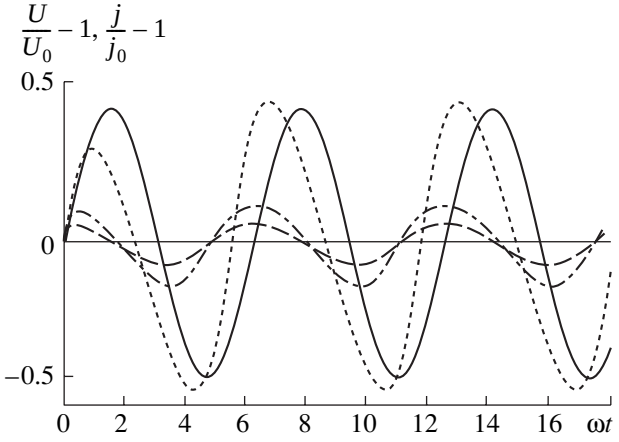

Fig. 2. Numerical solution to Eq. (16) at $\frac{U_m}{U_0} = 0.5$: voltage (solid line) and current for $C = 10$ (dashed line), 5 (dashed-and-dotted line), and 1 (dotted line).

At $U_m/U_0 \ll 1$ and $j - j_0 \ll j_0$, Eq. (17) reduces to the form

$$\frac{d(j' - 1)}{dt'} = \frac{3}{2}\frac{U_m}{U_0}\cos t' - (j' - 1)C. \quad (19)$$

Its solution is

$$j' - 1 = \frac{3}{2}\frac{U_m}{U_0}\frac{\sin(\omega t + \varphi)}{\sqrt{C^2 + 1}}; \quad \tan\varphi = C; \quad C \gg \frac{3}{2}\frac{U_m}{U_0}. \quad (20)$$

At $C \gg 1$, the sheath obeys the 3/2 law and we obtain from (20) that

$$\frac{j}{j_0} - 1 = \frac{3}{2}\frac{U_m}{CU_0}\cos\omega t. \quad (21)$$

Substituting C from Eq. (15) into Eq. (21), we obtain the following expression for the maximum current:

$$j_m - j_0 = \frac{(\varepsilon_0 eN)^{1/2}\omega U_m}{2U_0^{1/2}}\left(\frac{2eU_0}{kT}\right)^{1/4}, \quad N = \frac{(j_m - j_0)^2}{f^2}\frac{U_0}{\pi^2\varepsilon_0 eU_m^2}\sqrt{\frac{kT}{2eU_0}}. \quad (22)$$

Figure 2 shows a numerical solution to Eq. (16). It can be seen that, even at rather large values of U_m/U_0($\frac{U_m}{U_0} = 0.5$), solution (20) is valid to a high accuracy.

At a high-frequency sinusoidal probe voltage, the ion density does not vary: it obeys the 3/2 law for the

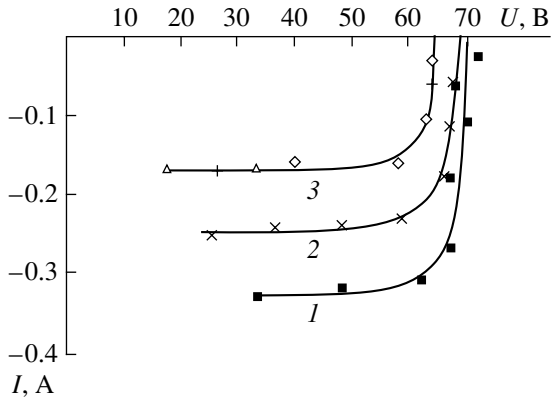

Fig. 3. Probe characteristics for discharge currents of (*1*) 30, (*2*) 20, and (*3*) 15 A. The argon pressure is 0.1 torr.

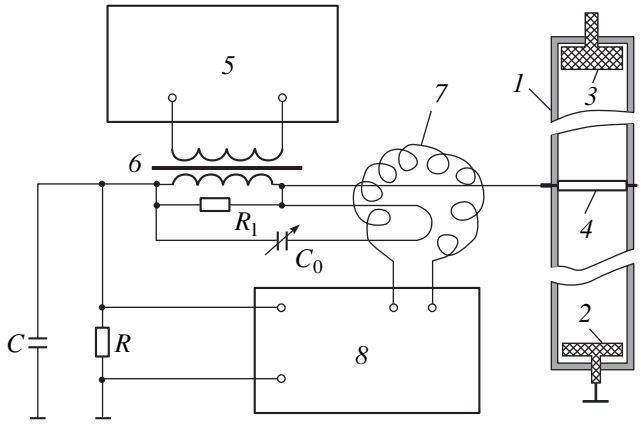

Fig. 4. Circuit for measurements of the dynamic *I–V* probe characteristic: (*1*) discharge tube, (*2*) cathode, (*3*) anode, (*4*) probe, (*5*) G6-37 high-frequency generator, (*6*) isolating transformer, (*7*) measuring transformer, and (*8*) C8-14 oscilloscope. The circuit parameters are R = 100–200 Ω, C = 0.01 μF, R_l = 100 Ω, and C_0 = 5–30 pF.

average probe potential U_0 inside the sheath and is constant outside it. Let x be the deviation of the sheath boundary from its mean value. At $U_m \ll U_0$, and $x \ll \delta_0$, we can assume that

$$U \approx U_0 + \frac{\delta_0}{\varepsilon_0}\int_0^x eN(x')dx'. \qquad (23)$$

Differentiation of this expression over time yields

$$\frac{dU}{dt} = \frac{dU}{dx}\frac{dx}{dt} = \frac{\delta_0}{\varepsilon_0}eN(x)\frac{dx}{dt} = \frac{\delta_0}{\varepsilon_0}(j - j_0). \qquad (24)$$

Expression (24) is valid at both $x > 0$ and $x < 0$. At a sinusoidal probe voltage (see (12)), we have

$$j - j_0 = \frac{\varepsilon_0\omega U_m\cos\omega t}{\delta_0} = \frac{3}{2}\frac{(eN\varepsilon_0)^{1/2}\omega U_m\cos\omega t}{\left(\frac{2eU_0}{kT}\right)^{1/4}U_0^{1/2}},$$
$$N = \frac{(j_m - j_0)^2\left(\frac{2eU_0}{kT}\right)^{1/2}U_0}{9\pi^2 e\varepsilon_0 f^2 U_m^2}. \qquad (25)$$

Therefore, the sheath is similar to a capacitor with a capacitance of $C = \frac{\varepsilon_0 S}{\delta_0}$, where S is the sheath area. At $\frac{2eU_0}{kT} = 9$, expressions (22) and (25) coincide.

4. EXPERIMENTAL VERIFICATION OF THE METHOD PROPOSED

The method was verified with the help of a ring wall probe with a diameter of 10.5 mm and width of 2 mm. The probe was placed in the middle of a discharge glass tube with a length of 0.7 m and an inner diameter of 11.5 mm. Experiments were performed with argon (P = 0.1 torr) at a discharge current of 15–30 A and discharge duration of 2–12 ms.

The plasma parameters were preliminarily measured by the conventional method with the use of the ion branch of the probe *I–V* characteristic. The voltage across the resistor placed between the probe and the grounded cathode was measured with the help of an oscilloscope. The resistance was varied from 40 Ω to 6 kΩ. The results of measurements were used to plot the ion branch of the probe *I–V* characteristic (Fig. 3). The processing of the *I–V* characteristic allowed us to determine the plasma potential, the electron temperature, and the electron density.

The electron temperature T_e was determined from the first-order derivative of the current with respect to the voltage in the region where the probe characteristic passed through the zero current and from the saturation ion current (I_i) by using the equation $\frac{kT_e}{e} = \frac{I_i}{dI/dU}$. The electron temperature was found to be 3 ± 1 eV. The plasma potential was determined from the expression $U_p = U_f + \Delta U$. Here, U_f is the floating plasma potential, $\Delta U = \frac{kT_e}{e}\ln\left(0.67\sqrt{\frac{M}{m}}\right)$, M is the mass of an argon ion, m is the electron mass, e is the electron charge, and k is Boltzmann's constant. For T_e = 3 eV, we have ΔU = 15 V.

The plasma density N at the sheath boundary was determined from formula (1), which is valid, as was mentioned above, over a wide range of pressures: N =

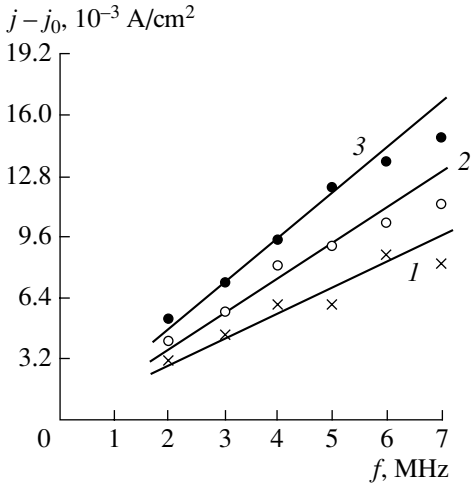

Fig. 5. High-frequency current density at the probe vs. frequency of the RF component of the probe voltage. The discharge current is (*1*) 15, (*2*) 20, and (*3*) 30 A.

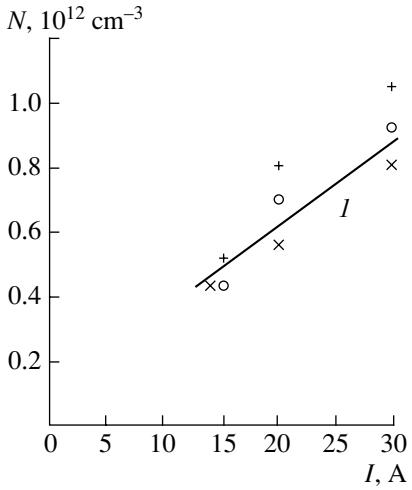

Fig. 6. Plasma density vs. discharge current. Curve *1* shows the data obtained by the conventional method, and the symbols show the data obtained from the dynamic *I–V* probe characteristic at different frequencies of the voltage applied to the probe: (+) 3 MHz, (○) 5 MHz, and (×) 7 MHz.

$\frac{j_i}{e}\sqrt{\frac{M}{kT_e}}$, where j_i is the density of the ion saturation current.

To measure the dynamic *I–V* probe characteristic, we used the measuring circuit shown in Fig. 4. The resistance R = 100–200 Ω was chosen such that the probe current corresponded to the regime of the ion saturation current. From G6-37 generator (*5*), the voltage signal with an amplitude of 5 V and a frequency of 2–7 MHz was applied to the probe through isolating transformer (*6*). The high-frequency component of the probe current was measured with the help of current transformer (*7*) and C8-14 oscilloscope (*8*). The additional current related to the parasitic capacitance of the probe circuit was compensated with the help of a reverse-current loop with a variable capacitance C_0 in the current transformer.

Figure 5 shows the measured dependence of the high-frequency component of the current density at the probe on the frequency of the voltage applied to the probe. This dependence is linear up to frequencies of 5–6 MHz. At higher frequencies, the slope of the curve decreases with increasing frequency; this is explained by the fact that, according to Eq. (20), the factor C (see Eq. (16)) approaches unity. Figure 6 shows the electron density determined by using the conventional method and from the dynamic *I–V* probe characteristic.

In the frequency range under consideration, the conditions for the 3/2 law were satisfied in the sheath and the electron density was calculated by formulas (20) and (22).

The values of the electron density determined from the dynamic *I–V* probe characteristic agree well with those obtained by the conventional method under the same discharge conditions.

ACKNOWLEDGMENTS

This study was supported in part by the U.S. Civilian Research and Development Foundation for the Independent States of the Former Soviet Union (CRDF), the RF Ministry of Education, and the Government of the Karelia Republic (project no. PZ-013-02).

REFERENCES

1. D. Bohm, in *The Characteristics of Electrical Discharges in Magnetic Fields*, Ed. by A. Guthrie and R. K. Wakerling (McGraw-Hill, New York, 1949).
2. F. G. Baksht and V. G. Yur'ev, Zh. Tekh. Fiz. **49**, 905 (1979) [Sov. Phys. Tech. Phys. **24**, 535 (1979)].
3. H. W. Friedman and E. Levi, Phys. Fluids **13**, 1049 (1970).
4. V. I. Sysun, Fiz. Plazmy **4**, 931 (1978) [Sov. J. Plasma Phys. **4**, 520 (1978)].
5. O. V. Oleshchuk, V. I. Sysun, and Yu. D. Khromoĭ, Élektron. Tekh., Ser. 4 Élektrovakuumnye Gazorazryadnye Pribory, No. 1, 92 (1977).
6. K. F. Sander, J. Plasma Phys. **3**, 353 (1969).

Translated by E.L. Satunina

Plasma Physics Reports, Vol. 30, No. 9, 2004, pp. 766–771. Translated from Fizika Plazmy, Vol. 30, No. 9, 2004, pp. 821–827.

DUSTY PLASMA

Charging of a Rodlike Grain in a Plasma Flow

S. A. Maiorov

Prokhorov Institute of General Physics, Russian Academy of Sciences, ul. Vavilova 38, Moscow, 119991 Russia

Received October 1, 2003; in final form, January 29, 2004

Abstract—The charging of a chain of spherical dust grains in a two-temperature plasma flow is analyzed numerically by the particle method. The cases of dielectric and metal grains are considered. © *2004 MAIK "Nauka/Interperiodica".*

1. INTRODUCTION

In recent years, dusty plasma has been an object of extensive experimental and theoretical research (see, e.g., [1, 2]). The present study continues of a series of papers devoted to numerical investigations of the dusty plasma properties [3–12]. So far, attention has been mainly focused on the charging of spherical dust grains and the structure of the space charge cloud surrounding a grain immersed in a one-temperature or two-temperature plasma with zero [3, 7, 11] or nonzero [11, 12] flow velocity, as well as on the Brownian motion and dynamics of dust grains in a plasma flow [6, 8]. In the present paper, the charging of rodlike grains is studied numerically for the first time using the particle method. At present, such grains are extensively studied experimentally, whereas theoretical studies of their properties are rather scanty (see recent papers [13, 14]; some results of the present paper were also published in [15]).

When a supersonic ion flow passes around a negatively charged spherical grain (such a situation can occur when a grain levitates in an electrode plasma sheath), a region with an enhanced ion density (a so-called ion focus) is formed downstream from the grain. The formation, structure, and characteristics of the ion focus were considered in [4]. The grains in the electrode sheath can form ordered structures, and ion focusing can substantially affect the interaction of grains. In this case, the grain interaction cannot be adequately described using potential interaction models (the screened Debye–Huckel potential is most commonly used for this purpose). An example is the influence of ion focusing on the charging of a grain located in the wake generated by another grain [10]. Calculations show that ion focusing produced by the upstream grain can substantially reduce the negative charge of the downstream grain because of the increase in the ion current density. This raises the question as to how ion focusing influences the charging of rodlike grains.

In the present paper, the formation of a space charge around a rodlike grain in a plasma flow is studied. In this case, ion focusing substantially influences the space charge distribution around the grain and, accordingly, the density of the current of charged plasma particles onto the different parts of the rodlike grain varies. The charging of a chain of micron-size grains that are in contact with one another and are immersed in a plasma flow is investigated numerically using the particle method. Such a chain of grains simulates a rodlike grain. The cases of conducting (metal) and nonconducting (dielectric) grains are considered.

2. ION FOCUSING IN THE BINARY BALLISTIC APPROXIMATION

Let us consider an analytic model of ion focusing by analogy to [3], where the binary radial correlation functions were derived in the approximation of binary Coulomb interaction of mobile particles with a fixed point charge.

Let a fixed point charge (a massive grain) with a negative charge $-Ze$ be located at the coordinate origin. The charge is immersed in a flow of ions with a mass m and positive charge e. The ion flow arrives from infinity, where it has a uniform density N_0 and velocity $V_\infty > 0$. Let the x axis be directed along the initial ion velocity. In the approximation of binary Coulomb interaction, an ion moves in a collision plane along the trajectory described by the equation [16]

$$r = p/(1 + \varepsilon\cos\varphi), \quad p = \rho_\infty^2/\rho_\perp,$$
$$\varepsilon = (1 + \rho_\infty^2/\rho_\perp^2)^{1/2}, \quad \rho_\perp = e^2Z/mV_\infty^2, \tag{1}$$

where r is the current distance from the fixed point charge, φ is the angle between the radius vectors of an ion and the point of its closest approach to the coordinate origin, ρ_∞ is the impact parameter, and ε is the eccentricity of a collision. It follows from expressions (1) that an ion arriving from infinity along the x axis with the velocity V_∞ and the impact parameter ρ_∞ intersects the x axis at the point $x_0(\rho_\infty) = \rho_\infty^2/2\rho_\perp$. The number of ions intersecting the x axis within the interval $0 < x_0 < x < x_0 + \Delta x$ per unit time is $\Delta j = 2\pi N_i V_\infty \rho_\perp \Delta x$; i.e., the flow density $J_x = 2\pi N_i V_\infty \rho_\perp$ per unit length does not depend on x.

1063-780X/04/3009-0766$26.00

In accordance with conservation of momentum, the ion velocity component orthogonal to the x axis at the point of intersection with the x axis is equal to $V_\rho(x_0) = V_\infty\rho_\infty/x_0 = V_\infty(2\rho_\perp/x_0)^{1/2}$. Hence, the ion density near the x axis is equal to

$$N(x, \rho) = N_0(2\rho_\perp x)^{1/2}/\rho. \quad (2)$$

From this expression, which was derived for a flow of noninteracting ions with collinear velocities at infinity, it follows that the ion density is infinite at the x axis ($\rho = 0$). The interaction between plasma particles and the thermal dispersion in their velocities result in a finite-width ion density peak at the x axis. Let us estimate the maximum ion density at the axis, taking into account the spread caused by the finite thermal ion velocity $V_T = (T/m)^{1/2}$.

We assume that the ion thermal velocity is much lower than the ion flow velocity. This condition is usually satisfied even for a subsonic flow, because the ion temperature is low in comparison to the electron temperature. We can then average the ion density over the region with a radius determined by the ion thermal velocity, $\rho_0 = xV_T/V_\infty$.

The number of ions that fall into a thin cylinder around the x axis in the interval $0 < x_0 < x < x_0 + \Delta x$ over a time τ is equal to $\Delta N = \tau\Delta x J_x$. Every ion will remain inside this cylinder for a time $\Delta t = 2\rho_0/V_\rho$. The cylinder volume is equal to $\Delta V = \pi\rho_0^2\Delta x$; hence, the average density in the cylinder is $\langle N\rangle = \Delta N\Delta t/\Delta V\tau$. Thus, for the ion density near the x axis, we obtain the following estimate:

$$N_0(x) = N_0(8\rho_\perp/x)^{1/2}V_\infty/V_T. \quad (3)$$

In its applicability range, $\rho_\perp \le x \le r_{De}$, this estimate satisfactorily agrees with the results of calculations of the ion focusing by one or two grains [4, 10].

We note that electron screening only slightly influences the peak density of the focused ions; hence, the parameters of ion focusing depend weakly on the Debye length $r_{De} = (T_e/4\pi N_e)^{1/2}$. A characteristic quantity that determines the parameters of ion focusing is the impact parameter $\rho_\perp = e^2Z/mV_\infty^2$, at which an ion passing near the grain is deflected through the right angle. The electron Debye length determines the width of the ion density peak rather than the parameters of ion focusing; i.e., in fact, it determines the upper applicability limit for formula (3).

Under conditions typical of dusty plasmas, in which $T_i \ll T_e$ and $V_T \ll V_\infty$, ion screening also plays a minor role in the formation of the ion focus. However, the ion Debye length $r_{Di} = (T_i/4\pi N_i)^{1/2}$, along with the particle size, determines the lower applicability limit for formula (3). The contribution from ions to the charge screening is comparable to the contribution from electrons, because the characteristic kinetic energy of the directed ion flow is on the order of the electron temperature; hence, the effective radius of ion screening nearly coincides with the electron Debye length [4, 8].

3. FORMULATION OF THE PROBLEM FOR NUMERICAL SIMULATIONS

The method for studying the properties of a dusty plasma by numerically integrating the dynamic equations for many particles is described in detail in [4, 5, 7, 12]. This method is here adapted to solve the problem of the interaction of a plasma with a rodlike grain. The simplest method (from the standpoint of its implementation) is to represent a grain as a chain of spherical particles. Assuming the charge of each spherical particle to be uniformly distributed over the particle surface, we reduce the problem to a usual scheme of solving the set of equations of molecular dynamics. The inaccuracy of this model leads to the loss of information about the charge density distribution over a length nearly equal to the grain radius. Because of the charge averaging over the particle surface, the ion and electron trajectories near the surface cannot be determined exactly. In addition, the effect related to a geometrical factor arising when an elongated cylindrical (rodlike) grain is replaced with a chain of spherical grains also can be of importance. When calculating the parameters of charging, it seems reasonable to choose the sizes of spheres such that the cylinder volume would coincide with the total volume of the spheres. However, at this stage of our study, we are interested in a qualitative character of the charge distribution over a rodlike dust grain, rather than in the exact determination of the charging parameters of such a grain in plasma. Therefore, this model seems to be quite applicable to our problem.

We consider a system of Coulomb particles consisting of mobile point particles (ions and electrons) and immobile spheres. The ions have a mass M and positive charge e. The electrons have a mass m and a negative charge $-e$. We consider the case where the positions of all spheres are fixed, the spheres have the same radius R, and all the electrons and ions touching their surfaces are absorbed. Accordingly, the charge of a sphere is determined by the number of the absorbed electrons and ions and depends on time. The case of a Brownian motion of mobile spheres with variable masses and charges is considered in [5, 9].

We consider the time evolution of a system that initially consists of $2n$ particles inside the computational box $0 < x < Lx, 0 < y < Ly$, and $0 < z < Lz$. The trajectories of n positively and n negatively charged particles are found by numerically integrating the Newton equations

$$d^2r_k/dt^2 = F_k/m_k, \quad F_k = \sum_{l\neq k}^{2n+n_g} f_{kl}, \quad k = 1, 2, \ldots, 2n, \quad (4)$$

where $r_k(t)$ is the radius vector of the kth particle, which has the mass m_k and charge q_k, and n_g is the number of spherical grains. The Coulomb interaction force f_{kl} between mobile particles at distances shorter than a certain distance r_0 was modified according to the interaction of uniformly charged, interpenetrating spheres of diameter r_0. This diameter was chosen to be much shorter than the average distance between the particles, so that its influence on the characteristics of the system could be ignored. This was usually verified by comparing the results of calculations with different values of r_0. When calculating the Coulomb interaction forces f_{kl} between mobile particles and spherical grains, the charge of a spherical grain was assumed to be uniformly distributed over its surface.

The initial spatial distributions of the electrons and ions were equiprobable within the volume of the computational box. The energy distributions corresponded to a Maxwell–Boltzmann distribution at infinity. Depending on the initial distance to the nearest spherical grain, the Maxwellian distribution over energies was shifted by the value equal to the interaction energy with the spherical grain. The velocity distribution was taken to be isotropic with a fixed additive corresponding to the directed motion with the plasma flow velocity. Thus, the initial distribution without bound particles (ions) was formed. When calculating the flow parameters, no consideration was given to a rather long initial time interval within which the flow relaxed to a steady gas-dynamic state and the charges of grains reached their averaged steady-state values.

The number of ions in the system was fixed, whereas the number of electrons was variable. An algorithm of injecting fresh particles (in place of absorbed ones) was used that provided the conservation of the electric neutrality of the system as a whole. In place of an absorbed particle, fresh particles from a randomly chosen point at the surface of the computational box were injected into the system so as to provide the neutrality of the entire system, including the grain charge.

When an electron was absorbed by a spherical grain, the number of electrons in the system decreased by one, whereas the absorption of an ion was accompanied by the injection an ion–electron pair from a random point at the surface of the computational box. The point at the surface was chosen such that the distribution function of the injected particles corresponded to a Maxwellian distribution shifted by the plasma flow velocity. In this way, the number of ions in the system was maintained constant, whereas the number of electrons was variable, thus providing the neutrality of the system.

The boundary conditions for the simulation of the ion flow were somewhat different from those previously used in [5, 7, 11], where the absorption and emission conditions were set at the right and left boundaries of the computational box. In this study, after an ion reached the wall, it was injected into the system from a random point at the surface of the computational box. The point at the surface was chosen such that the distribution function of the injected ions corresponded to a Maxwellian distribution shifted by the plasma flow velocity. In the absence of absorbing spherical grains, this procedure results in a uniform plasma flow. For electrons reflecting from the wall, thermostatic boundary conditions were used. In this way, a Maxwell–Boltzmann distribution was maintained for electrons, so that and there always were electrons in the system that had a kinetic energy sufficient to overcome the potential barrier near a negatively charged grain.

Such a formulation of the problem allows self-consistent calculations of the charging process and the fluctuations of the grain charge. In addition, such boundary conditions make it possible to more correctly (in comparison to the previous studies) simulate the plasma flow around the grain at low plasma flow velocities, even at velocities that are comparable to or lower than the ion thermal velocity.

Note that the number of ions in the system is constant, but the number of electrons can decrease due to their absorption by the spherical grains. In this case, the average electron density in the system can become substantially lower than the ion density. A decrease in the electron density can be estimated from the ratio of the grain charge to the number of ions in the system. A system in which the electron density is much lower than the ion density corresponds to dust clouds and crystals; in the electrode region, the electron density is also reduced.

4. RESULTS OF NUMERICAL SIMULATIONS

Here, we present the results of numerical simulations of a two-temperature argon plasma flow with $Z = 1$, an ion temperature of $T_i = 0.025$ eV, electron temperature of $T_e = 1$ eV, and ion density of $N_i = 2 \times 10^{12}$ cm^{-3}. The plasma flow velocity corresponds to an ion kinetic energy of $K_i = 1$ eV. For the given ion density, the Debye radius is 3.6 μm and the number of particles within the Debye sphere is equal to 876. This plasma is ideal both for ions and electrons.

The computational box, which was a parallelogram $20 \times 10 \times 10$ μm size, contained 4000 ions. Inside the box, there were six spherical grains that were in contact with one another and arranged along the x axis at the points with the coordinates $x = 5$, 6, 7, 8, 9, and 10 μm and $y = z = 5$ μm. There radius was $R = 0.5$ μm. The charging characteristics were calculated over a time interval of 26 ns. The ion Langmuir period was equal to 21 ns. The initial relaxation interval, which was typically equal to a few ion Langmuir periods, was omitted when calculating the average charging characteristics of the chain of grains.

The charging characteristics of nonconducting (dielectric) grains are presented in Fig. 1. The histograms show (a) the magnitude of the average negative charge of a spherical grain; (b) the ion flux to a grain,

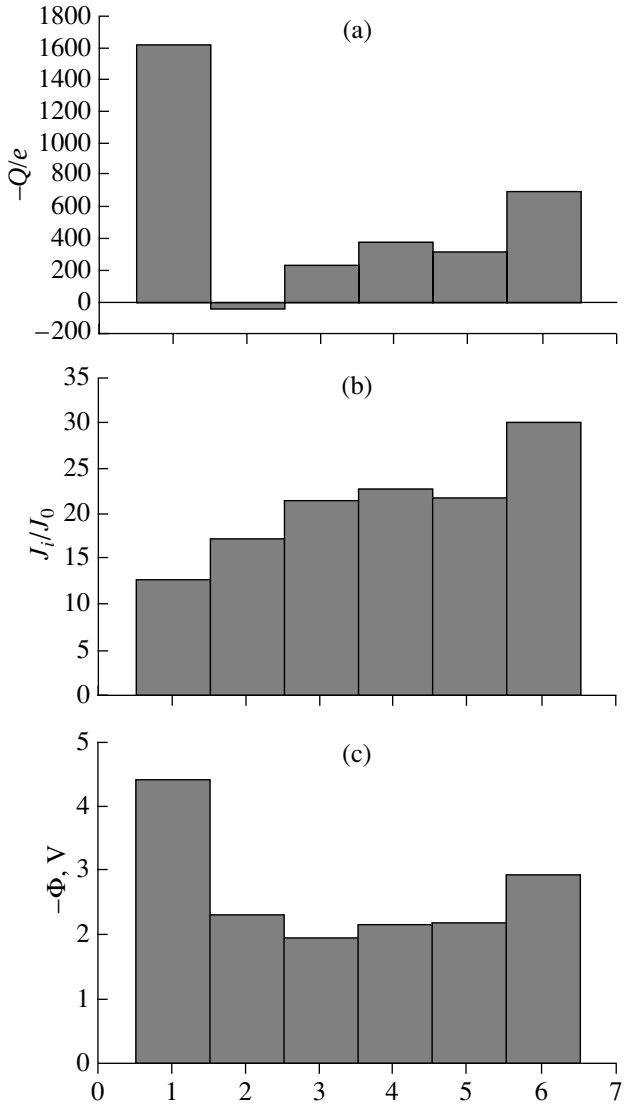

Fig. 1. Charging characteristics of nonconducting spherical grains: (a) the magnitude of the average negative charge Q of a grain in units of the electron charge; (b) the ion flux to a grain J_i, normalized to the flux of the unperturbed plasma flow $J_0 = \pi R^2 N_i (2K_i/M)^{1/2}$; and (c) the average surface potential Φ of a grain.

normalized to $J_0 = \pi R^2 N_i (2K_i/M)^{1/2}$, which is the gas-dynamic flux of cold ions moving in the same direction and having the same kinetic energy K as the unperturbed plasma flow; and (c) the average surface potential of a grain, which is determined by all the plasma particles and by the surface charge of all the spherical grains. When calculating the surface potential of a spherical grain, we assumed that the charge was uniformly distributed over the grain surface and the average potential produced by one spherical grain on the surface of another grain is nearly equal to the potential produced by the former spherical grain at the center of the latter spherical grain. The error introduced by these assumptions in the value of the average grain potential is insignificant.

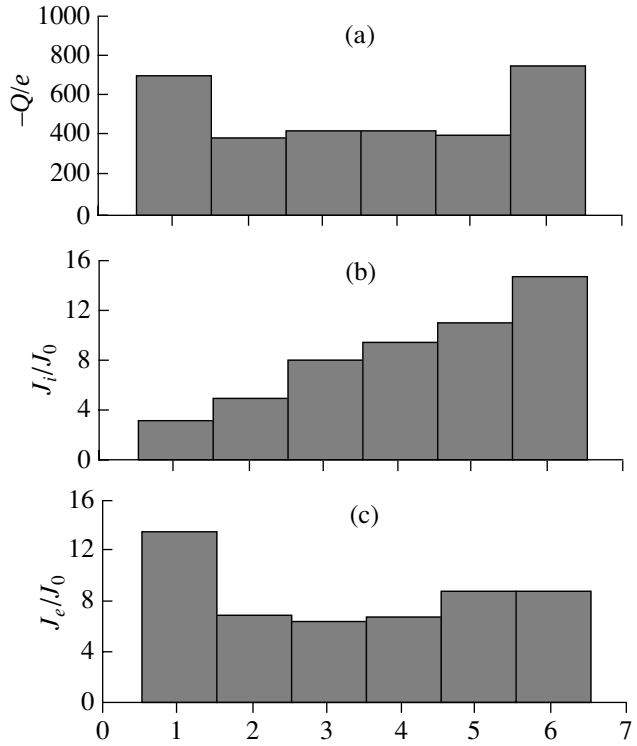

Fig. 2. Charging characteristics of conducting spherical grains: (a) the magnitude of the average negative charge of a grain Q in units of the electron charge and the (b) ion (J_i) and (c) electron (J_e) fluxes to a grain, normalized to the flux of the unperturbed plasma flow J_0.

Histograms for the case of conducting (metal) grains are presented in Fig. 2. The histograms show (a) the magnitude of the average negative charge of a spherical grain and the values of the (b) ion and (c) electron fluxes to a grain, which are normalized to the flux of the unperturbed plasma flow J_0. In contrast to dielectric grains, the metal grains have the same surface potential because they are in contact with one another; however, the ion and electron fluxes are different for different grains.

Charging parameters of a chain of spherical grains made of different materials: the average total charge in units of the electron charge, the ion flow normalized to the flux of the unperturbed plasma flow $J_0 = \pi R^2 N_i (2K_i/M)^{1/2}$, and the average surface potential φS normalized to the electron temperature. For comparison, the charging characteristics of an isolated grain are also presented

	$-Q/e$	J/J_0	$-e\varphi_S/T_e$
Dielectric	3157	125	3.08
Metal	3087	51	2.61
Isolated grain	1214	9	3.02

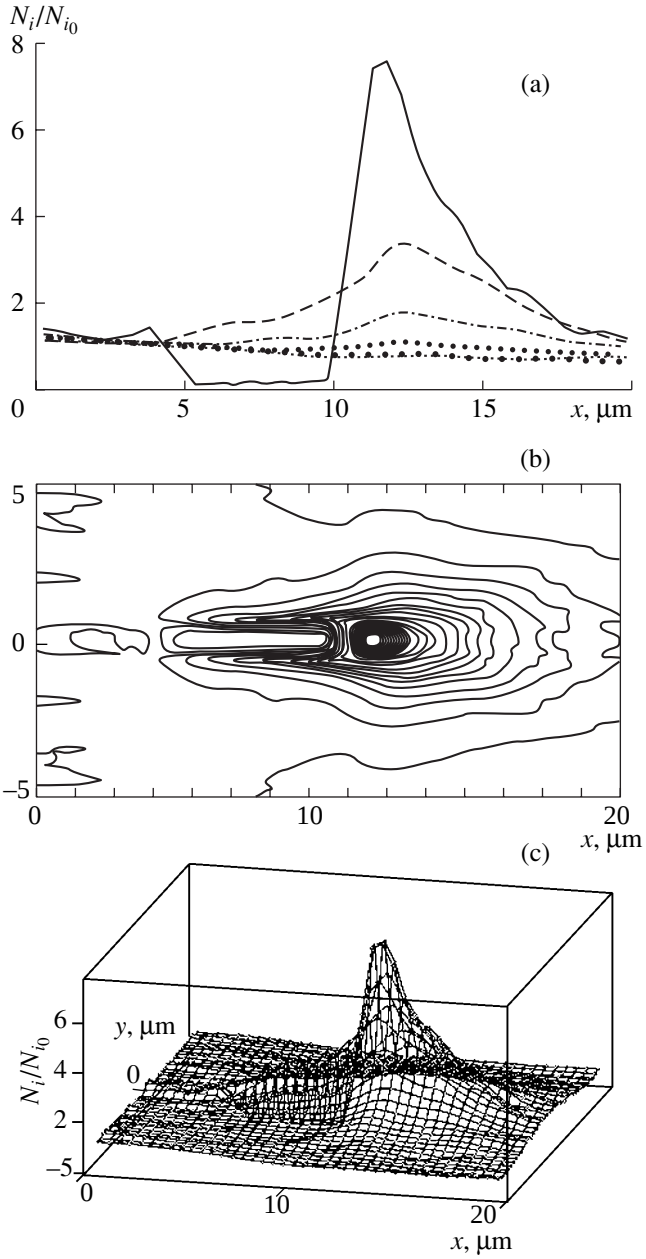

Fig. 3. Distribution of the ion density in the *xy* plane that passes through the chain of spherical dielectric grains: (a) the profiles of the ion density along the *x* axis at $y = 0.1$, 1, 2, 3, 4, and 5 μm; (b) the contour lines of the ion density in the *xy* plane; and (c) the relief of the ion density in the *xy* plane.

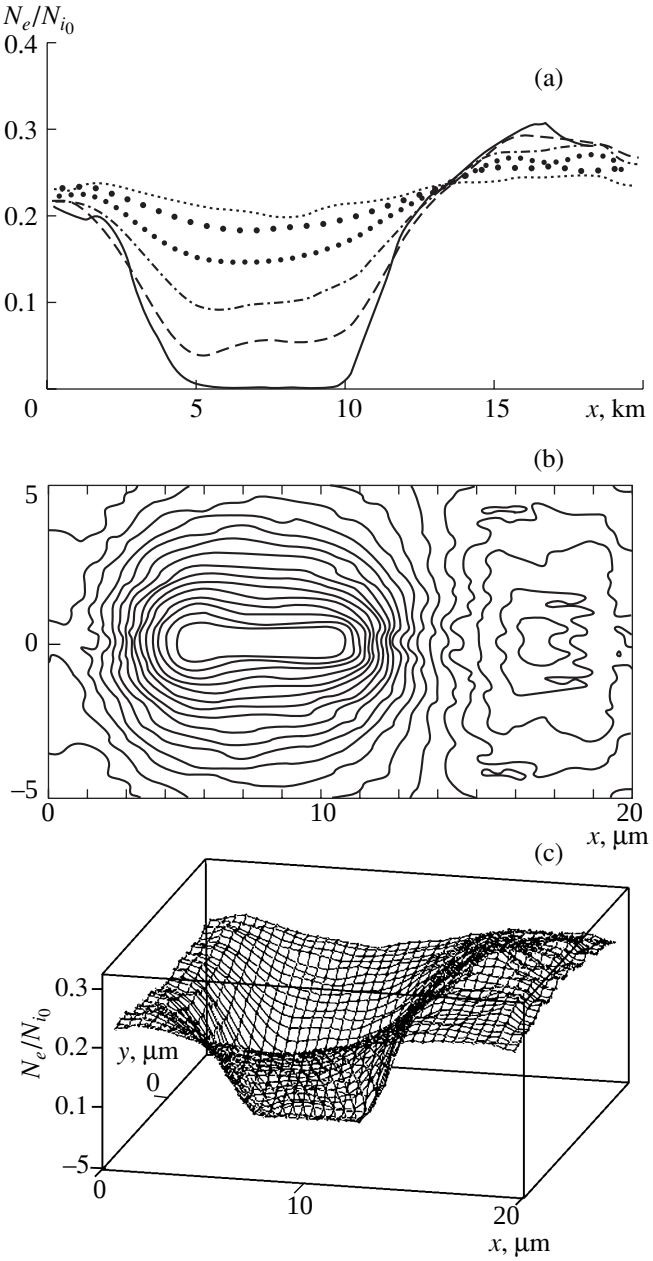

Fig. 4. The same as in Fig. 3, but for the electron density.

The table summarizes the integral characteristics of rodlike grains made of different materials: the time-averaged total charge of the chain of grains, the time-averaged total ion flux to the grains, and the time-averaged surface potential of the chain. The surface potential averaged over six grains is taken as the surface potential of a dielectric rodlike grain. For comparison, the charging characteristics of an isolated spherical grain of the same size under similar conditions are also presented.

The results of calculations of the ion and electron densities around dielectric grains are presented in Figs. 3 and 4. The densities are normalized to the average ion density $N_{i0} = 2 \times 10^{12}$ cm^{-3}. Figure 3 illustrates the ion density distribution in the *xy* plane that passes through the chain of grains. Figure 3a shows the profiles of the ion density along the *x* axis at $y = 0.1$, 1, 2, 3, 4, and 5 μm; Fig. 3b shows the contour lines of the ion density in the *xy* plane; and Fig. 3c shows the relief of the ion density in the *xy* plane.

Similar plots for the electron density are presented in Fig. 4.

5. DISCUSSION AND CONCLUSIONS

The results of calculations have demonstrated two new interesting effects: the influence of ion focusing on the character of charging of rodlike grains and the dependence of the charging process on the conductivity of the grain surface. Strictly speaking, for the surface to be equipotential, it is not necessary that the grain be highly conducting (metal). A finite (even rather low) conductivity can be quite sufficient to ensure the equipotentiality of the grain surface. Since the grain surface is subject to the action of a plasma, this circumstance should be taken into consideration in interpreting the experimental results.

The total grain charge for metal and dielectric grains differs only slightly (it is higher by 2% for dielectric grains); however, the character of the charge-density distribution over the grain changes radically. Nearly one-half of the charge of a dielectric grain is concentrated at its forward end; downstream from this region, the charge density substantially decreases in magnitude and can even change its sign. This is explained by the fact that the ion flow is focused onto this part of the grain and the electron flow is reduced there because of the geometrical factor. As a result, a dielectric grain possesses a considerable dipole moment, which can substantially influence its stability and can lead to the onset of oscillations [14].

Another interesting feature is that the plasma flux onto a dielectric grain is higher than that onto a metal grain by a factor of about 2.5 at approximately the same total grain charge (see table), because the accumulation of charge at the forward end of a dielectric grain results in a stronger ion focusing onto its tail.

Simulations by the model developed in this paper are the first numerical experiment on studying the electric characteristics of rodlike dust grains in the ion flow of an electrode sheath. In spite of the simplifying assumptions adopted here, the simulation results make it possible to clarify the character of charging of rodlike grains, to examine their properties, to analyze the kinetic processes resulting in the formation of dusty structures in plasma, and to verify theoretical models. These results are important for describing the processes that can occur under experimental conditions, including the analysis of the stability of levitating grains.

ACKNOWLEDGMENTS

I am grateful to S.V. Vladimirov and A.A. Samarian for fruitful discussions. This work was supported in part by the Australian Research Council (ARC) and the Russian Foundation for Basic Research, project no. 02-02-16439.

REFERENCES

1. V. N. Tsytovich, Usp. Fiz. Nauk **167**, 57 (1997) [Phys. Usp. **40**, 53 (1997)].
2. M. Lampe, G. Jouce, G. Ganduli, and V. Gavrishchaka, Phys. Plasmas **7**, 3851 (2000).
3. S. A. Maiorov, Fiz. Plazmy **26**, 669 (2000) [Plasma Phys. Rep. **26**, 628 (2000)].
4. S. A. Maiorov, S. V. Vladimirov, and N. F. Cramer, Phys. Rev. E **63**, 017401 (2001).
5. A. M. Ignatov, S. A. Maiorov, S. A. Triger, and P. P. J. Schram, Kratk. Soobshch. Fiz., No. 7, 7 (2000).
6. S. V. Vladimirov, N. Kramer, and S. A. Maiorov, Kratk. Soobshch. Fiz., No. 9, 33 (2001); Phys. Rev. E **63**, 045401 (2001).
7. S. A. Maiorov, Teplofiz. Vys. Temp., No. 6, 794 (2001).
8. S. A. Maiorov, Kratk. Soobshch. Fiz., No. 11, 3 (2002).
9. A. M. Ignatov, S. A. Trigger, S. A. Maiorov, and W. Ebeling, Phys. Rev. E **65**, 046 413 (2002).
10. S. V. Vladimirov, S. A. Maiorov, and N. F. Cramer, Phys. Rev. E **67**, 016407 (2003).
11. S. V. Vladimirov and S. A. Maiorov, Kratk. Soobshch. Fiz., No. 2, 30 (2002).
12. S. A. Maiorov, S. V. Vladimirov, and N. F. Kramer, Fiz. Plazmy **28**, 1025 (2002) [Plasma Phys. Rep. **28**, 946 (2002)].
13. A. V. Ivlev, A. G. Khrapak, S. A. Khrapak, *et al.*, Phys. Rev. E **68**, 026403 (2003).
14. M. P. Hertzberg, S. V. Vladimirov, and N. F. Cramer, Phys. Rev. E **68**, 026402 (2003).
15. S. A. Maiorov, Kratk. Soobshch. Fiz., No. 2, 31 (2003).
16. L. D. Landau and E. M. Lifshitz, *Mechanics* (Nauka, Moscow, 1982; Pergamon Press, New York, 1988).

Translated by N.F. Larionova

Plasma Physics Reports, Vol. 30, No. 9, 2004, pp. 772–778. Translated from Fizika Plazmy, Vol. 30, No. 9, 2004, pp. 828–834.

PLASMA ELECTRONICS

A High-Power Vircator Operating as an X-ray Bremsstrahlung Generator

V. D. Selemir, A. E. Dubinov, E. A. Ryaslov, V. I. Kargin, I. A. Efimova, and M. V. Loyko

All-Russia Research Institute of Experimental Physics, Russian Federal Nuclear Center, pr. Mira 37, Sarov, Nizhni Novgorod oblast, 607190 Russia

Received June 23, 2003; in final form, September 4, 2003

Abstract—A vircator capable of generating high-power X-ray pulses due to the multiple transitions of electrons through a thin anode foil transparent to X radiation has been created and put into operation for the first time. The vircator is created on the basis of a direct-action electron accelerator supplied from an inductive energy storage operating with a plasma opening switch. Self-consistent two-dimensional simulations of the electron beam dynamics in the vircator chamber are performed, and the spectra of the generated microwave radiation are determined. Self-consistent one-dimensional simulations of the beam dynamics with allowance for electron scattering in the foil were also carried out, and the X-ray bremsstrahlung spectra were measured. Results are presented from the first experiments on the generation of X-ray bremsstrahlung in vircators with thin (10 μm) and thick (100 μm) tantalum anode foils. For a thin foil, the X-ray ($E_\gamma > 30$ keV) dose is eight times as high as that for a thick foil and the average photon energy is 30 keV (against 80 keV for a thick foil).

1. INTRODUCTION

In radiation studies, it is sometimes necessary to use intense X-ray pulses with photon energies of $E_\gamma = 20$–60 keV. *Z*-pinches, in which the kinetic energy of the imploding plasma is converted into thermal energy, make it possible to produce radiation fluxes with photon energies of $E_\gamma < 5$ keV [1]. On the other hand, the use of electron beams with electron energies of $E_e = 100$–200 keV is limited by the low beam currents and the small cross section for radiative losses. The problem of increasing the intensity of X radiation can be solved only by increasing the accelerating voltage. However, for beams of electrons with energies of $E_e = 1$–10 MeV, the high efficiency of energy conversion into bremsstrahlung can only be achieved with sufficiently thick targets (0.1–1 mm Ta). Most of the photons from such targets have energies above 200 keV, whereas photons with lower energies are absorbed in the target. One way of increasing the fraction of soft photons is to use schemes with the multiple transitions of electrons through a thin target that is transparent to X radiation (in reflex triodes and vircators, the anode foil can serve as such a target [2]). In this case, the maximum intensity of the generated bremsstrahlung lies in the X-ray range with photon energies lower than those in bremsstrahlung generators with thick targets.

In reflex triodes and vircators, the electron flow oscillates in the potential well formed by the cathode, the anode foil, and the virtual cathode, while X radiation is generated due to the multiple transitions of electrons through a thin (10–30 μm) foil of a high-*Z* material (e.g., Ta). The possibility of generating high-power X-ray pulses with the help of a reflex triode was successfully demonstrated in [3]. The results of calculations of a reflex triode in the YUPITER device with a stored energy of 30 MJ are presented in [4], where it is asserted that this device with an electron beam current of 60 MA and electron energy of 5 MeV is capable of generating radiation pulses with an energy of up to 160 kJ in the photon energy range of 20–60 keV.

Note that, in [3, 4], only reflex triodes were considered, in which the high voltage is known to be applied to the anode foil, whereas the cathode and the reflecting electrode (the collector behind the anode) are grounded. However, the presence of the reflecting electrode can hamper the use of the generated X-ray emission in radiation studies.

In the present paper, a vircator is used for the first time in experiments on X-ray generation. The advantages of vircators over reflex triodes for generating X-ray pulses were pointed in [2, 5]: the vircator design is simpler, the high voltage is applied to the cathode, and the anode foil and collector are grounded. Therefore, in vircators in which the longitudinal magnetic field is uniform near the anode foil and decreases near the collector, there is no problem with utilizing X radiation.

The paper presents the results of one- and two-dimensional self-consistent calculations of the electron beam dynamics in a vircator, as well as the results of the first experiments on studying X-ray bremsstrahlung in vircators with thin and thick anode foils.

1063-780X/04/3009-0772$26.00 © 2004 MAIK "Nauka/Interperiodica"

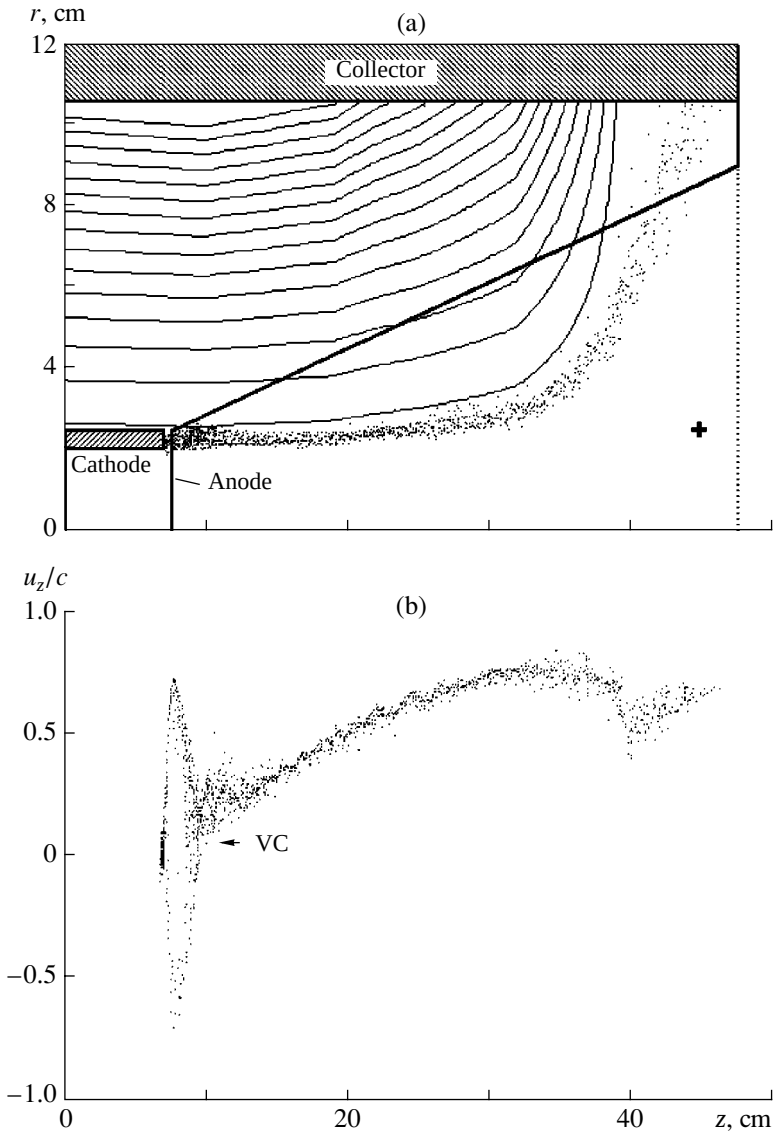

Fig. 1. Results of simulations of the dynamics of an electron beam in a vircator: (a) the instantaneous configuration of the beam (the figure also shows the magnetic field lines; the cross indicates the location of a "detector"—the place where the microwave field was calculated) and (b) the phase portrait of the beam (VC is the virtual cathode).

2. COMPUTER SIMULATIONS OF A VIRCATOR

Before carrying out our experiments, we performed a series of computer simulations:

(i) simulations of the self-consistent two-dimensional dynamics of an electron beam in a nonuniform magnetic field with the aim of determining the region where the electrons reach the collector and searching for the place where X-ray detectors will be best protected from high-energy electrons,

(ii) simulations of the self-consistent two-dimensional dynamics of the formation of a virtual cathode with the aim of calculating the limiting current and the spectrum of the generated microwave radiation (in experiments, the presence of high-power microwaves in the proper spectral range would be indicative of the presence of a virtual cathode in the beam), and

(iii) simulations of the self-consistent one-dimensional dynamics of a beam with a virtual cathode with allowance for electron scattering in the anode foil with the aim of calculating X-ray bremsstrahlung spectra.

All simulations were performed by the particle-in-cell (PIC) method. In the first two cases, we used the well-known KARAT relativistic electromagnetic code [6], while in the third case, we used an original relativistic electrostatic code elaborated by us (see [7]).

First, we present the results of simulations with the KARAT code for an optimized geometry of a vircator and operating conditions used in real experiments.

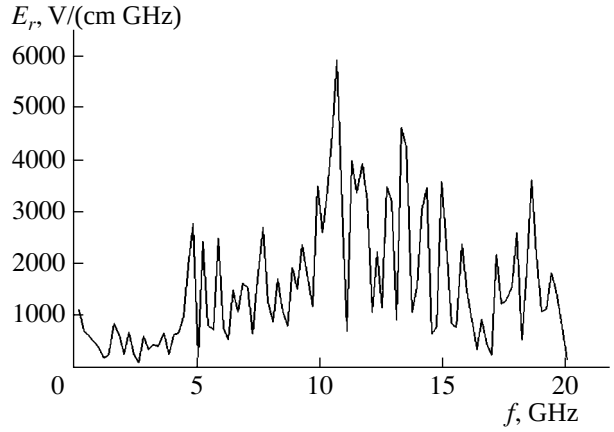

Fig. 2. Calculated spectrum of the radial component of the microwave field at the "detector" location.

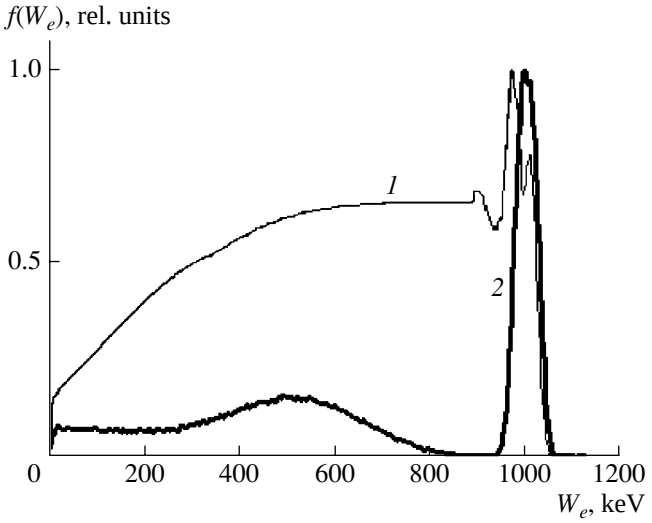

Fig. 3. Normalized spectra of electrons passed through the foil for anode foil thicknesses of (*1*) 10 and (*2*) 100 μm. The spectra are normalized to their peak values.

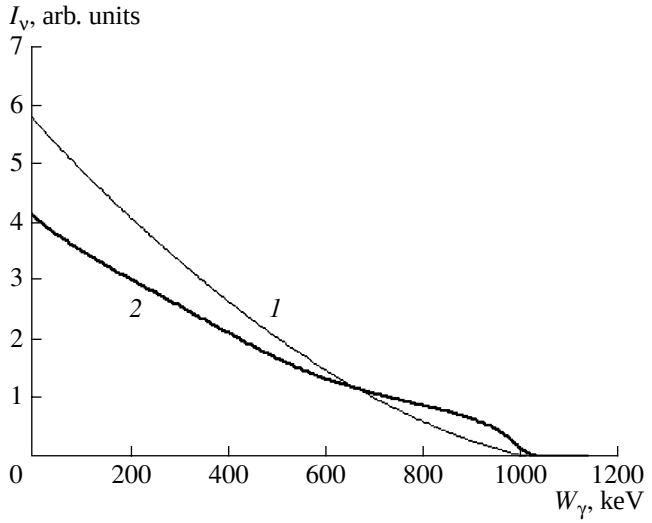

Fig. 4. Normalized X-ray bremsstrahlung spectra for anode foil thicknesses of (*1*) 10 and (*2*) 100 μm. The spectra are normalized to the areas under the curves.

The geometry of the vircator electrode system is shown in Fig. 1a. The electrode system consisted of a hollow cathode, an anode electrode containing a massive collector, a conical holder of the anode (the holder was made of a low-*Z* material transparent for electrons), and a tantalum anode acting as a target. It was assumed that an external magnetic field was applied the vircator, the strength of this field in its uniform part being 4.4 kG. The measured spatial distribution of the magnetic field in the vircator is also shown in Fig. 1a.

The diode voltage was 1 MV, and the beam current was 90 kA. The instantaneous beam configuration is shown in Fig. 1a, from which we determined the region where the electrons reach the collector.

Figure 1b shows an instantaneous phase portrait of the beam. It can be seen from this figure that a virtual cathode is formed in the system; i.e., the beam current exceeds the limiting current.

At the point marked by a cross in Fig. 1a, we calculated the time evolution of the electric field. It was found that intense microwave oscillations were generated at this point in the presence of a virtual cathode. Since the beam electrons near this point move almost along the radius, the oscillations of the radial component of the electric field are most informative. From the Fourier spectrum of the radial electric field shown in Fig. 2, we determined the spectral range of microwave oscillations expected in experiment ($\lambda = 3$ cm).

Let us consider the results of simulations of bremsstrahlung generation with the code elaborated in [7]. In these simulations, the vircator consisted of two cylindrical metal chambers. The first chamber acted as an accelerating diode, while the other acted as a drift space. The diode and drift chambers were separated by a foil. The electron energy loss for ionization in the foil were calculated by the Monte-Carlo method. Hence, we could take into account not only the average energy loss for ionization in the foil, but also fluctuations in this loss. The problem was solved by the PIC method with allowance for relativistic effects. The model particles were identical and shaped as thin washers with given initial inner and outer radii. The simulations were performed for the following vircator parameters: In the diode region, the outer beam diameter was 5 cm, and the beam thickness was 1 cm. The accelerating gap was 0.7 cm long, the drift region of the vircator was 24 cm long, and the outer diameter of the diode and drift chambers was 21 cm. A voltage of 1 MV was applied to the cathode. The injected cathode current was 90 kA. The thickness of the foil anode was 10 μm in the first version and 100 μm in the second version. The anode material was tantalum.

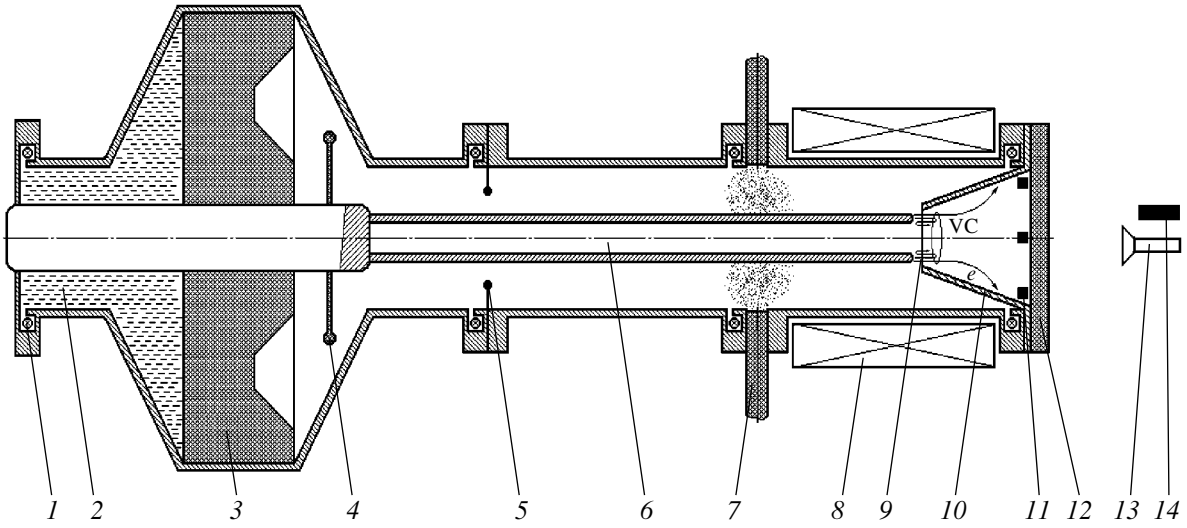

Fig. 5. Schematic of the PIRIT-1 device with a vircator load and the arrangement of the diagnostic equipment: (*1*) Rogowski coil, (*2*) oil-filled section of the inductive storage, (*3*) high-voltage insulator, (*4*) protecting dielectric ring, (*5*) protecting metal ring between the vacuum sections of the inductive storage, (*6*) cathode, (*7*) cable plasma guns of the current opening switch, (*8*) solenoid, (*9*) anode foil, (*10*) conical anode holder, (*11*) thermoluminescent dosimeters, (*12*) microwave output window, (*13*) microwave hot-carrier detector, and (*14*) semiconductor X-ray detectors.

The energy spectra of the particles passing through the anode foil are shown in Fig. 3. It can be seen that, for a 100-μm foil (Fig. 3, curve *2*), the number of low-energy particles is small compared to the case of a 10-μm foil (Fig. 3, curve *1*).

From the data obtained, we calculated X-ray bremsstrahlung spectra by the following formula [8]:

$$I_\nu = k\nu^{2/3}\nu_0^{-2}[(\nu_0-\nu)^{-1/2}-\nu_0^{-1/2}]^{-2/3}, \qquad (1)$$

where I_ν is the spectral intensity, ν_0 is the frequency corresponding to the short-wavelength boundary of spectrum, ν is the bremsstrahlung frequency, and k is a proportionality factor. The calculated spectra are presented in Fig. 4. It can be seen from these spectra that, in the case of a thin foil, X-ray spectrum is indeed displaced to the soft X-ray region.

3. EXPERIMENTAL STUDIES OF THE VIRCATOR

A vircator for generating X-ray pulses was created on the basis of a direct-action accelerator supplied from an inductive energy storage operating with a plasma opening switch [9]. The maximum current of the inductive storage was 130 kA, and the amplitude of the voltage pulse at the instant at which the storage circuit was open was 1.3 MV.

In the last section of the inductive storage, a load was installed. The load was a vircator vacuum diode containing a 50-mm-diameter thin-walled hollow cathode with a wall thickness of 500 μm. In front of the cathode, a conical thin-walled anode holder with a wall thickness of 500 μm was installed. A 10- or 100-μm tantalum foil was mounted at the end of the anode holder. The length of the interelectrode gap in the diode was 9 mm. The solenoid that was mounted around this

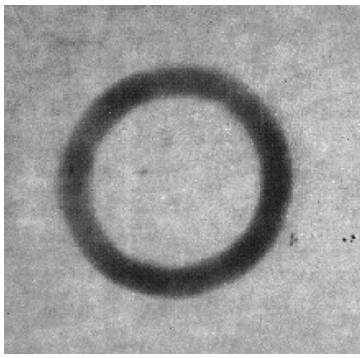

Fig. 6. Pinhole image of the beam.

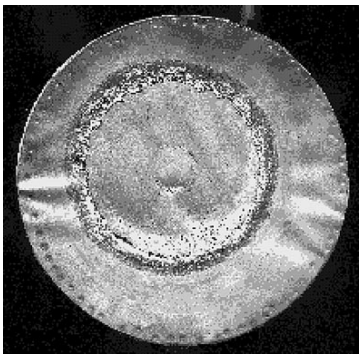

Fig. 7. Beam print on the anode.

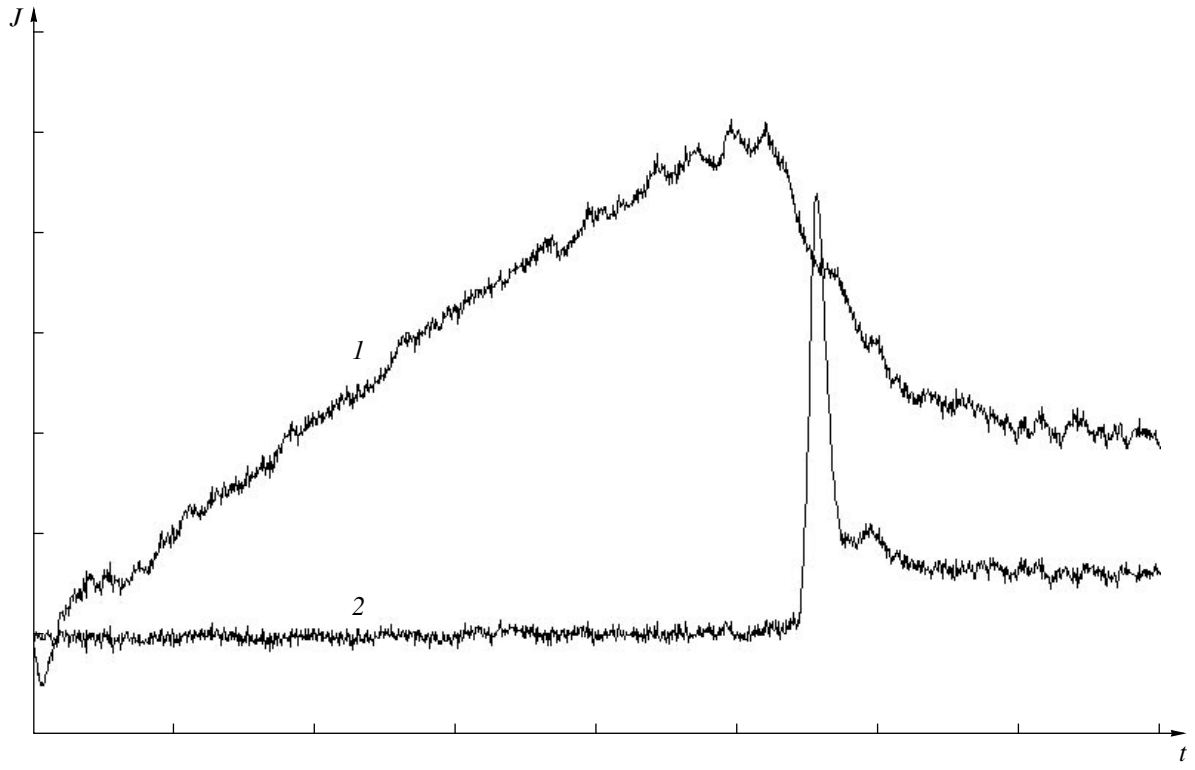

Fig. 8. Waveforms of (*1*) line current and (*2*) load current (20 kA/division) for the case of a 10-μm anode foil. The time scale is 100 ns/division.

section produced an axial magnetic field of 4.4 kG in the diode region.

A schematic of the device with a vircator load is shown in Fig. 5, where the locations of the detectors for measuring various parameters of the system are also indicated.

Currents in different parts of the device were measured with Rogowski coils.

From a pinhole image of the electron beam and its print on the anode foil (see Figs. 6 and 7, respectively), we determined the transverse structure of the beam. The beam cross section was a ring with an outer diameter equal to the cathode diameter. Figures 6 and 7 allow us to determine the shape of the bremsstrahlung source in the anode foil; they also confirm that the results of the above calculations agree well with the experimental results.

The X-ray dose was measured with TLD thermoluminescent dosimeters made of aluminum-phosphate glass containing 87% $MgOP_2O_5$, 13% $Al_2O_{33}P_2O_5$, and 0.1% MnO_2. To measure the duration of X-ray pulses and to estimate their spectrum, we used semiconductor detectors. The detectors were placed at a distance of 700 mm from the anode foil. The emission spectrum was measured by the absorbing foil technique using 2-, 4-, and 7-mm-thick aluminum filters. Microwave pulses were recorded with the help of a hot-carrier microwave detector placed in a 23×10-mm waveguide (see [10]). The microwave detector was located 500 mm from the output window.

Microwave radiation was output from the vacuum chamber of the vircator through a 35-mm-thick dielectric window. The thickness of the window was chosen such that it could not be destroyed by the evaporation products of the anode foil. At this thickness, the intensity of X-rays with photon energies of 30 keV (the lower boundary for TLD dosimeters) was attenuated by a factor of 6. For this reason, the TLDs were placed inside the vacuum chamber at a distance of 70 mm from the anode foil, behind a shield protecting them from high-energy electrons.

Figures 8 and 9 show the current waveforms measured in the experiments with a thin anode foil (10 μm Ta). The line-current amplitude is 100 kA, while the load-current amplitude is 90 kA. From the ratio of charges accumulated on the detectors with different filters, we estimated the absorption coefficient and the average photon energy: $\mu \approx 1$ cm^{-1} and $E_\gamma \approx 50$ keV, respectively. The X-ray dose at the TLDs totaled 200 rad.

The experiments with a thick anode foil (100 μm Ta) were performed using the same procedure as in the case of a thin anode (see Fig. 10). A comparison of the waveforms of the X-ray pulses (Figs. 9 and 10) shows that, in the case of a thick foil, the amplitudes of the signals measured behind the filters of different thickness differ

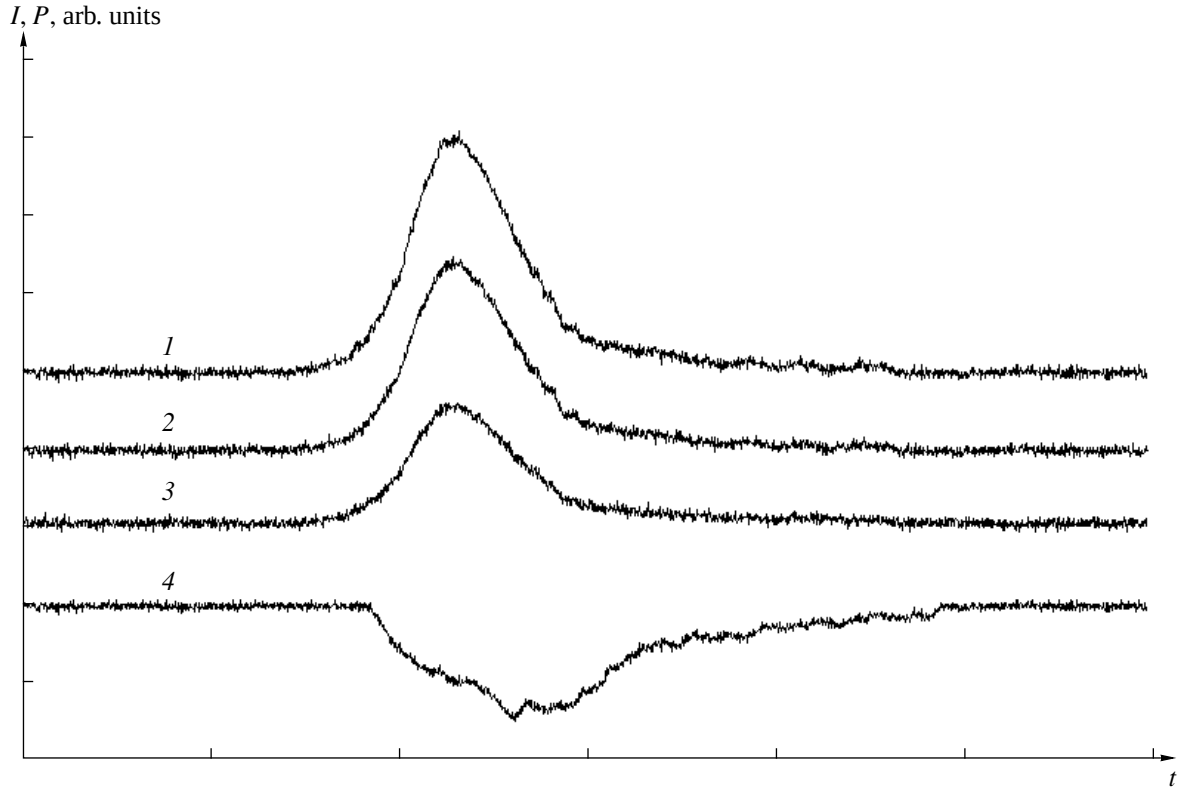

Fig. 9. Waveforms of the X-ray intensity *I* behind Al filters of different thickness: (*1*) 2, (*2*) 4, and (*3*) 7 mm. The anode foil thickness is 10 μm. Curve *4* shows the waveform of the microwave intensity *P* (2 V/division). The time scale is 50 ns/division.

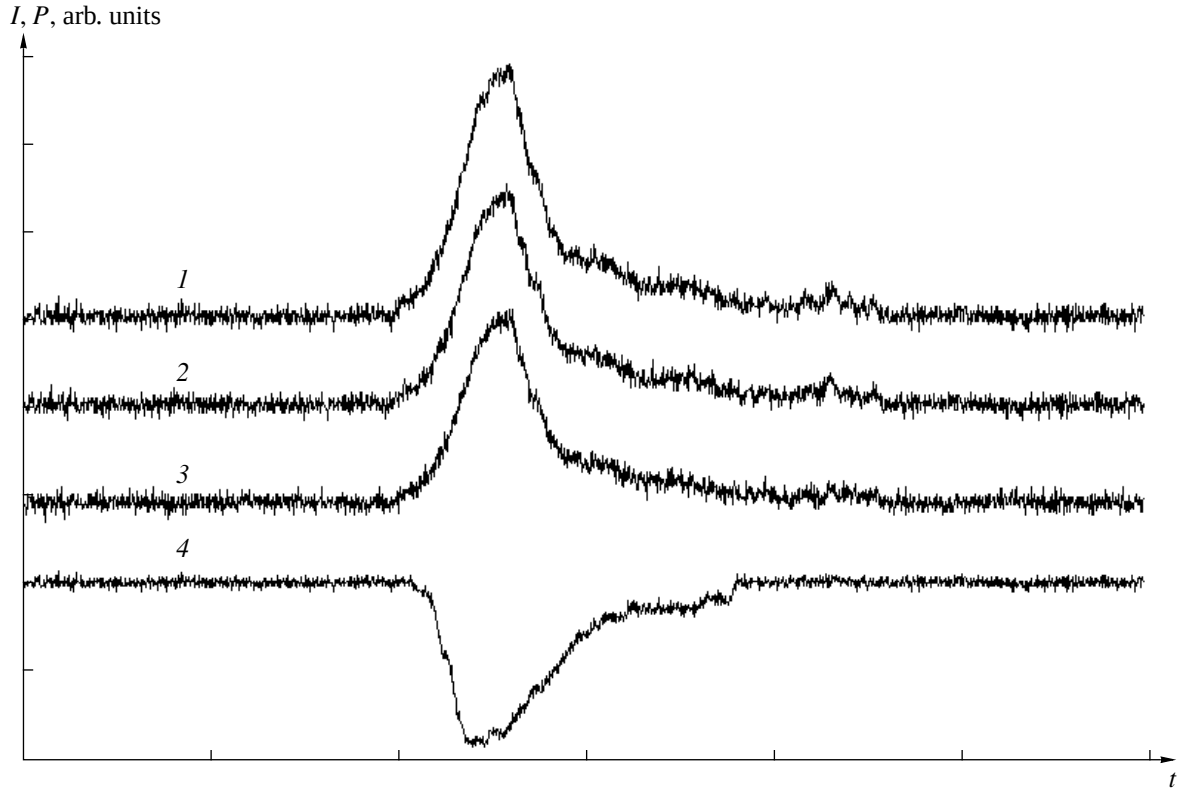

Fig. 10. Waveforms of the X-ray intensity *I* behind Al filters of different thickness: (*1*) 2, (*2*) 4, and (*3*) 7 mm. The anode foil thickness is 100 μm. Curve *4* shows the waveform of the microwave intensity *P* (2 V/division). The time scale is 50 ns/division.

insignificantly. Hence, the emission spectrum contains photons with higher energies as compared to the case of a thin foil. For the thick foil, the absorption coefficient was equal to $\mu \approx 0.54$ cm^{-1} for photon energies of $E_\gamma \approx 80$ keV. The X-ray dose at the TLDs totaled 25 rad.

The signal from the microwave detector confirms the formation of a virtual cathode. The range of 1-MeV electrons in tantalum is ≈ 0.5 mm; hence, a fraction of the beam electrons penetrated into the region behind the anode. However, because of the small number of electron oscillations, the soft X-ray intensity was relatively low. The experiments showed that, for a thin anode, the X-ray dose at energies $E_\gamma > 30$ keV is eight times as high as that for a thick anode.

4. CONCLUSIONS

A vircator capable of generating high-power X-ray pulses due to the multiple transitions of electrons through a thin anode foil has been created and put into operation for the first time. The vircator was created on the basis of a direct-action accelerator supplied from an inductive energy storage operating with a plasma opening switch.

Results have been presented from theoretical and experimental studies on the generation of X-ray bremsstrahlung in vircators with thin (10 μm) and thick (100 μm) tantalum anode foils. For a thin foil, the X-ray dose is found to be eight times as high as that for a thick foil. The spectra of the generated X-ray bremsstrahlung have been measured.

REFERENCES

1. N. R. Pereira and J. Davis, J. Appl. Phys. **64** (3), R1 (1988).
2. A. E. Dubinov and V. D. Selemir, Radiotekh. Élektron. (Moscow) **47**, 645 (2002).
3. N. I. Zavada, I. A. Troshkin, K. F. Zelenskiĭ, *et al.*, Vopr. At. Nauki Tekh., Ser.: Fiz. Radiats. Vozd. Radiofiz. Apparat., Nos. 3–4, 23 (1994).
4. T. W. L. Sanford, J. A. Halbleib, G. Cooperstein, and B. V. Weber, IEEE Trans. Nucl. Sci. **42**, 1902 (1995).
5. A. E. Dubinov, V. D. Selemir, and N. N. Makarova, RF Patent No. 2128411; Byull. Izobret., No. 9 (1999).
6. V. P. Tarakanov, *User's Manual for Code Karat* (Berkley, Springfield, 1992).
7. A. E. Dubinov and M. V. Loyko, Vychisl. Tekhnol. **8** (2), 53 (2003).
8. M. A. Blokhin, *X-ray Physics* (GITTL, Moscow, 1957).
9. N. F. Popkov, V. I. Kargin, E. A. Ryaslov, and A. S. Pikar', J. X-Ray Sci. Technol., No. 5, 289 (1995).
10. M. D. Raĭzer and L. E. Tsopp, Radiotekh. Élektron. (Moscow) **20**, 1691 (1975).

Translated by N.F. Larionova

Plasma Physics Reports, Vol. 30, No. 9, 2004, pp. 779–787. Translated from Fizika Plazmy, Vol. 30, No. 9, 2004, pp. 835–844.

LOW-TEMPERATURE PLASMA

Phenomenology of a High-Current Negative Point-to-Plane Corona in Nitrogen

Yu. S. Akishev, G. I. Aponin, V. B. Karal'nik, A. E. Monich, and N. I. Trushkin

Troitsk Institute for Innovation and Fusion Research, Troitsk, Moscow oblast, 142190 Russia

Received November 19, 2003; in final form, March 3, 2004

Abstract—Results are presented from experimental studies of a steady-state negative point-to-plane corona in atmospheric-pressure nitrogen at anomalously high (milliampere) currents. The evolution of the corona glow with increasing discharge current is traced up to the corona conversion into a spark. It was found that the structure and current–voltage characteristic of the corona change significantly when the working gas is slowly blown trough the discharge cell. It is shown that, starting from a current of $I \geq 0.5$ mA, a negative corona in a nitrogen flow acts as a streamer corona, whereas there are no streamers in the absence of gas blowing. In contrast to the quadratic dependence of the current versus voltage in a low-current corona, the current–voltage characteristic of a high-current corona is linear. The time evolution of the radial profile of the current density at the anode is studied under different experimental conditions. © *2004 MAIK "Nauka/Interperiodica".*

1. INTRODUCTION

It is commonly believed that a negative point-to-plane corona (the point electrode is the cathode) is a low-current and low-power discharge with a current of no higher than a few hundred microamperes and a power of no higher than a few watts [1, 2]. However, this is not true for a negative corona in nitrogen. It will be shown below that, for such a corona operating in steady-state and dynamic regimes, one can achieve rather high currents (from 3 to 30 mA) and high powers (from 80 to 500 W). The possibility of implementing such extraordinary operating regimes show that a high-current corona in atmospheric-pressure nitrogen can be used as a new promising source of nonequilibrium plasma (or a plasmochemical reactor) and is thus of great interest for gas-discharge physics and various applications.

However, available data on the properties of a negative corona in nitrogen are rather poor and fragmentary. Thus, the current–voltage (I–V) characteristic of a low-current ($I \leq 0.1$ mA) discharge presented in one of the first experimental studies on a point-to-plane negative corona in nitrogen [3] shows that the ignition voltage U^* of a nitrogen corona is higher than its operating voltage. In [4], where the I–V characteristic was measured over a more wide current range (up to 1 mA), a sharp jump in the current and a decrease in the voltage were observed after corona ignition. It was also found in [4] that the ignition voltage was not strictly constant even for a fixed electrode geometry and that the corona current decreased over time when operating with a static gas (i.e., in a sealed-off chamber without nitrogen blowing).

In [3, 4], an interesting circumstance was pointed out: at currents of a few hundred microamperes, a thin short bright filament was observed near the point tip; the filament could be oriented not only along the discharge axis (as was expected) but also at a certain angle with respect to the axis. It was also unusual that the cathode spot on which this filament rested could be located not only at the very tip of the point electrode but somewhere aside of it.

In [5], it was found that a negative corona in nitrogen can operate at currents lower than the ignition current (the corona current that is established immediately after ignition). To ensure the operation of a corona at such low currents, one should first ignite the corona and then decrease the applied voltage. The experiments with a nitrogen corona [5] showed the presence of hysteresis within a certain range of the corona parameters. The properties of a negative corona in the hysteresis region, within which the discharge current underwent regular pulsations, were thoroughly studied.

Clearly, the above literature data on the negative corona in nitrogen (especially at high currents) are insufficient to trace its evolution with increasing current up to its transformation into a spark. The aim of the present study, which is intended to fill this gap, is to experimentally investigate the high-current negative corona in nitrogen over a wide range of the discharge currents under different experimental conditions.

2. EXPERIMENT

Experiments were performed with a cylindrical organic-glass discharge cell with an inner diameter of 120 mm and a height of 150 mm. In the point–plane electrode system, a stainless-steel or tungsten rod was used as a cathode. The diameter of the rod and its tip radius were varied in the ranges of 0.5–3 mm and 0.06–0.5 mm, respectively. Either a 110-mm-diameter cop-

1063-780X/04/3009-0779$26.00 © 2004 MAIK "Nauka/Interperiodica"

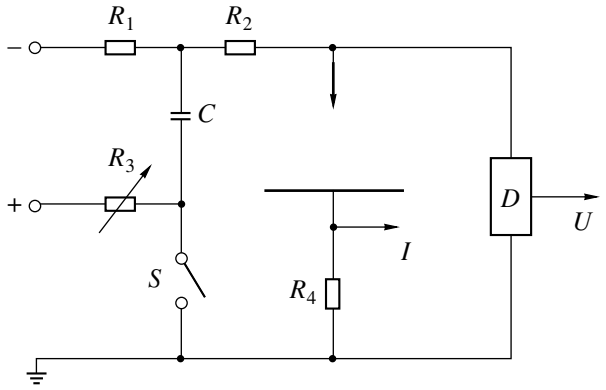

Fig. 1. Schematic of the experimental device for studying the evolution of a discharge after applying a voltage pulse to a steady-state negative corona: R_1 and R_2 are ballast resistances, R_3 is a variable resistance for controlling the rise time τ of the voltage pulse, R_4 is the current shunt, C is the capacitance of the circuit for voltage pulse formation, S is the switch of the circuit for voltage pulse formation, and D is a voltage divider.

per disc or a 80-mm-diameter sectioned electrode composed of nine coaxial rings separated by thin dielectric layers was used as a plane electrode (anode). The interelectrode distance was varied from 10 to 40 mm.

The high-current negative corona was powered from a high-voltage stabilized ($\delta U/U \le 10^{-6}$) power supply with an output voltage U of up to 30 kV. The voltage drop across the interelectrode gap was measured with an S-196 electrostatic voltmeter and a calibrated high-voltage divider. The average corona current was measured with a Ts4311 current meter. The ballast resistance in the external circuit was varied from 1 to 10 MΩ.

Special electric circuits based on TGI-400/16 thyratrons were designed and implemented to apply a voltage pulse to a steady-state negative corona. These schemes enabled the formation of 10-ms trapezoidal voltage pulses with an amplitude of 3.0–16.5 kV and a rise time of 1–700 μs (see Fig. 1). The waveforms of the discharge current and voltage were recorded with S8-17 and S1-104 oscilloscopes.

The evolution of the radial current distribution over the anode surface with increasing corona current was studied using a sectioned anode. Both the currents through the individual anode sections and the total discharge current were monitored. The measurements were performed in two regimes: a steady-state regime and a dynamic regime. In the steady-state regime, the currents through the anode sections were measured with a microammeter. In the dynamic regime, a voltage pulse with an amplitude Δu and a rise time τ was applied to a steady-state corona with a current I_s and voltage V_s. The time evolution of the currents through the anode sections up to the transition to a spark was simultaneously measured with several oscilloscopes. In more detail, the technique for studying the evolution of the radial current distribution was described in [6].

Two pairs of 50-mm-diameter optical windows were mounted on the side wall of the discharge cell, the windows in each pair being coaxial with one another. The spectrum of the corona emission was measured using an MUM-2 monochromator with a 1200 line/mm diffraction grating. Light emerging from the exit slit of the monochromator was monitored with an FEU-100 photomultiplier. The spectral and time resolutions of these measurements were 0.8 nm and 1 μs, respectively.

In our experiments, we used very-high-purity nitrogen (with a certified purity of 99.999%). Before each experiment, the discharge cell was pumped out to a pressure of $P \cong 10^{-3}$ torr and then filled with nitrogen at a pressure slightly exceeding atmospheric pressure (usually, $P = 770$ torr). The experiments were carried out both in a sealed-off regime and a continuous gas-flow regime with a gas flow rate small enough ($\le 10^{-2}$ l/s) to exclude any gasdynamic effect on the discharge.

In the nitrogen used in our experiments, the certified oxygen density (among 0.001% of residual impurities) was no higher than 10^{14} cm^{-3}. The slow blowing of nitrogen ensured that the density of oxygen in the cell did not increase above this value. This, in turn, guaranteed that the density of negative oxygen ions was much lower than the electron density. Let us make some estimates:

Negative ions can be produced from the residual oxygen through the dissociative and three-body electron attachment reactions,

$$e + O_2 \longrightarrow O^- + O; \quad e + O_2 + N_2 \longrightarrow O_2^- + N_2.$$

The former process is threshold in character; its efficiency is high only at sufficiently high values of the reduced electric field. Under our experimental conditions, such high reduced fields can be achieved only in the contracted region of a corona. The gas in this region is, however, strongly heated, which leads to a substantial decrease in the oxygen density (to $N_{O_2} \cong 2 \times 10^{13}$ cm^{-3}). Moreover, negative oxygen ions in this region undergo thermal destruction (it is well known [7] that there are practically no negative ions in hot air at a temperature of $T \ge 1000$ K) and efficiently recombine with positive ions. Assuming that there is a local balance for O^- ions, $k_a N_{O_2} n_e \cong \beta_{ii} n_+ / N_{O^-}$ (where $k_a \cong 10^{-12}$ cm^3/s [8] is the coefficient of dissociative attachment and $\beta_{ii} \cong 10^{-7}$ cm^3/s [8] is the coefficient of ion–ion recombination in the contracted region), we find that the relative concentration of negative atomic oxygen ions is $\dfrac{N_{O^-}}{n_e} \cong \dfrac{k_a N_{O_2}}{\beta_{ii} n_+}$. In the contracted region, this concentration is no higher than 2×10^{-4}.

Three-body attachment can occur in the drift zone, where the electric field is low. The rate constant for this

process is $k_T \cong 2 \times 10^{-33}$ cm^6/s [8]. Assuming that the lifetime of the negative O_2^- ions in the drift zone is mainly determined by the time during which they drift between the electrodes ($\tau \cong 300$ μs), we find that the relative concentration of the negative molecular oxygen ions, $\frac{N_{O_2^-}}{n_e} \cong k_T N_{O_2} N_{N_2} \tau$, is no higher than 1.5×10^{-3}.

Thus, the above estimates show that the negative ion density that can be provided by the oxygen impurity is at least three order of magnitude lower than the electron density.

3. EXPERIMENTAL RESULTS

Before describing the results obtained, let us briefly discuss the experimental problems that arise in studying the high-current corona. The high power dissipated in the interelectrode gap and at the point cathode in a steady-state regime results in both an appreciable heating of the working gas near the discharge axis and a strong heating of the tip of the point cathode. As was mentioned above, to maintain a sufficiently low gas temperature near the wall of the discharge cell ($T \leq$ 40°C), we had to use gentle gas blowing; this enabled convective heat removal from the discharge cell but did not had any gasdynamic effect on the discharge.

When a thin (with a diameter of less than 1 mm) stainless-steel needle was used as a cathode, the needle tip became melted, the melting time being dependent on the corona current. For this reason, most of experiments were carried out with a massive (3-mm-diameter) tapered tungsten rod with a tip radius of 0.1 mm. The use of tungsten ensured the thermal stability of the cathode and made it possible to operate with a steady-state corona. However, in this case, the corona ignition voltage turned out to be higher than in [4], where a point electrode with a tip radius of 0.5 mm (i.e., five times larger than in our experiments) was used.

To verify the correctness of our experiments, we thoroughly reproduced the electrode geometry from [4] and obtained the same corona ignition voltage as in [4] (Fig. 2b). This means that (i) the gas purity in our discharge cell was no worse than in [4] and (ii) the ignition voltage is determined by not only the point tip radius but also the size and geometry of the side surface of the massive tapered electrode (see [9]).

It was found that gentle nitrogen blowing significantly affected the *I–V* characteristic and the glow structure of a negative corona. Let us first consider the *I–V* characteristic. As was expected, the ignition voltage of a corona discharge in nitrogen at a fixed pressure turned out to be independent of gas blowing (see Fig. 2) and was only determined by the geometry of the discharge gap and the shape of the cathode. It can be seen from the figure that the ignition voltage is higher than the corona operation voltage. As a result, the discharge

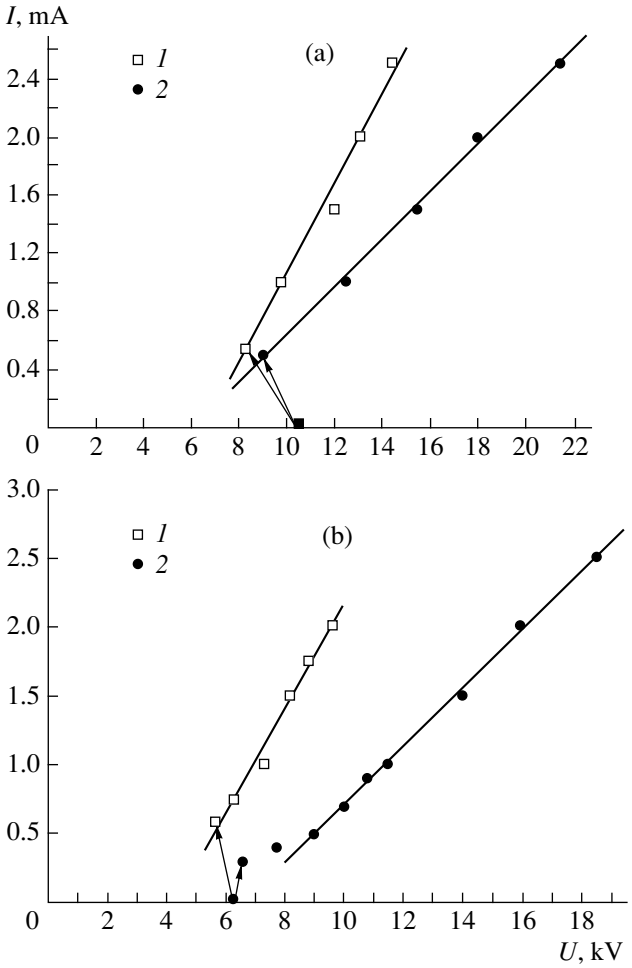

Fig. 2. *I–V* characteristic of a steady-state negative corona in nitrogen at a pressure of P = 770 torr (*1*) with and (*2*) without gas blowing through the discharge gap (d = 40 mm) for a cathode made of (a) 3-mm-diameter tungsten rod with a tip radius of r_c = 0.1 mm and (b) 1-mm-diameter stainless-steel rod with a tip radius of r_c = 0.5 mm (the arrows show the jumps in the current and voltage after corona ignition).

current increases abruptly and the interelectrode voltage decreases after the ignition of a discharge. We note that the *I–V* characteristic is linear. At the same currents, the corona voltage turns out to be lower with gas blowing. It is true for any geometry of the interelectrode gap and any shape and material of the rod cathode. This is illustrated in Fig. 2, which presents the *I–V* characteristics of a corona discharge with a thin stainless-steel rod and a massive tungsten rod.

The measured *I–V* characteristics of a corona discharge with nitrogen blowing are shown in Fig. 3 for a slow and fast (virtually jumplike) increase in the discharge voltage. The quasi-steady *I–V* characteristics obtained either by slowly (manually) increasing the discharge voltage or applying a sawtooth voltage with a rise time of 0.7 ms are almost identical. The dynamic *I–V* characteristic obtained by applying a rapidly

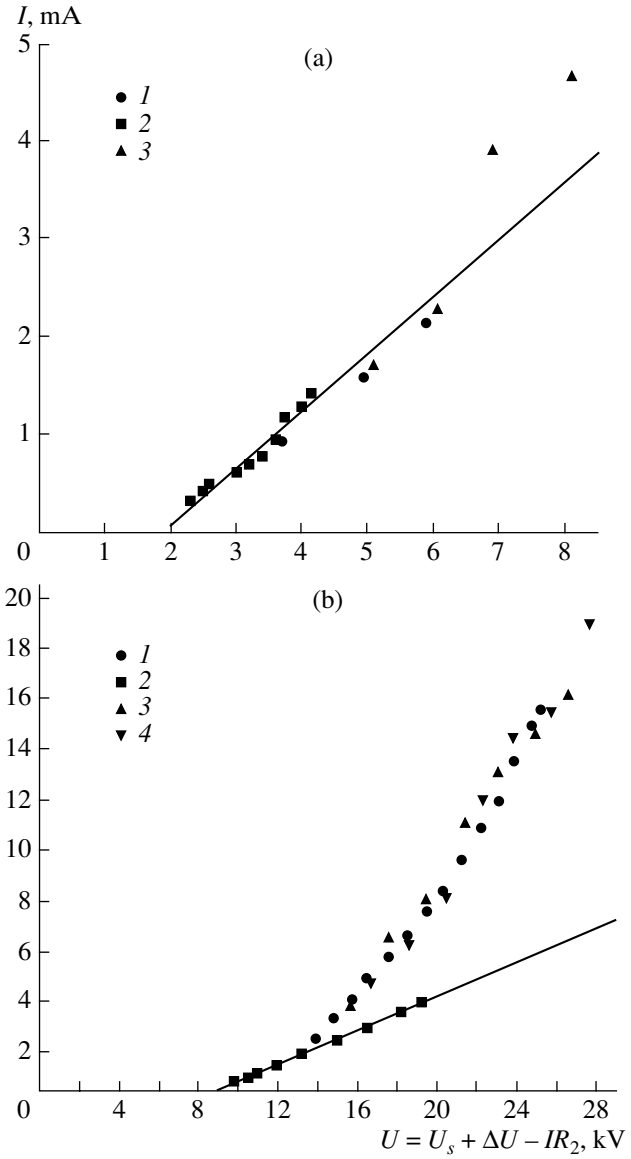

Fig. 3. *I–V* characteristics of a corona discharge for a (*1*) slow and (*2–4*) stepwise increase in the discharge voltage for (a) d = 10 mm, r_c = 0.1 mm, and τ = (*2*) 0.7 ms and (*3*) 10 μs and (b) d = 40 mm, r_c = 0.1 mm, and τ = 10 μs: (*2*) I_s = 1.24 mA and U_s = 10.9 kV, (*3*) I_s = 1.8 mA and U_s = 12.85 kV, and (*4*) I_s = 2.2 mA and U_s = 14 kV.

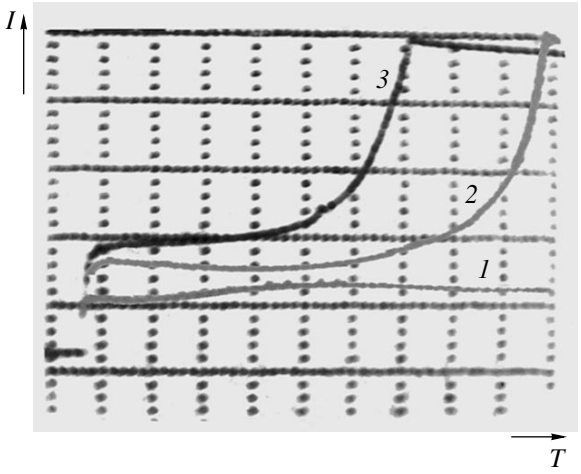

Fig. 4. Oscillogram of the corona current for a stepwise increase in the voltage ΔU = (*1*) 10, (*2*) 15, and (*3*) 16 kV. The gap length is d = 40 mm, r_c = 0.1 mm, I_s = 2.5 mA, and U_s = 14.3 kV. The current scale (major ticks) is 10 mA/division and the time scale is 50 μs/division.

increasing voltage (with a rise time of 1–10 μs, depending on the voltage amplitude) to a steady-state corona progressively deviates from the quasi-steady *I–V* characteristic (i.e., becomes nonlinear) with increasing discharge current (starting from a current of $I \geq 1.5$ mA). Each point of the dynamic *I–V* characteristic corresponds to the current recorded by an oscilloscope 10 μs after a jump in the discharge voltage (Fig. 4).

Let us now consider the glow structure of a high-current corona in nitrogen. For definiteness, we present the results obtained for a gap length of d = 40 mm, a tungsten cathode, and a current of $I \geq 1$ 1 mA. In the absence of gas blowing, there is a blue glowing spot around the tip of the tungsten point. The emission spectrum of this glow contains intense lines of the first negative system of nitrogen (the emission from positive nitrogen ions), which is characteristic of the cathode sheath of a glow discharge in nitrogen. The emission intensity from this spot is the highest at the very tip of the point. A thin (with a diameter of no more than 0.5 mm) and short (a few mm long) orange plasma filament is adjacent to the cathode spot. All the other space around the plasma filament and between the head (free end) of the filament and the plane electrode remains dark. The color of the plasma filament is determined by the emission from the first positive system of nitrogen ($B^3\Pi_g \longrightarrow A^3\Sigma_u^+$ transitions); this emission is characteristic of the positive column of a glow discharge. The emission intensity from the plasma filament increases with corona current. The filament length also (however, slightly) increases with corona current. Visually, the cathode spot seems to remain at the point tip, whereas the filament is spatially unstable: it slowly and randomly twists, and the head of the filament undergoes the largest deviation from the gap axis.

Apparently, the shape of the point also affects the spatial stability of the plasma filament. Thus, for a thin point (all other conditions being the same), the plasma filament more strongly deviates from the axis and can slowly (but irregularly in time and space) precess as a whole within a cone with a vertex angle of ~15°.

A comparison of the results of visual observations of a corona with the waveforms of the corona current shows that, at currents of $I < 1$ mA, the spatial instability of the filament correlates with the small-amplitude (about 1%) low-frequency (about 5 Hz) noise modulation of the current. At currents of $I \cong 1$ mA, the current

waveforms exhibit a deep (about 10%) high-frequency (with a characteristic frequency of ~1 kHz) noise modulation. As the current increases, the modulation frequency increases to 3–5 kHz and the modulation depth increases to 30%.

Measurements of the emission from different regions of a discharge showed that the emission intensity of the first positive system from the plasma filament (especially from its head) was modulated at both low and high frequencies, whereas the intensity of the first negative system of nitrogen from the cathode region was only modulated at the frequency of current pulsations. In our opinion, the source of high-frequency current pulsations is the instability of the cathode region. This instability results in a spontaneous conversion of the glowing cathode sheath at the point into an unsteady prearc spot [10].

Gas blowing decreases the discharge voltage at a fixed current. This results in a decrease in the emission intensity from the plasma filament, whereas the filament length increases by 1–2 mm. A distinctive feature of a corona with gas blowing is that, starting from currents of $I \geq 0.5$ mA, a diverging beam of thin (with a thickness on the order of the human hair diameter) yellowish streamers continuously emerges from the head of the plasma filament. The emission intensity from the streamers decreases with distance from the plasma filament. The average length of the streamers increases with corona current (Fig. 5). The beam of streamers is highly unstable in space. It can be seen by a naked eye that this beam waves as if it fluttered in wind. This is explained by the fact that the streamers randomly propagate within a ±10° cone with respect to the discharge axis. At the same time, the maximum diameter of the channel occupied by the streamers does not exceed 1.5 cm.

With gas blowing, both the low-frequency and high-frequency current pulsations are also present; however, the former are very weak, whereas the latter are clearly pronounced. The increase in the intensity of high-frequency current pulsations can be attributed to the presence of streamers in the gap. The rate of streamer generation seems to correspond to the pulsation rate of the unsteady cathode region; i.e., each spontaneous conversion of a glow cathode sheath into an unsteady prearc spot at the point tip induces the generation of streamers in the gap.

In our opinion, the reason why the streamers induced by an unsteady cathode sheath in the absence of gas blowing do not propagate (i.e., they decay immediately after their onset) is that a large amount of the products of plasmochemical reactions (e.g., nitrogen atoms in the ground and metastable states) is accumulated in the interelectrode gap. These products may affect the kinetics of charged particles, e.g., induce electron attachment, thereby quenching the electron avalanche and preventing the development and propagation of the streamer precursors provoked by the above instability of the cathode region. The electron attachment and the generation of negative ions from the accumulated products of plasmochemical reactions can lead to a decrease in the discharge current at a given voltage, as was observed in our experiments (see also [4]).

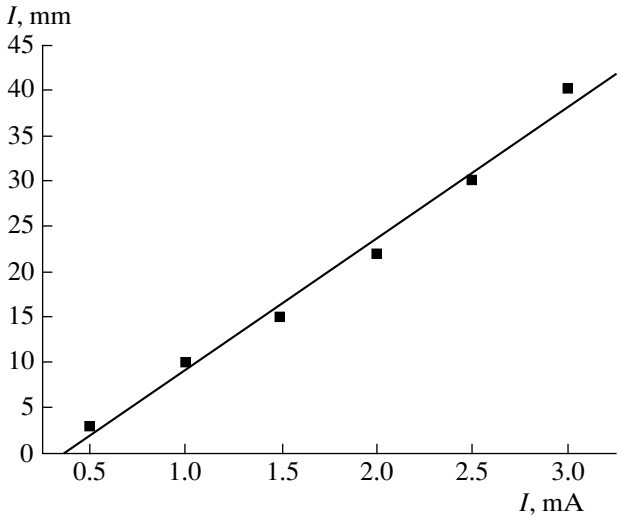

Fig. 5. Streamer length vs. negative corona current in blowing nitrogen for $P = 770$ torr, $d = 40$ mm, and a 3-mm-diameter tungsten cathode with a tip radius of $r_c = 0.1$ mm.

We believe that the $N(^2D^0_{5/2,\,3/2})$ metastable nitrogen atoms can be a source of negative ions in a high-current negative corona in nitrogen [11]. These ions are intensely produced in the contracted region of a corona. The $N(^2D)$ doublet state with an energy of about 2.39 eV has an enormously large radiation lifetime of 10^5 s. Atoms in the doublet state are very weakly quenched by both nitrogen molecules ($k < 10^{-14}$ cm^3/s) and nitrogen atoms in the $N(^4S)$ ground state ($k \cong 1.8 \times 10^{-12}$ cm^3/s). Their volume recombination is also very slow (the rate constant for the $N + N + M \longrightarrow N_2 + M$ process is $k \cong 8.3 \times 10^{-34}\exp(500/T)$ cm^6/s). These atoms can form negative ions in the $N^-(^1D)$ metastable autoionization state [8], the electron binding energy of which is about 1 eV and the lifetime is much longer than 1 μs.

Thus, the experiments show that a high-current negative corona in blowing nitrogen is a streamer corona, whereas there are no streamers in the absence of gas blowing. The presence of streamers in a negative corona is an extraordinary phenomenon because, in air, streamers are observed only when the point electrode is at a positive potential.

In the prearc regime, when some streamers have already reached the plane electrode, they induce blue unsteady spots with a diameter of ~1 mm on the anode. The color of these spots is mainly determined by the emission from the second positive system of nitrogen

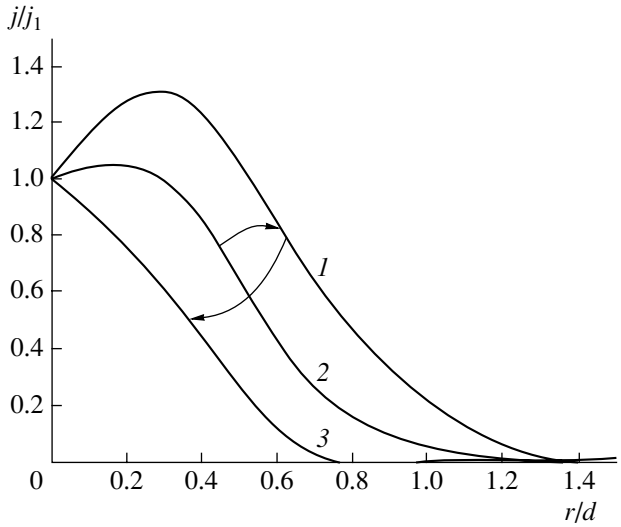

Fig. 6. Characteristic curves illustrating the evolution of the current density at the anode of a point-to-plane negative corona in nitrogen for a slow (1 ⟶ 2 ⟶ 3) and stepwise (2 ⟶ 1 ⟶ 2 ⟶ 3) increase in the discharge voltage.

(the $C^3\Pi_u \longrightarrow B^3\Pi_g$ transitions). The onset of anode spots can be related to the beginning of the conversion of a negative corona into a glow discharge [12], which accompanied by the formation of a quasineutral plasma in the interelectrode gap.

The current corresponding to the onset of anode spots depends on the state of the anode surface. For example, for a mechanically cleaned anode, these spots arise at a current of about 3 mA. After some time, the anode gets covered with an oxide film and the threshold current for the formation of anode spots decreases. For example, after 10-h continuous discharge operation, the threshold current decreases to 2.2 mA; after 20-h operation, it decreases to 1.5 mA. A similar effect was also observed for a negative corona in air [12].

After the interelectrode gap is bridged with streamers, a short-lived spark arises, which is accompanied by a bright flash and a sharp increase in the current up to 0.5–1.5 A. Since the corona is fed from a power supply with an output voltage of $U \cong 10$–20 kV, such a large current cannot be steadily maintained in the external circuit with a ballast resistance of a few megaohms. Hence, the spark is a short-duration transient process, which is sustained by the charging current of stray capacitances in the external circuit.

It is important to know the evolution of the current distribution over the anode surface for a smooth and an abrupt increase in the discharge voltage. Figure 6 shows how the normalized current density changes for different means of increasing the discharge voltage. For a slow increase in the voltage, the distribution $j(r/d)$ varies according to the scheme 1 ⟶ 2 ⟶ 3, where the numerals correspond to the curve numbers in Fig. 6. For a stepwise increase in the corona voltage, the distribution $j(r/d)$ varies according to the scheme 2 ⟶ 1 ⟶ 2 ⟶ 3. It can be seen that applying a step voltage to a steady-state corona with a narrow current distribution (caused by the presence of a beam of streamers in the gap) first significantly widens the current distribution on the anode. However, the distribution then narrows again; this is related to the formation of an anode sheath. The initial widening of the current distribution after applying a step voltage is related to the disappearance of the beam of streamers at sufficiently high overvoltages; this is confirmed by streak images showing no streamers.

At low corona currents, immediately after applying a step voltage, the current distribution on the anode of a steady-state negative corona in nitrogen differs substantially from the Warburg distribution in air [13, 14]. In this case, the current distribution has a dip on the discharge axis, which was also observed in [15].

We note that, after a transient spark, an almost steady-state glow discharge can be established in the gap. For example, for a gap with $d = 40$ mm, the current and voltage of a glow discharge are equal to 20 mA and 7 kV, respectively. An atmospheric-pressure discharge shares all the features of a conventional glow discharge: a blue glow cathode sheath, a short (about 1 mm) Faraday dark space, a diffuse pink-lilac positive (plasma) column, and a small-size anode spot. The diameter of the plasma column is 2–3 mm. Estimates show that the gas in the plasma column is highly heated (up to a temperature of higher than 1500 K).

For a horizontal arrangement, the hot plasma column came up from the gap axis. It was significantly bent, and its length was approximately 50 mm (instead of 40 mm for a vertical arrangement). Since the anode spot could freely slide upward along the plane anode and the cathode end of the plasma column was fixed at the point electrode, the column configuration looked like the Z letter stretched by its ends in the horizontal direction.

In some regimes, a glow discharge pulsated with a period of several seconds. The beginning of the pulsation period corresponded to the breakdown of the gap, the plasma column being oriented strictly along the horizontal axis of the point–plain gap. The column was then heated, its anode end slowly rose up, and the column increased in length. After reaching a certain maximum length, the column broke, which corresponded to the end of the period. Then, the process repeated.

We note that a steady-state glow discharge with a long thin plasma filament was also ignited by us in atmospheric-pressure air.

4. DISCUSSION

An analysis of the literature data and our experimental results shows that, in the voltage range $U \geq U^*$, the time-averaged I–V characteristic of a high-current neg-

Summary data on the negative corona in nitrogen

References	Point parameters	Gap length, mm	Gas blowing	Igniting and extinguishing voltages, kV	*I–U* characteristic of a corona (*I* is in mA and *U* is in kV)
[3]	Platinum wire 0.5 mm in diameter with a tip radius of $r_0 = 0.25$ mm	40	Absent	$U^* \cong 4.8$ $U_0 \cong 2.5$	$I \cong kU_0(U - U_0)$ $k \cong 0.1$ mA/kV^2
[4]	Platinum wire 1.0 mm in diameter with a tip radius of $r_0 = 0.5$ mm	40	Absent	$U^* \cong 6.2$ $U_0 \cong 3.5$	$I \cong kU_0(U - U_0)$ $k \cong 0.087$ mA/kV^2
This study	Stainless-steel wire 1.0 mm in diameter with a tip radius of $r_0 = 0.5$ mm	40	Absent	$U^* \cong 6.3$ $U_0 \cong 4.7$	$I \cong kU_0(U - U_0)$ $k \cong 0.09$ mA/kV^2
This study	Stainless-steel wire 1.0 mm in diameter with a tip radius of $r_0 = 0.5$ mm	40	Present	$U^* \cong 6.3$ $U_0 \cong 4.1$	$I \cong kU_0(U - U_0)$ $k \cong 0.088$ mA/kV^2
This study	Conically tapered tungsten wire 3.0 mm in diameter with a with a vertex angle of 60° and tip radius of $r_0 = 0.1$ mm	40	Present	$U^* \cong 10.5$ $U_0 \cong 7.5$	$I \cong kU_0(U - U_0)$ $k \cong 0.044$ mA/kV^2
This study	Stainless-steel wire 0.5 mm in diameter with an ellipsoidal tip of radius $r_0 = 0.1$ mm	10	Present	$U^* \cong 2.4$ $U_0 \cong 1.4$	$I \cong kU_0(U - U_0)$ $k \cong 0.28$ mA/kV^2
This study	Stainless-steel wire 0.5 mm in diameter with an ellipsoidal tip of radius $r_0 = 0.1$ mm	10	Present	$U^* \cong 2.8$ $U_0 \cong 1.7$	$I \cong kU_0(U - U_0)$ $k \cong 0.18$ mA/kV^2
This study	Stainless-steel wire 0.5 mm in diameter with an ellipsoidal tip of radius $r_0 = 0.1$ mm	20	Present	$U^* \cong 3.5$ $U_0 \cong 1.7$	$I \cong kU_0(U - U_0)$ $k \cong 0.12$ mA/kV^2
This study	Stainless-steel wire 1.0 mm in diameter with a hemispherical tip of radius $r_0 = 0.5$ mm	20	Present	$U^* \cong 7.5$ $U_0 \cong 2.8$	$I \cong kU_0(U - U_0)$ $k \cong 0.12$ mA/kV^2
This study	Stainless-steel wire 0.5 mm in diameter with an ellipsoidal tip of radius $r_0 = 0.1$ mm	30	Present	$U^* \cong 3.8$ $U_0 \cong 2.75$	$I \cong kU_0(U - U_0)$ $k \cong 0.069$ mA/kV^2
This study	Stainless-steel wire 0.5 mm in diameter with an ellipsoidal tip of radius $r_0 = 0.1$ mm	40	Present	$U^* \cong 4.0$ $U_0 \cong 2.8$	$I \cong kU_0(U - U_0)$ $k \cong 0.033$ mA/kV^2

ative corona in nitrogen can be approximated by the linear function

$$I \cong kU_0(U - U_0). \quad (1)$$

At high currents ($I > 150$ μA), the approximation accuracy is a few percent. Note that a similar formula for an air corona, first obtained by Townsend, is valid for currents of no higher than 10–20 μA.

The factor k in expression (1) is a dimensional coefficient depending on the shape and material of the corona point and the interelectrode gap length. In contrast to the expression for an air corona, in which U_0 corresponds to the corona ignition voltage U^*, the quantity U_0 in expression (1) approximately corresponds to the voltage at which the corona is extinguished (in nitrogen, $U^* > U_0$). Thus, the *I–V* characteristic of a negative corona in nitrogen shows hysteresis. The corona properties in the hysteresis range ($U^* > U > U_0$) were studied in [5], where it was shown that, at low currents (i.e., in the hysteresis region), approximation (1) is no longer valid.

A summary of our results on approximating the *I–V* characteristic of a steady-state negative corona in nitrogen at currents of $I \geq 0.1$ mA by a linear function is presented in the table.

For short gap lengths ($d = 10$ mm), there is a scatter in the data obtained: within the same experiment, the current depends linearly on the voltage; however, the parameters U^*, U_0, and k are slightly different in different experiments. As an illustration, the table presents the data for two regimes with $d = 10$ mm. The reason for such a minor scatter in the *I–V* characteristic of a negative corona in nitrogen is apparently related to the above effect of the state of the plane electrode (anode) surface on the discharge properties. It is interesting that all of the approximations presented in the table lie within the range $I \cong (0.1–0.4)(U - U_0)$, where the current and voltage are in milliamperes and kilovolts,

respectively. Therefore, the differential resistance $\partial U/\partial I$ of a negative corona in nitrogen in the presence of a plasma filament near the point slightly depends on the geometrical factors and lies in the range 2.5–10 MΩ.

According to commonly accepted opinion, the volume charge in the drift zone of a negative corona in nitrogen is determined by electrons only; in this case, the corona *I–V* characteristic should be nonlinear at high currents: $I \sim (U - U_0)^2$. Since our experiments demonstrate a linear *I–V* characteristic, we assume that this discrepancy is related to the presence of negative ions in a high-current corona. As was mentioned above, these ions can be metastable $N^-(^1D)$ ions created due to the electron attachment to $N(^2D^0_{5/2,\,3/2})$ metastable nitrogen atoms, abundantly produced in the contracted region of a corona discharge.

Unfortunately, the available data on the rate constants for the processes determining the concentrations of metastable atoms and negative ions in nitrogen are still lacking. For this reason, we can only specify conditions under which negative ions can significantly affect corona, namely, those under which the parameters of a volume charge in the gap are determined by the negative ions, but the current is mainly carried by the electrons. We will show that the corona *I–V* characteristic is linear under such conditions.

Let us assume that, within the current channel of a corona, the metastable $N(^2D)$ atoms are distributed quite uniformly due to diffusion. Since the electric field in the contracted region of a corona discharge slightly varies with current, the averaged concentration N of the metastable atoms in the channel is proportional to the discharge current, $N \sim I$. We also assume that the lifetime τ_i of the negative ions in the metastable state is small compared to the time during which these ions escape from the interelectrode gap. In this case, the profile of the relative density of the negative ions in the gap is determined by the local balance equation

$$\frac{N^-(x)}{n_e(x)} \cong k_a N \tau_i, \qquad (2)$$

where k_a is the rate constant for the electron attachment to metastable atoms, n_e is the electron density, and x is the longitudinal coordinate counted from the point electrode. Since $N \sim I$, the fraction of negative ions in the corona increases with total current.

Let us estimate the rate constant for electron attachment at which the density of negative ions exceeds the electron density. Assuming that $\tau_i \cong (1–3) \times 10^{-5}$ s and $N \cong (1–3) \times 10^{15}$ cm^{-3} (which seems to be quite reasonable), we find that the desired value of the attachment rate constant is $k_a \cong 10^{-10}$ cm^3/s.

Using Eq. (2) and Poisson's equation, one obtains a qualitative relation between the current I and voltage U in the drift region of a corona, where the space charge of negative ions prevails:

$$U \cong \frac{e}{\varepsilon_0} n_e d^2 k_a \tau_i N. \qquad (3)$$

Here, e is the electron charge, ε_0 is the permittivity of free space, and d is the gap length. Taking into account that $n_e \sim \frac{I}{U}$ and $N \sim I$, it follows from Eq. (3) that the *I–V* characteristic of a negative corona in nitrogen is linear; i.e., $I \sim U$.

Thus, the assumption about the presence of metastable negative ions in nitrogen allows a qualitative explanation of the linearity of the *I–V* characteristic of a high-current negative corona in nitrogen. Deriving a more exact expression for the *I–V* characteristic requires more detailed knowledge of the rate constants for elementary processes governing the kinetics of negative ions.

5. CONCLUSIONS

It has been experimentally found that, starting from currents of $I \geq 0.5$ mA, a steady-state negative corona in nitrogen in the presence of gentle gas blowing through a discharge acts as a streamer corona, whereas there are no streamers in the absence of gas blowing.

It has been shown that, regardless of gas blowing, the *I–V* characteristic of a steady-state negative corona is linear at currents of $I \geq 0.5$ mA (in contrast to the parabolic *I–V* characteristic of a low-current corona).

An analysis based on the available data on the rate constants for elementary processes (electron attachment and detachment, ion–ion recombination, etc.) has shown that the certified purity of nitrogen employed in our experiments ensures that the concentration of negative oxygen ions in a discharge is low enough to have no appreciable effect on the corona *I–V* characteristic.

It has been suggested that both the increase in the discharge voltage with decreasing gas flow rate and the linearity of the *I–V* characteristic of a high-current corona in nitrogen are related to the presence of negative metastable $N^-(^1D)$ ions produced due to the electron attachment to metastable $N(^2D^0_{5/2,\,3/2})$ atoms.

ACKNOWLEDGMENTS

This study was supported by the Russian Foundation for Basic Research (project no. 02-02-16913) and the RF Program for State Support of Leading Scientific Schools (project no. NSh-794.2003.2).

REFERENCES

1. L. B. Loeb, *Electrical Coronas: Their Basic Physical Mechanism* (Univ. California Press, Berkeley, 1965).

2. Yu. P. Raizer, *Gas Discharge Physics* (Nauka, Moscow, 1987; Springer-Verlag, Berlin, 1991).
3. G. L. Weissler, Phys. Rev. **63**, 96 (1943).
4. H. Korge, Uch. Zap. Tartusk. Gos. Univ., No. 479, 107 (1979).
5. Yu. S. Akishev, M. E. Grushin, V. B. Karal'nik, and N. I. Trushkin, Fiz. Plazmy **27**, 550 (2001) [Plasma Phys. Rep. **27**, 520 (2001)].
6. Yu. S. Akishev, M. E. Grushin, V. B. Karal'nik, *et al.*, Fiz. Plazmy **29**, 198 (2003) [Plasma Phys. Rep. **29**, 176 (2003)].
7. É. M. Bazelyan and A. Yu. Goryunov, in *Proceedings of the All-Union Conference on the Physics of Electric Breakdown in Gases, Tartu, 1984*, Part 2, p. 262.
8. H. S. W. Massey, *Negative Ions* (Cambridge Univ. Press, Cambridge, 1976; Mir, Moscow, 1979).
9. I. P. Vereshchagin, *Corona Discharge in Electronic and Ionic Technology* (Énergoatomizdat, Moscow, 1985).
10. Yu. S. Akishev, A. P. Napartovich, V. V. Ponomarenko, and N. I. Trushkin, Zh. Tekh. Fiz. **55**, 655 (1985) [Sov. Phys. Tech. Phys. **30**, 388 (1985)].
11. B. M. Smirnov, *Negative Ions* (Atomizdat, Moscow, 1978; McGraw-Hill, New York, 1982).
12. Yu. S. Akishev, M. E. Grushin, I. V. Kochetov, *et al.*, Fiz. Plazmy **26**, 172 (2000) [Plasma Phys. Rep. **26**, 157 (2000)].
13. M. Goldman and A. Goldman, in *Corona Discharges. Gaseous Electronics*, Vol. 1: *Electrical Discharges*, Ed. by M. N. Hirsh and H. J. Oskam (Academic, New York, 1978), p. 219.
14. A. Goldman, M. Goldman, J. E. Jones, and M. Yumoto, in *Proceedings of the 9th International Conference on Gas Discharges and Their Applications, Venice, 1988*, p. 197.
15. Yu. S. Akishev, A. P. Napartovich, M. V. Pan'kin, and N. I. Trushkin, in *Proceedings of the 8th All-Russian Conference on Gas-Discharge Physics, Ryazan', 1996*, Part 2, p. 11.

Translated by N.N. Ustinovskiĭ

Plasma Physics Reports, Vol. 30, No. 9, 2004, pp. 788–796. Translated from Fizika Plazmy, Vol. 30, No. 9, 2004, pp. 845–854.

LOW-TEMPERATURE PLASMA

Balance of CO Molecules in the Plasma of a Sealed-off CO Laser

G. M. Grigorian* and I. V. Kochetov**

**Fock Research Institute of Physics, St. Petersburg State University, Ul'yanovskaya ul. 1, Petrodvorets, St. Petersburg, 198504 Russia*

***Troitsk Institute for Innovation and Fusion Research, Troitsk, Moscow oblast, 142090 Russia*

Received July 7, 2003; in final form, October 29, 2003

Abstract—The processes of dissociation and recombination of CO molecules in the plasmas of discharges in He/CO and He/CO/Xe mixtures under conditions characteristic of sealed-off CO lasers are investigated. The concentrations of CO molecules and the main products of their dissociation—O and C atoms and CO_2 molecules—are measured simultaneously for the first time, and the time evolution of the initial working mixture composition in the discharge is calculated. It is shown that the main channel for the regeneration of CO molecules in a sealed-off discharge is the heterogeneous recombination of C and O atoms. The rate constants for this process are estimated. © *2004 MAIK "Nauka/Interperiodica".*

1. INTRODUCTION

So far, most of the studies of elementary processes in the plasmas of molecular gases have been performed in gas flow discharges, whereas the processes in sealed-off systems (operating without gas circulation through the discharge tube) have received little study in spite of the widespread use of such discharges in sealed-off molecular (CO_2 and CO) lasers. In particular, it is yet unclear how CO molecules are regenerated in the plasmas of sealed-off discharges in the mixtures used as active media in sealed-off CO lasers, which are capable of operating for tens (or even hundreds) of hours without mixture regeneration. At the same time, it is well known that CO molecules efficiently dissociate in gas discharge plasmas, the degree of dissociation being up to ten percent even in systems with rapid gas circulation [1, 2]. The scheme of plasmochemical processes that is capable of adequately describing quite slow variations in the CO concentration in discharges and the long-term operation of sealed-off lasers is still lacking. To construct such a scheme, one needs the data on the concentrations of the dissociation products of CO molecules as functions of the experimental conditions. Until now, the concentrations of only two plasmochemical products generated during a discharge in a CO-containing mixture, namely, CO_2 molecules and O atoms, have been measured [3–6]. No calculations of the change in the gas mixture composition during a discharge without gas circulation have been performed.

The goals of this study were as follows:

(i) to examine the processes in the plasma of sealed-off discharges in He/CO and He/CO/Xe mixtures that lead to a change in the initial mixture composition and to study mechanisms for the regeneration of CO molecules dissociated in a discharge;

(ii) to simultaneously measure the concentrations of CO molecules and the products of their dissociation (C and O atoms), as well as the concentration of the produced CO_2 molecules; and

(iii) to numerically calculate the concentrations of these products and compare them to the experimental data.

2. EXPERIMENTAL SETUP

The experimental setup was similar to that described in [6]. The experiments were carried out with a 15-mm-diameter discharge tube made of molybdenum glass and cooled with running water. The length of the discharge region was 50 cm. Hollow cylindrical tantalum electrodes were installed in the side branches of the discharge tube at a distance of 4 cm from its axis. A dc discharge was ignited in He/CO and He/CO/Xe mixtures in the sealed-off regime. The concentrations of CO molecules and Xe atoms were 4–12% and 5–12%, respectively. The pressure was varied in the range 5–15 torr. Before puffing into the tube, the working mixtures were purified using a system of silica-gel and zeolite traps. The mixture composition in the discharge tube was analyzed with an MSC-6 time-of-flight mass spectrometer. The time evolution of the concentrations of stable products in the discharge plasma was monitored by periodically analyzing gas samples taken from the discharge region located at a distance of ~2 cm from the cathode. The gas samples could be supplied either directly to the mass spectrometer or into a special gas cylinder. The cylinder was then disconnected from the system, and the gas in it was analyzed. Both methods yielded similar results.

1063-780X/04/3009-0788$26.00 © 2004 MAIK "Nauka/Interperiodica"

The emission from the positive column of the discharge in the spectral range of 200–3000 nm was recorded with a spectrometer. The analysis of the emission spectra allowed us to determine the populations of the vibrational levels of $CO(X^1\Sigma)$ molecules, the gas temperature at the discharge axis and its radial profile (by analyzing the rotational structure of the bands of CO molecules), and the concentrations of the electronically excited particles in the gas discharge plasma.

The monitoring of the emission intensities of the CO molecular bands at different points along the discharge tube axis showed that the cataphoresis effect (the spatial separation of the mixture components that can be caused by the presence of a directed flow of ions and the charge exchange of the mixture components with them) was insignificant.

The electric field in the discharge was determined by measuring the voltage drops across the discharge gap and the electrode sheaths. The electrode sheath voltages were found from the voltage measurements in experiments with different discharge lengths. A typical electrode sheath voltage was 350–400 V. The measured value of the reduced electric field E/N was $(1.7–3.2) \times 10^{-16}$ V cm^2 in He/CO mixtures and $(0.9–1.5) \times 10^{-16}$ V cm^2 in He/CO/Xe mixtures.

2.1. Method for Measuring the Concentrations of Oxygen and Carbon Atoms

The concentration of atomic oxygen in the ground state was determined from the measurements of the absolute population of an electronically excited state [7]; in our experiments, the concentration of atomic oxygen in the $3p^5P$ state was measured. A detailed analysis of the processes resulting in the population of this electronic state (see [8] for details) showed that the main population mechanism was electron-impact excitation,

$$O(2p\ S_0) + e \longrightarrow O^*(3p^5P) + e. \quad (1)$$

The remaining population mechanisms were insignificant. This state was mainly depopulated via radiative transitions because collisional quenching could be ignored at fairly low pressures characteristic of our experiments (≤10 torr):

$$O^*(3p^5P) \longrightarrow O^*(3s^5S_0) + h\upsilon. \quad (2)$$

The concentration of atomic oxygen in the ground electronic state was found from the balance equation

$$[O] = [O^*(3p^5P)]A/(n_eK_1), \quad (3)$$

where A is the Einstein coefficient for the $3p^5P$ state of atomic oxygen, n_e is the plasma electron density, and K_1 is the rate constant for electron-impact excitation of the $3p^5P$ state. The value of the cross section for electron-impact excitation, which was necessary to find K_1, was taken from [9, 10]. To determine the electron density from the discharge current, we used the computed electron drift velocity. The results of calculations of the rate constant for the excitation of the $O(3p^5P)$ state under our experimental conditions are shown in Fig. 1.

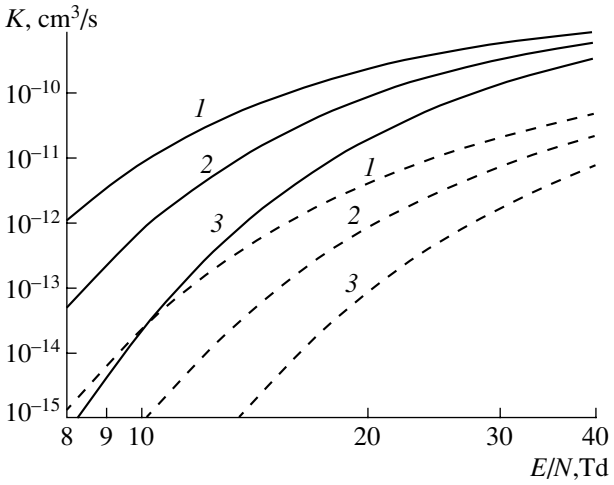

Fig. 1. Rate constants for the electron-impact excitation of $C(2p3p^1P_1)$ (solid curves) and $O(3p^5P)$ (dashed curves) atomic states in the CO : He = (*1*) 4 : 96, (*2*) 7 : 93, and (*3*) 12 : 88 mixtures.

The accuracy of determining the concentration of atomic oxygen in the ground state by this method depends mainly on the accuracy with which the cross section for the electron-impact excitation of the $3p^5P$ state is known; in our case, the latter was no worse than 50%. The sensitivity of the method is very high and allows one to measure atomic oxygen concentrations as low as ~10^{11} cm^{-3}.

The concentration of carbon atoms was determined in a similar way. In [11], this method for determining the concentration of atoms in the ground state by measuring the population of an excited state was used to monitor the concentration of carbon atoms in a gas-flow discharge. In [11], the absolute population of the $2p3s\,^1P_1^0$ state was measured by the intensity of the 247.8-nm line, corresponding to the $2p3s\,^1P_1^0 \longrightarrow 2p^2\,^1S_0$ transition.

In our study, two spectral lines of carbon atoms were used to determine the concentration of these atoms in the ground electronic state. In addition to the 247.8-nm line, we also used the 1.45-μm IR line, corresponding to the transition from the $2p3p\ ^1P_1$ state, from which, according to our estimates, the $2p3s\,^1P_1^0$ state is mainly populated.

Under our conditions, the contribution from population via the reaction of dissociative recombination,

$$CO + e \longrightarrow C^* + O + e, \quad (4)$$

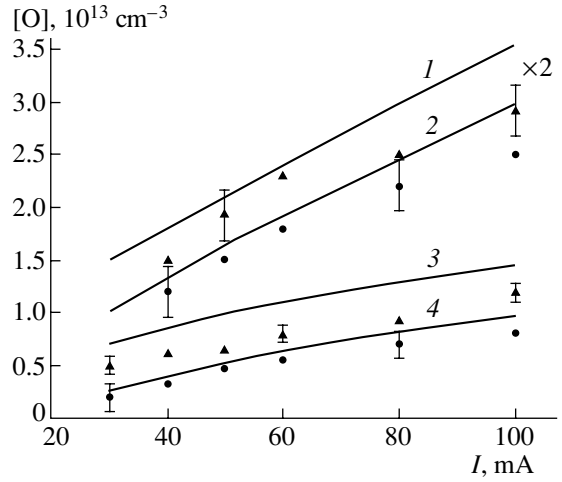

Fig. 2. Concentration of atomic oxygen 10 min after the discharge is switched on vs. discharge current for (*1*, *2*) He + 7% CO and (*3*, *4*) He + 4% CO mixtures. The symbols show the experimental data for p = 5 (circles) and 10 (triangles) torr, and the curves show the calculated results for p = (*1*, *3*) 10 and (*2*, *4*) 5 torr.

is insignificant. The cross sections for the excitation of electronic states were calculated in the Born approximation using the approximation formulas from [12]. For metastable states, we used the cross sections calculated in [13].

The effect of reabsorption on the measured intensity of the 247.8-nm line can be ignored (when estimating the concentration, it was assumed that the diffusion coefficient for metastable atoms was equal to the diffusion coefficient for carbon atoms in the ground state [14]).

The main mechanism for the population of the $2p3p\ ^1P_1$ state is direct electron-impact excitation from the ground state. The $2p3s\,^1P_1^0$ and $2p3p^1P_1$ states are depopulated via radiative transitions. The concentration of carbon atoms in the ground electronic state can be determined from the population balance for either the $2p3p\ ^1P_1$ state,

$$n_e[\mathrm{C}]k_{e2} = [\mathrm{C}(2p3p^1P_1)]A_p \qquad (5)$$

or the $3s\,^1P_1^0$ state,

$$n_e[\mathrm{C}]k_{e1} + [\mathrm{C}(2p3p^1P_1)]A_p = [\mathrm{C}(2p3s\,^1P_1^0)]A_s, \qquad (6)$$

where A_p and A_s are the Einstein coefficients for the $2p3p^1P_1$ and $2p3s\,^1P_1^0$ states, respectively.

If the population mechanisms for these electronically excited states are determined correctly, then the concentrations of carbon atoms in the ground state measured by the two different methods will be close to one another. Figure 1 shows the calculated rate constants for the excitation of the $\mathrm{C}(2p3p^1P_1)$ state as functions of the reduced electric field.

3. THEORETICAL MODEL

To calculate the concentrations of CO, CO_2, $CO(a^3\Pi)$, C_2O, C_2, and O_2 molecules, as well as C, O, and Xe* (the lowest metastable state of Xe) atoms, we solved a set of tine-dependent balance equations with allowance for particle diffusion to the discharge tube wall.

The rate constants for the processes with the participation of electrons were obtained by numerically solving the kinetic Boltzmann equation for the electron energy distribution function (EEDF). In simulations, we took into account the scattering of electrons by the vibrationally excited CO molecules. The molecule distribution over vibrational levels was assumed to be Boltzmann, and the vibrational temperature was taken from the experimental data. The used sets of cross sections and the solving technique were described in detail in [6].

The plasmochemical processes taken into account in calculating the components produced in the discharge under study are listed in the table. When there is more than one value of the rate constant for the same process, the value used in calculations is underlined.

The diffusion coefficients for different mixture components are taken from [15]. Since no data on the diffusion of atomic oxygen in CO are available in the literature, we used the value of the diffusion coefficient for oxygen atoms in nitrogen [15]. The diffusion coefficient for carbon atoms in a He/CO mixture was taken from [14].

4. He/CO MIXTURES: EXPERIMENTAL RESULTS AND DISCUSSION

The measured concentration of atomic oxygen in He/CO mixtures as functions of the discharge current are shown in Fig. 2. Throughout the entire range of the discharge current, the concentration of atomic oxygen is ~10^{12}–10^{13} cm^{-3}. It can be seen from Fig. 2 that the O concentration increases significantly with pressure. The dependence of the concentration on the discharge current is close to linear. The error bars in Fig. 2 (and in the subsequent figures) stand for variations in the experimental data.

As is seen from the table, there are a number of processes leading to the production of atomic oxygen in discharges in He/CO mixtures. However, the simulations showed that, under our experimental conditions, only a few of them were really able to affect the O concentration (all the processes with the participation of oxygen molecules can be ignored since the mass-spectroscopic measurements showed that the O_2 concentration was very low, ≤10^{13} cm^{-3}). Estimates show that the main channels for the production of atomic oxygen are

Table

	Reaction	Rate constant (cm^3/s, cm^6/s)	References
R1	$CO + CO(a^3\Pi) \longrightarrow CO_2 + C$	1.2×10^{-12}	[16]
		1.4×10^{-12}	[17]
R2	$CO + O + He \longrightarrow CO_2 + He$	1.7×10^{-36}	[18]
		3×10^{-36}	[19]
R3	$CO + O + CO \longrightarrow CO_2 + CO$	3.2×10^{-36}	[18]
R4	$CO + O + CO_2 \longrightarrow CO_2 + CO_2$	4×10^{-35}	[20]
R5	$CO + O \longrightarrow CO_2 + \Delta E$	$10^{-14}\exp(-1630/T)$	[21]
R6	$CO_2 + CO(a^3\Pi) \longrightarrow 2CO + O$	$\ll 3 \times 10^{-11}$	[22]
		10^{-12}	[23]
R7	$CO + C + He \longrightarrow C_2O + He$	6.3×10^{-32}	[24]
R8	$CO + C + CO \longrightarrow C_2O + CO$	1.5×10^{-31}	[25]
R9	$C + O \longrightarrow CO + \Delta E$	10^{-20}	[26]
R10	$C + O + He \longrightarrow CO + He$	1×10^{-32}	[27]
R11	$C + CO_2 \longrightarrow CO + CO$	$<1 \times 10^{-15}$	[28]
R12	$CO(a^3\Pi) + O_2 \longrightarrow CO_2 + O$	$\leq 5 \times 10^{-12}$	[22]
		6×10^{-12}	[29]
R13	$C_2O + O \longrightarrow CO + CO$	**1.2×10^{-11}**	[30]
		9.5×10^{-11}	[31]
R14	$C_2O + CO_2 \longrightarrow$ Products	$<1 \times 10^{-14}$	[32]
R15	$C_2O + C \longrightarrow C_2 + CO$	3×10^{-10}	[14]
R16	$C_2O + CO(a^3\Pi) \longrightarrow C + 2CO$	$\leq 2 \times 10^{-9}$	[14]
R17	$CO(a^3\Pi) + O_2 \longrightarrow CO + 2O$	5×10^{-12}	[22]
R18	$He + 2O \longrightarrow O_2 + He$	1.3×10^{-36}	[33]
R19	$He + 2C \longrightarrow C_2 + He$	1.2×10^{-32}	[33]
		1.12×10^{-31}	[34]
R20	$CO + 2O \longrightarrow O_2 + CO$	2×10^{-35}	[35]
R21	$CO_2 + 2O \longrightarrow O_2 + CO_2$	8×10^{-36}	[35]
R22	$C + CO_2 \longrightarrow CO + CO$	$<1 \times 10^{-15}$	[22]
R23	$C_2 + O \longrightarrow$ Products	1×10^{-12}	Estimate
R24	$C_2 + CO_2 \longrightarrow$ Products	$<3 \times 10^{-14}$	[22]
R25	$C + C_3O_2 \longrightarrow$ Products	1.8×10^{-10}	[28]
R26	$CO_2 + Xe^m \longrightarrow CO + O + Xe$	4×10^{-10}	[36]
R27	$CO + O + Wall \longrightarrow CO_2$	1×10^{-17}	[22]
R28	$O + O^w \longrightarrow O_2$	$4 \times 10^{16}/[CO]$ [cm/s]	[37]
R29	$C + O^w \longrightarrow CO$	$6 \times 10^{18}/[CO]$ [cm/s]	This work
R30	$C + O^w$ (+Xe) $\longrightarrow$ CO (+Xe)	$2 \times 10^{10}/[CO]^{0.5}$ [cm/s]	This work

Note: The upper index *w* refers to the atoms adsorbed on the discharge tube wall. The values of rate constants used in calculations are underlined.

the processes of dissociation of CO and CO_2 molecules,

$$CO + e \longrightarrow C + O + e, \quad (7)$$

$$CO_2 + e \longrightarrow CO + O + e. \quad (8)$$

Oxygen atoms are lost via heterogeneous recombination and volume plasmochemical reactions. In [7], gas-flow discharges in similar mixtures were used to study the loss rate of oxygen atoms due to their diffusion to the tube wall. This rate can be written as

$$Z^{-1} = \Lambda^2/D + (2 - \varepsilon)r/(\varepsilon U), \quad (9)$$

where Λ is the characteristic diffusion length determined by the discharge geometry (for a cylindrical dis-

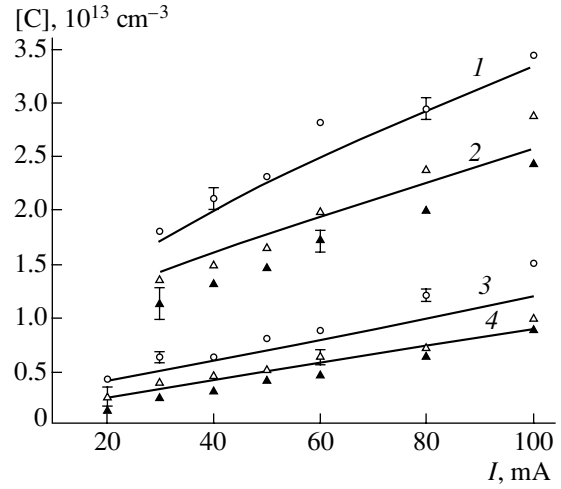

Fig. 3. Concentration of carbon atoms 10 min after discharge is switched on vs. discharge current for (*1*, *2*) He + 7% CO and (*3*, *4*) He + 4% CO mixtures. The symbols and curves show the experimental and calculated results, respectively. The concentrations were measured from the populations of the $3s^1P$ (triangles) and $3p^1P$ (circles) states for p = 5 torr (closed symbols) and 10 (open symbols) torr. The curved were calculated for p = (*1*, *3*) 10 and (*2*, *4*) 5 torr.

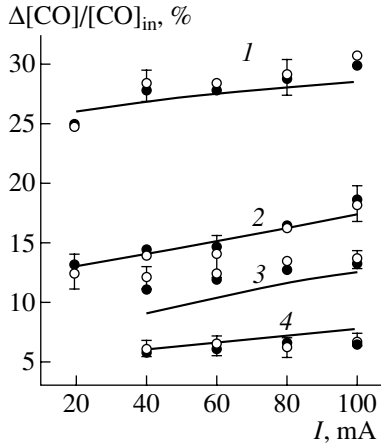

Fig. 4. Variations in the normalized CO concentration vs. discharge current for different He/CO mixtures: (*1*) He + 4% CO, p = 5 torr; (*2*) He + 4% CO, p = 15 torr; (*3*) He + 7% CO, p = 10 torr; and (*4*) He + 12% CO, p = 10 torr. The curves show the calculated results, while the symbols show the concentrations measured 5 min (closed circles) and 30 min (open circles) after the discharge was switched on.

charge whose length is much larger than its radius r, we have $\Lambda = \frac{r}{2.4}$) D is the diffusion coefficient for oxygen atoms, ε is the accommodation coefficient, and U is the mean thermal velocity of atoms. It was found in [7] that, for discharges in He/CO and He/CO/Xe mixtures, the accommodation coefficient is ≥ 0.1. It can be shown that, for $\varepsilon \geq 0.1$, the rate of heterogeneous recombination of atomic oxygen under our experimental conditions is mainly determined by its diffusion rate (the second term in (9) is smaller than the first one and, hence, can be ignored). In our experiments, atomic oxygen was produced via the dissociation of CO and CO_2 molecules (reactions (7) and (8), respectively) and was lost due to its diffusion to the wall. In calculating the concentration of atomic oxygen (see Fig. 2), we used the experimental data on the concentrations of CO and CO_2 in a discharge. It can seen from Fig. 2 that calculated results are in good agreement with the experiment.

Figure 3 shows the measured concentration of carbon atoms in a discharge plasma as a function of the discharge current. The concentrations determined from the absolute populations of the $2p3s\,^1P_1^0$ and $2p3p\,^1P_1$ states are shown by triangles and circles, respectively. It can be seen that these concentrations differ by no more than ~70%. Taking into account that the cross sections for the excitation of the electronic states of carbon atoms were calculated in the Born approximation [12], the agreement between the C concentrations obtained from the populations of different electronic states may be regarded as good. The fact that both methods for determining the C concentration provide close results confirms the validity of the chosen scheme of the processes responsible for populating the electronically excited states used to calculate the concentration of carbon atoms in the ground electronic state. Under our experimental conditions, the concentration of carbon atoms varied in the range ~10^{12}–10^{13} cm^{-3} (Fig. 3). The dependence of the concentration on the discharge current was close to linear.

The main processes resulting in the production of carbon atoms in the discharge plasma under study is reaction R1 (see table) and the electron-impact dissociation of CO molecules, whereas the main channel for their loss is diffusion to the wall. The rate constants for reactions of C atoms with O_2 and C_2O molecules are large (10^{-11}–10^{-10} cm^3/s); however, the concentrations of these molecules in the discharge are too low (~10^{12} cm^{-3}) to appreciably affect the concentration of carbon atoms. At pressures higher than 5–7 torr, the only process that can be comparable to diffusion in the loss rate of carbon atoms is reaction R25. In some experiments carried out at low currents, the mass spectrometer detected C_3O_2 molecules near its sensitivity limit. The C_3O_2 concentration can be estimated very roughly as ~10^{13} cm^{-3} with an accuracy of a factor of 2. At such a concentration, the loss of carbon atoms in reaction R25 is close to their diffusive loss at the tube wall. The calculated concentrations of carbon atoms presented in Fig. 3 are seen to agree satisfactorily with experiment.

The measurements showed that, under our experimental conditions, the CO_2 concentration varied in the range ~5–10%. The main process for the production of CO_2 molecules is reaction R1, whereas the main loss

channel is their electron-impact dissociation. The mechanisms for the production and loss of CO_2 molecules are discussed in detail in [6].

Let us consider how the CO concentration varies in the plasma of a discharge in a He/CO mixture. Figure 4 shows the degree of dissociation of CO molecules, $\Delta[CO]/[CO]_0$ (where $[CO]_0$ is the CO concentration in the initial mixture and $\Delta[CO]$ is the variation in the CO concentration during a discharge), measured at different times τ_d after switching on the discharge. These concentrations are seen to be in good agreement with the data from [[3, 4].

Under our experimental conditions, the main channel for the dissociation of CO molecules is electron-impact dissociation reaction (7) and collisions with metastable $CO(a^3\Pi)$ molecules (reaction R1). Which of these processes will prevail in a discharge depends on the electron energy. Since metastable CO molecules are produced via the electron-impact excitation reaction

$$CO + e \longrightarrow CO(a^3\Pi) + e, \qquad (10)$$

and decay mainly via the quenching reaction

$$CO + CO(a^3\Pi) \longrightarrow CO + CO, \qquad (11)$$

we find that the concentration of metastable molecules is $[CO(a^3\Pi)] = n_e k_{10}/k_{11}$. The rates of dissociation in reactions (7) and R1 are $\nu_1 = n_e k_7$ and $\nu_2 = n_e k_{R1} k_{10}/k_{11}$, respectively, with $\nu_2/\nu_1 = k_{10}k_{R1}/(k_7 k_{11})$. The ratio between the rates of processes R1 and (7) in a He/CO mixture as a function of the reduced field is shown in Fig. 5. The rate constants for reactions (7) and R1, which lead to the loss of CO molecules, are fairly large (10^{-11}–10^{-12} cm^3/s), whereas volume recombination resulting in the production of CO molecules (reactions R9 and R10) is highly inefficient ($k_{R9} = 10^{-20}$ cm^3/s and $k_{R10} = 10^{-32}$ cm^6/s). If one considers the recombination of CO molecules to proceed only via reactions similar to reactions R9 and R10, then the CO concentration will decrease by more than two orders of magnitude in a time less than 1 s; this, however, contradicts the experimental results (see Fig. 4). In the system under study, heterogeneous processes resulting in the production of CO molecules should play an important role. An analysis of the possible channels for these processes shows that, to explain the experimental data, one needs to consider the heterogeneous recombination of O and C atoms resulting in the production of CO molecules. The heterogeneous processes have been poorly studied; hence, it is father difficult to analyze the kinetics of the possible mechanisms for the recombination of C and O atoms at the tube wall and to estimate the corresponding rate constants. To do this, one would have to consider a great number of processes with the participation of atoms physically and chemically adsorbed at the wall, the rates of these processes being unknown. Moreover, it is necessary to know the concentration of active sites at the discharge tube wall (as well as the evolution of this concentration during a discharge). Under our experimental conditions, the model of a perfectly pure glass wall, for which the data on this concentration are available (in this case, the active sites are the coordination-unsaturated silicon atoms [38]), is inapplicable because, in the course of a discharge in a He/CO mixture, the tube wall becomes covered with both the reaction products created in the discharge and the results of their polymerization (e.g., C_n, C_nO_m, etc.) [39].

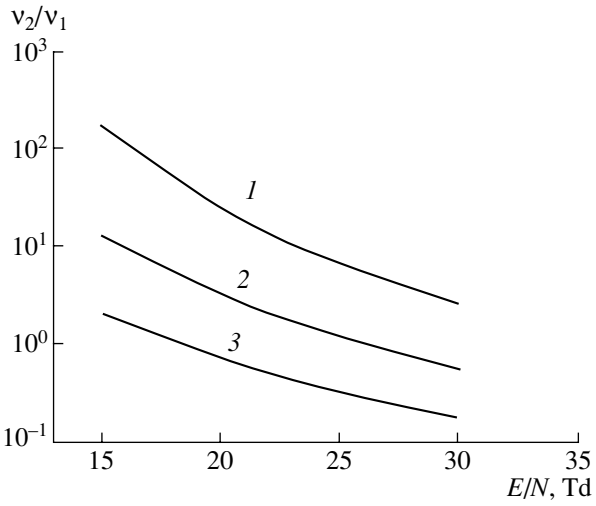

Fig. 5. Ratio between the rates of reactions R1 and (7) vs. reduced electric field for the (*1*) He + 12% CO, (*2*) He + 6% CO, and (*3*) He + 3% CO mixtures.

Estimates show that, to achieve agreement between the theoretical and experimental results on the CO concentration, it is necessary to take into account the production of CO molecules in the processes of heterogeneous recombination such that one atom in the gas phase interacts with one atom adsorbed at the wall (the Eley–Rideal process):

$$C + O^w \longrightarrow CO \qquad (12a)$$

and/or

$$O + C^w \longrightarrow CO. \qquad (12b)$$

For this purpose, the balance equation for CO molecules was supplemented with the terms corresponding to different processes of heterogeneous recombination, of which, according to our calculations, the main process is the recombination of C and O atoms:

$$d[CO]/dt = [C]K_{eff}^{O} + [O]K_{eff}^{C} + [C][O]k_{R9} + [C][O][He]k_{R10} - [CO](n_e k_7 + [CO^m]k_{R1}), \qquad (13)$$

where $K_{eff}^{C,O} = \dfrac{k_{rc}^{C,O}\dfrac{S}{V}\nu_{diff}}{k_{rc}^{C,O}\dfrac{S}{V} + \nu_{diff}}$; S and V are the surface area and volume of the discharge tube, respectively;

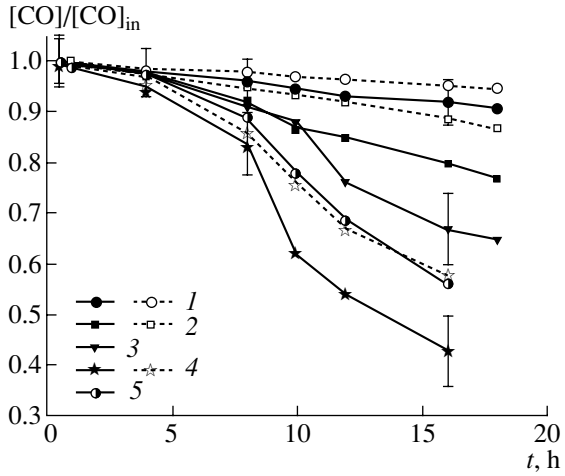

Fig. 6. Time evolution of the normalized CO concentration in discharges with (*1*) Ta, (*2*) Cu, (*3*) Al, (*4*) Ni electrodes and (*5*) with a Ta anode and Ni cathode for $I = 70$ (solid curves) and 20 (dashed curves) mA.

$\nu_{diff} = D/\Lambda^2$ is the atomic diffusion rate; and D is the atomic diffusion coefficient. It is difficult to make a certain conclusion about the prevalence of one of the processes (12) because, in our case, the concentrations of carbon and oxygen atoms are close to each other (see Figs. 2 and 3) and depend similarly on the experimental conditions. For definiteness, it was assumed that heterogeneous recombination proceeds via channel (12a). The value of k_{rc}^{C} was varied until the best agreement between the calculated and measured CO concentrations was achieved. By comparing the calculated and experimental results, the effective rate constant for the production of CO molecules at the wall was found to be $k_{rc}^{C} = (6 \pm 2) \times 10^{18}/[\mathrm{CO}]$ cm/s (where [CO] is in units of cm^{-3}).

The rate constant for heterogeneous recombination, k_{rc}^{C}, is inversely proportional to the CO concentration. Note that a similar dependence on the CO concentration was previously observed in [37] for the heterogeneous recombination of two oxygen atoms in a discharge in a CO-containing mixture:

$$O + O^{w} \longrightarrow O_2, \qquad (14)$$

where $k_{rc} = 4 \times 10^{16}/[\mathrm{CO}]$ cm/s. The authors of [37] explained such an inversely proportional dependence by the competition between the adsorption of O atoms and CO molecules at the same active sites (it is well known that CO molecules possess strong adsorption ability). In our experiments, we could not check whether there was such a dependence for the recombination of atomic oxygen because the O_2 concentration was too low.

The calculated CO concentrations in a discharge as functions of the discharge current are shown in Fig. 4, which demonstrates good agreement between the experimental data and the calculated results obtained with allowance for the heterogeneous recombination of C and O atoms. The heterogeneous Eley–Rideal process (12) is the main channel for the regeneration of CO molecules in the discharge under study.

The experiments show that the mixture composition that is established in the beginning of a discharge (in a time on the order of few tenths of second) can be retained rather long, for ten hours and more (depending on the discharge conditions). After this, a stage begins in which a slow decrease in the CO concentration and an increase in the concentrations of plasmochemical products become appreciable. Moreover, the voltage and pressure also decrease (these trends were studied in detail in [4]). Variation in the concentrations of CO and plasmochemical products observed in this stage are caused by the processes that were not taken into account in the above model (in particular, by the processes occurring at the discharge electrodes). Special experiments carried out with electrodes made of other materials and with different surface areas showed that, with all other factors being the same, variations in the electrode material and surface area do not affect the particle concentrations in plasma in the initial stage of a discharge ($t < 10$ h), so that our model can be used to predict the mixture composition in a discharge plasma. For longer discharges, their parameters begin to depend on the electrode material and surface area. Figure 6 illustrates the time evolution of the CO concentration in a long-lasting discharge for different electrode materials (every curve in Fig. 6 was measured for three days, and each day the discharge operated for six hours). The CO concentration is normalized to the concentration that is established 30 min after switching on the discharge. Since the processes at the electrodes have not yet been studied even qualitatively, we did not attempt to incorporate the processes at the electrode surface in our model.

5. He/CO/Xe MIXTURE: EXPERIMENTAL RESULTS AND DISCUSSION

After adding xenon to a He/CO mixture, the discharge plasma parameters change significantly, which is related to a decrease in E/N. Under our experimental conditions, the reduced electric field decreased approximately by half. In He/CO/Xe mixtures, regardless of the experimental conditions, E/N did not exceed 1.5×10^{-16} V cm^2. Because of such a low reduced field, we were not able to measure the concentration of atomic oxygen in Xe-containing mixtures. It can be seen from Fig. 1 that, at low E/N values, the rate constants for the excitation of the ^5P state of atomic oxygen are very small; accordingly, the line intensity corresponding to the transition used to measure the atomic oxygen concentration is too low.

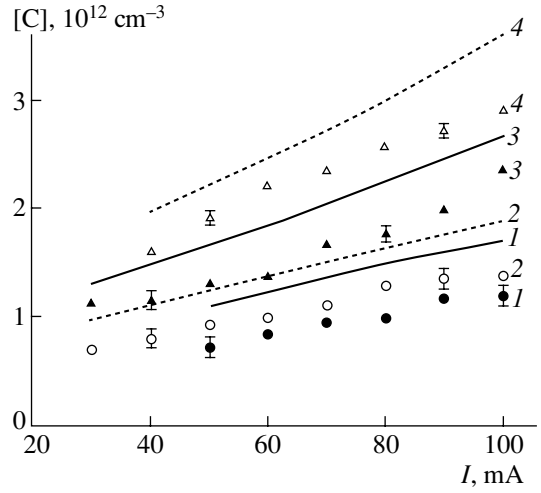

Fig. 7. Concentration of carbon atoms vs. discharge current for the (*1*, *2*) He/CO/Xe = 96 : 3 : 1 and (*3*, *4*) 90 : 5 : 5 mixtures at p = (*1*, *3*) 5 and (*2*, *4*) 10 torr. The symbols and curves show the experimental and calculated results, respectively.

The measured concentration of carbon atoms as a function of the discharge current is shown in Fig. 7. Adding Xe to a He/CO mixture leads to a decrease in the concentration of carbon atoms by a factor of 3–4 because of a decrease in the rate of dissociation of CO molecules. The calculated concentrations of carbon atoms are in fair agreement with the experiment; this indicates that, in Xe-containing mixtures, the main processes determining the concentration of carbon atoms in the discharge plasma are the same as in He/CO mixtures (in particular, the reactions of the excitation transfer from metastable Xe* atoms do not affect the population of the p^1P^1 state of carbon used to determine the concentration of carbon atoms in the ground electronic state).

After adding Xe, the CO_2 concentration decreased by approximately one order of magnitude because of the dissociation of CO_2 molecules in collisions with Xe* and was ~0.5–3%, depending on the experimental conditions. This issue was previously discussed in detail in [6].

The decrease in E/N caused by adding Xe to a He/CO mixture and the change in the EEDF (a decrease in the fraction of high-energy electrons) lead to a significant decrease in the rate of the electron-impact dissociation of CO molecules. In such mixtures, reaction R1 (the production of C and CO_2 in collisions between two CO molecules, one of which is in the $a^3\Pi$ electronically excited state) becomes the main dissociation process. Figure 8 illustrates the relative contribution of these two processes to the dissociation of CO in He/CO/Xe mixtures.

A comparison of the calculated and experimental results on the CO concentration in He/CO/Xe mixtures shows that the rate constant for heterogeneous recombination reaction (12a) differs from that in He/CO mixtures; namely, it is $k_{rc}^{C} = (2 \pm 0.5) \times 10^{10}/[\mathrm{CO}]^{0.5}$ cm/s. The calculated value of k_{rc}^{C} in He/CO/Xe mixtures is close to that measured in He/CO mixtures; however, the dependence of k_{rc}^{C} on the CO concentration is weaker, which can be related to the change in the wall properties under the action of the discharge plasma in He/CO/Xe mixtures. Figure 9 shows the measured and calculated $\Delta[\mathrm{CO}]/[\mathrm{CO}]$ ratios, which are seen to be in fair agreement with one another.

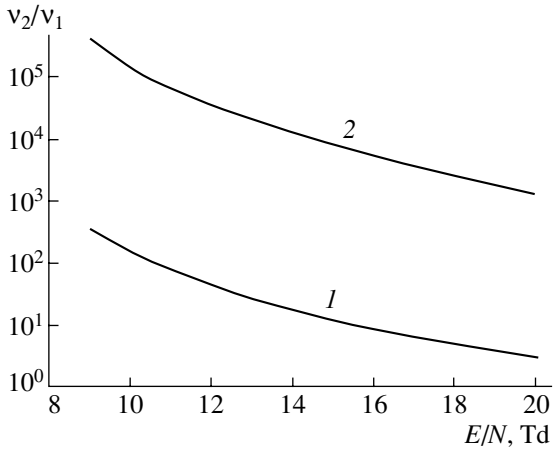

Fig. 8. Ratio between the rates of reactions R1 and (7) vs. reduced electric field for the He : CO : Xe = (*1*) 85 : 3 : 12 and (*2*) 90 : 5 : 5 mixtures.

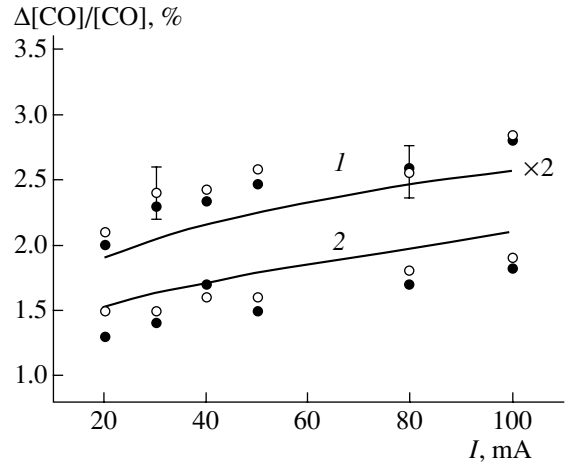

Fig. 9. Variations in the normalized CO concentration vs. discharge current for two He/CO/Xe mixtures: (*1*) 85 : 3 : 12, p = 5 torr and (*2*) 90 : 5 : 5, p = 10 torr. The curves show the calculated results, while the symbols show the concentrations measured 5 min (closed circles) and 30 min (open circles) after the discharge was switched on.

6. CONCLUSIONS

We have measured the time evolution of the degree of dissociation of CO molecules and the concentrations of the main products of plasmochemical reactions in the plasma of a sealed-off CO laser. A comparison of the calculated results with the experimental data on the concentrations of CO_2, C, and O in the initial stage of a discharge (for an operation time of less than 10 h) have shown that the plasmochemical model proposed in this study can be successfully used to predict the mixture composition in the plasma.

A comparison of the calculated and measured concentrations has shown that the main process leading to the regeneration of CO molecules in a sealed-off discharge is the heterogeneous recombination of C and O atoms. The rate constants for this process were estimated under different conditions.

ACKNOWLEDGMENTS

We are grateful to A.P. Napartovich for supporting this work and fruitful discussions. This study was supported in part by the Russian Foundation for Basic Research, project no. 04-02-16961.

REFERENCES

1. G. M. Grigorian and Yu. Z. Ionikh, Khim. Vys. Énerg. **23**, 548 (1989).
2. A. I. Maksimov, L. S. Polak, D. I. Slovetskiĭ, and A. F. Sergienko, Khim. Vys. Énerg. **13**, 134 (1979).
3. É. A. Trubacheev, Tr. Fiz. Inst. Akad. Nauk SSSR **102**, 3 (1977).
4. V. S. Aleĭnikov and V. I. Masychev, *CO Lasers* (Radio i Svyaz', Moscow, 1990).
5. P. G. Brawne and A. L. S. Smith, J. Phys. E **8**, 870 (1975).
6. G. M. Grigorian, N. A. Dyatko, and I. V. Kochetov, Fiz. Plazmy **29**, 768 (2003) [Plasma Phys. Rep. **29**, 709 (2003)].
7. Yu. Z. Ionikh, A. L. Kuranov, and Yu. V. Ermolaev, in *Proceedings of the 6th All-Union Conference on the Physics of Low-Temperature Plasma, Leningrad, 1983*, Vol. 1, p. 86.
8. A. L. Kuranov, Candidate's Dissertation (Leningrad. Gos. Univ., Leningrad, 1985).
9. E. E. Gulcicek and J. P. Doering, J. Geophys. Res. **92**, 3445 (1987).
10. E. E. Gulcicek and J. P. Doering, J. Geophys. Res. **93**, 5879 (1988).
11. Yu. Z. Ionikh, I. N. Kostyukevich, and N. V. Chernysheva, Opt. Spektrosk. **74**, 455 (1993) [Opt. Spectrosc. **74**, 274 (1993)].
12. L. A. Vaĭnshteĭn, I. I. Sobel'man, and E. A. Yukov, *Cross Sections for the Excitation of Atoms and Ions by Electrons* (Nauka, Moscow, 1973), p. 141.
13. L. D. Tomas and R. K. Nesbet, Phys. Rev. A **12**, 2378 (1975).
14. Yu. Z. Ionikh, I. N. Kostyukevich, and N. V. Chernysheva, Opt. Spektrosk. **76**, 406 (1994) [Opt. Spectrosc. **76**, 361 (1994)].
15. *Tables of Physical Quantities: A Handbook*, Ed. by I. K. Kikoin (Atomizdat, Moscow, 1976), p. 1006.
16. A. I. Maksimov, L. S. Polak, D. I. Slovetskiĭ, and A. F. Sergienko, Khim. Vys. Énerg. **13**, 358 (1979).
17. E. E. Ivanov, Yu. Z. Ionikh, N. P. Penkin, and N. V. Chernysheva, Khim. Fiz. **7**, 1694 (1988).
18. F. Stuhl and J. Niki, J. Chem. Phys. **55**, 3943 (1971).
19. T. S. Slanger and S. Black, J. Chem. Phys. **53**, 3722 (1970).
20. J. L. Black and H. I. Green, Chem. Phys. **32**, 675 (1978).
21. S. Toby, Int. J. Chem. Kinet. **16**, 149 (1984).
22. D. I. Slovetskiĭ, *Mechanisms of Chemical Reactions in Nonequilibrium Plasma* (Nauka, Moscow, 1980), p. 342.
23. G. M. Grigorian, in *Proceedings of the All-Russia Conference on the Physics of Low-Temperature Plasma, Petrozavodsk, 2001*, p. 36.
24. D. Hussain and L. J. Kirsch, Trans. Faraday Soc. **67**, 2025 (1971).
25. F. Goss, K. Sadeghi, and J. C. Pebay-Peyroula, Chem. Phys. Lett. **13**, 557 (1972).
26. V. N. Kondrat'ev, *Rate Constants for Gas-Phase Reactions: A Handbook* (Nauka, Moscow, 1971), p. 200.
27. M. E. McEnroy and N. McConnel, J. Geophys. Res. **75**, 667 (1971).
28. D. Hussain and R. N. Young, J. Chem. Soc., Faraday Trans. 2 **71**, 525 (1975).
29. E. E. Ivanov, Yu. Z. Ionikh, N. P. Penkin, and N. V. Chernysheva, Khim. Fiz. **8**, 1528 (1989).
30. K. N. Becker, O. Horse, W. H. Schmidt, and P. Weiscen, Chem. Phys. Lett. **30**, 64 (1982).
31. F. Shechelforce and I. N. Mastrup, J. Chem. Phys. **57**, 3733 (1972).
32. V. Donnelly, W. Pitts, and J. McDonald, Chem. Phys. **49**, 289 (1980).
33. F. F. Martinotti, M. J. Welch, and A. P. Wolf, Chem. Commun. **3**, 115 (1968).
34. H. Tahara, K. Minami, *et al.*, Jpn. J. Appl. Phys. **34**, 1972 (1995).
35. G. K. Reachlend, J. Chem. Phys. **56**, 745 (1984).
36. J. Balamuta and M. F. Bolde, J. Chem. Phys. **76**, 2430 (1982).
37. L. S. Polak, D. I. Slovetskiĭ, and A. G. Sokolov, *Nonequilibrium Chemical Kinetics and Its Applications* (Nauka, Moscow, 1979), p. 326.
38. V. F. Kiselev, *Surface Phenomena in Semiconductors and Dielectrics* (Nauka, Moscow, 1970).
39. D. I. Slovetskiĭ, *Plasma Chemistry* (Énergoatomizdat, Moscow, 1984), Vol. 11.

Translated by N.N. Ustinovskiĭ

Plasma Physics Reports, Vol. 30, No. 9, 2004, pp. 797–803. Translated from Fizika Plazmy, Vol. 30, No. 9, 2004, pp. 855–862.

LOW-TEMPERATURE PLASMA

Influence of a Transverse Magnetic Field on the Characteristics of a DC Gas Discharge

V. K. Pashnev, V. E. Strel'nitskij, O. A. Opalev, V. I. Gritsyna, I. I. Vyrovets, and Yu. A. Bizyukov

Kharkov Institute for Physics and Technology, National Science Center, ul. Akademicheskaya 1, Kharkov, 61108 Ukraine

Received October 29, 2003

Abstract—The influence of a transverse magnetic field and the working-gas pressure on the rotation frequency of the current channel, as well as on the electric field in the positive column and the cathode voltage drop in a dc gas discharge, was studied experimentally. The working gases were pure hydrogen and hydrogen–methane, hydrogen–argon, and hydrogen–argon–methane mixtures. It is shown that a transverse (with respect to the discharge current) magnetic field stabilizes a normal glow discharge against a transition to an arc discharge at specific absorbed powers above 300 W/cm^3. The cathode voltage drop and the electric field in the positive column are measured. It is shown that the electric field does not depend on the magnetic field strength, whereas the cathode voltage drop increases with increasing magnetic field. It is found that the rotation frequency of the current channel is a complicated function of the discharge parameters and attains 400 Hz. © *2004 MAIK "Nauka/Interperiodica".*

1. INTRODUCTION

Low-temperature gas-discharge plasma sources play an important role in the development of new technologies. Gas discharges have received wide application in gas-discharge switches and plasmochemistry. They are also widely used to clean surfaces, to pump gas-discharge lasers, to deposit thin films (including the synthesis of diamond coatings by the method of chemical vapor deposition from a gaseous phase), etc. [1–4]. An important research trend in the physics of gas discharges used to deposit coatings is the search for discharge regimes that would provide the high density of the released power, would be characterized by the low concentration of uncontrolled impurities in the working gas, and will make it possible to coat large surfaces.

DC gas discharges have significant advantages, because the energy sources used to supply them are rather simple and cheap. DC arc discharges provide the greatest power density; however, the high concentration of the electrode-material impurity in the working gas substantially restricts their field of application. In normal glow discharges, the impurity content is much lower than in arc discharges; their disadvantage, however, is the low density of the absorbed power. At higher power densities, a glow discharge transforms into an arc discharge. For this reason, we are now looking for various methods for increasing the power density absorbed in a glow discharge, while retaining a low impurity content. One of these methods is to operate with abnormal glow discharges. Another method is to apply various techniques that prevent a glow discharge from transforming into an arc discharge.

A glow discharge can be stabilized by applying a transverse (with respect to the discharge current) magnetic field [5]. In [6–9], results are presented from preliminary studies of a gas discharge stabilized by a transverse magnetic field. It is shown that, in the presence of a transverse magnetic field, it is possible to maintain a diffuse glow discharge at a high (above 300 W/cm^3) power density, working-gas pressures higher than 200 torr, and a low concentration of the cathode-material impurity in the working gas. A significant advantage of this type of discharge is that the transverse magnetic field makes it possible to activate the working gas over a large area.

The objective of the present study was to experimentally investigate the influence of a transverse magnetic field, as well as the pressure and composition of the working gas, on the discharge parameters, such as the rotation frequency of the current channel, the electric field in the positive column, and the cathode voltage drop.

2. EXPERIMENTAL RESULTS AND DISCUSSION

A schematic of the experimental device is shown in Fig. 1. The current channel is formed between a cathode and an orificed anode in a transverse magnetic field. The magnetic field is produced by an annular magnet. The current channel rotates in the magnetic field around the cathode–anode axis. In the plasma device presented in Fig. 1, the cathode is placed outside the magnet in a decaying magnetic field. We also performed experiments in which the cathode was placed inside a magnetic coil that produced a slightly nonuni-

1063-780X/04/3009-0797$26.00 © 2004 MAIK "Nauka/Interperiodica"

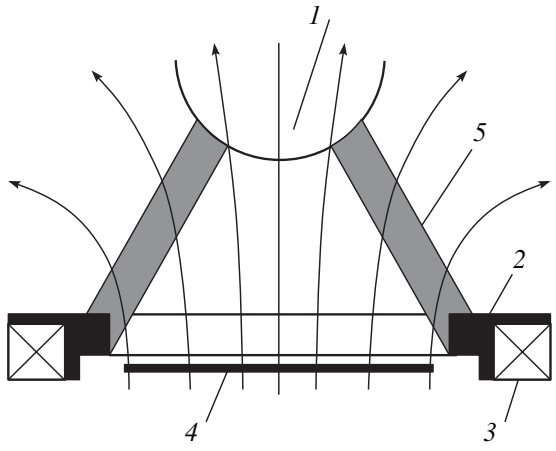

Fig. 1. Experimental setup: (*1*), cathode, (*2*) anode, (*3*) annular magnet, (*4*) substrate's holder, and (*5*) current channel.

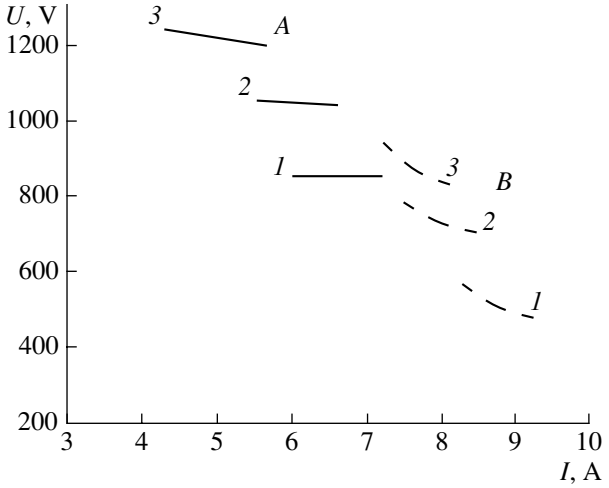

Fig. 2. *V–I* characteristic of a gas discharge in hydrogen for *P* = (*1*) 100, (*2*) 160, and (*3*) 200 torr. Segments *A* and *B* are shown by the solid and dashed lines, respectively.

form field (up to $B \approx 500$ G at the axis). The experiments were performed at working-gas pressures of P = 75–200 torr. The distance between the cathode and anode was l = 3–5 cm, the diameter of the substrate's holder was 5 cm, and the power absorbed in a discharge was 4–7 kW. The cathode was made of molybdenum and was cooled with water, and the anode was made of stainless steel or copper. In experiments, the discharge current was varied in the range I = 3–10 A and the voltage was varied in the range U = 400–1300 V. As a working gas, we used pure hydrogen and hydrogen-containing mixtures: hydrogen and methane (1 vol %); hydrogen and argon (10 vol %); and hydrogen, methane (1 vol %), and argon (10 vol %).

Figure 2 shows the voltage–current (*V–I*) characteristic of a gas discharge in hydrogen. An addition of methane or argon to hydrogen does not qualitatively change the *V–I* characteristic: an addition of methane somewhat increases the discharge voltage, while an addition of argon somewhat decreases it. It can be seen from Fig. 2 that, at a given working-gas pressure, the *V–I* characteristic consists of two segments, *A* and *B*. The discharge voltage in segment *A* depends only slightly on the discharge current. This segment of the *V–I* characteristic is similar to the characteristic of a normal glow discharge [10]. At low pressures (10–50 torr), a dark space is observed between the positive column and the cathode and a cathode glow is observed at the cathode. As the pressure increases, the length of the dark space decreases and, at pressures above 100 torr, the dark space almost disappears. The diffusive character of the positive column is retained up to pressures above 200 torr.

Under certain conditions, the discharge can abruptly pass to the regime described by segment *B*. In this case, the discharge resembles an arc discharge: a cathode spot is formed at the cathode; the voltage decreases with increasing discharge current; the current channel sharply contracts; etc. Below, we only present results of experiments for discharges operating in the regime described by segment *A*.

An important characteristic of the discharge under study is the rotation frequency of the current channel under the action of the force

$$\mathbf{F} = \mathbf{j} \times \mathbf{B}. \quad (1)$$

Here, $\mathbf{j}$ is the density of the current flowing across the magnetic field. The rotation frequency and azimuthal size of the current channel were measured with the help of photoelectric detectors, from variations in the intensity of emission collected from a local plasma volume between the anode and cathode. As such detectors, we used photodiodes or a monochromator with a photomultiplier. In the latter case, the emission of individual spectral lines was resolved. In addition, the rotation frequency was estimated from variations in the signal from an electric probe located 1 cm from the current channel. The azimuthal size of the current channel was determined in a hydrogen discharge at a pressure of P = 120 torr from the line emission of the Balmer series, H_β and H_γ. The thickness of the current channel was determined from geometrical considerations and was estimated at 4 mm. From these data, the current density was found to be $j \approx 1.2$ A/cm^2 [6]. As the pressure was increased at a fixed absorbed power, the azimuthal size of the current channel decreased. The frequency characteristics of the recording equipment did not allow us to determine the thickness of the current channel and the current density at high pressures; however, estimates show that, at a pressure of P = 200 torr, the current density in the channel can be as high as a few amperes per cm^2.

Results of measurements of the rotation frequency of the current channel in a decaying magnetic field are

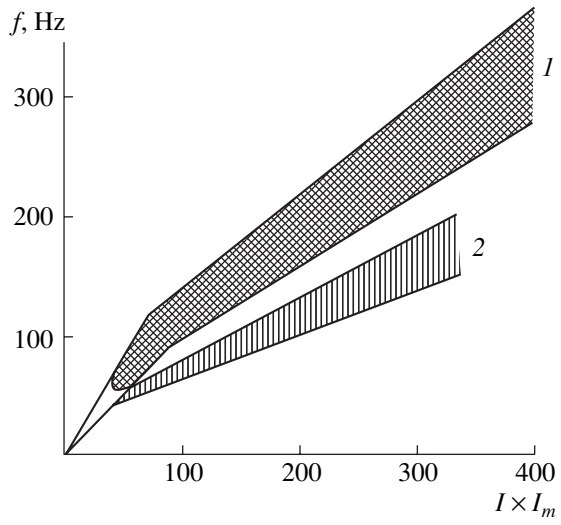

Fig. 3. Rotation frequency of the current channel as a function of the product of the discharge current I and the current I_m flowing in the magnetic coil. The shaded regions correspond to the experimental data obtained at different pressures. The working gas is (*1*) H_2 or H_2 + CH_4 (1 vol %) and (*2*) H_2 + Ar (10 vol %).

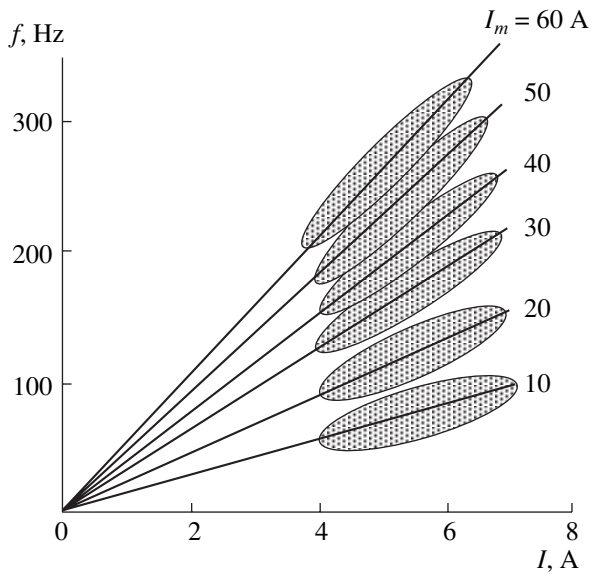

Fig. 4. Rotation frequency of the current channel vs. discharge current. The working gas is H_2 or H_2 + CH_4. The shaded regions correspond to the experimental data obtained at different pressures.

presented in [6–8]. Below, we present the dependences of the rotation frequency of the current channel on the discharge parameters for the case of a cathode placed inside a magnetic coil. It can be seen from expression (1) that the driving force is $F \propto I \cdot I_m/S$, where I_m is the current in the magnetic coil and S is the cross-sectional area of the current channel. Figure 3 shows the dependence of the rotation frequency of the current channel, $f = 1/T$ (where T is the rotation period), on the quantity $I \cdot I_m$. It can be seen that the frequency depends linearly on $I \cdot I_m$; however, this dependence begins not from the coordinate origin. The rotation frequency depends weakly on the working-gas pressure and on the concentration of a small addition of methane to hydrogen. With a 10% addition of argon to hydrogen, the rotation frequency of the current channel decreases significantly. Figure 4 shows the rotation frequency of the current channel as a function of the discharge current. We can see that the rotation frequency depends linearly on the discharge current. The position of the cathode with respect to the magnetic-field source significantly influences both the value and the functional dependence of the rotation frequency of the current channel on the discharge parameters. If the cathode is located inside the magnetic coil, then the rotation frequency depends only slightly on the hydrogen pressure. However, when the cathode is located outside the magnetic-field source, the rotation frequency is substantially lower and varies, e.g., in a hydrogen discharge, as $f \sim 1/P^{1/2}$ [6].

We measured fluctuations in the discharge current δI, in the voltage δU, in the integral emission from a discharge, and in the emission collected from a small local volume inside a discharge. Typical waveforms of the signals observed are presented in Fig. 5. It can be seen that the current signals differ from sinusoidal, have a frequency of 300 Hz, and coincide in shape and frequency with pulsations in the voltage of the three-phase rectifier of the discharge-current source. The amplitude of the current pulsations was $\delta I/I$ = 0.25–0.7 and increased with pressure. Fluctuations in the integral emission correlate well with the current fluctuations. Fluctuations in the emission collected from a local volume are related to the motion of the current channel in the field of view of the photoelectric detector.

Voltage fluctuations in the range $\delta U/U$ = 0.02–0.08 are generally uncorrelated with current fluctuations (see Fig. 5); only at pressures of P > 160 torr, correlation between voltage and current fluctuations was

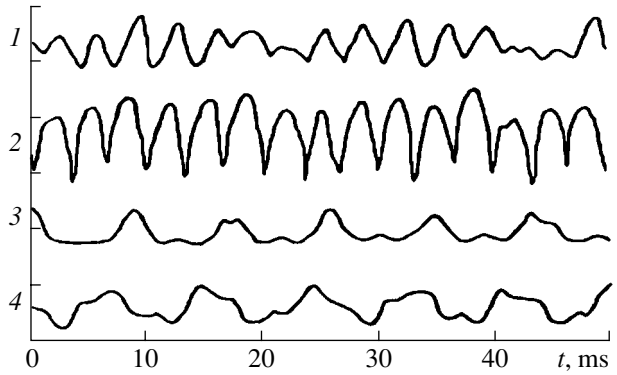

Fig. 5. Waveforms of the main discharge parameters (P = 158 torr, I = 5.9 A, U = 1068 V, the working gas is hydrogen): (*1*) integral glow, (*2*) current, (*3*) emission collected from a local plasma volume, and (*4*) voltage.

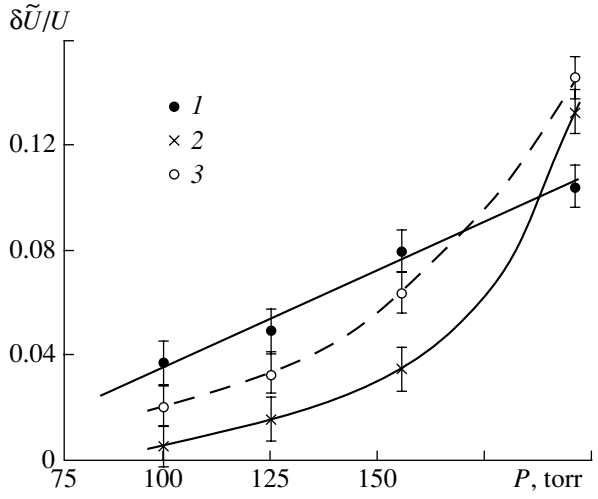

Fig. 6. Amplitude of the voltage fluctuations vs. hydrogen pressure (I_m = 30 A): (*1*) $\delta U_f/U$, (*2*) $\delta U_I/U$, and (*3*) $\delta U_\omega/U$.

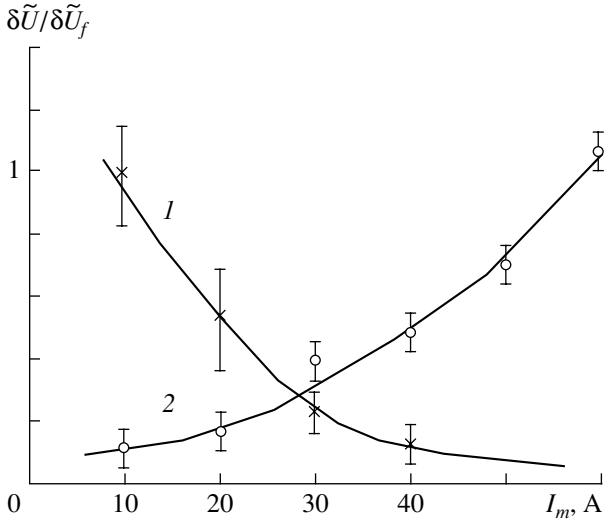

Fig. 7. Influence of the magnetic field on voltage fluctuations in a hydrogen discharge (P = 130 torr): (*1*) $\delta U_I/\delta U_f$ and (*2*) $\delta U_\omega/\delta U_f$.

observed. The correlation analysis of the spectrum of voltage fluctuations makes it possible to represent them in the form

$$\delta U = \delta U_f + \delta U_\omega + \delta U_I. \quad (2)$$

Here, δU_f are the voltage fluctuations related to the regular rotation of the current channel and caused by the misalignment of the anode and the cathode, δU_ω are the fluctuations related to the nonuniform rotation of the current channel, and δU_I are the fluctuations related to the current pulsations. Figure 6 shows how the amplitudes of voltage fluctuations related to the current pulsations, the rotation of the current channel, and the nonuniformity of this rotation depend on the hydrogen pressure. It can be seen that the value of $\delta U_f/U$ increases linearly with pressure, whereas the values of $\delta U_\omega/U$ and $\delta U_I/U$ increase appreciably only at pressures $P > 160$ torr and become comparable to $\delta U_f/U$ at $P \cong 200$ torr. Figure 7 shows $\delta U_\omega/U_f$ and $\delta U_I/U_f$ as functions of the magnetic field. It can be seen from Fig. 7 that, as the magnetic field increases, the voltage fluctuations related to the current decrease, while the rotation of the current channel becomes more nonuniform.

If the positive channel is much longer than the lengths of the cathode and anode regions, then the discharge voltage can be represented in the form

$$U \approx \bar{E} l + U_{ca}. \quad (3)$$

Here, $\bar{E}$ is the average electric field in the positive column and U_{ca} is the sum of the cathode and anode voltage drops. The cathode voltage drop in glow discharges far exceeds the anode drop [10]; consequently, the value of U_{ca} is primarily determined by the cathode voltage drop. According to formula (3), the general expression for voltage fluctuations has the form

$$\delta U = l\delta\bar{E} + \bar{E}\,\delta l + \delta U_{ca}. \quad (4)$$

It is of interest to find out how the magnetic-field fluctuations affect the discharge parameters. The magnetic coil is powered from a biphase rectifier with a characteristic pulsation frequency of 100 Hz. The amplitude of the current variations in the magnetic coil attained 50% of the average current. The experimental results show that the spectra of the current and voltage fluctuations do not contain frequencies typical of the magnetic-field fluctuations. Hence, the discharge under study "feels" only the average magnetic field.

Parameters determining the main characteristics of a gas discharge are the electric field in the positive column and the cathode voltage drop. The correlation analysis of the voltage fluctuations allows us to separate out the term related to the regular rotation of the current channel:

$$\delta U_f = \bar{E}\delta l. \quad (5)$$

Knowing the misalignment of the cathode relative the anode, we can determine the value of $\bar{E}$ from expression (5) and find the value of U_{ca} from expression (3). Figure 8 shows the dependence of the ratio $\bar{E}/P$ on the working-gas pressure. One can see that the ratio $\bar{E}/P$ is a function of the working-gas pressure. The experiments show that the value of $\bar{E}$ for discharges in pure hydrogen and in hydrogen–methane mixtures depends only slightly on the position of the cathode with respect to the magnetic-field source. In experiments with hydrogen–argon mixtures, the cathode was placed

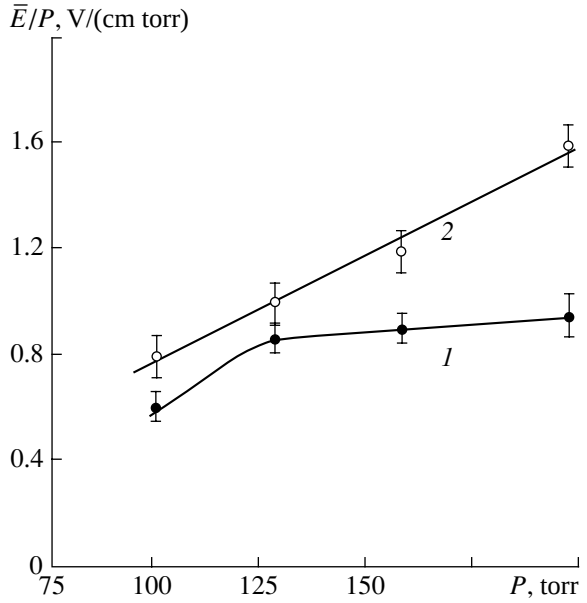

Fig. 8. Ratio $\bar{E}/P$ as a function of the hydrogen pressure: (*1*) H_2 and (*2*) $H_2 + CH_4$.

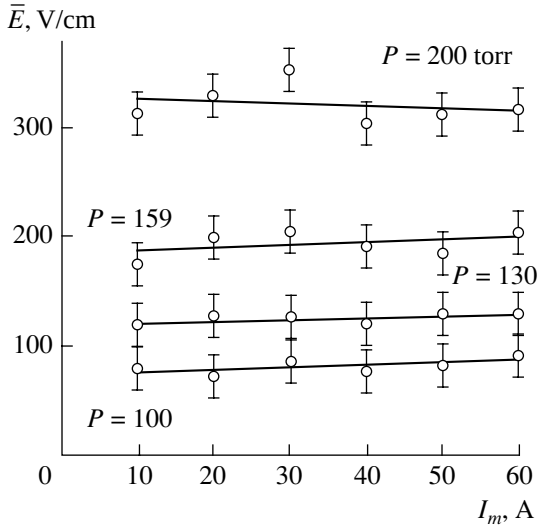

Fig. 9. Average electric field $\bar{E}$ in the positive column as a function of the current in the magnetic coil at different pressures of the hydrogen–methane mixture.

inside the magnetic coil and the value of $\bar{E}$ could not be determined with a sufficient accuracy because of the high level of the voltage fluctuations related to the current pulsations.

Figure 9 shows $\bar{E}$ as a function of the magnetic field. It can be seen that the electric field in the positive column depends only slightly on the magnetic field. At the same time, the cathode voltage drop increases with increasing magnetic field (see Fig. 10). It follows from these data that the increase in the discharge voltage with increasing magnetic fields is primarily related to the influence of the magnetic field on the cathode voltage drop. This influence can be explained by a change in the electron Larmor radius and the related change in the fraction of electrons returning to the cathode. Variations in the cathode voltage drop with changing the position of the cathode with respect to the magnetic-field source can also be attributed to the influence of the magnetic field.

In our experiments, the cathode voltage drop varied from 120 to 800 V, depending on the pressure, the working-gas composition, and the position of the cathode with respect to the magnetic coil. When the cathode was placed inside the magnetic coil, the cathode voltage drop only slightly depended on the pressure (see Fig. 10). It can be seen from Fig. 10 that, in hydrogen discharges at pressures from 100 to 200 torr and in discharges with 1% addition of methane at pressures from 100 to 160 torr, the cathode voltage drop (within the measurement accuracy) varies only slightly. At the same time, for discharges in hydrogen–methane mixtures at pressures higher than 200 torr, the cathode voltage drop decreases significantly. As the pressure increases further, the cathode voltage drop decreases, and, at low magnetic fields (I_m < 40 A), the discharge transforms into an arc. For hydrogen discharges with a cathode placed outside the magnetic coil, the value of U_{ca} varied from 400 to 700 V as the pressure varied from 100 to 200 torr. In argon discharges with this cathode position, U_{ca} reached its minimum value ($U_{ca} \approx$ 120 V) at P = 150 torr [8].

It follows from the results obtained that the *V–I* characteristic of the discharge under study corresponds

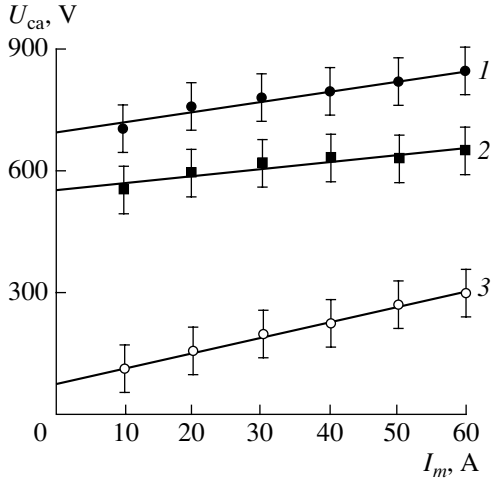

Fig. 10. Cathode voltage drop U_{ca} as a function of the current I_m in the magnetic coil for different working gases: (*1*) $H_2 + Ar + CH_4$ at P = 200 torr; (*2*) H_2 at P = 100, 130, 159, and 200 torr; $H_2 + CH_4$ at P = 100, 130, and 159 torr; and (*3*) $H_2 + CH_4$ at P = 200 torr.

to a normal glow discharge. Measurements of the voltage fluctuations show that the electric field in the positive column does not depend on the current at pressures of up to ~160 torr. At higher pressures, the current substantially influences the value of δU_I (see Fig. 6).

It is well known that, in a normal discharge, the following condition is satisfied:

$$\mathbf{j} = \sigma \cdot \mathbf{E} = \text{const}, \quad (6)$$

where σ is the electric conductivity. Condition (6) is obviously satisfied when E = const and σ = const, as is the case in our experiments up to pressures of $P \approx$ 160 torr, when $\delta U_l/U \ll \delta U_f/U$. Condition (6) can also be satisfied when

$$\frac{\delta E}{E} = -\frac{\delta \sigma}{\sigma}, \quad (7)$$

i.e., when a change in the electric field is caused by a change in the conductivity. The fulfillment of condition (7) can be associated, e.g., with a small change of the voltage in a normal glow discharge as the discharge current increases (see Fig. 2) due to an increase in the gas temperature [10]. The same mechanism can also operate in the presence of current fluctuations $\delta I/I$. In this case, the level of fluctuations $\delta U_I/U$ can be estimated from a change in the discharge voltage with increasing current ($\partial U/\partial I$ in the V–I characteristic). For a pressure of $P \approx 200$ torr, we have

$$\frac{\delta U_I}{U} \approx \left|\frac{\partial U}{\partial I}\right| \frac{\delta I}{I}\frac{I}{U} \approx 0.1. \quad (8)$$

This value agrees well with the experimental data presented in Fig. 6. From this estimate, we can conclude that, in the discharge under study, condition (7) is apparently satisfied at pressures above 160 torr. As a result, the level of the voltage fluctuations related to the current pulsations, $\delta U_I/U$, increases. Hence, we can conclude that, in the pressure range 75–200 torr, the discharge is similar to a normal glow discharge in the absence of a magnetic field and the quantity δU_I is related to the conductivity fluctuations, which are substantially affected by the transverse magnetic field (see Fig. 7).

It is of interest to compare the data obtained with the results of theoretical and experimental studies of classical normal glow discharges in the absence of a magnetic field. Most of the available information concerns glow discharges in hydrogen. For this reason, the results of our experiments with hydrogen discharges will only be used for such a comparison. In normal glow discharges under conditions close to our experimental conditions, the ratio E/P is about 0.4 V/(cm torr) and is almost independent of the pressure [10]. Our experimental data show that the minimum value of E/P is 0.6 V/(cm torr) and the dependence of this ratio on the hydrogen pressure is rather complicated and typical of abnormal glow discharges (see Fig. 8).

The experiments showed that the cathode voltage drop in hydrogen discharges varied from 400 to 700 V and was a function of the pressure, the magnetic field, and the position of the cathode with respect to the magnetic coil. In classical normal glow discharges in the absence of a magnetic field, the cathode voltage drop does not depend on the working-gas pressure and is a function of the working-gas composition and the cathode material. The value of U_{ca} is difficult to compare with data of other authors because such information for molybdenum cathodes is lacking. However, according to [10], the value of the cathode voltage drop in normal glow discharges for fifteen different cathode materials lies in the range from 94 V (for potassium) to 276 V (for platinum). Thus, the measured value of U_{ca} in our experiments substantially exceeds the literature data. This difference, which is characteristic of abnormal glow discharges, cannot be explained by experimental errors because the measured values of both $\bar{E}$ and U_{ca} exceed the literature data for normal glow discharges and the accuracy of the measurements of the discharge voltage in our experiments was no worse than 10^{-3}.

In normal glow discharges, the ratio j/P^2 is constant and depends only on the working gas composition and the cathode material. In our experiments at P = 120 torr, this ratio was j/P^2 = 80 μA/(cm^2 torr^2). Data on the value of j/P^2 in hydrogen discharges with a molybdenum cathode are lacking. According to [10], the values of j/P^2 in hydrogen discharges with different cathodes lie in the range 64–110 μA/(cm^2 torr^2). Our experimental results fall into this range.

The results obtained show that, with respect to a number of parameters (the V–I characteristic, the voltage, and the value of j/P^2), the discharge under study behaves as normal glow discharge in the absence of a magnetic field. However, the values of $\bar{E}/P$ and U_{ca} better correspond to an abnormal glow discharge. It is likely that the motion of the current channel in the working gas and over the cathode surface increases the values of $\bar{E}$ and U_{ca} to those required to maintain a normal glow discharge. It is due to this motion that the positive diffuse column is retained at such high pressures.

Note that there are some difficulties in understanding the observed motion of the current channel. Estimates show that, assuming that the driving force is balanced by the friction of plasma ions against the neutral gas, the rotation frequency of the current channel should be almost two orders of magnitude higher than its measured value. It is also difficult to explain some of the experimental results. First of all, we note that the linear dependence of the rotation frequency on the driving force begins not from the coordinates origin (see Fig. 3). Another surprising fact is that the rotation frequency of the current channel depends on the discharge current (see Fig. 4). As is known, the current density in a normal glow discharge is constant and, hence, driving

force (1) should not vary in a fixed magnetic field. Apparently, the motion of the current channel is diffusive in character and the plasma-density and temperature gradients are produced and maintained by the driving force.

The power density absorbed in a discharge is defined by the expression

$$w = \mathbf{j} \cdot \mathbf{E}. \quad (9)$$

For a normal glow discharge in hydrogen under conditions close to our experimental conditions, the power density is $w \approx 3.2 \times 10^{-5} P^3$ W/cm^3; for P = 200 torr, we have $w \approx 256$ W/cm^3. Assuming that, in the discharge under study, the ratio $j/P^2 = 80$ μA/(cm^2 torr^2) remains constant with increasing pressure, we can expect the current density to be $j = 3.2$ A/cm^2 at P = 200 torr. This estimate does not contradict the preliminary experimental results. In this case, in a hydrogen discharge at P = 200 torr, the specific absorbed power in the current channel is 640 W/cm^3. Taking into account that, at such pressures, the current channel occupies a sector of nearly 70° in the space between the anode and cathode, the average power density above the substrate is 120 W/cm^3. The average power density can further be increased by enlarging the cross-sectional area of the current channel and/or increasing the working-gas pressure; this will certainly require higher magnetic fields. Our experiments showed that, in the discharge under study, at power densities comparable to those in arc discharges, the amount of impurity arriving from the cathode is rather low [9]. Moreover, such a discharge can activate the working gas over a large area, and we do not see any physical and technical obstacles to activating the working gas above a surface as large as 0.1 m^2.

3. CONCLUSIONS

(i) A transverse magnetic field of $B \leq 500$ G makes it possible to maintain a diffuse discharge at pressures higher than 200 torr and specific absorbed powers in the current channel above 0.5 kW/cm^3 at a low content of impurity arriving from the cathode.

(ii) At specific absorbed powers characteristic of arc discharges, the discharge under study in many respects resembles a normal glow discharge.

(iii) The cathode voltage drop and the electric field in the positive column exceed their values in classical normal glow discharges in the absence of a magnetic field.

(iv) The rotation frequency of the current channel is a complicated function of the discharge parameters and, at a magnetic field of about 300 G near the anode, is as high as 400 Hz.

(v) Owing to its stable operation at working gas pressures of about 200 torr, the high energy characteristics, the low content of cathode-material impurity, and the capability of activating a gas above a large surface, this type of discharge can be used in various plasmochemical processes, in particular, for the synthesis of diamond coatings from a gaseous phase.

REFERENCES

1. E. P. Velikhov, A. S. Kovalev, and A. T. Rakhimov, *Physical Phenomena in Gas-Discharge Plasma* (Nauka, Moscow, 1987).
2. D. I. Slovetskiĭ, *Mechanisms of Chemical Reactions in Nonequilibrium Plasma* (Nauka, Moscow, 1980).
3. D. V. Rusanov and A. A. Fridman, *Physics of Chemically Active Plasma* (Nauka, Moscow, 1984).
4. B. V. Spytsin, L. L. Bouilov, and B. V. Deryagin, J. Cryst. Growth **52**, 219 (1981).
5. M. Nesladek, Diamond Relat. Mater. **2**, 357 (1993).
6. V. K. Pashnev, O. A. Opalev, V. A. Belous, and V. E. Strel'nitskij, in *Proceedings of the 4th International Symposium on Diamond Films and Related Materials, Kharkov, 1999*, p. 18.
7. O. A. Opalev, V. K. Pashnev, I. K. Koval'chuk, *et al.*, Vopr. At. Nauki Tekh., Ser.: Fiz. Radiats. Povrezhd. Radiats. Materialovedenie, No. 4, 158 (2000).
8. V. K. Pashnev, V. E. Strel'nitskij, O. A. Opalev, *et al.*, in *Proceedings of the 5th International Symposium on Diamond Films and Films of Diamond-Like Materials, Khar'kov, 2002*, p. 6.
9. V. K. Pashnev, O. A. Opalev, I. I. Vyrovets, *et al.*, in *Proceedings of the 12th International Symposium on Thin Films in Electronics, Kharkov, 2001*, Ed. by V. I. Lapshin, M. A. Prelas, B. V. Spitsyn, and V. M. Shulaev, p. 87.
10. Yu. P. Raizer, *Gas Discharge Physics* (Nauka, Moscow, 1987; Springer-Verlag, Berlin, 1991), p. 355.

Translated by N.F. Larionova

Plasma Physics Reports, Vol. 30, No. 9, 2004, pp. 804–805. Translated from Fizika Plazmy, Vol. 30, No. 9, 2004, pp. 863–864.

On the 80th Anniversary of the Birth of Yuriĭ L'vovich Klimontovich
(September 28, 1924–November 27, 2002)

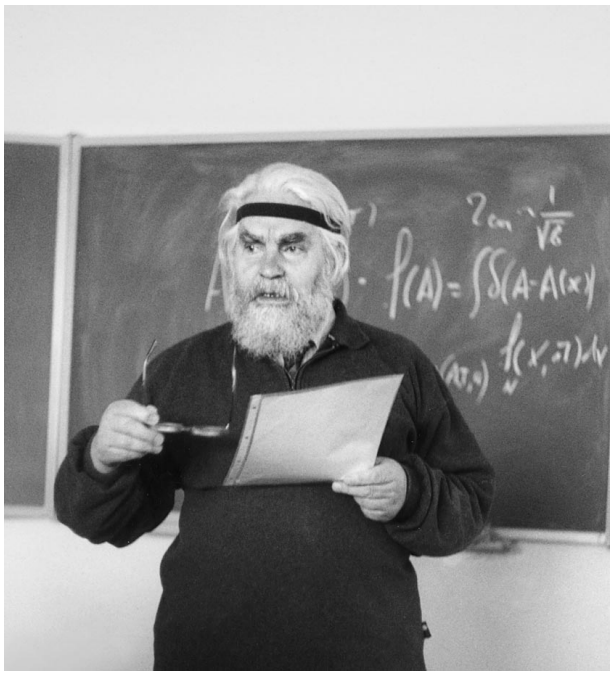

Yuriĭ L'vovich Klimontovich, an eminent theoretical physicist, was an outstanding representative of Moscow University's school of physics. The readers of our journal know him as the author of the self-consistent method for describing plasma kinetics (as well as the kinetics of any ensemble of many particles) in terms of the microscopic particle density in phase space. The equation for the particle densities in phase space follows from the conservation of the number of particles of each sort (electrons and ions):

$$\frac{dN}{dt} = \frac{\partial N(\mathbf{r}, \mathbf{p}, t)}{\partial t} + \mathbf{v}\frac{\partial N}{\partial \mathbf{r}} + \dot{\mathbf{p}}\frac{\partial N}{\partial \mathbf{p}} = 0.$$

Here, $\dot{\mathbf{p}} \equiv d\mathbf{p}/dt$ is expressed through the equation of motion of a particle under the action of a microscopic force, $\dot{\mathbf{p}} = \mathbf{F}(\mathbf{r}, t)$. For a fully ionized plasma, this is the microscopic Lorentz force $\mathbf{F}(\mathbf{r}, t) = e\left(\mathbf{E} + \frac{1}{c}\mathbf{v} \times \mathbf{B}\right)$, in which the vectors **E** and **B** are determined from Maxwell's equations with the total (summed over all of the ions and electrons) microscopic space-charge and current densities:

$$q(\mathbf{r}, t) = \sum_i e_i \delta(\mathbf{r} - \mathbf{r}_i(t)),$$

$$\mathbf{j}(\mathbf{r}, t) = \sum_i e_i \mathbf{v}_i \delta(\mathbf{r} - \mathbf{r}_i(t)).$$

This method was then generalized by Klimontovich to the case of a system of many particles with arbitrary interactions.

The advantage of the method of microscopic phase density (in comparison to the more formal classical Bogolyubov–Born and Green–Kirkwood–Yvon methods, in which the kinetics of a system of interacting particles is described by the chain of coupled equations for the one-particle, two-particle, etc., distribution functions over coordinates and momenta) is that it is not only more descriptive but also more constructive. Thus, the collision integral in the kinetic equation is expressed through the fluctuation correlations δN and $\delta\mathbf{E}$ and does not require the solving of an equation for the two-particle distribution function. This method was then extended by Klimontovich to the statistical theory of quantum systems. He also developed advanced methods for describing continuous media.

Over the last few decades of his life, Klimontovich concentrated on the kinetic theory of electromagnetic processes. He obtained a number of important results on the theory of spectral line broadening and nonlinear laser spectroscopy. With his own special keenness, he sought new approaches to the universal description of highly nonequilibrium systems.

For more than 40 years, Klimontovich taught at Moscow State University (MSU). His profound and highly informative lectures found great success among students. He read lectures at foreign universities and was an honorary member of several foreign academies and an honorary doctor of a number of foreign universities. He wrote a series of monographs on plasma kinetics and statistical plasma physics, as well as three monographs in which he formulated his ideas about the statistical theory of open systems.

The course of his life was not easy. He was born into the family of a nobleman. In 1937, his father was

1063-780X/04/3009-0804$26.00 © 2004 MAIK "Nauka/Interperiodica"

arrested and soon executed. After graduating from school, Klimontovich entered the Transport Engineering Institute. During the Second World War, he worked as an electrician at the Ministry of Communications. After the end of the war, Klimontovich passed additional examinations and was enrolled as a third-year student at the Physics Department of MSU. Here, he rose to the position of professor and head of the Theoretical Laboratory. At MSU, he was greatly influenced by two people: N.N. Bogolyubov, his graduate advisor, who determined the area of his scientific interests (physical kinetics), and R.L. Stratonovich, his friend and colleague, the author of the mathematical theory of fluctuations in radiophysics.

The personal human qualities of Klimontovich were his exceptional kindness, politeness, and delicacy, in combination with firmness in defending his opinion.

For everyone who knew Yuriĭ L'vovich Klimontovich, he will remain an outstanding representative of the Russian intellectuals and an eminent physicist who made a fundamental contribution to science.

V.I. Kogan, Yu.A. Kukharenko, V.S. Lisitsa, and V.D. Shafranov

Some monographs by Yu.L. Klimontovich:

1. Yu. L. Klimontovich, *The Statistical Theory of Nonequilibrium Processes in a Plasma* (Izd. Mosk. Gos. Univ., Moscow, 1964; Pergamon, Oxford, 1967).
2. Yu. L. Klimontovich, *Kinetic Theory of Nonideal Gases and Nonideal Plasmas* (Nauka, Moscow, 1975; Pergamon, Oxford, 1982).
3. Yu. L. Klimontovich, *The Kinetic Theory of Electromagnetic Processes* (Nauka, Moscow, 1980; Springer-Verlag, Berlin, 1983).
4. Yu. L. Klimontovich, *Statistical Physics* (Nauka, Moscow, 1982; Harwood, New York, 1986).
5. Yu. L. Klimontovich, H. Wilhelmsson, I. P. Yakimenko, and A. G. Zagorodny, *Statistical Theory of Plasma–Molecular Systems* (Izd. Mosk. Gos. Univ., Moscow, 1990).
6. Yu. L. Klimontovich, *Statistical Theory of Open Systems* (Yanus, Moscow, 1995; Kluwer Academic, Dordrecht, 1998), Vol. 1.
7. Yu. L. Klimontovich, *Statistical Theory of Open Systems* (Yanus, Moscow, 1998–2001), Vols. 2–3.